Mechanics and Multi-Physics Deformation Behavior of Polymer Electrolyte Membranes

by

Meredith Natania Silberstein

Bachelor of Science
Massachusetts Institute of Technology, 2005

Master of Science
Massachusetts Institute of Technology, 2008

Submitted to the Department of Mechanical Engineering
in partial fulfillment of the requirements for the degree of

Doctor of Philosophy in Mechanical Engineering

at the

MASSACHUSETTS INSTITUTE OF TECHNOLOGY

June 2011

Author . . . . . .

Department of Mechanical Engineering
May 23, 2011

Certified by . . . . . .

Mary C. Boyce
Kendall Family Professor of Mechanical Engineering
Thesis Supervisor

Accepted by . . . . . .

David E. Hardt
Cross Professor of Mechanical Engineering
Chairman, Department Committee on Graduate Students

Mechanics and Multi-Physics Deformation Behavior of Polymer Electrolyte Membranes

by

Meredith N. Silberstein

Submitted to the Department of Mechanical Engineering
on May 23, 2011, in partial fulfillment of the
requirements for the degree of
Doctor of Philosophy in Mechanical Engineering

Abstract

Fuel cells are a developing technology within the energy sector that offer both efficiency and environmental advantages over traditional combustion processes. In particular, proton exchange membrane fuel cells (PEMFC) are promising for transportation and portable devices due to their low operating temperature, reduced CO_2 emissions, and scalability. A central component is the polymer electrolyte membrane (PEM) which conducts protons from the fuel source (typically either hydrogen or methanol) at the anode to the cathode where it reacts with oxygen while preventing the transport of either electrons or the fuel itself. Historically membranes have been designed primarily in terms of maximizing proton conductivity, but it is also important that they prevent fuel crossover and have minimal chemical and mechanical degradation over the target lifetime of the fuel cell. Membrane mechanical integrity is thus a critical concern for commercial distribution of PEMFC technology.

This thesis has two primary focus areas: (1) characterization and modeling of Nafion, the benchmark PEM, in order to understand hygro-thermal loading in the existing technology and (2) mechanical characterization and modeling toward the development of an alternative polymer electrolyte membrane. These two areas are linked by the common technological application of low temperature fuel cells and can also be placed more broadly in the field of microstructurally and micromechanically informed constitutive modeling.

The persulfonated polytetrafluoroethylene membrane Nafion is perhaps the most commercially prominent and widely studied polymer electrolyte membrane (PEM). Here Nafion is experimentally characterized first under monotonic and cyclic uniaxial tensile loading as a function of rate, temperature, and hydration. The data is used to develop a microstructurally motivated three-dimensional constitutive model. The Nafion model is validated under uniaxial tension for monotonic, cyclic, stress relaxation, and creep loading at various environmental conditions. Small and wide angle x-ray scattering characterization is then performed during uniaxial tensile testing in order to assign a microstructural interpretation to the mechanical behavior.

The model is then validated for loading conditions which are expected to occur in the fuel cell, specifically, biaxial tension in the membrane plane and constrained swelling. Biaxial characterization is conducted via in-plane tensile testing of cruciform shaped specimens. The biaxial response is found to be qualitatively similar to the uniaxial response with the stiffness and strength in a given direction dependent on the degree of biaxiality. The constitutive model was shown to well predict this complex multiaxial deformation response when the model is implemented in the experimental geometry and reduced by the same methods as the experimental results. Bimaterial strip swelling of Nafion and typical gas diffusion layer material (GDL) is used to probe the partially constrained swelling behavior of Nafion. When the strip is hydrated the membrane swells causing the strip to curl with the membrane on the convex side until the force from the membrane is balanced by a moment in the GDL. Upon drying, plastic deformation that occurred during hydration induces a

residual curvature of the opposite convexity. The hydrated and dried radii are found to agree with the finite element simulation predictions for two thicknesses of Nafion to within experimental error. Finally, the Nafion constitutive model is used to simulate a simplified fuel cell cycle. A negative hydrostatic pressure develops in the membrane upon drying, suggesting a driving force for cavitation or crazing. A study of the effect of ramp rate and hold time reveal a significant time dependence of the pressure, which is not surprising given the significant rate dependence observed for Nafion under uniaxial mechanical loading. Simulations of this nature are useful in guiding startup and shutdown procedures for fuel cells, for designing/validating potential procedures for accelerated lifetime testing, and for designing alternative fuel cell geometries.

Focus is then shifted to the design of new polymer electrolyte membranes for direct methanol fuel cells (DMFC) which are a special case of PEMFC. DMFC operate under the same principal as PEMFC, however the fuel is liquid methanol rather than hydrogen. The high energy density of methanol makes DMFC particularly promising for portable applications where they could replace Li-ion batteries. In contrast to PEMFC, fuel crossover is a major design concern even when the membrane is fully intact. Given the multi-functionality of a DMFC PEM, it is natural to look to a composite solution. For the proton transport and fuel crossover resistance we use a chemistry and synthesis technique developed in the Hammond lab at MIT. This membrane is itself a composite of sulfonated Poly(2,6-dimethyl 1,4-phenylene oxide) (sPPO) and poly(diallyl dimethyl ammonium chloride) (PDAC) assembled via layer-by-layer (LBL) deposition. Unfortunately these films tear easily under dry conditions and are almost fluid like under hydrated conditions. The PDAC/sPPO membrane must therefore be combined with a mechanical support component. Here we use a highly porous and mechanically robust mat produced by electrospinning polyamide (EFM). In this thesis, focus is on the mechanical aspects of the design.

A model for the mechanical behavior of the composite is developed based on experiments and models of the component materials. Uniaxial tensile tests are conducted on each of the materials (LBL, EFM, and LBL coated EFM) and the material morphology is examined via scanning electron microscopy where appropriate (EFM and LBL coated EFM). A micromechanically motivated constitutive model is then developed separately for the LBL and the EFM. The LBL model is a single mechanism elastic-plastic model that is highly hydration sensitive. The EFM structure is idealized as a layered triangulated network of elastic-plastic fibers. The behavior of the constituent fibers is taken to be elastic-plastic accounting for stretching and bending of the fibers when subjected to end tensile and compressive loads; the bending of the fibers when a fiber is locally under compression is found to be the key mechanism enabling the mat to consolidate during tensile loading. The layers of triangles impose mutual kinematic constraints emulating the layered structure of real mats, providing greater isotropy to the yield and post-yield behavior. A composite model is then developed as the superposition of the two materials. It is found that a composite model consisting of a weighted summation of the two component behaviors can capture the dry behavior, but not the hydrated behavior. In the hydrated state, the LBL, which is itself quite compliant under uniaxial loading, is found to inhibit fiber bending, thereby lending initial elastic stiffness and reducing post-yield hardening in a non-additive manner.

Thesis Supervisor: Mary C. Boyce
Title: Kendall Family Professor of Mechanical Engineering

Acknowledgements

First, I wish to express my gratitude towards my thesis advisor Professor Mary Boyce for her support and guidance throughout my undergraduate and graduate education. I would also like to thank the rest of my thesis committee for their advice and contribution to my education throughout my MS and PhD research: Professor Yang Shao-Horn, Professor Paula Hammond, and Professor Zhigang Suo.

Many thanks to Una Sheehan, Ray Hardin, Pierce Hayward, Joan Kravit, and Leslie Regan, for their support, which always far exceeded administrative details. I would like to thank the graduate students that directly contributed to my research: Nathan Ashcraft, Chia-Ling Pai, David Liu, Matthew Mannarino, and Priam Pillai; as well as my lab mates, basement mates, and other grad students and postdocs who somehow don't work in a basement, for their help throughout the last 5 years: Juha Song, Tim Johnson, Carlos Castro, Jeff Palmer, Katia Bertoldi, Damien Eggenspieler, Karen Shu, Lifeng Wang, Brian Greviskes, Renaud Rinaldi, Shawn Chester, Dave Henann, Ethan Crumlin, Yaning Li, Ashley Browning, Hansohl Cho, Jie Yin, Ting Ting Chen, and Shawna Liff. Lastly I'd like to thank my family, friends, and sMITe teammates for drastically improving the grad school experience.

Contents

List of Figures

List of Tables

1 Introduction

Polymer electrolytes are solid phase materials which are ionically conducting. They are abundant in biopolymers and also exist in many synthetic forms(Oosawa, 1971). Synthetic polymer electrolytes offer advantages over liquid electrolytes in terms of stability, safety, and packaging, and advantages over traditional ceramic type solid electrolytes in terms of the ability to deform without cracking and forming good interfaces with electrodes(Bruce and Vincent, 1993). These advantages of polymer electrolytes situate them at a powerful place within the field of electrochemistry.

A few of the major applications of polymer electrolytes will be discussed here before moving to a more in depth discussion of polymer electrolytes for low temperature fuel cells. Lithium ion batteries rely on the transfer of lithium ions between intercalation compounds at the anode and cathode during charging and discharging. Traditionally this is accomplished via a liquid electrolyte with a separator to electronically insulate the anode and cathode, however liquid electrolytes decompose under the high oxidation potential. A solid polymer electrolyte can serve as both the separator and electrolyte and tends to be more chemically and mechanically stable than its liquid counterpart. Although the conductivities are still not high enough for practical application, modifications such as swelling the crosslinked network with a conductive solvent make this a promising technology in which the understanding of and modeling capabilities for polymer electrolytes can assist development(Meyer, 1998). Another device which requires a chemically and mechanically stable ion conducting medium is the dye sensitized solar cell (DSSC) or Grätzel cell. Electricity generation in a DSSC relies on the oxidation of iodide to triiodide within the electrolyte and the transfer of electrons from the counter-electrode to the electrolyte to reduce the triiodide, however the long term performance is limited by leakage and volatization of the liquid electrolyte. Solid and gel polymer electrolytes are currently being investigated to replace liquid electrolytes(Li et al., 2006; Wang, 2009) in the cell. One application that capitalizes on the solid elastic nature of the ionically conducting polymer electrolyte is ionic polymer metal composites (IPMC). These devices which can act as either actuators or sensors consist of a polyelectrolyte membrane coated with electrically conductive particles on both sides. When a voltage is applied to the metal faces, the composite undergoes a large bending motion and vice versa. The bending occurs as a result of the depletion of cations from a boundary layer at the anode and a surplus of cations at the cathode which causes either a swelling or shrinkage at each end depending on the specific interplay of elastic and electrostatic forces within the microstructure(Nemat-Nasser, 2008). These applications are amongst the expanding opportunities for polymer electrolytes.

1.1 Fuel Cells

Fuel cells are a developing technology within the energy sector that offer both efficiency and environmental advantages over traditional combustion processes. In particular, proton exchange membrane fuel cells (PEMFC) are promising for transportation and portable devices due to their low operating temperature, reduced CO_2 emissions, and scalability. A schematic of this type of fuel cell is shown in Figure 1. The central component is the polymer electrolyte membrane (PEM) which conducts protons from the fuel source (typically either hydrogen or methanol) at the anode to the cathode where it reacts with oxygen while preventing the transport of either electrons or the fuel itself. In this way the electric current is forced through an external load and the chemical reaction is harnessed as useful work. Fuel cell units are assembled into stacks of bipolar plates and membrane electrode assemblies (MEA) in order to get a useful voltage and power output (Figure 2).

The bipolar plates which are responsible for distributing fuel to the MEA and conducting electrons are typically made of either steel or graphite. The MEA consists of the PEM sandwiched by gas diffusion electrodes which catalyze the fuel breakup, transport electrons back to the bipolar plates, and transport protons to the membrane. The stack is clamped together into a rigid structure. An optical microscopy image of a typical structure used in industry is shown in Figure 3. The extra channels are the coolant channels required to maintain the fuel cell at the desired operating temperature since the hydrogen-oxygen reaction is exothermic.

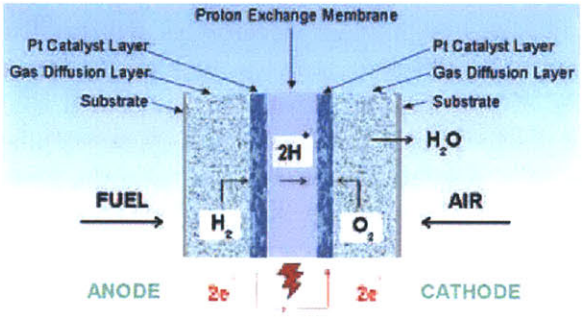

Figure 1: Schematic of proton exchange membrane fuel cell (PEMFC)(Matthey, 2007).

Historically membranes have been designed primarily in terms of maximizing proton conductivity, but it is also important that they prevent fuel crossover and have minimal chemical and mechanical degradation over the target lifetime of the fuel cell. Any holes which develop in the membrane lead to fuel crossover which in turn means the chemical reaction will be wasted as heat and typically accelerate degradation of the membrane. Due to the series configuration of the fuel cell stack, a drop in (or termination of) current in one cell will lead to a drop in current of all the cells. Unless each cell is individually instrumented it is difficult to find and replace the broken cell. Membrane durability is thus a critical concern for commercial distribution of PEMFC technology.

The benchmark membrane for PEMFC is Nafion, a perfluorosulfonated ionomer manufactured by Dupont. Proton transport in Nafion has a strong positive correlation with water content and a weaker positive correlation with temperature (Figure 4). PEMFCs typically operate with humidified fuel streams at $80 - 90^oC$ since pressurization is required to maintain liquid water above 100^oC. There is also a self hydration that occurs due to the production of water as a waste product at the cathode. Nafion swells approximately 50% volumetrically from the ambient conditions at which it is stored when not in operation to the hydrated and elevated temperature state at which it operates best electrochemically. Within the constraint of the fuel cell (primarily enforced by the

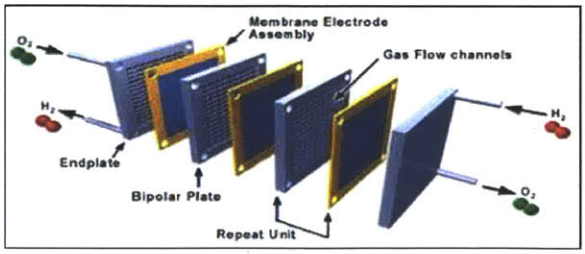

Figure 2: Schematic of fuel cell stack(Kar, 2007).

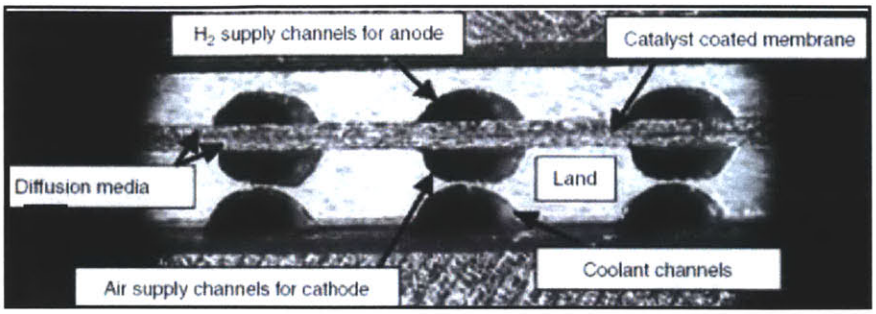

Figure 3: Cross-section of a typical fuel cell (Vielstich et al., 2003).

comparatively rigid bipolar plates), this swelling cannot occur freely. Cycling of the fuel cell between on and off states hence results in significant mechanical loading of the membrane. Over time on/off cycling has been shown to cause pinhole or crack formation which leads to fuel crossover and an accelerating drop in power output (Haung et al., 2006). Chemical degradation mechanisms have been studied extensively leading to targeted changes in the membrane composition and synthesis, however it is only in the last 5 to 10 years that researchers have begun to study the phenomena from a mechanical perspective (Hubner and Roduner, 1999; Inaba et al., 2006; Borup et al., 2007b).

This thesis has two primary focus areas: (1) characterization and modeling of Nafion in order to understand the existing technology and (2) mechanical characterization and modeling toward the development of an alternative polymer electrolyte membrane. These two areas are linked by the common technological application of low temperature fuel cells and can also be placed more broadly in the field of microstructurally and micromechanically informed constitutive modeling.

1.2 Microstructurally and micromechanically informed modeling

Microstructurally and micromechanically informed modeling is a continuum level constitutive modeling approach which seeks to base the modeled macroscopic behavior on the underlying microscopic structure and physical deformation mechanisms such that a small data set as possible can be used to predict a wide range of material behavior. This approach lies in contrast to the approach sometimes taken in industry where experiments are run over the full range of expected loading conditions in order to develop material models via automated curve fitting for simulating a process/function. This modeling methodology offers three primary/potential advantages: (1) material and equipment costs toward model development are significantly reduced; (2) a model for one material can be readily adapted to describe a similar material; and (3) the model can be used to guide design of new materials. A fourth longer term advantage of this approach is that each new well validated model adds to the body of literature for the development of future micromechanical models. The details of this approach depend heavily on the material under investigation, but in polymer based materials it generally relies upon any readily identifiable microscale features and combinations of established molecular level mechanisms. An example of capturing a microscale feature would be using a representative volume element (RVE) of a rubber sphere embedded within a polymer matrix to represent the response of a glassy polymer with randomly distributed rubbery particles. An example of this molecular mechanism approach is modeling the viscoelastic-viscoplastic behavior of glassy polymers based on their random macromolecular network microstructure. Established mechanisms for amorphous glassy polymers include an elastic shear and volumetric response based

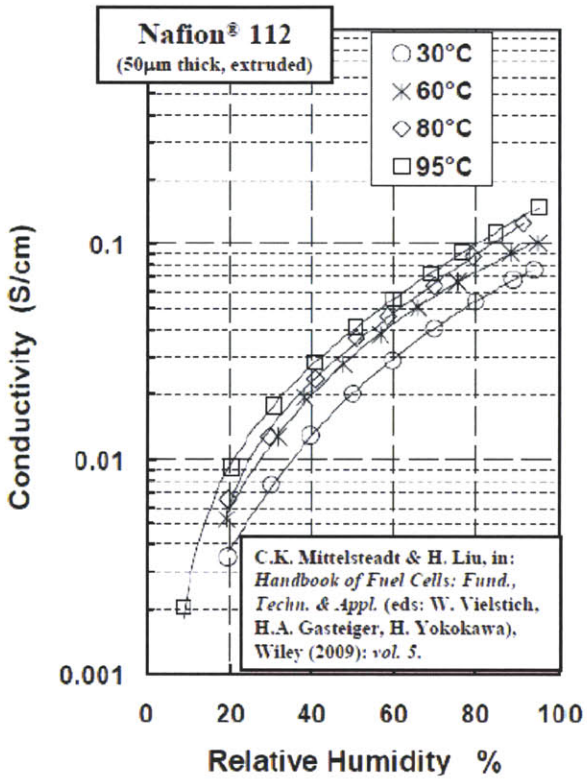

Figure 4: Proton conductivity in Nafion as a function of relative humidity and temperature (Vielstich et al., 2003).

on short range intermolecular interactions, shear driven linear viscoelasticity, rate and temperature dependent shear stress activated viscoplasticity, and long range molecular entropic (or network) elasticity. This thesis will utilize both the microscale and the molecular mechanism approaches with the former applied primarily to the alternative membrane under development and the latter applied to both Nafion and the alternative membrane.

1.3 Technical Overview

Following this introduction chapters 2-4 concern the characterization and modeling of Nafion, chapters 5-7 concern the development of an alternative polymer electrolyte membrane, and chapter 8 discusses future research directions in line with this thesis work.

Chapter 2. The elastic-plastic behavior of the polymer electrolyte membrane (PEM) Nafion is characterized via monotonic and cyclic uniaxial tension testing as a function of strain rate, temperature, and hydration. Dynamic mechanical analysis shows that, under dry ($30\%RH$) conditions, the material begins to transition from the glassy to the rubbery state at 75^oC, with a glass transition of 105^oC. DMA reveals the fully hydrated state to be significantly more compliant than the dry state, with a glass transition beginning at 40^oC. Large strain monotonic tensile tests find the rate-dependent stress-strain behavior to be highly dependent on temperature and hydration. The dry state transitions from an elastic-plastic behavior at 25^oC to an increasingly more compliant behavior and lower yield stress as temperature is increased through the glass transition, until exhibiting a rubbery-like behavior at 100^oC. At 25^oC, the stress-strain behavior remains elastic-plastic for all hydrated states with the stiffness and yield stress decreasing with increasing hydration. Increasing hydration at all temperatures acts to decrease the initial elastic stiffness and yield stress. Unloading from different strains reveals the elastic-plastic nature of the behavior even for the elevated temperature and hydrated states. Cyclic loading-unloading-reloading excursions to different strains show significant nonlinear recovery at all strains past yield with a highly nonlinear reloading behavior which rejoins the initial loading path.

A microstructurally-motivated constitutive model consisting of an intermolecular resistance in parallel with an elastic network resistance is shown to be capable of capturing the rate, temperature, and hydration dependence of the monotonic stress-strain behavior. The intermolecular resistance captures the local intermolecular barriers to initial elastic deformation and also captures the thermally-activated nature of yield; these intermolecular barriers are modeled to decrease with increasing temperature and hydration, in particular mimicking the reduction in these barriers as the material approaches and enters the glass transition regime, successfully capturing the strong temperature and hydration dependence of the stress-strain behavior. The highly nonlinear post-yield unloading and reloading suggest the development of a back stress during inelastic deformation which aids reverse plastic flow during unloading. Inclusion of a back stress which saturates after reaching a critical level provides an ability to capture the highly nonlinear cyclic loading stress response. Hence, the proposed model provides the capability to describe the complex evolution of stress and strain that occurs in PEM membranes due to the constrained hygrothermal cyclic swelling/deswelling characteristic of membranes in operating fuel cells.

Chapter 3. In chapter 3 an x-ray scattering experimental study is conducted to better understand the microstructural origin of the micromechanical model developed in Chapter 2. X-ray scattering is a technique used to deduce nano to microscale aspects of a structure by taking advantage of diffraction due to electron density contrasts. Small and wide angle x-ray scattering (SAXS, WAXS) patterns are collected real time during uniaxial tensile testing. These patterns

are used in conjunction with available literature to analyze the strain, stress, and time dependent microstructural evolution. Four peaks are identified (2 each in the SAXS and WAXS) revealing information about three microstructural features: elongated crystallites, cylindrical ionomer clusters, and intermediate amorphous regions. Each of these peaks (and hence microstructural features) is found to have an evolution strongly correlated with strain, with a secondary dependence on time and stress. From the slopes (and changes in slopes) of these evolutions during monotonic, cyclic, and stress relaxation loading, features in the stress-strain behavior, such as the elastic response, yield, and inelastic recovery can be attributed to specific microstructural aspects. Based on the details of this microstructural assignment, an alternative constitutive model is proposed, further decomposing the intermolecular mechanism. This model will not be implemented in this thesis since it would require additional parameters which cannot be directly evaluated at this time, but it does present an interesting future prospect which could perhaps address existing deficiencies in the model.

Chapter 4 Durability is a major limitation of current proton exchange membrane fuel cells. Mechanical stress due to hygro-thermal cycling is one failure mechanism of the polymer electrolyte membrane (PEM). In a fuel cell the PEM is highly constrained in the membrane plane and relatively unconstrained in the through-thickness direction, leading to primarily biaxial loading upon hygro-thermal cycling. Here, the important effects of the biaxiality and constrained swelling loading conditions on the elastic-viscoplastic Nafion stress-strain behavior are investigated for the first time via experiments and simulation. Biaxial stress-strain behaviors are shown to exhibit similar features to uniaxial behavior including linear elasticity followed by a highly nonlinear transition to yield followed by post-yield strain hardening with highly nonlinear unloading and reloading; these features are each quantitatively dependent on the biaxiality of the loading conditions. The constitutive model is used to quantitatively predict these features and their dependence on biaxiality, demonstrating the validity of the model for multiaxial loading.

Two types of swelling related loading are investigated: partially constrained swelling via a bimaterial swelling test and hygro-thermal cycling within a fuel cell. The bimaterial swelling conditions are examined via experiments in conjunction with modeling. Nafion/GDL bimaterial strips are hydrated and observed to curl significantly with the membrane on the convex side due to the large Nafion hygro-expansion coefficient. Upon drying, the bimaterial strips develop a slight reverse curvature with the membrane on the concave side due to the plastic deformation which had occurred in the membrane during hydration. Finite element simulations utilizing the Nafion constitutive model successfully predict the behavior during hydration and drying, providing insight on the constrained swelling physics and the ability of the model to predict such events. Simulations of in-situ fuel cell hygro-thermal cycling are performed via a simplified two dimensional fuel cell model. The simulation results confirm the finding of other studies that a tensile stress develops in the membrane during drying. Further, a concentration of negative hydrostatic pressure is found to develop just inside the channel region in the dried state supporting the theory of hygro-thermal driven mechanical stresses causing pinhole formation in the channel. This pressure peak is then characterized over multiple cycles as a function of characteristic cycle times.

Chapter 5. While a model of an existing material can be a useful design tool, sometimes an alternative material is needed. Chapter 5 introduces a direct methanol fuel cell membrane being developed in conjunction with the Hammond lab in chemical engineering at MIT. In the design, a material that performs well electrochemically but poorly mechanically, is combined with a material that serves no electrochemical function, but performs well mechanically. Specifically,

poly(diallyl dimethyl ammonium chloride) and sulfonated Poly(2,6-dimethyl 1,4-phenylene oxide) are deposited via the layer-by-layer method onto a highly porous electrospun polyamide mat. Each of the materials (stand alone layer-by-layer film, electrospun mat, and composite) is characterized under monotonic loading at ambient conditions and when wet. The behavior of these materials in each state is contrasted in order to begin to understand the governing composite mechanics.

Chapter 6. Electrospinning is a novel method for creating non-woven polymer mats that have high surface area and high porosity. These attributes make them ideal candidates for multifunctional composites, including direct methanol fuel cells, where they serve as the scaffold for the layer-by-layer polymer electrolyte of Chapter 7. Understanding the mechanical properties as a function of fiber properties and mat microstructure can aid in designing these composites. Further, a constitutive model which captures the membrane stress-strain behavior as a function of fiber properties and the geometry of the fibrous network would be a powerful design tool. Here, mats electrospun from amorphous polyamide are used as a model system. The elastic-plastic behavior of single fibers are obtained in tensile tests. Uniaxial monotonic and cyclic tensile tests are conducted on non-woven mats. The mat exhibits elastic-plastic stress-strain behavior. The transverse strain behavior provides important complementary data, showing a negligible initial Poisson's ratio followed by a transverse:axial strain ratio greater than $-1 : 1$ after an axial strain of 0.02. A triangulated fibrous network framework is developed to emulate the fibrous network structure of the mat. The micromechanically-based model incorporates the elastic-plastic behavior of single fibers into a macroscopic membrane model of the mat. This representative volume element based model is shown to capture the uniaxial elastic-plastic response of the mat under monotonic and cyclic loading. The initial modulus and yield stress of the mat are governed by the fiber properties, the network geometry, and the network density. The transverse strain behavior is linked to discrete deformation mechanisms of the fibrous mat structure including fiber alignment, fiber bending, and network consolidation. The model is further validated in comparison to experiments under different constrained axial loading conditions and found to capture the constraint effect on stiffness, yield, post-yield hardening, and post-yield transverse strain behavior. The model is then used to anticipate the dependence of stress-strain and transverse strain behavior on fiber geometry and mat network structure.

Chapter 7. Finally, a micromechanical model of the composite mechanical behavior is developed. This model will combine the electrospun fiber mat model developed in Chapter 6 with a model for the stand alone layer-by-layer film. First the layer-by-layer film experimental behavior is discussed and a model for the film is presented. Then, simple methods for combining the two material behaviors are explored in order to develop a composite model. These models are evaluated with respect to the composite experimental data. The composite models are used to gain insight into the physics governing the composite mechanical behavior.

2 Nafion uniaxial stress-strain behavior

Most of this chapter has been reprinted from Journal of Power Sources, Vol. 195, M.N. Silberstein and M.C. Boyce, "Constitutive modeling of the rate, temperature, and hydration dependent deformation response of Nafion to monotonic and cyclic loading", pages 5692-5706, copyright 2010.

Portions of this chapter have been reprinted from Journal of Power Sources, Vol. 196, M.N. Silberstein and M.C. Boyce, "Hygro-thermal Mechanical Behavior of Nafion During Constrained Swelling", pages 3452-3460, copyright 2011.

2.1 Background

The persulfonated polytetrafluoroethylene membrane Nafion is perhaps the most commercially prominent and widely studied polymer electrolyte membrane (PEM). The mechanical behavior has been a subject of investigation in recent years (e.g. Kundu et al. (2005), Tang et al. (2006a), Satterfield et al. (2006), Majsztrik et al. (2008), Satterfield and Benziger (2009), Liu et al. (2006b), Liu et al. (2006a), and Kusoglu et al. (2010b)). Collectively, through various experiments including DMA, monotonic tensile, stress relaxation, and creep, studies have identified the dependence of the modulus, yield stress, and post-yield behavior on rate, temperature, and hydration level. The elastic modulus and yield stress were found to decrease significantly with increasing temperature and hydration and to increase slightly with increasing strain rate.

On the modeling front, Weber and Newman (2004) were the first to incorporate mechanical properties into a Nafion model for fuel cell applications. Their one-dimensional model included conductivity, water transport, swelling, and the hydrostatic mechanical behavior of Nafion. This model demonstrated the importance of mechanical constraints on the membrane water content and electrochemical performance. The effect was primarily due to volumetric changes altering the transport lengths, but was also due to hydrostatic stress directly altering water content. Tang et al. (2006a) modeled the membrane behavior as isotropic linear-elastic with isotropic thermal and hydration expansion, where the elastic and expansion properties were taken as constants independent of temperature and hydration. Kusoglu et al. (2006) expanded this model to include yielding assuming elastic-perfectly-plastic behavior and included more detailed characterizations of the thermal and hydration expansion behaviors. Both the elastic modulus and yield stress were given as functions of temperature and relative humidity based on experimental data from Tang et al. (2006a). Kusoglu et al. (2009) further improved the model, fitting experimental data to a phenomenological model to capture the temperature and relative humidity dependence of the stress-strain behavior under constant strain rate monotonic loading. Recently these authors have shown that when Nafion is submerged in water it is more appropriate to model it as a rubber rather than as a semicrystalline polymer(Kusoglu et al., 2010b). Solasi et al. (2008) used a constitutive model consisting of two dissipative mechanisms to capture the nonlinear time dependent hygro-thermomechanical behavior. The model was able to simulate monotonic uniaxial tension with hydration and strain rate dependent yield, moderate strain hardening, and stress relaxation at low to moderate strains. Lai et al. (2009b) modeled Nafion as linear viscoelastic with linear expansion with increasing temperature and water content, using relaxation master curves to account for shifts due to temperature and hydration. In situ simulations that were performed with this model suggest that a model which incorporates the viscoplastic nature of Nafion is required.

Given that the critical loading conditions of a fuel cell membrane arise due to cyclic temperature and hydration conditions under constrained conditions, the aim of this chapter is to develop a

model that captures the rate, temperature, and hydration dependent elastic-plastic stress-strain behavior during monotonic and cyclic (load-unload-reload) loading conditions. The mechanics of such constrained conditions result in significant stresses in the plane of the membrane as further supported by simulations of the in situ fuel cell membrane (Kusoglu et al., 2006; Hector et al., 2007) underlying the importance of the in plane mechanical behavior of the membrane. Hence, the experimental portion of this study explores and quantifies the effect of temperature and hydration (via liquid water rather than relative humidity) on the uniaxial tensile stress-strain response of Nafion NRE212 under monotonic and cyclic loading profiles. This comprehensive data set is then used to develop a microstructurally motivated three-dimensional constitutive model. Constitutive model results are then compared to the experimental data, identifying which key elements of the model govern the important features and dependencies of the stress-strain behavior.

2.2 Experiments: Methods

2.2.1 Materials

Commercially available dispersion cast NRE212 films (thickness $t = 54\mu m$, Dupont, Ion Power Inc) were used for the experimental characterization of Nafion. The films were stored in a desiccator cabinet upon removal from the initial packaging to minimize variability in data from aging and humidity effects. The material was tested either as-received or after a chemical pre-treatment commonly used to purify and acidify the membrane in experimental fuel cell systems.

The pre-treatment entailed soaking the membrane in hydrogen peroxide (H_2O_2) for 1 hour at $85°C$ to remove any impurities, soaking in deionized water for 1 hour $85°C$ to rinse the hydrogen peroxide, soaking in sulfuric acid (H_2SO_4) for 1 hour at $85°C$ to fully acidify the membrane, and finally soaking in de-ionized water at $80°C$ for an additional hour to rinse away the excess sulfuric acid. The pre-treated specimens were dried in a desiccator cabinet for at least 24 hours prior to testing.

2.2.2 Dynamic Mechanical Analysis

Dynamic mechanical analysis (DMA) testing was performed on a TA Instruments Q800 Dynamic mechanical analyzer. Specimens were cut $5mm$ wide with a set of parallel blades. The specimens were positioned in the grips to have a gauge length of approximately $10mm$ and were tested in uniaxial tension at a frequency of $1Hz$ and amplitude of $15\mu m$. The temperature was increased from $-10°C$ to $170°C$ at a heating rate of $3°C$ per minute. Tests were also conducted on specimens submerged in deionized water. For these tests the temperature was increased from $10°C$ to $80°C$ at $1°C$ per minute as this is the temperature limit imposed by the device. For consistency the submerged specimens are compared to "in air" specimens undergoing the same temperature sweep.

2.2.3 Tensile Testing

Uniaxial tension tests were conducted at constant engineering strain rates from $0.001s^{-1}$ to $0.1s^{-1}$, at temperatures from $25°C$ to $100°C$, and at various water contents. The film was cut into tensile specimens using a dogbone shaped die with gauge length of either $9.54mm$ or $4.0mm$ and gauge width of $3.14mm$. The nominal thickness is $54\mu m$. The thickness of each specimen was determined from the average of three measurements taken along the gauge length with a Mitutoyo micrometer. All tensile tests were conducted on an EnduraTEC Electroforce 3200 (ELF). All tests were

conducted in displacement control mode. The maximum strain achieved in each trial is limited by the $12mm$ stroke length of the ELF. Strain was measured with a Qimagine Retiga 1300 video extensometer. The force-displacement data as taken from the ELF and the videoextensometer, respectively, were reduced to true stress-true strain results assuming isotropic incompressible behavior. True stress is defined as the ratio of force to current (deformed) cross-sectional area and true strain is defined as the natural logarithm of the ratio of current length to original length (length being the axial distance between video-imaged marks). For completeness, specimens were tested in multiple directions and the membrane was found to be isotropic in the plane(Silberstein, 2008); hence, results will be presented for one direction only.

Temperatures above room temperature were achieved using a Sun Systems ET1 Environmental Chamber. The specimens were allowed to equilibrate at temperature for 30 minutes prior to testing.

Hydration tests were conducted either "in air" or while immersed in water. For the "in air" tests, the specimens were imaged when dry, then submerged in deionized water ($pH = 7$) for at least 30 minutes, removed from the water for a variable amount of time in accordance with desired water content, and then placed in the tensile grips and tested immediately. The "water immersed" tests were conducted in a custom built water chamber fitted to the ELF. The specimen was mounted in the grips and imaged. Water was then added to completely submerge the specimen. The top grip was raised until the specimen reached a zero-stress position at which point the tension test was conducted. For both types of hydration tests, the swelling percentage was calculated from the change in the distance between dots marked on the specimen from the dry state to the hydrated state at the start of the test; this change was found using video extensometer images and was calculated as the average of at least five pairs of dots. The standard deviation of the swelling calculation was typically 20% of the calculated value. Stress was calculated from the swollen cross section assuming through-thickness swelling to be equal to in-plane swelling. The stress may therefore be overestimated by roughly 5% if the through thickness swelling is indeed as much 50% greater than the in-plane swelling as suggested by studies on other forms of Nafion(Gebel et al., 1993; Morris and Sun, 1993). This linear swelling measurement can be converted to an approximation of the mole ratio, ϕ, of water to sulfonic acid groups assuming additive volumes and an initial value of 1.5 at ambient conditions (25^oC, $30\%RH$)(Yeo and Eisenberg, 1977). $\phi = 31\left[(\lambda^s + 0.016)^3 - 1\right]$ where λ^s is the swelling stretch (derivation in Section 2.5). It is expected that the water content will not change during the test under these loading conditions which have low hydrostatic pressures associated with them. According to Weber and Newman (2004) and Silverman et al. (2010) which rely on the isotherm data of Escoubes et al. (1984) one would expect a reduction in swelling relative to the unconstrained swelling around 20% at a hydrostatic pressure of $15MPa$.

Hydration tests at elevated temperatures were conducted by heating the water prior to pouring it into the water chamber. The procedure was otherwise identical to that for a "water immersed" test.

2.3 Experiments: Results and Discussion

2.3.1 Dynamic Mechanical Analysis

The storage modulus, E', and loss factor (tan delta) from DMA testing of Nafion "in air" showed a broad transition temperature regime(Figure 5a). While the peak of the tan delta curve occurs at $105°C$, the storage modulus begins to drop noticeably as early as $20°C$ with a steep drop beginning at approximately $70°C$. There is no marked change in the storage or loss curves or glass

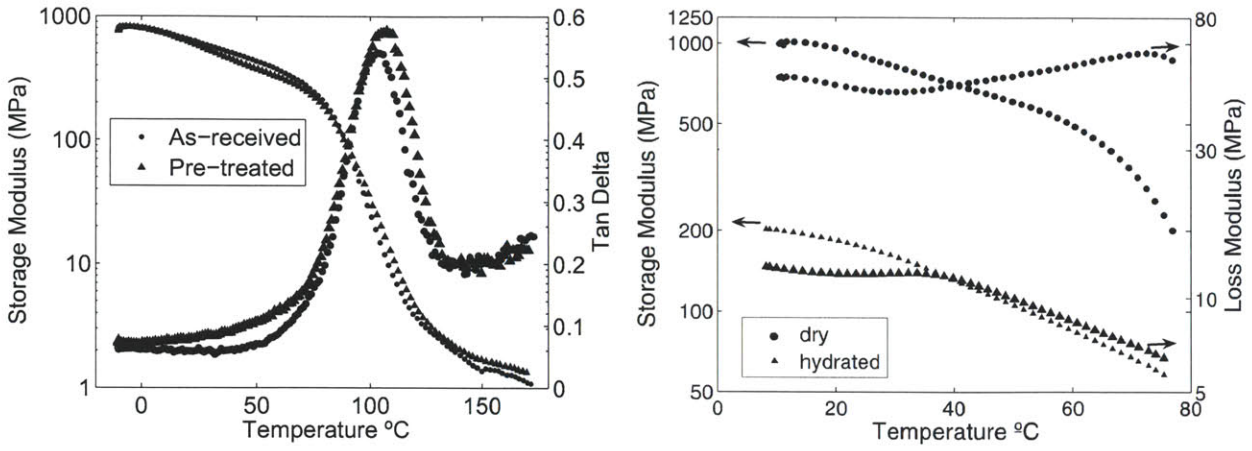

(a) (b)

Figure 5: (a) Storage modulus and loss factor as a function of temperature for as-received and pre-treated NRE212, conducted at 1Hz. (b) Storage modulus and loss modulus as a function of temperature for dry and hydrated as-received NRE212, conducted at 1Hz.

transition due to the chemical pretreatment. This peak location is in agreement with previous studies including the seminal paper of Yeo and Eisenberg and is considered the glass transition temperature of Nafion(Yeo and Eisenberg, 1977). Hydration is seen to dramatically reduce the storage and loss modulus at all temperatures(Figure 5b). The storage modulus for 25^oC and hydrated is the same as that for 80^oC and dry. The glass transition in the hydrated data is hard to identify due to the limited temperature range; taking the point where the loss modulus begins to drop; the start of the glass transition region has shifted to a lower temperature of $\sim 40°C$ from around $\sim 75°C$.

2.3.2 Tensile Testing

The uniaxial tensile behavior of Nafion during loading at $25°C$, as shown in Figure 38, is characterized by a small linear-elastic region at strains less than about 0.02 followed by a gradual rollover yield occurring over a strain ranging from approximately 0.05 to 0.11. Post-yield strain hardening is then observed with the strain hardening slope increasing slightly with increasing strain. The unloading behavior after a strain of 0.60 is initially linear, it then transitions to a nonlinear recovery prior to reaching zero stress, resulting in an initial unloaded strain of 0.47. Further recovery occurs during the time when the grip displacement is still changing (the grips are programmed to return to their original position and then to separate again to give the reloading; the thin flexible specimen elastically buckles during the unloading), and the specimen begins its reload from a strain of 0.40. The reload curve shows a shoulder at a stress below that of the initial yield and essentially rejoins the initial loading curve when it reaches the maximum strain for the second time.The yield stress σ_y is taken to be the stress at the intersection of linear fits to the initial elastic slope and the immediate post-yield strain hardening slope(Figure 38).

The pre-treated material was shown to exhibit a slightly lower stiffness, yield stress, and sub-

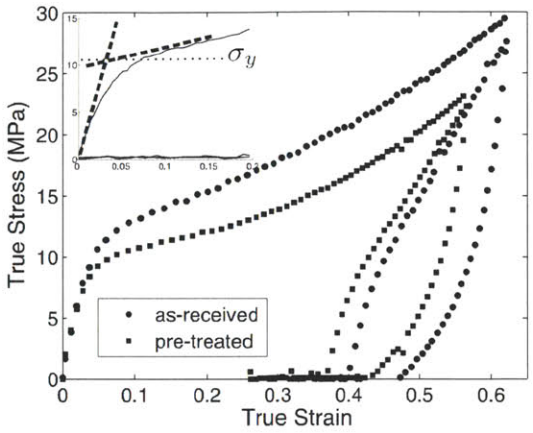

Figure 6: Comparison of pre-treated and as-received material true stress-true strain behavior in uniaxial tension at $0.01s^{-1}$ and $25°C$ (inset: yield stress definition).

sequent post-yield stress than that of the as-received material, but to have qualitatively the same behavior as the as-received material (Figure 38). Additional results will be presented only for the as-received material, but the discussion also holds for behavior observed in the pre-treated material(Silberstein, 2008).

Strain Rate Dependence: The strain rate dependence of the stress-strain behavior at $25°C$ is shown in Figure 7. There is a slight increase in the elastic modulus and a significant increase in the yield stress as the strain rate is increased. The yield stress has a logarithmic dependence on strain rate (Figure 7 inset). The post-yield strain hardening slope is relatively insensitive to strain rate.

Cyclic Loading: The viscoplastic behavior is further quantified in cyclic loading profiles. The stress-strain behavior during loading, unloading, and reloading to increasing strain values is shown in Figure 8. The unloading behavior is characterized by a relatively stiff linear region which becomes increasingly more compliant as unloading progresses and the stress decreases; this behavior indicates the development of a significant back stress during loading which aids recovery during unloading (e.g. Hasan and Boyce (1993, 1995)). Further strain recovery occurs during the time period when the grip displacement is still returning to its initial position(while the specimen is essentially unloaded), leading to reloading curves beginning at a smaller strain than the strain immediately after unloading. Reloading is characterized by an initially stiff linear region with a rollover to a more compliant behavior. The reloading stiffness is lower than the initial stiffness. The reloading rollover yield stress level is substantially lower than the initial yield stress and is followed by a relatively steep post-yield slope until rejoining the initial loading curve. The reloading rollover yield stress is found to decrease with an increase in the applied strain, but tends toward a steady value. Figure 8 shows the cyclic behavior at three different strain rates, exhibiting the expected rate dependence of these hysteresis loops.

Temperature and Hydration Dependence: The mechanical behavior has a strong dependence on temperature and hydration. Tests conducted at an engineering strain rate of $0.01s^{-1}$ at temperatures from $25°C$ to $100°C$ are shown in Figure 9a. In agreement with the trends observed on other forms of Nafion(Tang et al., 2006a; Satterfield et al., 2006), there is a decrease in the initial elastic modulus and the yield stress, an increase in the yield strain, and a slight decrease in the post-yield tangent modulus when the temperature is increased. The yielding event tends more towards a

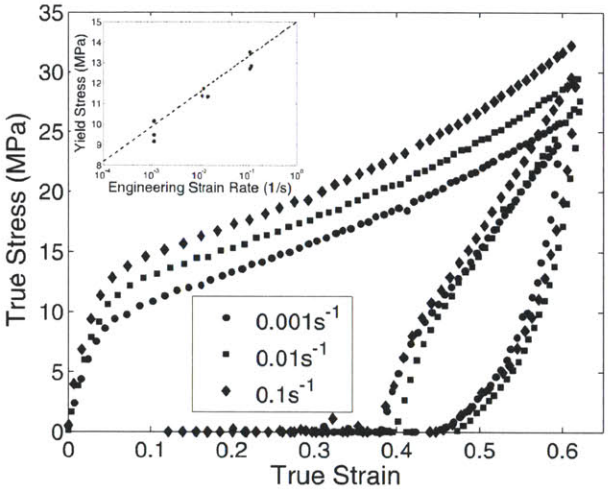

Figure 7: True stress-true strain behavior at $25°C$ at multiple strain rates (inset: logarithmic rate dependence of yield stress).

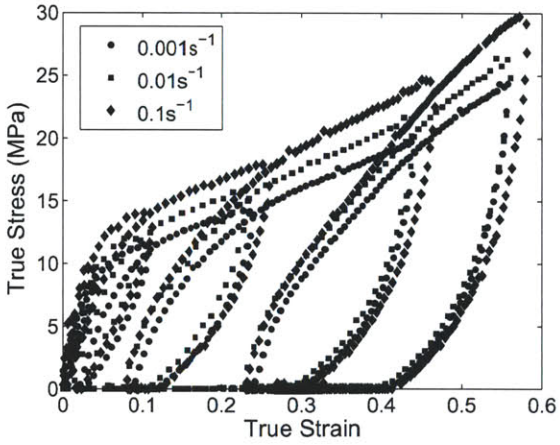

Figure 8: True stress-true strain behavior under uniaxial tensile cyclic loading conditions at $25°C$ at multiple strain rates.

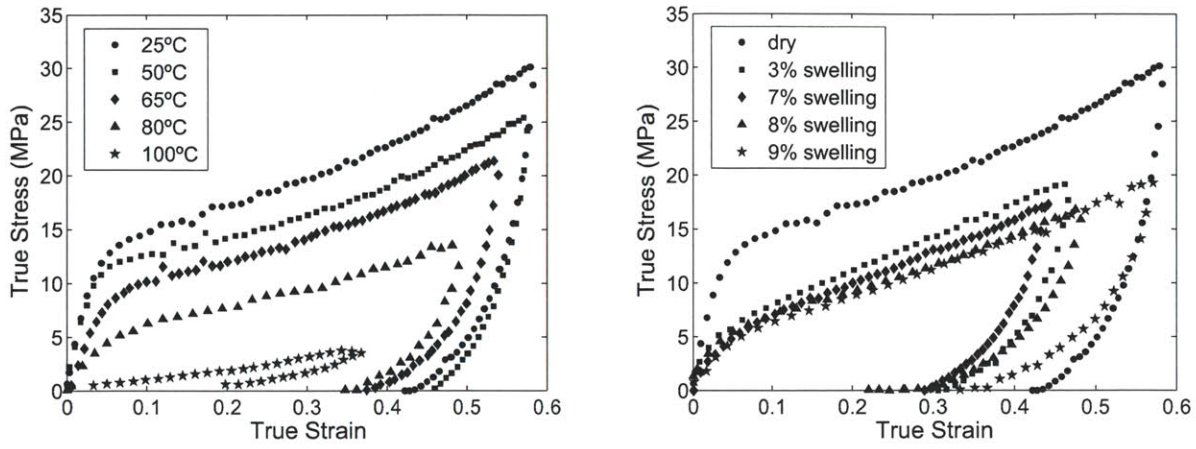

Figure 9: True stress-true strain curve at $0.01s^{-1}$ and (a) as a function of temperature; (b) as a function of hydration.

rollover rather than a clear yield point as the temperature is increased.

The strong dependence of the mechanical behavior on hydration is shown in Figures 9b and 10, in accordance with the observations of other investigations on other forms of Nafion (Kundu et al., 2005; Tang et al., 2006a; Satterfield et al., 2006; Majsztrik et al., 2008; Satterfield and Benziger, 2009; Liu et al., 2006b). The elastic modulus and yield stress decrease rapidly and then plateau as the water content is increased (Figure 9b). Under cyclic loading the same characteristic hysteresis features are observed at elevated temperature and hydration as at dry 25^oC conditions, albeit at lower stress levels(Figure 10).

The yield stress dependence on temperature for both the dry and water immersed cases is summarized in Figure 11. For the dry case, the yield stress shows a small temperature dependence from 20^oC to 50^oC and then a more dramatic decrease from 50^oC to 100^oC; this decrease is consistent with the DMA data where the storage modulus decreases gradually at first and then has a sharp drop centered around 100^oC. As expected, at every temperature the yield stress for the hydrated specimen is lower than that for the dry specimen. These data also suggest that hydration shifts the glass transition regime to lower temperatures in agreement with the DMA data. These data are consistent with the water acting as a "plasticizer", lowering the glass transition temperature as well as reducing the modulus and yield stress at all temperatures.

Based on the preceding experimental results an accurate and useful model for the loading scenarios encountered in fuel cell systems should capture:

- Initial elastic behavior
- Rate dependent distributed yield event
- Strain hardening
- Nonlinear unloading and reloading

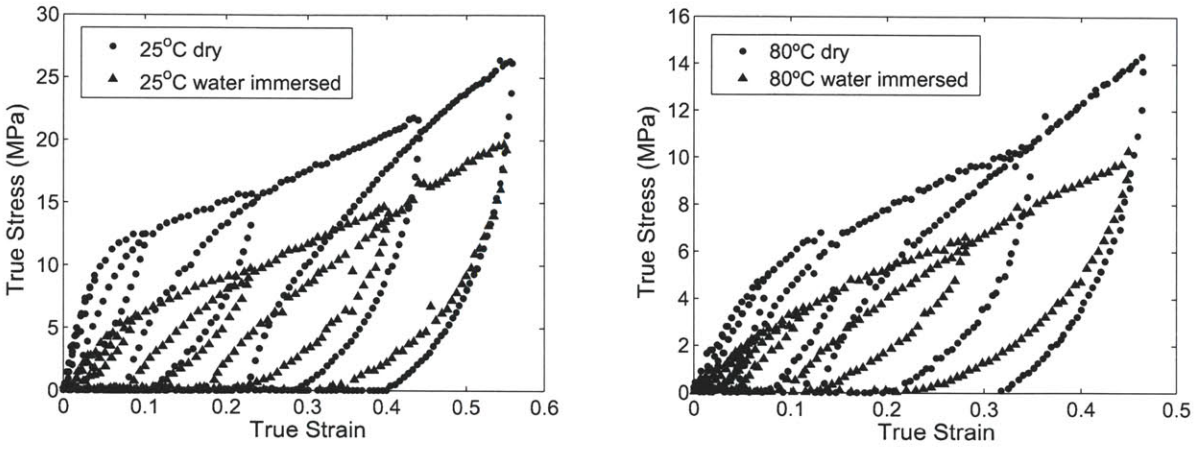

(a) (b)

Figure 10: True stress-true strain behavior under uniaxial tensile cyclic loading conditions at elevated temperature and hydration at a strain rate of $0.01s^{-1}$ (a) 25^oC (b) 80^oC.

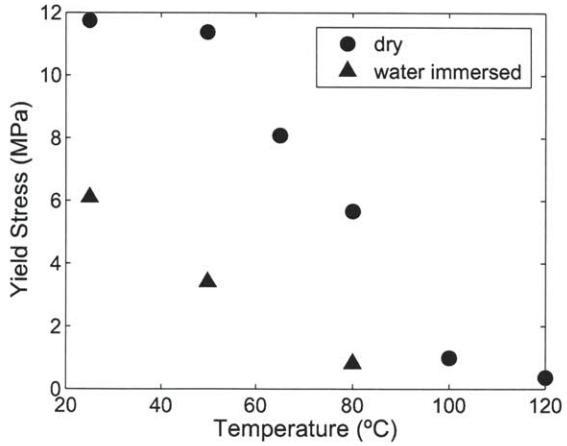

Figure 11: Yield stress as a function of temperature at an engineering strain rate of $0.01s^{-1}$.

- Strain dependent reloading yield stress
- Strain dependent reloading post-yield hardening behavior
- Temperature and hydration dependence of all of the above, including transitioning from the glassy state at 25^oC, $RH = 30\%$ into the glass transition regime with increasing temperature and hydration

Although prior Nafion models have included viscoelasticity, our data suggest linear viscous effects are rather negligible compared to the nonlinear viscous (i.e. the viscoplastic) effects and therefore linear viscous effects will be neglected here. Further Nafion uniaxial experimental data is given in Silberstein (2008).

2.4 Modeling

An elastic-viscoplastic constitutive model consisting of an intermolecular deformation mechanism acting in parallel with a molecular network alignment mechanism is adopted to capture the features of the mechanical behavior of Nafion discussed above. The model framework follows those presented for thermoplastics and time dependent elastomers in the prior work of Boyce and coworkers(Boyce et al., 1988; Arruda and Boyce, 1993; Arruda et al., 1995; Bergstrom and Boyce, 1998; Boyce et al., 2000; Mulliken and Boyce, 2006; Dupaix and Boyce, 2007), Buckley and Jones (1995), Bergstrom and Hilbert (2005), and more recently adopted by Anand and coworkers(Anand et al., 2009; Ames et al., 2009). First, a simplified version of the model (Model I) will be presented which is found to capture the monotonic loading behavior. Second, in order to capture the cyclic (unloading, reloading) behavior, additional sophistication will be added to the model (Model II).

2.4.1 Model I

A rheological schematic of the proposed Model I is shown in Figure 12. A fundamental assumption in the model structure is that the stress response of a material can be decomposed into multiple mechanisms. In this case two mechanisms are needed to model the material behavior: Mechanism I, rheologically depicted as an elastic spring in series with a viscoplastic dashpot, represents the resistance to deformation due to the intermolecular interactions where the spring captures the stiffness of these interactions and the nonlinear dashpot captures the yielding of these interactions; Mechanism N is a nonlinear spring which represents a resistance due to the stretching and orientation of the molecular network. The intermolecular resistance (Mechanism I) is strongly dependent on temperature and hydration, it is important to note that intermolecular interactions decrease significantly when the polymer goes from the glassy state into the glass-rubber transition regime. The network resistance (Mechanism N) is operational at all temperatures.

The model is fully three-dimensional but will be expressed in principal stretch space for simplicity. Throughout this discussion $i = 1, 2, 3$ are taken to indicate the three principal stretch directions with no sum on repeated i unless otherwise noted. The macroscopic deformation is given by the principal stretches λ_i. Each mechanism is taken to experience the same deformation and the total stress acting on the system is equal to the sum of the contributions from each mechanism:

$$\lambda_{Ii} = \lambda_{Ni} = \lambda_i \tag{1}$$

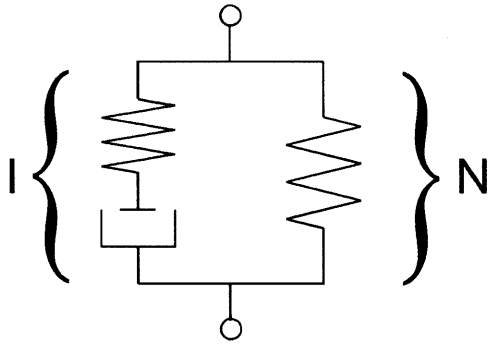

Figure 12: Rheological representation of Model I: elastic-viscoplastic.

$$T_i = T_{Ii} + T_{Ni} \tag{2}$$

where λ_{Ii} and λ_{Ni} are the principal stretches of the intermolecular (I) and network (N) mechanisms, respectively, and T_{Ii} and T_{Ni} are the Cauchy (true) stress contributions of the intermolecular and network mechanisms, respectively.

Mechanism I: At 25^oC, the intermolecular mechanism provides the dominant resistance to deformation at small to moderate strains. The stretch λ_{Ii} is accommodated by both elastic deformation and plastic deformation as captured through the Kroner-Lee decomposition $\lambda_{Ii} = \lambda^e_{Ii}\lambda^p_{Ii}$, where λ^e_{Ii} are the elastic stretches and λ^p_{Ii} are the plastic stretches. The plastic deformation is assumed isochoric such that the plastic volume ratio $J^p = \lambda^p_1\lambda^p_2\lambda^p_3 = 1$. The corresponding rate kinematics are described by the velocity gradient $D_{Ii} = \dot{\lambda}_{Ii}\lambda^{-1}_{Ii}$, which can be decomposed into elastic and plastic contributions:

$$D_{Ii} = D^e_{Ii} + D^p_{Ii} \tag{3}$$

where $D^e_{Ii} = \dot{\lambda}^e_{Ii}\left(\lambda_{Ii}{}^e\right)^{-1}$ is the elastic velocity gradient and $D^p_{Ii} = \dot{\lambda}^p_{Ii}\left(\lambda_{Ii}{}^p\right)^{-1}$ is the plastic velocity gradient. D^p_{Ii} will be constitutively prescribed later.

The intermolecular contribution to the Cauchy stress is taken to be a function of the elastic stretches:

$$T_{Ii} = \frac{1}{J^e}\left[2\mu\left(\ln\lambda^e_{Ii}\right)' + \kappa\ln J^e\right] \tag{4}$$

where $J^e = \lambda^e_{I1}\lambda^e_{I2}\lambda^e_{I3}$ is the elastic mechanical volume ratio, μ is the shear modulus, and κ is the bulk modulus.

The plastic velocity gradient is constitutively prescribed to follow a thermally-activated process driven by the stress deviator (note that we neglect linear viscous contributions since these were measured to be small compared to nonlinear viscous contributions):

$$D^p_{Ii} = \dot{\gamma}^p_I\frac{T'_{Ii}}{\sqrt{2}\tau_I} \tag{5}$$

$$\dot{\gamma}^p_I = \dot{\gamma}^o\exp\left[\frac{-\Delta G}{k_b\theta}\right]\sinh\left[\frac{\Delta G}{k_b\theta}\frac{\tau_I}{s}\right] \tag{6}$$

where $\dot{\gamma}_I^p$ is the magnitude of the plastic velocity gradient, $T'_{Ii} = T_{Ii} - \frac{1}{3}(T_{I1} + T_{I2} + T_{I3})$ is the stress deviator, $\tau_I = \sqrt{\frac{1}{2}\left({T'_{I1}}^2 + {T'_{I2}}^2 + {T'_{I3}}^2\right)}$ is the scalar equivalent shear stress, $\dot{\gamma}^o$ is a pre-exponential factor proportional to the attempt frequency, ΔG is the activation energy, s is the isotropic shear resistance, k_b is Boltzmann's constant, and θ is the absolute temperature.

A constant value for the shear resistance s would give a sharp transition from elastic to plastic behavior. The heterogeneous nature of the Nafion molecular structure makes this physically unrealistic, as is evident in the gradual yielding observed in the stress-strain curves. The distributed microstructure provides a spatial distribution in the strength of interactions which in turn corresponds to progressively activating plastic deformation at different levels of stress. At a critical stress, the site with the lowest resistance to shear will begin to deform plastically while the rest of the material will continue to deform elastically. The plastically deforming sites harden slightly which, in turn, raises the overall stress level, activating deformation of higher strength sites. As more sites reach their respective critical stress state, plasticity percolates and the material behavior will macroscopically roll over from elastic to plastic behavior. Rheologically this would be represented as an infinite number of spring-dashpot pairs in parallel, however, it is much simpler to capture this effect mathematically as an evolution in shear resistance s. Hence, the initial shear resistance $\tilde{s}_o$ is taken to increase with $\dot{\gamma}_I^p$ until reaching a saturated state $\tilde{s}$ during plastic deformation:

$$\dot{\tilde{s}} = \tilde{h}\left(1 - \frac{\tilde{s}}{\tilde{s}_{sat}}\right)\dot{\gamma}_I^p \tag{7}$$

where $\tilde{h}$ controls the approach of $\tilde{s}$ to $\tilde{s}_{sat}$ with plastic strain. Molecular alignment provides an additional increase in the intermolecular shear resistance captured by the contribution $\bar{s}$:

$$\bar{s} = \bar{h}\left(\lambda_{chain}^{\bar{n}} - 1\right) \tag{8}$$

where $\bar{h}$ controls the initial slope, $\bar{n}$ controls the nonlinearity, and $\lambda_{chain} = \sqrt{\frac{\lambda_1^2+\lambda_2^2+\lambda_3^2}{3}}$ is a measure of network stretch. The shear resistance (s) is then given by:

$$s = \tilde{s} + \bar{s}. \tag{9}$$

The plastic deformation gradient can then be updated by integrating $\dot{\lambda}_{Ii}^p = D_{Ii}^p \lambda_{Ii}^p$ with time; the elastic stretch is calculated via $\lambda_{Ii}^e = \lambda_{Ii}\left(\lambda_{Ii}^p\right)^{-1}$.

Mechanism N: The stress arising from the network resistance to deformation (T_{Ni}) is taken to be deviatoric and is derived from the resistance to stretching and orientation of the molecular network; here we use the Neo-Hookean model:

$$T_{Ni} = \frac{1}{J}\mu_N B'_{Ni} \tag{10}$$

where $J = \lambda_1\lambda_2\lambda_3$ is the volume ratio, μ_N is the rubbery shear modulus, and B'_{Ni} is the deviatoric part of the Cauchy Green tensor given by $B'_{Ni} = \lambda_{Ni}^2 - \lambda_{chain}^2$.

Temperature and hydration: Temperature and hydration influence both the kinematics (due to the volumetric expansion associated with changes in temperature and water content) and the resistances to deformation, having a strong effect on the intermolecular interactions and a modest effect on the network resistance. Kinematically, the total principal intermolecular stretches can be decomposed into mechanical and swelling contributions as

$$\lambda_{Ii} = \lambda^e_{Ii}\lambda^p_{Ii}\lambda^s_{Ii} \tag{11}$$

where $\lambda^s_{Ii} = \lambda^s\left(1 + \beta\Delta\phi + \alpha\Delta\theta\right)$ is the deformation due hygrothermal swelling, $\beta = \frac{\partial \ln \lambda^s_{Ii}}{\partial \phi}$ is the coefficient of hygro expansion, $\alpha = \frac{\partial \ln \lambda^s_{Ii}}{\partial \theta}$ is the coefficient of thermal expansion, $\Delta\phi$ and $\Delta\theta$ are the changes in ϕ and θ respectively relative to a reference state at which the model is calibrated (here chosen as 25^oC, $30\%RH$). We have assumed the hygro-swelling and thermal-swelling to be isotropic, linear, and uncoupled from each other and from the plastic deformation, but these can be generalized to depend on temperature and hydration and may be coupled (note that the water content for a given relative humidity or liquid water boundary condition will depend on temperature, but this is manually controlled in the simulations shown here). While there is some evidence that through-thickness swelling can be larger than in-plane swelling for some Nafion materials(Lai et al., 2009b), we neglect that possible effect here since this model will be applied primarily to in-plane loading. As an aside we note that a multiplicative decomposition of the deformation gradient into swelled and mechanical contributions was utilized by Flory and Rehner (1943) for swelling rubber elastic materials as reviewed in Boyce and Arruda (2001). Here we have the additional complexity of inelastic deformation and also changes in temperature.

The rate kinematics are described by the velocity gradient, which can be decomposed into elastic, plastic, and hygrothermal-swelling contributions:

$$D_{Ii} = D^e_{Ii} + D^p_{Ii} + D^s_{Ii} \tag{12}$$

where $D^s_{Ii} = \dot{\lambda}^s_{Ii}\left(\lambda^s_{Ii}\right)^{-1}$ is the hygrothermal-swelling velocity gradient. D^p_{Ii} is constitutively prescribed as before.

The shear modulus (μ) and the plasticity dependent portion of the shear resistance to plastic flow ($\tilde{s}$) are defined as functions of temperature and hydration deduced from the dependencies of the elastic modulus as a function of temperature and hydration; these dependencies closely mirror those of the shear storage modulus and those of the yield stress(see section 2.5). Temperature is given in absolute temperature or Kelvin. Hydration is given in moles of water per mole of sulfonic acid group in the membrane. As a first approximation the effect of temperature and hydration are taken to be uncoupled and multiplicative; this multiplicative factor will be referred to as the reduction factor. The current state values of μ and $\tilde{s}$, independent of temperature and hydration, are multiplied by this corrective reduction factor to obtain $\mu(\theta,\phi)$ and $\tilde{s}(\theta,\phi)$ respectively.

The network stretch can be decomposed into mechanical and swelling contributions as:

$$\lambda_{Ni} = \lambda^m_{Ni}\lambda^s_{Ni} \tag{13}$$

where λ^m_{Ni} are the network mechanical stretches and $\lambda^s_{Ni} = \lambda^s_{Ii}$ is the hygrothermal swelling. The network mechanical deformation is calculated as $\lambda^m_{Ni} = \lambda_{Ni}{\lambda^s_{Ni}}^{-1}$ for a known temperature and water content.

The swelling decreases the network crosslink density thereby decreasing the mechanical stiffness. The hydration dependent network response is therefore constitutively prescribed by

$$T_{Ni} = \frac{\mu_N}{J^m_N \lambda^s} B^{m\prime}_{Ni} \tag{14}$$

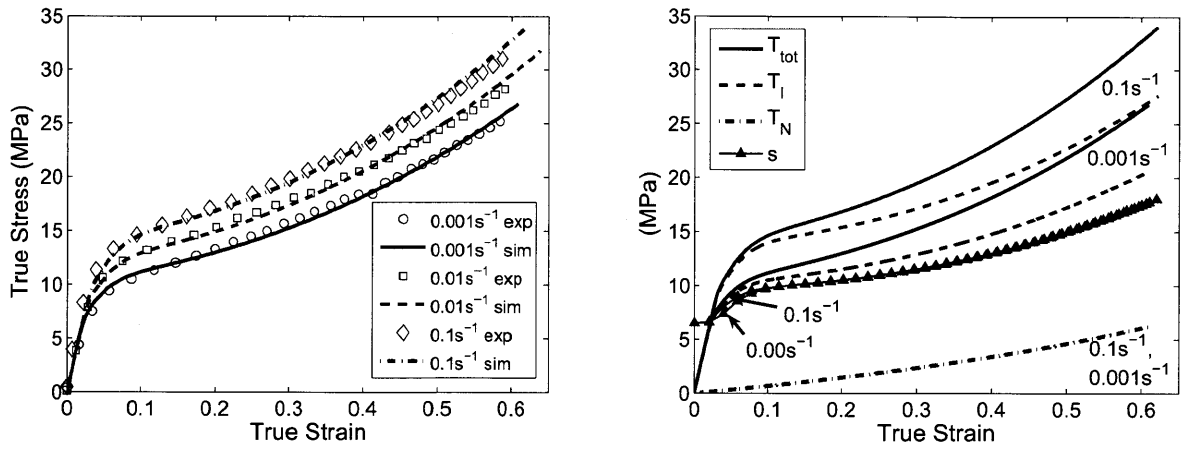

Figure 13: Model I in uniaxial extension at ambient conditions at three different strain rates (a)comparison with experiments (b)contributions of the individual mechanisms to the overall response.

where $J_N^m = \lambda_{N1}^m \lambda_{N2}^m \lambda_{N3}^m$ is the mechanical volume ratio, μ_N the rubbery shear modulus is not a function of temperature or hydration, and $B_{Ni}^{m\prime}$ is the deviatoric part of the mechanical Cauchy Green tensor given by $B_{Ni}^{m\prime} = {\lambda_{Ni}^m}^2 - {\lambda_{chain}^m}^2$.

A method for reducing material properties is provided in section 2.5 along with the parameter values; this method decomposes the stress-strain curve into contributions associated with the various components of the model which helps provide a more systematic fitting of the material properties.

Results: *Strain and Strain Rate:* This relatively simple elastic-viscoplastic model is able to capture the linear-elastic response, the rate dependent distributed yield event, and the nonlinear strain hardening(Figure 13a). Various key contributions to the model stress-strain curve are shown in Figure 13b. The initial elastic response is dominated by the intermolecular contribution since the network stiffness is much lower than the intermolecular stiffness. The intermolecular contribution to stress is seen to govern the rate dependent yield with the distributed rollover yield following the shape of the evolution in s. The post yield strain hardening results in part from the network stiffness (which is an anisotropic contribution) and in part from the evolution in s (which is an isotropic contribution).

Temperature and Hydration: The model is compared to experimental data as a function of temperature and hydration in Figure 14. The model is able to capture the dependence of the elastic modulus and yield stress on temperature and hydration as well as the combined influence of changes in both temperature and hydration. This dependency is primarily in the intermolecular component; the network does not change at all with temperature (Figure 14b) and changes only a small percentage with hydration(Figure 14d,f).

Unloading and Cyclic Loading: Figure 15 shows the model results including unloading and reloading from strains after yield. Clearly, Model I fails to capture the highly nonlinear unloading behavior. The unloading, reloading, and cyclic behavior is key to modeling membrane behavior

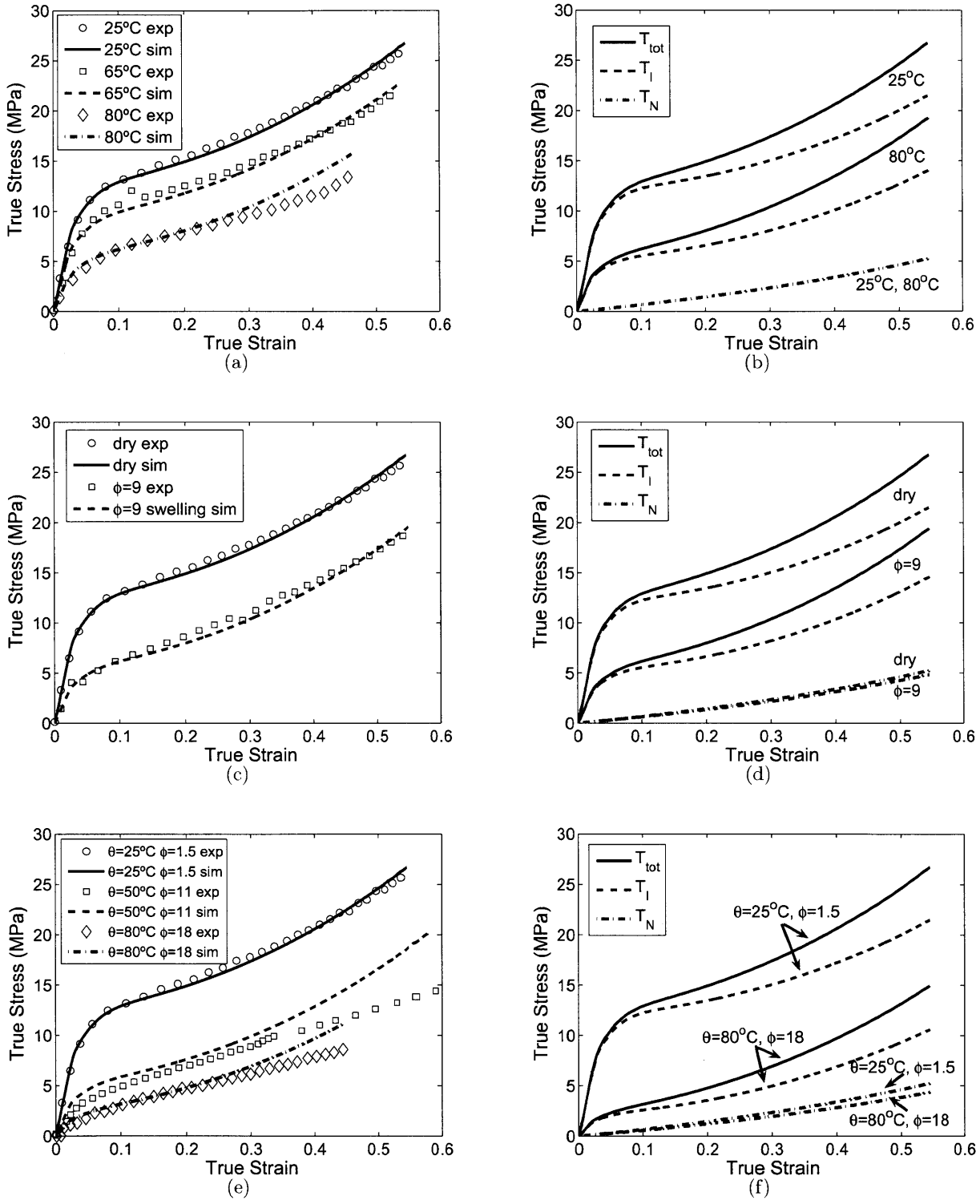

Figure 14: Model I in uniaxial extension at a strain rate of $0.01s^{-1}$ (a-b) at varied temperature (c-d) at varied hydration at 25^oC (e-f) at varied hydration and temperature; (a,c,e) comparison with experiments (b,d,f) contributions of the individual mechanisms to the overall response.

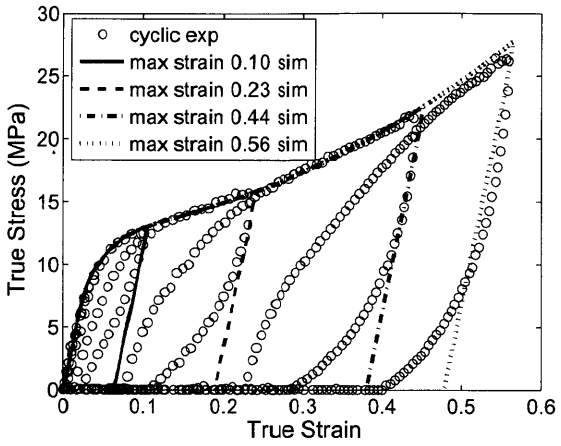

Figure 15: Model I vs experiment under tensile cyclic loading at a strain rate of $0.01s^{-1}$ and ambient conditions showing the linear unloading behavior predicted by Model I in contrast to the nonlinear unloading that is experimentally observed.

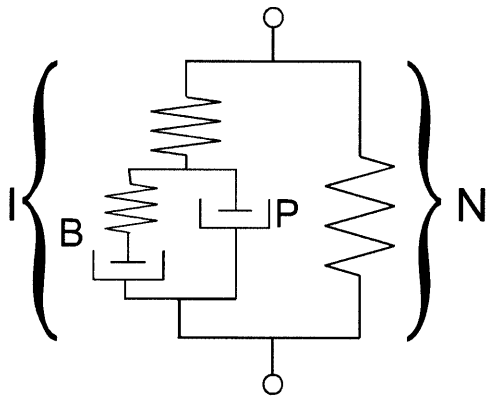

Figure 16: Rheological representation of Model II: elastic-viscoplastic with back stress.

in a functioning fuel cell due to the cyclic nature of fuel cell operation. This important effect is addressed next by including a back stress feature in Model II.

2.4.2 Model II

In order to address the inability of Model I to capture the cyclic behavior, a backstress component (B) is added to the intermolecular mechanism, as expressed rheologically in Figure 16. It is assumed that during loading, due to the distributed heterogenous nature of the Nafion microstructure, a back stress locally develops and is stored around plastically deforming regions. This back stress then assists reverse deformation during unloading. Calorimetric measurements (Hasan and Boyce, 1993; Salamantina et al., 1992) have indeed measured the development of such an energy storage mechanism during inelastic deformation of polymers. When the direction of loading is reversed, this back stress acts to assist inelastic deformation in the opposing direction and hence gives the nonlinear unloading response with a reverse yield. Here, the back stress is taken to evolve linearly

with plastic deformation and to then saturate out as the plastically deformed regions percolate. The saturation is also observed in the calorimetry measurements (Hasan and Boyce, 1993; Salamantina et al., 1992). The back stress saturation is captured by initiating a thermally-activated plateau stress within a nonlinear viscous element physically governed by the same yielding mechanism as the intermolecular barrier. As indicated in the schematic of Figure 16, the stretch acting on the back stress element is equal to that acting on the intermolecular viscoplastic dashpot ($\lambda_{Bi} = \lambda^p_{Ii}$). The back stress stretch can be decomposed into elastic and plastic components, $\lambda_{Bi} = \lambda^e_{Bi}\lambda^p_{Bi}$. The rate kinematics are given by $D_{Bi} = \dot{\lambda}_{Bi}\lambda^{-1}_{Bi}$, which can be further decomposed into elastic and plastic contributions

$$D_{Bi} = D^e_{Bi} + D^p_{Bi} \tag{15}$$

where $D^e_{Bi} = \dot{\lambda}^e_{Bi}\left(\lambda^e_{Bi}\right)^{-1}$ is the elastic velocity gradient and $D^p_{Bi} = \dot{\lambda}^p_{Bi}\left(\lambda^p_{Bi}\right)^{-1}$ is the plastic velocity gradient which will be constitutively prescribed later.

The elastic response of the back stress is given by:

$$T'_{Bi} = \frac{1}{J}2\mu_B \ln \lambda_{Bi} \tag{16}$$

where the back stress T'_{Bi} is naturally deviatoric since $\lambda_{B1}\lambda_{B2}\lambda_{B3} = 1$, μ_B is the back stress shear modulus.

The back stress velocity gradient is constitutively prescribed as:

$$D^p_{Bi} = \dot{\gamma}^p_B \frac{T'_{Bi}}{\sqrt{2}\tau_B} \tag{17}$$

$$\dot{\gamma}^p_B = \dot{\gamma}^o \exp\left[-\frac{\Delta G}{k_b\theta}\right] \sinh\left[\frac{\Delta G}{k_b\theta}\frac{\tau_B}{s_B}\right] \tag{18}$$

where $\tau_B = \sqrt{\frac{1}{2}\left({T'_{B1}}^2 + {T'_{B2}}^2 + {T'_{B3}}^2\right)}$ is the corresponding equivalent shear stress and s_B is the isotropic shear resistance to inelastic deformation. $\dot{\gamma}^o$ and ΔG are the same constants as for the intermolecular plastic deformation since the rate dependence of unloading is similar to that of loading (Figure 8). s_B is taken to evolve to a maximum with $\dot{\gamma}^p_B$ such that the saturation of the back stress occurs gradually.

$$\dot{s}_B = h_B\left(1 - \frac{s_B}{s_{Bsat}}\right)\dot{\gamma}^p_B \tag{19}$$

where h_B controls the evolution with shear and s_{Bsat} is the saturation value. λ^p_{Bi} can be updated by integrating $\dot{\lambda}^p_{Bi} = D^p_{Bi}\lambda^p_{Bi}$ with time; the elastic deformation gradient is then calculated via $\lambda^e_{Bi} = \lambda_{Bi}\left(\lambda^p_{Bi}\right)^{-1}$.

The addition of a back stress as defined above does not alter the existing kinematics for Model I, but the constitutive definitions are modified slightly.

The cyclic experimental data show that the post-yield elastic unloading and reloading slopes are smaller than that of initial elastic loading; hence the shear modulus μ is taken to decrease with plastic strain to a minimum saturation state. This evolution reflects a rearrangement to a softened microstructure during the yielding process.

$$\dot{\mu} = h\left(1 - \frac{\mu}{\mu_{sat}}\right)\dot{\gamma}_I^p \tag{20}$$

where h controls the rate at which μ approaches the saturation value μ_{sat}.

The stress driving deformation of the intermolecular yield is now $[T_{Ii} - T_{Bi}]'$ and will be referred to as T'_{Pi}. Hence the expression for the plastic velocity gradient becomes

$$D_{Ii}^p = \dot{\gamma}_I^p \frac{T'_{Pi}}{\sqrt{2}\tau_P} \tag{21}$$

$$\dot{\gamma}_I^p = \dot{\gamma}^o \exp\left[\frac{-\Delta G}{k_b\theta}\right] \sinh\left[\frac{\Delta G}{k_b\theta}\frac{\tau_P}{s}\right] \tag{22}$$

where $\tau_P = \sqrt{\frac{1}{2}\left({T'_{P1}}^2 + {T'_{P2}}^2 + {T'_{P3}}^2\right)}$ is the scalar equivalent shear stress. Since a different stress drives yielding, the nonlinear viscous material parameters associated with the shear resistance s in Model II will differ from those of Model I. s will have an initial increase during yield($\tilde{s}$), a softening with further plasticity($\hat{s}$), and an increase with network alignment($\bar{s}$). As in Model I, the initial shear resistance $\tilde{s}_o$ is taken to increase with $\dot{\gamma}_I^p$ until reaching a saturated state during plastic deformation reflecting the distributed nature of yield.

$$\dot{\tilde{s}} = \tilde{h}\left(1 - \frac{\tilde{s}}{\tilde{s}_{sat}}\right)\dot{\gamma}_I^p \tag{23}$$

where $\tilde{h}$ controls the rate of approach of $\tilde{s}$ to its saturation value $\tilde{s}_{sat}$. To capture a softening that occurs upon percolation, $\hat{s}_o = 0$, which is subtracted from $\tilde{s}$, is taken to increase with $\dot{\gamma}_I^p$ at a slower rate than $\tilde{s}$, to its saturated value $\hat{s}_{sat}$.

$$\dot{\hat{s}} = \hat{h}\left(1 - \frac{\hat{s}}{\hat{s}_{sat}}\right)\dot{\gamma}_I^p \tag{24}$$

where $\hat{h}$ controls the rate of approach of $\hat{s}$ from its initial value of 0 to its saturation value $\hat{s}_{sat}$. An evolution of this nature is something that is commonly seen in glassy polymers (e.g. Hasan and Boyce (1995)). Molecular alignment provides an additional increase to the intermolecular shear resistance captured by the contribution $\bar{s}$.

$$\bar{s} = \bar{h}\left(\lambda_{chain}^{\bar{n}} - 1\right) \tag{25}$$

where $\bar{h}$ controls the initial slope and $\bar{n}$ controls the nonlinearity. The shear resistance (s) is then given by:

$$s = \tilde{s} - \hat{s} + \bar{s}. \tag{26}$$

The network mechanism is unchanged by the addition of the back stress to the intermolecular mechanism.

Temperature and Hydration Dependence Features: The existing kinematics and constitutive definitions for the inclusion of the effects of temperature and hydration in Model I are unchanged in Model II. μ and the plasticity dependent portion of the shear resistance to plastic flow $\tilde{s} - \hat{s}$ are multiplied by the reduction factor to obtain $\mu(\theta, \phi)$ and $[\tilde{s} - \hat{s}](\theta, \phi)$ respectively. Additionally the

current state values of μ_B and s_B independent of temperature and hydration are multiplied by the reduction factor to obtain $\mu_B(\theta,\phi)$ and $s_B(\theta,\phi)$ respectively.

A method for reducing the additional material parameters required for Model II is provided in section 2.5 along with the parameter values. The full three dimensional formulation is presented in section 2.6.

Results: Model II retains the ability to capture all stress-strain loading features and dependencies captured in Model I. Model II is able to capture the nonlinear unloading and reloading both as a function of strain and as a function of strain rate as shown in Figure 17a,b. Focusing on the unloading curves, the highly nonlinear unloading behavior is captured as a reverse yield event that occurs during unloading assisted by a back stress. The evolution in the intermolecular stress and the back stress enable yield rollovers to occur at the appropriate total stress during unloading and reloading for different strains and strain rates(Figure 17c,d). Model II accurately reproduces both the decrease in yield stress observed during reloading (as captured by the initial yield stress) and the increased post-yield slope until the reloading curve reaches the monotonic curve. These same features are experimentally observed at elevated temperature and hydration and are captured by Model II (Figure 18). The temperature and hydration reduction factors which work for capturing the effect of temperature and water content on the shear modulus and yield stress are also successful in capturing the effect of temperature and water content on the reverse and reloading yield stresses. Finally, it is verified that the evolution of stress relaxation and creep through yield are also well predicted by the model (Figure 19). This further validates the decision to neglect linear viscous effects.

2.5 Determination of material constants

All parameter determination is done with data at a strain rate of $0.01s^{-1}$ and at ambient conditions (25^oC, $30\%RH$) unless otherwise stated.

2.5.1 Model I

Mechanism I: The Cauchy stress due to the intermolecular component is prescribed by:

$$T_{Ii} = \frac{1}{J^e}\left[2\mu\left(\ln\lambda^e_{Ii}\right)' + \kappa \ln J^e\right] \tag{27}$$

Any two elastic constants can define the intermolecular elastic response. The elastic modulus (E) is found from the slope of the initial linear-elastic region of the stress-strain curve. The Poisson's ratio ($\nu = 0.35$) is estimated from the ratio of horizontal to vertical strain found via the video extensometer in this same region. These two constants are then converted into the required shear(μ) and bulk modulus(κ) via equations 28 and 29 respectively. The dependence of the elastic constants on temperature and hydration will be discussed later.

$$\mu = \frac{E}{2\left(1+\nu\right)} \tag{28}$$

$$\kappa = \frac{E}{3\left(1-2\nu\right)} \tag{29}$$

The magnitude of the rate of plastic deformation is described by:

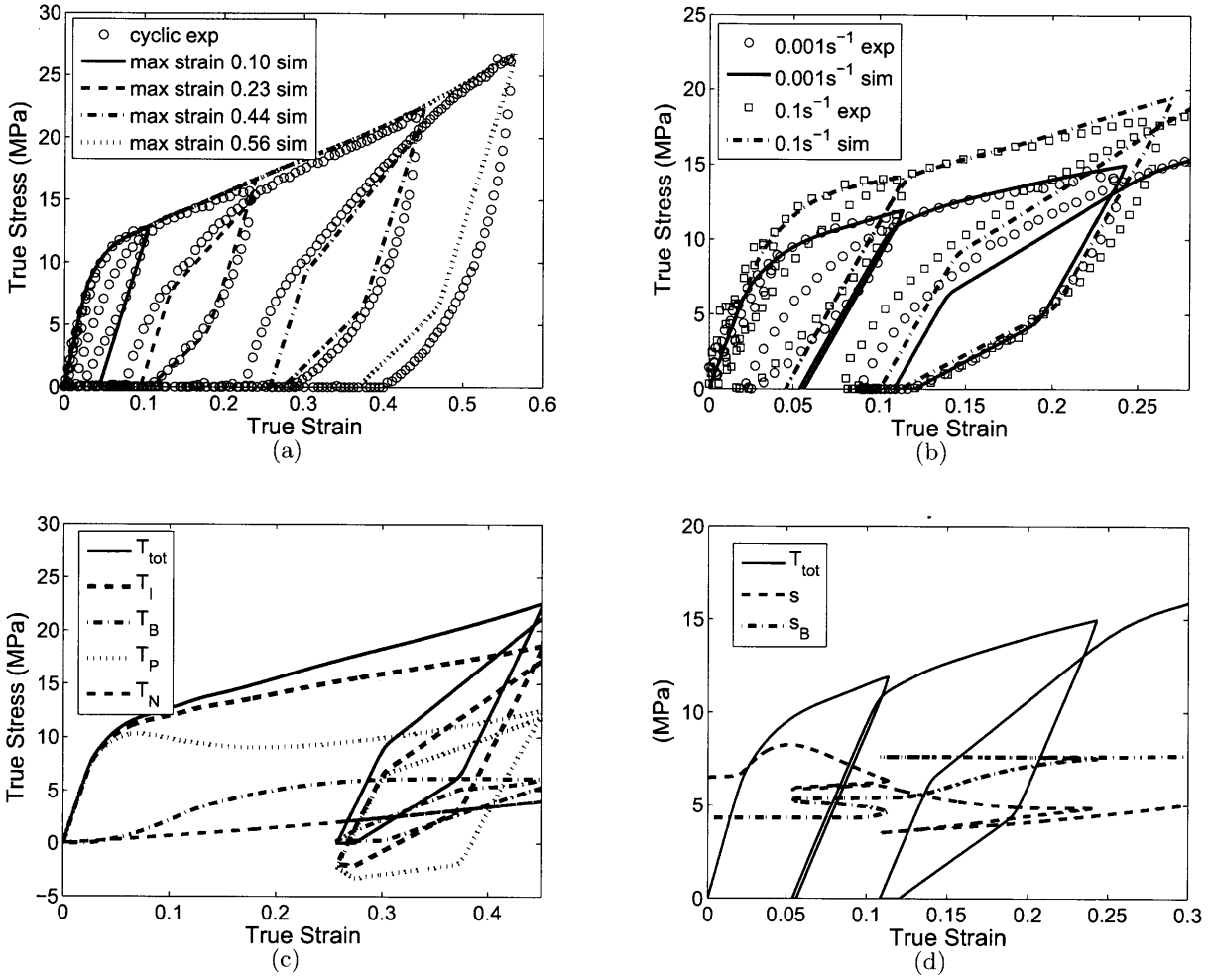

Figure 17: Model II under tensile cyclic loading at ambient conditions (a) comparison to experimental data at different maximum strain values at a strain rate of $0.01s^{-1}$ (b) comparison to experimental data at different strain rates (c) contribution of the individual mechanisms to the overall response at $0.01s^{-1}$ (d) evolution of s and s_B at a strain rate of $0.001s^{-1}$.

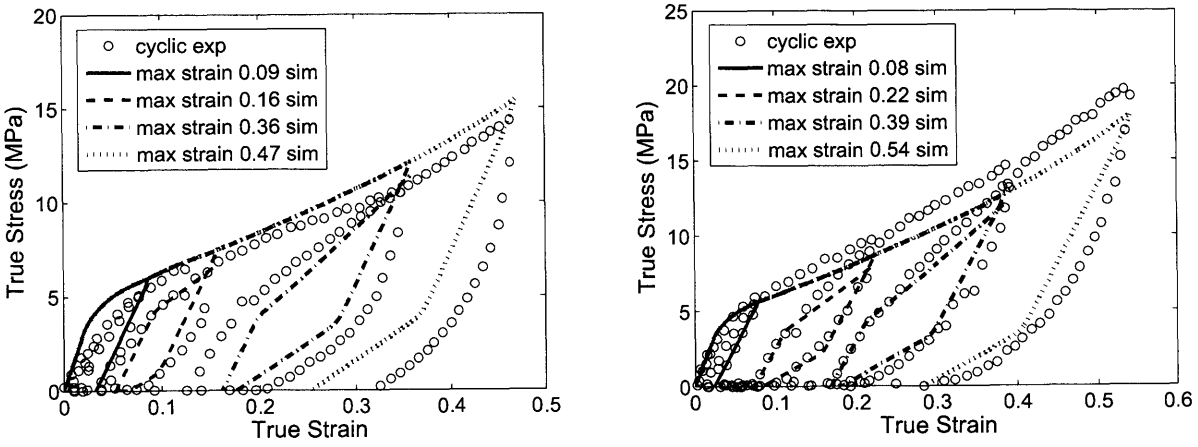

Figure 18: Model II vs experiment under tensile cyclic loading at a strain rate of $0.01s^{-1}$ (a) at 80^oC and ambient relative humidity (b) in water at 25^oC.

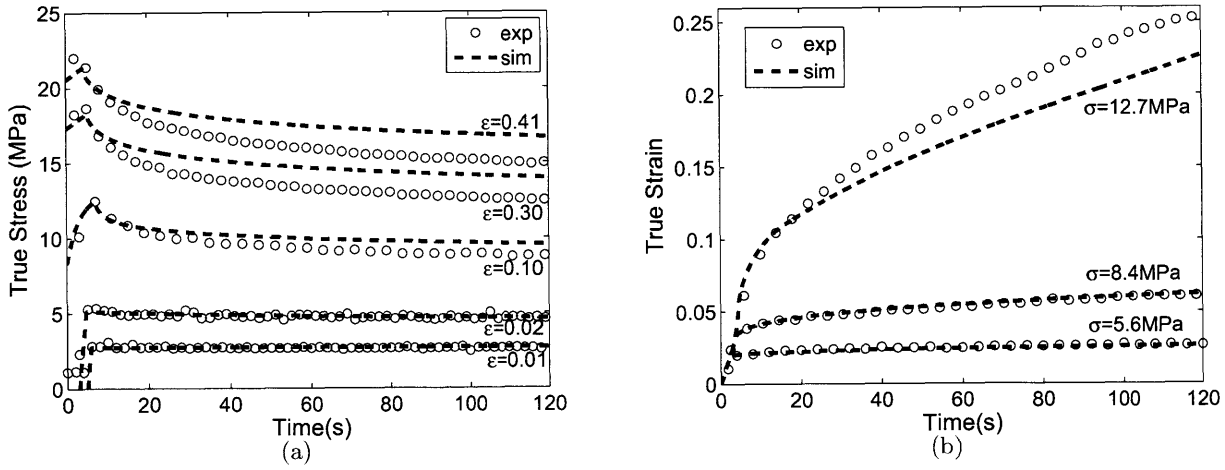

Figure 19: Model II vs experiment under tensile cyclic loading at ambient conditions (a) stress relaxation(b) creep.

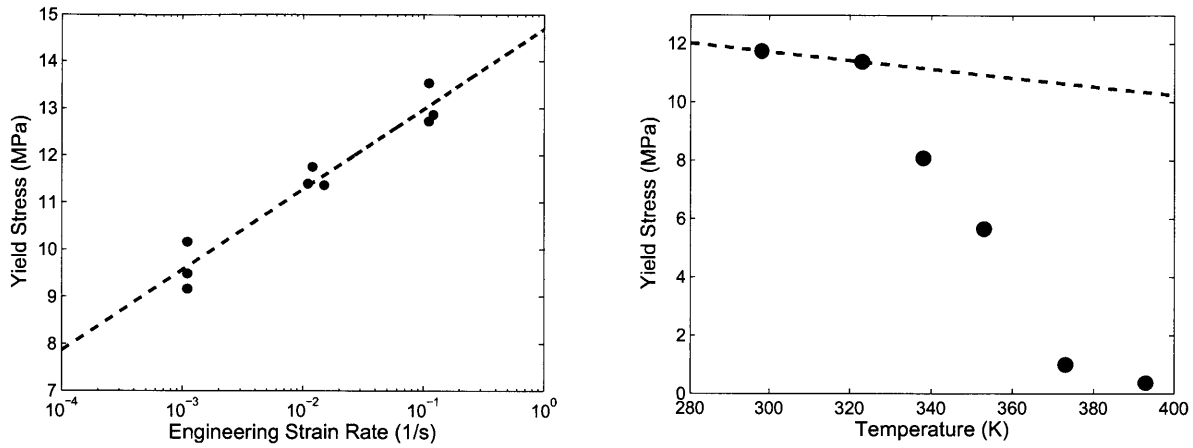

(a) (b)

Figure 20: Data used to fit rate of plastic deformation. (a) Yield stress as a function of engineering strain rate (b)Yield stress as a function of temperature at an engineering strain rate of 0.01/s.

$$\dot{\gamma}_I^p = \dot{\gamma}^o \exp\left[-\frac{\Delta G}{k_b\theta}\right] \sinh\left[\frac{\Delta G}{k_b\theta}\frac{\tau_I}{s}\right] \tag{30}$$

$$s = \tilde{s} + \bar{s} \tag{31}$$

The network stress contribution is negligible at yield, so the stress on the plastic component can be approximated by the total stress. Therefore, the three constants ($\dot{\gamma}^o$,ΔG,s) that characterize this rate of plastic deformation are fit to the yield stress as a function of rate and temperature. For fitting purposes it is assumed that only the forward process is active, equation 30 can then be rewritten as:

$$\dot{\gamma}_I^p = \dot{\gamma}^o \exp\left[-\frac{\Delta G}{k_b\theta}\right] \exp\left[\frac{\tau\Omega}{k_b\theta}\right] \tag{32}$$

where the Ω is the activation volume related to the other material properties as $\Omega = \frac{\Delta G}{s}$. Equation 32 can be solved for the uniaxial stress $\sigma = \sqrt{3}\tau$ as a function of the uniaxial strain rate $\dot{\epsilon}$, the temperature θ and the three unknown constants ($\dot{\gamma}^o$,ΔG,Ω). The slope of σ versus $\ln\dot{\epsilon}$ (Figure 20a), which equals $\frac{\sqrt{3}k_b\theta}{\Omega}$, gives the value for Ω. The slope of σ versus θ (Figure 20b), which equals $\sqrt{3}\frac{k_b}{\Omega}\ln\frac{\sqrt{3}\dot{\epsilon}}{\dot{\gamma}^o}$, gives the value for $\dot{\gamma}^o$. The y-intercept of σ versus θ, which equals $\frac{\sqrt{3}\Delta G}{\Omega}$, gives the value for ΔG. The equation is put back in terms of s using $s = \frac{\Delta G}{\Omega}$, where this s is the value of s at the end of the rollover yield and is approximately $\tilde{s}_{sat}$.

The evolution of $\tilde{s}$ is controlled via:

$$\dot{\tilde{s}} = \tilde{h}\left(1 - \frac{\tilde{s}}{\tilde{s}_{sat}}\right)\dot{\gamma}_I^p \tag{33}$$

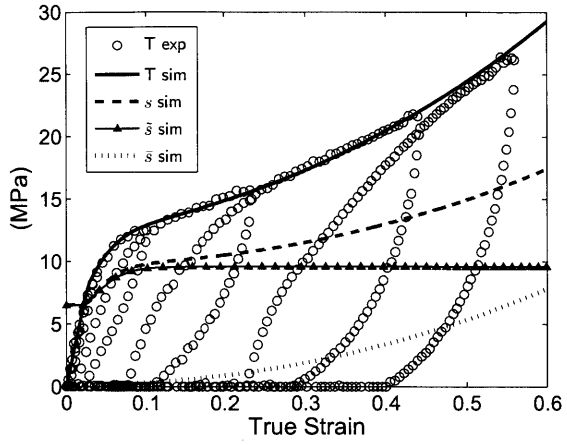

Figure 21: Evolution of s and its components during monotonic tensile loading for Model I.

$\tilde{s}_o$ determines the initial yield condition and is set according to the stress at which the rollover yield starts. $\tilde{s}$ increases according to the shape of the rollover yield to $\tilde{s}_{sat}$. $\tilde{h}$ controls the rate of this evolution to match the shape of the rollover yield.

$\bar{s}$ captures the portion of the strain hardening that does not arise from the network component.

$$\bar{s} = \bar{h}\left(\lambda_{chain}^{\bar{n}} - 1\right) \tag{34}$$

where $\bar{h}$ controls the initial slope and $\bar{n}$ controls the nonlinearity.

The overall evolution in s as well as the separate contributions of $\tilde{s}$ and $\bar{s}$ are shown in Figure 21.

Mechanism N: The orientation hardening is described by:

$$T_{Ni} = \frac{\mu_N}{J_N^m \lambda^s} B_{Ni}^{m\prime} \tag{35}$$

The rubbery shear modulus μ_N is fitted to monotonic extension data at 100^oC for which it is assumed that the intermolecular contribution is minimal.

Thermal and hydration dependence: The bulk modulus is assumed to be independent of temperature and water content. The intermolecular and back stress shear moduli and isotropic plastic deformation resistances are defined as uncoupled functions of temperature and water content as taken from the independent variation in elastic modulus stress with these two factors. Two reduction factors (one each) are calculated independently for the temperature and water content effect from elastic modulus data normalized relative to the modulus at ambient conditions (25^oC,$30\%RH$). These fits are shown in Figure 22. In the simulation the product of these two factors give the total reduction factor that is multiplied by μ and $\tilde{s}$ at room temperature and relative humidity to find $\mu(\theta,\phi)$ and $\tilde{s}(\theta,\phi)$ respectively. The reduction factor does not effect evolution of these parameters, it is applied at each step to the current evolved values and is not stored for the following step.

The swelling deformation is prescribed by:

$$\lambda^s = 1 + \beta\Delta\phi + \alpha\Delta\theta \tag{36}$$

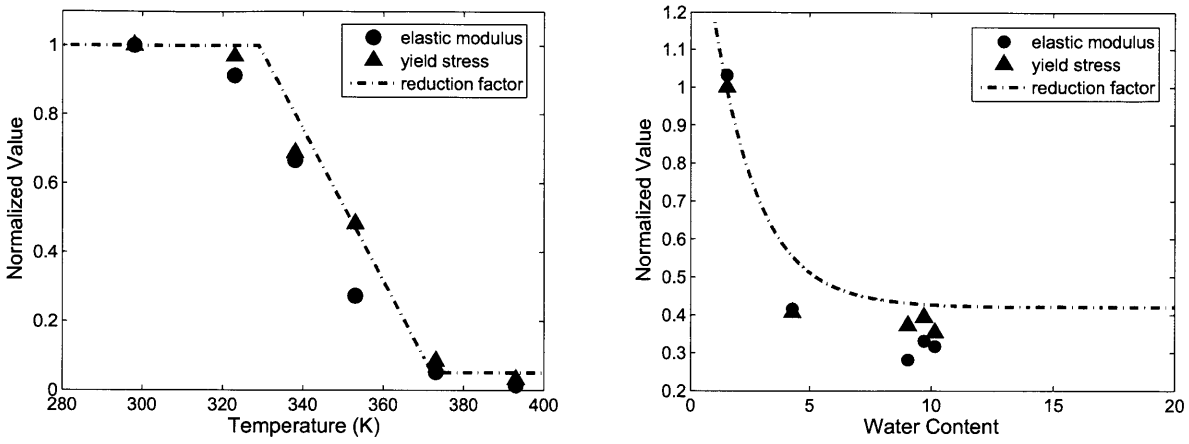

(a) (b)

Figure 22: Shear modulus adjustment factor fit to normalized elastic modulus and yield stress data for (a)temperature (b)water content.

The thermal expansion coefficient $\alpha = 1.23e-4/K$ is taken from literature (DuPont, 2004). The hygro expansion coefficient, β, is determined from the relation between water content and linear expansion based on the additive volume assumption. Starting from a completely dehydrated condition the total volume of the membrane can be expressed as:

$$V_{tot} = V_{dry} + V_{water}. \tag{37}$$

where V_{dry} is the volume of the dry membrane and V_{water} is the volume of water added to the membrane. If isotropic swelling is assumed then the stretch associated with this swelling is:

$$\lambda^s = \left(1 + \frac{V_{water}}{V_{dry}}\right)^{\frac{1}{3}} \tag{38}$$

The volume ratio can be written in terms of the molecular volumes of the membrane($M_{membrane}$) and water(M_{water}), and the mole ratio of water to sulfonic acid groups as:

$$\lambda^s = \left(1 + \phi\frac{M_{water}}{M_{membrane}}\right)^{\frac{1}{3}} \tag{39}$$

where

$$M_{membrane} = \frac{EW}{\rho_{membrane}} = \frac{1100}{1.906g/cm^3} = 558.8cm^3 \tag{40}$$

$$M_{water} = 18.016cm^3/g \tag{41}$$

where EW is the equivalent weight of the membrane defined as the weight of the membrane per mole of sulfonic acid group and $\rho_{membrane}$ is the membrane density. Both values are taken from the Dupont specifications sheet associated with NRE212. We chose to use ambient conditions($25^oC, 30\%RH$)

as the reference state. It is estimated from literature that $\phi = 1.5$ at ambient conditions (Majsztrik et al., 2008; Yeo and Eisenberg, 1977). Substituting in numbers we therefore adjust the formula for λ^s such that $\lambda^s = 0$ at $\phi = 1.5$.

$$\lambda^s = \left(\frac{\phi}{31} + 1\right)^{\frac{1}{3}} - 0.016. \tag{42}$$

To find ϕ as a function of λ^s we invert this equation

$$\phi = 31\left[(\lambda^s + 0.016)^3 - 1\right]. \tag{43}$$

The hygro expansion coefficient, defined as $\beta = \frac{\partial \ln \lambda^s}{\partial \phi}$ is then equal to

$$\beta = \frac{1}{93}\frac{1}{\left(\frac{\phi}{31}+1\right)^{\frac{1}{3}} - 0.016}\left(\frac{\phi}{31}+1\right)^{-\frac{2}{3}} \tag{44}$$

For simplicity we chose to estimate β as independent of ϕ and take for it the mean value for a range of ϕ from 1.5 to 22. Since water content (ϕ) is an input parameter rather than solved from environmental boundary conditions, there is no coupling included between stress and water content.

The parameters used in the Model I are listed in Table 1.

Table 1: Material parameters for Model I.

Model Component	**Material Parameter**	**Value**
Elastic	κ	$3.3 \times 10^8 Pa$
	μ	$1.1 \times 10^8 Pa$
Rate Dependent Yield	$\dot{\gamma}^o$	$6.72 s^{-1}$
	ΔG	$8.98 \times 10^{-20} J$
	$\tilde{s}_o$	$6.5 \times 10^6 Pa$
Distributed Yield	$\tilde{h}$	$4 \times 10^8 Pa$
	$\tilde{s}_{sat}$	$9.6 \times 10^6 Pa$
Isotropic Hardening	$\bar{h}$	$3.6 \times 10^7 Pa$
	$\bar{n}$	1
Network	μ_N	$3.3 \times 10^6 Pa$
Thermal Expansion	α_θ	$1.23 \times 10^{-4} K^{-1}$
Hygro Expansion	β_ϕ	$8.1 \times 10^{-3} \phi^{-1}$

2.5.2 Model II

In order to fit the enhanced version of the model (Model II) parameters are required for the evolution of μ, the revised evolution of s, and the back stress. All other parameters will remain the same.

Mechanism I: The evolution of μ from its initial value μ_o to a minimum value through yield is governed by:

$$\dot{\mu} = h\left(1 - \frac{\mu}{\mu_{sat}}\right)\dot{\gamma}_I^p \tag{45}$$

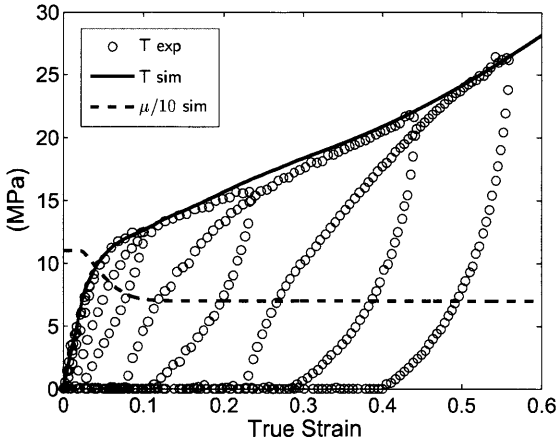

Figure 23: Evolution of μ during monotonic tensile loading for Model II.

where μ_{sat} is set to the unloading slope of a cycle to a peak strain of 0.1 (just past yield) and h is set such that that minimum value has been nearly reached by that strain(Figure 23). A cycle to a strain of this value has been chosen because this slope is found to be smaller than the unloading and reloading slopes of cycles at smaller strains and consistent with the unloading and reloading slopes of cycles at larger strains when the network contribution is accounted for.

The elastic portion of the back stress is prescribed by:

$$T'_{Bi} = \frac{1}{J} 2\mu_B \ln \lambda_{Bi} \tag{46}$$

μ_B is set according to the slope as the stress approaches zero during unloading of a cycle to a peak strain of 0.23. In this region the back stress dominates the stress-strain behavior; the intermolecular contribution to the slope is negligible because it has yielded, s is not evolving strongly, and the network contribution to the slope is negligible because the strain is still relatively small.

The magnitude of the rate of plastic deformation is described by:

$$\dot{\gamma}_I^p = \dot{\gamma}^o \exp\left[-\frac{\Delta G}{k_b\theta}\right] \sinh\left[\frac{\Delta G}{k_b\theta}\frac{\tau_P}{s}\right] \tag{47}$$

$$s = \tilde{s} - \hat{s} + \bar{s} \tag{48}$$

Both the back stress and the network stress contributions are negligible at yield, so the stress on the plastic component can be approximated by the total stress. $\dot{\gamma}^o$, ΔG, and s at the end of the rollover yield are therefore unchanged from Model I.

The evolution of $\tilde{s}$ is controlled via:

$$\dot{\tilde{s}} = \tilde{h}\left(1 - \frac{\tilde{s}}{\tilde{s}_{sat}}\right)\dot{\gamma}_I^p \tag{49}$$

$\tilde{s}_o$ sets the initial yield condition and is set according to the stress at which the rollover yield starts. $\tilde{s}$ increases according to the shape of the rollover yield with $\tilde{s}_{sat}$ equal to the s value at the end of the yield rollover. $\tilde{h}$ controls the rate of this evolution to match the shape of the rollover and will

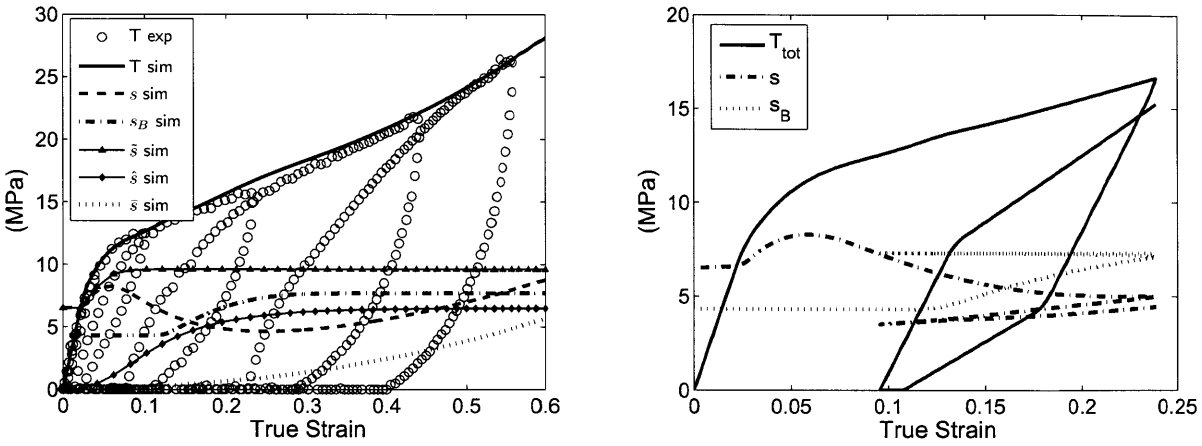

(a) (b)

Figure 24: Evolution of s and its components and s_B in Model II (a) during monotonic tensile loading (b) during cyclic loading.

differ somewhat from $\tilde{h}$ in Model I because of the simultaneous evolution of μ and $\hat{s}$. The evolution of the $\hat{s}$ and $\bar{s}$ components of s are given below. They are intricately tied with the evolution of s_B and the back stress and determination of the associated parameters will be discussed shortly.

$$\dot{\hat{s}} = \hat{h}\left(1 - \frac{\hat{s}}{\hat{s}_{sat}}\right)\dot{\gamma}_I^p \tag{50}$$

$$\dot{\bar{s}} = \bar{h}\left(\lambda_{chain}^{\bar{n}} - 1\right) \tag{51}$$

The magnitude of the rate of plastic back stress deformation is described by:

$$\dot{\gamma}_B^p = \dot{\gamma}^o \exp\left[-\frac{\Delta G}{k_b\theta}\right] \sinh\left[\frac{\Delta G}{k_b\theta}\frac{\tau_B}{s_B}\right] \tag{52}$$

$\dot{\gamma}^o$ and ΔG are the same as for the intermolecular plastic deformation. The evolution of s_B is governed by:

$$\dot{s}_B = h_B\left(1 - \frac{s_B}{s_{Bsat}}\right)\dot{\gamma}_B^p \tag{53}$$

s and s_B work in conjunction to set the unloading and reloading corners at the appropriate stress levels. However, since s has a direct effect on the intermolecular stress and s_B has an indirect effect on the intermolecular stress, each has a strong influence on the shape of the loading curve as well. $\hat{h}$, $\bar{h}$, h_B, $\hat{s}_{sat}$, s_{Bsat}, and $\bar{n}$ are simultaneously fit to the cyclic data. In general $\hat{s}_{sat}$ and s_{Bsat} are responsible for setting the unloading yield for small to moderate strains (< 0.3); $\bar{h}$ and $\bar{n}$ are responsible for setting the unloading yield for moderate to large strains (> 0.3); and $\hat{h}$, h_B, and the initial value of s_B provide a smooth loading curve. The overall evolutions in s and s_B as well as those of the individual components $\tilde{s}$, $\hat{s}$, and $\bar{s}$ are shown in Figure 24.

The temperature and hydration reduction factor which is used to calculate $\mu(\theta,\phi)$, $[\tilde{s}-\hat{s}](\theta,\phi)$, $\mu_B(\theta,\phi)$ and $s_B(\theta,\phi)$ from μ, $\tilde{s}-\hat{s}$, μ_B, and s_B is unchanged from that used in Model I.

The parameters used in Model II are listed in Table 2.

Table 2: Material parameters for Model II.

Model Component	**Material Parameter**	**Value**
Elastic	κ	$3.3 \times 10^8 Pa$
	μ_o	$1.1 \times 10^8 Pa$
Elastic Evolution	h	$4.7 \times 10^9 Pa$
	μ_{sat}	$7.0 \times 10^7 Pa$
Rate Dependent Yield	$\dot{\gamma}^o$	$6.72 s^{-1}$
	ΔG	$8.98 \times 10^{-20} J$
	$\tilde{s}_o$	$6.5 \times 10^6 Pa$
Distributed Yield	$\tilde{h}$	$1.2 \times 10^9 Pa$
	$\tilde{s}_{sat}$	$9.6 \times 10^6 Pa$
	$\hat{h}$	$7.5 \times 10^7 Pa$
	$\hat{s}_{sat}$	$6.5 \times 10^6 Pa$
Isotropic Hardening	$\bar{h}$	$2.6 \times 10^7 Pa$
	$\bar{n}$	1
Back Stress	μ_B	$2.65 \times 10^7 Pa$
	s_{Bo}	$4.3 \times 10^6 Pa$
	h_B	$2.3 \times 10^8 Pa$
	s_{Bsat}	$7.7 \times 10^6 Pa$
Network	μ_N	$3.3 \times 10^6 Pa$
Thermal Expansion	α_θ	$1.23 \times 10^{-4} K^{-1}$
Hygro Expansion	β_ϕ	$8.1 \times 10^{-3} \phi^{-1}$

2.6 3D Model Formulation

The fully 3D form of the full model (model II) is presented here for completeness. The total deformation gradient $\mathbf{F} \equiv \frac{\partial \mathbf{x}}{\partial \mathbf{X}}$, mapping a material point from the reference position $\mathbf{X}$ to its current location $\mathbf{x}$, acts in full on both major mechanism of the model.

$$\mathbf{F} = \mathbf{F}_I = \mathbf{F}_N \tag{54}$$

where $\mathbf{F}_I$ is the intermolecular deformation gradient and $\mathbf{F}_N$ is the network deformation gradient.

The Cauchy (true) stress ($\mathbf{T}$) is the sum of the stress contributions from the two mechanisms.

$$\mathbf{T} = \mathbf{T}_I + \mathbf{T}_N \tag{55}$$

where $\mathbf{T}_I$ is the stress due to the intermolecular mechanism and $\mathbf{T}_N$ is the stress due to the network mechanism.

2.6.1 Mechanism I

Forward Process Kinematics:

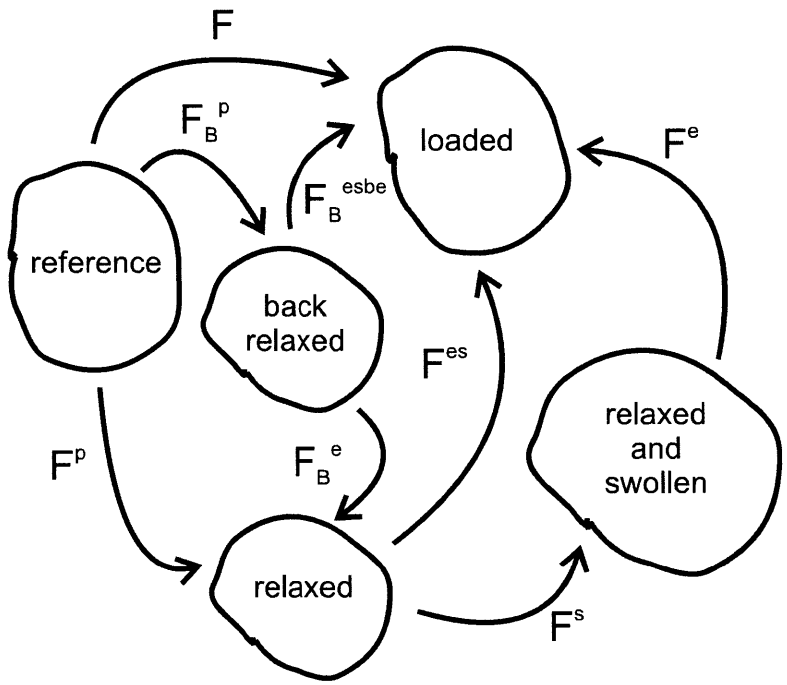

Figure 25: Schematic representation of elastic-viscoplastic framework with hygrothermal swelling and back stress.

Following polar decomposition, the intermolecular deformation gradient can be expressed as the product of a stretch and a rotation:

$$\mathbf{F}_I = \mathbf{V}_I \mathbf{R}_I \tag{56}$$

where $\mathbf{V}_I$ is the left stretch tensor and $\mathbf{R}_I$ is the rotation.

The deformation gradient for the intermolecular mechanism can be decomposed into its elastic, swelling, and plastic contributions (Figure 25).

$$\mathbf{F}_I = \mathbf{F}_I^e \mathbf{F}_I^s \mathbf{F}_I^p \tag{57}$$

where $\mathbf{F}_I^e$, $\mathbf{F}_I^s$, $\mathbf{F}_I^p$ are the elastic, swelling, and plastic components of the intermolecular deformation gradient. Plastic deformation is assumed to be incompressible such that $J_I^p = \det \mathbf{F}_I^p = 1$.

For later use, the elastic deformation gradient is decomposed into stretch and rotation components.

$$\mathbf{F}_I^e = \mathbf{V}_I^e \mathbf{R}_I^e \tag{58}$$

where $\mathbf{V}_I^e$ is the elastic left stretch tensor and $\mathbf{R}_I^e$ is the elastic rotation.

The rate kinematics are described by the velocity gradient $\mathbf{L}_I \equiv \dot{\mathbf{F}}_I \mathbf{F}_I^{-1}$ which can be decomposed into its elastic-swelling ($\mathbf{L}_I^{es}$) and plastic ($\tilde{\mathbf{L}}_I^p$) components. The elastic and swelling deformation gradients are combined here for mathematical simplicity, since the rate kinematics will be needed only to prescribe the plastic deformation.

$$\mathbf{L}_I = \mathbf{L}_I^{es} + \tilde{\mathbf{L}}_I^p \tag{59}$$

$$\mathbf{L}_I^{es} = \dot{\mathbf{F}}_I^{es} (\mathbf{F}_I^{es})^{-1} \tag{60}$$

$$\tilde{\mathbf{L}}_I^p = \mathbf{F}_I^{es} \dot{\mathbf{F}}_I^p (\mathbf{F}_I^p)^{-1} (\mathbf{F}_I^{es})^{-1} \tag{61}$$

where $\mathbf{F}_I^{es} = \mathbf{F}_I^e \mathbf{F}_I^s$ is the combined elastic and swelling deformation gradient and $\tilde{\mathbf{L}}_I^p$ is the plastic velocity gradient expressed in the loaded configuration. The plastic velocity gradient in the loaded configuration can be taken as the sum of the rate of stretching and the rate of spin.

$$\tilde{\mathbf{L}}_I^p = \tilde{\mathbf{D}}_I^p + \tilde{\mathbf{W}}_I^p \tag{62}$$

where $\tilde{\mathbf{D}}_I^p$ (symmetric tensor) is the rate of plastic stretching and $\tilde{\mathbf{W}}_I^p$ is the rate of plastic spin. Without loss of generality we choose $\tilde{\mathbf{W}}_I^p = 0$. The plastic deformation gradient is then updated by:

$$\dot{\mathbf{F}}_I^p = \mathbf{L}_I^p \mathbf{F}_I^p = (\mathbf{F}_I^{es})^{-1} \tilde{\mathbf{D}}_I^p \mathbf{F}_I \tag{63}$$

where $\tilde{\mathbf{D}}_I^p$ must be constitutively prescribed.

Back Stress Kinematics:

The back stress mechanism deformation gradient ($\mathbf{F}_B$) is equal to the plastic deformation gradient, and can be further decomposed into elastic ($\mathbf{F}_B^e$) and plastic ($\mathbf{F}_B^p$) components.

$$\mathbf{F}_B = \mathbf{F}_I^p = \mathbf{F}_B^e \mathbf{F}_B^p \tag{64}$$

For later use, the back stress elastic deformation gradient can be decomposed into stretch and rotation components.

$$\mathbf{F}_B^e = \mathbf{V}_B^e \mathbf{R}_B^e \tag{65}$$

where $\mathbf{V}_B^e$ is the back stress elastic left stretch tensor and $\mathbf{R}_B^e$ is the back stress elastic rotation.

The rate kinematics are again described by the velocity gradient which can be decomposed into its back stress plastic ($\mathbf{L}_B^p$) and its other ($\mathbf{L}_I^{esbe}$) components. The elastic, swelling, and back stress elastic deformation gradients are combined here for mathematical simplicity, since the rate kinematics will be needed only to prescribe the back stress plastic deformation.

$$\mathbf{L}_I = \mathbf{L}_I^{esbe} + \tilde{\mathbf{L}}_B^p = \mathbf{L}_I^{esbe} + \mathbf{F}_I^{esbe} \mathbf{L}_B^p \left(\mathbf{F}_I^{esbe} \right)^{-1} \tag{66}$$

$$\mathbf{L}_I^{esbe} = \dot{\mathbf{F}}_I^{esbe} (\mathbf{F}_I^{esbe})^{-1} \tag{67}$$

$$\mathbf{L}_B^p = \dot{\mathbf{F}}_B^p (\mathbf{F}_B^p)^{-1} \tag{68}$$

where $\mathbf{F}_I^{esbe} = \mathbf{F}_I^e \mathbf{F}_I^s \mathbf{F}_B^e$ is the combined elastic, swelling, and back stress elastic deformation gradient. $\mathbf{L}_B^p$ is defined in the relaxed configuration and $\tilde{\mathbf{L}}_B^p$ is the back stress plastic velocity gradient in the loaded configuration. The back stress plastic velocity gradient in the loaded configuration can be taken as the sum of the rate of stretching and the rate of spin.

$$\tilde{\mathbf{L}}_B^p = \tilde{\mathbf{D}}_B^p + \tilde{\mathbf{W}}_B^p \quad . \tag{69}$$

where $\tilde{\mathbf{D}}_B^p$ (symmetric tensor) is the rate of back stress plastic stretching and $\tilde{\mathbf{W}}_B^p$ is the rate of back stress plastic spin. Without loss of generality we choose $\tilde{\mathbf{W}}_B^p = 0$. The back stress plastic deformation gradient is then updated by:

$$\dot{\mathbf{F}}_B^p = \mathbf{L}_B^p \mathbf{F}_B^p = (\mathbf{F}_B^{esbe})^{-1} \tilde{\mathbf{D}}_B^p \mathbf{F}_I \tag{70}$$

where $\tilde{\mathbf{D}}_B^p$ must be constitutively prescribed.

Material description:

The material stress state is related to the deformation by the constitutive law for a linear elastic spring:

$$\mathbf{T}_I = \frac{1}{J} \mathcal{L}_I^e [\ln \mathbf{V}_I^e] \tag{71}$$

where $J = \det \mathbf{F}$ is the volume change, $\mathcal{L}_I^e$ is the fourth-order modulus tensor, and $\ln \mathbf{V}_I^e$ is the Hencky strain. It is assumed that the material is initially isotropic and can therefore be defined by any two elastic constants. Here we use the shear modulus μ and the bulk modulus κ.

$$\mathcal{L}_I^e = 2\mu \mathcal{I} + \left(\kappa - \frac{2}{3} \mu \right) \mathbf{I} \otimes \mathbf{I} \tag{72}$$

where $\mathcal{I}$ and $\mathbf{I}$ are the fourth-order and second-order identity tensors, respectively, and μ evolves as described in section 2.4.2.

The elastic portion of the back stress is prescribed by:

$$\mathbf{T}'_B = \frac{1}{J} 2\mu_B [\ln \mathbf{V}_B^e]' \tag{73}$$

where $\ln \mathbf{V}_B^e$ is the back stress Hencky strain and μ_B is the back stress shear modulus. Since the back stress is prescribed to be deviatoric there is no bulk modulus.

The plastic behavior, including the back stress, is now prescribed. The plastic stretching tensor in the loaded configuration is given as the product of the scalar rate of plastic deformation and a direction tensor:

$$\tilde{\mathbf{D}}_I^p = \dot{\gamma}_I^p \mathbf{N}_P^p \tag{74}$$

where the direction $\mathbf{N}_P^p$ is taken to be coaxial with the deviatoric portion of the stress tensor driving the plastic deformation $\mathbf{T}'_P = [\mathbf{T}_I - \mathbf{T}_B]'$.

$$\mathbf{N}_P^p = \frac{\mathbf{T}'_P}{|\mathbf{T}'_P|} \tag{75}$$

The scalar rate of plastic deformation is constitutively prescribed to follow a rate dependent process driven by the shear stress:

$$\dot{\gamma}_I^p = \dot{\gamma}^o \exp \left[\frac{-\Delta G}{k_b \theta} \right] \sinh \left[\frac{\Delta G}{k_b \theta} \frac{\tau_P}{s} \right] \tag{76}$$

where $\tau_P = \sqrt{\frac{1}{2}\mathbf{T}'_P\mathbf{T}'_P}$ is the scalar equivalent shear stress, $\dot{\gamma}^o$ is a pre-exponential factor proportional to the attempt frequency, ΔG is the activation energy, s is the isotropic shear resistance, k_b is Boltzmann's constant, and θ is the absolute temperature. s evolves as described in section 2.4.2.

The back stress velocity gradient is given as the product of the scalar rate of plastic deformation and a direction tensor:

$$\tilde{\mathbf{D}}^p_B = \dot{\gamma}^p_B \mathbf{N}^p_B \tag{77}$$

where the direction $\mathbf{N}^p_B$ is taken to be coaxial with the back stress which is deviatoric.

$$\mathbf{N}^p_B = \frac{\mathbf{T}'_B}{|\mathbf{T}'_B|} \tag{78}$$

The scalar rate of back plastic deformation is constitutively prescribed to follow a rate dependent process driven by the back shear stress:

$$\dot{\gamma}^p_B = \dot{\gamma}^o \exp\left[-\frac{\Delta G}{k_b\theta}\right] \sinh\left[\frac{\Delta G}{k_b\theta}\frac{\tau_B}{s_B}\right] \tag{79}$$

where $\tau_B = \sqrt{\frac{1}{2}\mathbf{T}'_B\mathbf{T}'_B}$ is the scalar equivalent shear stress. s_B, the isotropic shear resistance to inelastic deformation, evolves as described in section 2.4.2.

The swelling portion of the intermolecular response is given by:

$$\mathbf{F}^s_I = \lambda^s \mathbf{I} = (1 + \beta\Delta\phi + \alpha\Delta\theta)\,\mathbf{I} \tag{80}$$

where the swelling is isotropic, λ^s is the scalar swelling stretch, β is the coefficient of hygro expansion, α is the coefficient of thermal expansion, $\Delta\phi$ and $\Delta\theta$ are the changes in ϕ and θ respectively relative to a reference state at which the model is calibrated (here chosen as 25^oC, $30\%RH$).

2.6.2 Mechanism N

Kinematics:

Using the polar decomposition, the network deformation gradient can be expressed as the product of a stretch and a rotation:

$$\mathbf{F}_N = \mathbf{V}_N\mathbf{R}_N \tag{81}$$

where $\mathbf{V}_N$ is the left stretch tensor and $\mathbf{R}_N$ is the rotation.

The network deformation gradient can also be multiplicatively decomposed into a mechanical and a swelling component.

$$\mathbf{F}_N = \mathbf{F}^m_N\mathbf{F}^s_N \tag{82}$$

where $\mathbf{F}^m_N$ is the deformation gradient due to mechanical stretching of the network and $\mathbf{F}^s_N = \mathbf{F}^s_I$ is the deformation gradient due to hygrothermal swelling. The mechanical component can then be expressed according to the polar decomposition as

$$\mathbf{F}^m_N = \mathbf{V}^m_N\mathbf{R}^m_N \tag{83}$$

where $\mathbf{V}^m_N$ is the mechanical network left stretch tensor and $\mathbf{R}^m_N$ is the mechanical network rotation.

Constitutive:

The Cauchy (true) stress on the network ($\mathbf{T}_N$) is described by the Neo-Hookean relation:

$$\mathbf{T}_N = \frac{1}{J}\mu_N \mathbf{B}'_N \tag{84}$$

where $J = \det \mathbf{F}$ is the volume ratio, μ_N is the network shear modulus, $\mathbf{B}_N = \mathbf{V}_N^2$ is the left Cauchy-Green tensor, and $\mathbf{B}'_N$ is the deviatoric portion of $\mathbf{B}_N$.

Alternatively the network stress can be expressed with the swelling explicitly taken into account.

$$\mathbf{T}_N = \frac{1}{J_N^m \lambda^s}\mu_N \mathbf{B}_N^{m\prime} \tag{85}$$

where $J_N^m = \det \mathbf{F}_N^m$ is the network mechanical volume ratio, $\mathbf{B}_N^m = \mathbf{V}_N^{m2}$ is the network mechanical left Cauchy-Green tensor, and $\mathbf{B}_N^{m\prime}$ is the deviatoric portion of $\mathbf{B}_N^m$. These two formulations are identical.

This network portion of the model can be readily compared to a typical Flory-Huggins type Gaussian model of a swelling rubber. The Cauchy stress in such an idealized material is:

$$\mathbf{T} = \frac{nk\theta\nu_p^{1/3}}{J^m}\mathbf{B}^m - \frac{nk\theta}{J^m}\mathbf{I} \tag{86}$$

where $nk\theta$ is equivalent to the shear modulus μ_N in the unswollen state and $\nu_p = \left(\frac{1}{\lambda^s}\right)^3$ is the polymer volume fraction. Substituting in this notation and separating the shear and the bulk response can then be rewritten to more closely resemble the network expression here as:

$$\mathbf{T} = \frac{1}{J^m\lambda^s}\mu_N \mathbf{B}^{m\prime} - \frac{1}{J^m}\mu_N\left(1 + \frac{1}{3\lambda^s}\mathrm{tr}\mathbf{B}^m\right)\mathbf{I} \tag{87}$$

where the second term is the bulk response which has been lumped into the intermolecular mechanism in the constitutive model presented in this chapter.

2.7 Concluding Remarks

The mechanical behavior of the Nafion (NRE212), which typically serves as the polymer electrolyte membrane in low temperature fuel cells, has been experimentally characterized as a function of rate, temperature, and hydration for both monotonic and cyclic loading. These experiments provide details on the subtleties of the time, temperature, and hydration dependence as well as new details on the cyclic behavior which are critical to understanding membrane deformation and failure in fuel cell operation. The behavior of NRE212 was found to be transversely isotropic and quantitatively, but not qualitatively, dependent on the chemical pre-treatment. Dynamic mechanical analysis showed that, under dry ($30\%RH$) conditions, the material begins to transition from the glassy to the rubbery state at 75^oC, with a glass transition of 105^oC. DMA further revealed that the fully hydrated state is significantly more compliant than the dry state, with the material beginning to transition from the glassy to the rubbery state at 40^oC. Large strain monotonic tensile tests revealed an initial elastic response followed by a rollover type yield and moderate post-yield strain hardening. The rate-dependent stress-strain behavior was seen to be highly dependent on temperature and hydration: the dry state transitions from an elastic-plastic behavior at 25^oC to an increasingly rubbery behavior with decreasing elastic modulus and yield stress as temperature is increased

through the glass transition to 100^oC. At all temperatures, increasing hydration acts to decrease the elastic stiffness and yield stress. Unloading from different strains revealed the elastic-plastic nature of the behavior even for the elevated temperature and hydrated states. Cyclic loading-unloading-reloading excursions to different strains showed significant nonlinear recovery at all strains past yield with a highly nonlinear reloading behavior which has an apparent reduced yield stress and then rejoins the initial loading path. The significant time, temperature, and hydration dependent mechanical behavior evident from this uniaxial tensile data suggests that the rate of heating/cooling and hydrating/drying the MEA during startup/shutdown of the fuel cell as well as whether these operations are done simultaneously or sequentially will be critical to the nature and magnitude of the stresses that develop in the membrane.

A constitutive model was developed in two stages to capture the mechanical behavior of Nafion NRE212; the first to capture all the key elements of monotonic loading and the second to capture all the key elements of more general loading histories. Model I, consisting of a linear elastic-plastic intermolecular component and a nonlinear network component, was shown to be capable of capturing the rate, temperature, and hydration dependence of monotonic loading but not the unloading or reloading behavior. The intermolecular resistance captures the local intermolecular barriers to initial elastic deformation and also captures the thermally-activated nature of yield; these intermolecular barriers are modeled to decrease with increasing temperature and hydration, in particular mimicking the reduction in these barriers as the material approaches and enters the glass transition regime, successfully capturing the strong temperature and hydration dependence of the stress-strain behavior. Model II, a version of Model I enhanced with the addition of a back stress to the viscoplastic element in the intermolecular component, was shown to additionally be capable of capturing the rate, temperature, and hydration dependence of the cyclic response. The back stress has similar properties to the intermolecular elastic-plastic element, with an initial elastic portion, a rate dependent saturation, and barriers which decrease in the same way with temperature and hydration. The back stress develops during inelastic deformation and then helps to drive reverse deformation during unloading. This enables the model to capture the highly nonlinear nature of unloading and reloading including the reduction in reloading yield stress which occurs with increasing strain. Impressively, this model captures the temperature and hydration dependence of the cyclic behavior without any additional material parameters. Model II is capable of capturing the behavior of Nafion over the wide range of strains, environmental conditions, and loading conditions relevant to modeling the membrane within the fuel cell. This will enable analysis of the pertinent complex hygrothermal-mechanical loading conditions. The constitutive model has been formulated for use within nonlinear finite element analysis enabling more general application.

While this model has been developed to match experimental data obtained from Nafion in consideration of the physics which generally occurs in polymers, it is not explicitly tied to the microstructure and deformation mechanisms in Nafion. It is desirable to make this connection more explicit in order to make the model more readily applicable to similar materials and in order to relate the mechanics to proton channel orientation. This will be addressed to some extent in the following chapter using x-ray scattering. It would also be interesting to experimentally characterize and develop models for materials of similar chemistry (such as Flemion, which has the same backbone but shorter side chains) in order to further assess the origin of features seen in the mechanical behavior of each.

The main mechanical loading of the membrane in a fuel cell is biaxial in the membrane plane and occurs via constrained hygro-thermal swelling. In this chapter only uniaxial loading at a

constant hygro-thermal condition has been considered. In order to have confidence in fuel cell in-situ simulations, the model must be validated under these more relevant conditions. This validation will be discussed in chapter 4.

3 Nafion microstructure

3.1 Background

Nafion is the membrane of choice for Proton Exchange Membrane Fuel Cells (PEMFC) because its unique microstructure allows rapid transport of protons in a hydrated environment while maintaining mechanical integrity. Its teflon-like backbone is hydrophobic while the sulfonated side chains are hydrophilic (Figure 26). The initial introduction of water molecules into this hydrophobic-hydrophillic structure is thought to cause the side chains to aggregate into clusters (somewhere between spherical and cylindrical). Upon further hydration these clusters then percolate the membrane, providing increased ionic conductivity, while the backbone remains relatively dry providing the mechanical integrity (Figure 27). Extensive studies have been conducted over the last 30 years in order to deduce the size and shape of the microstructural features (see Mauritz and Moore (2004) for a comprehensive review).

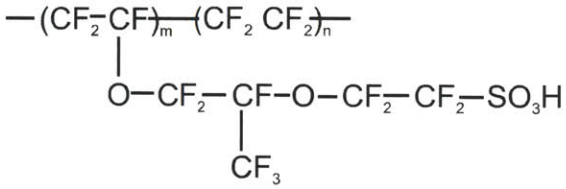

Figure 26: Chemical structure of Nafion.

Small angle x-ray scattering (SAXS) and wide angle x-ray scattering (WAXS) are techniques frequently used to deduce aspects of the structure of Nafion. SAXS is an x-ray scattering technique used to examine features roughly 5 to $25nm$ by measuring diffraction angles approximately $0.1nm^{-1}$ to $2nm^{-1}$. WAXS records larger diffraction angles, on the order of $5nm^{-1}$ to $50nm^{-1}$, thereby allowing the examination of smaller features. Peaks in SAXS and WAXS patterns are a result of electron density differences among structural features. When an x-ray is passed through a material it diffracts off the electrons orbiting around atoms in the material. Depending on the spacing of those atoms, the diffracted parts of the beam will interfere either constructively or destructively. The averaged effects of these constructive and destructive interferences throughout the beam path will result in a spectrum of intensities at different angles at the exit of the beam from the material. These spectrums are generally recorded as intensity versus q-value, where q is a measure of the exit angle with units of either inverse angstroms or inverse nanometers. Unlike with crystallography, SAXS and WAXS can be used to analyze materials that are only partially ordered. While there are

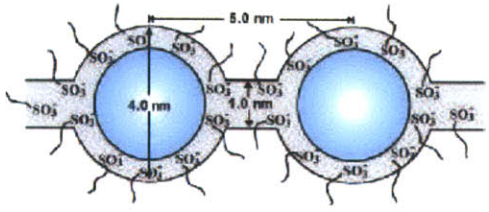

Figure 27: Early representation of clustering of hydrophillic side chains in Nafion from Hsu and Gierke (1982) as updated by Mauritz and Moore (2004).

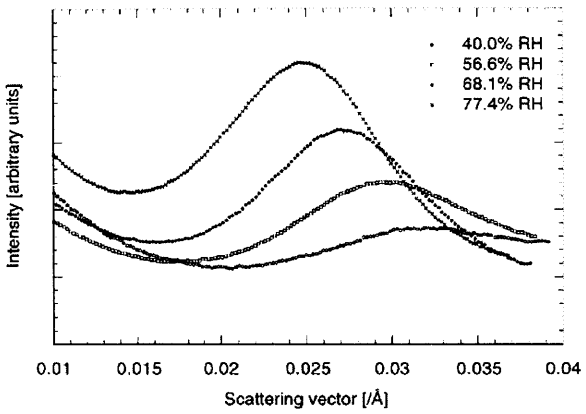

Figure 28: Evolution of the ionomer cluster peak in Nafion N115 with relative humidity from Elliott et al. (2000).

not sharp spikes in the spectrum as there are in crystalline structures, there are clear peaks whose location, width, and relative magnitude can be used to infer the size, distribution, and orientation of different semi-ordered structures in a non-crystalline or semi-crystalline material.

Elliott and coworkers (James et al., 2000; Elliott et al., 2000) conducted SAXS tests on Nafion N115 (extruded, $127\mu m$ thick) in dry, swollen, and oriented states. They found that the ionomer (or cluster) peak, the major peak in the SAXS spectrum which is generally attributed to agglomeration of the sulfonic acid side chains, moved to a lower angle and increased in intensity with swelling, suggesting an increase in spacing between clusters and an increase in the size of individual clusters (Figure 28). Using the Maximum Entropy analysis method they suggest that this increase in size is accounted for largely by the coalescing of multiple clusters into single clusters thereby accounting for the frequently observed discrepancy between the magnitude of the microscopic and macroscopic swelling in Nafion (microscopic is significantly larger, 29.3% vs 9% linear swelling at 100%RH). Specimens were drawn under atmospheric conditions to 50% strain in the direction parallel to and perpendicular to the direction of extrusion. In the former case the applied strain increases the arcing perpendicular to the extrusion direction, in the latter the intensity parallel to the extrusion increases but it does not result in a symmetric scatter profile (Figure 29)(James et al., 2000; Elliott et al., 2000). The initial anisotropy in the extruded form of Nafion makes interpretation of the changes with applied strain difficult.

Rubatat and coworkers have used SAXS, WAXS, small angle neutron scattering (SANS), birefringence, atomic force microscopy (AFM), and transmission electron microscopy (TEM) to study the structure of Nafion and its evolution with hydration and mechanical orientation (Rubatat et al., 2002, 2004; Heijden et al., 2004b; Rubatat and Diat, 2007; Heijden et al., 2004a). The four peaks found in the various SAXS and WAXS studies are shown and labeled in Figure 30a. The four peaks are (1) the matrix peak associated with a correlation distance of crystalline parts, (2) the ionomer peak associated with the distance between polymer aggregates, (3) the low angle WAXS peak associated with combined amorphous and crystalline intermolecular distances, and (4) the wide angle WAXS peak associated with multiple crystalline intramolecular distances (Heijden et al., 2004b). Rubatat et al. (2002) used SAXS on Nafion 117(extruded, $178\mu m$ thick) to study the microstructure as a function of polymer volume fraction by progressively diluting Nafion with water. Both the ionomer peak and the matrix peak were shown to move to larger angles with increasing polymer

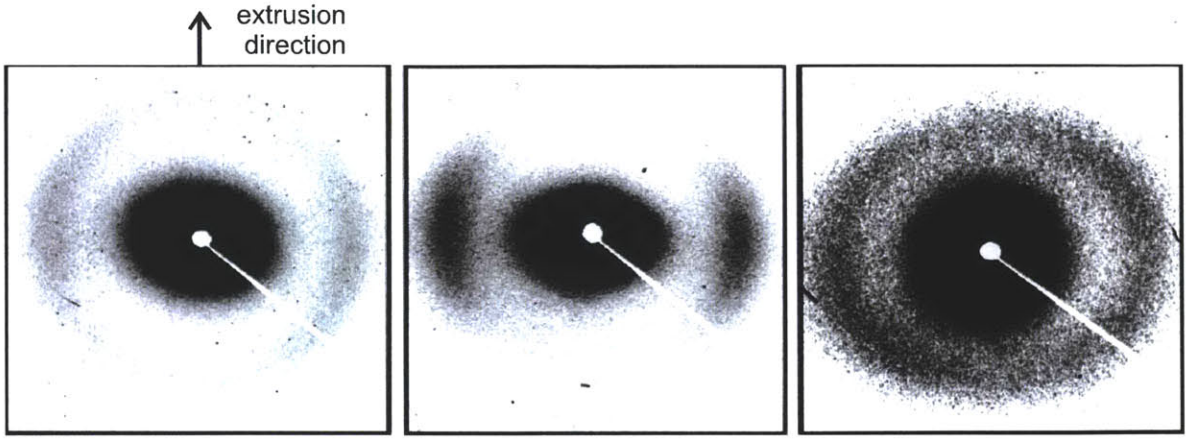

Figure 29: SAXS intensity map for Nafion N115 from Elliot et. al. (2000)Elliott et al. (2000). (a) In the as-received state the scattering has arcing in the direction perpendicular to the extrusion direction. (b) When the specimen is strained parallel to the extrusion direction the arcing increases and the scattering peak becomes more elliptical. (c) When the specimen is strained perpendicular to the extrusion direction the intensity parallel to the extrusion direction increases but the scattering profile does not become symmetric.

fraction. The continual evolution of the scattering profile with dilution was used to refute the earlier belief that a strong structural reorganization occurs during swelling. Rubatat et al. (2004) further confirmed the lack of major structural reorganization with swelling, using microscopy techniques in addition to SAXS on Nafion from dry membrane to aqueous dispersion. The fibrillar morphology was present throughout the dilution process. Heijden et al. (2004b) examined Nafion N117 with SAXS and WAXS while subjected to uniaxial tension in order to establish a relationship between structural orientation and stretch as well as determine any stretch induced crystallinity changes. They determined that crystallinity content is not altered by applying strain. Evolution of the Hermans' orientation function of each SAXS and WAXS peak with strain indicates that the molecular and ionomer orientation differ at small to moderate strains but coincide at large strain (Figure 30b). The results were explained in terms of a bundle-cluster model in which sections of the backbone are assumed to exist in locally aligned bundles that are randomly aligned with respect to other bundles; under small strains ($\lesssim 0.4$) the bundles rotate so that they are aligned with each other; under large strain ($\gtrsim 0.4$) the bundles are all aligned and the aggregates are aligned within the bundles (Figure 31). The water lays outside the bundle. Rubatat and Diat (2007) used SANS to show that the clusters orient but do not deform during applied strain confirming their earlier rejection of spherical clusters. The evolution of the ionomer peak during uniaxial deformation was reasonably simulated using the bundle-cluster model.

Barbi et al. (2003) conducted SAXS on Nafion N117 (extruded, 178μm thick) at different strains in both the machine direction and the transverse direction. A chord distribution function (CDF, autocorrelation of the gradient of the electron density distribution) approach was used to interpret the structure. This analysis method is chosen to facilitate visualization of the structure including domain size, shape, and spacing. They propose a structure of ionomer channels that open to form hollow ionomer layers oriented parallel to the strain direction (Figure 32). For the crystalline

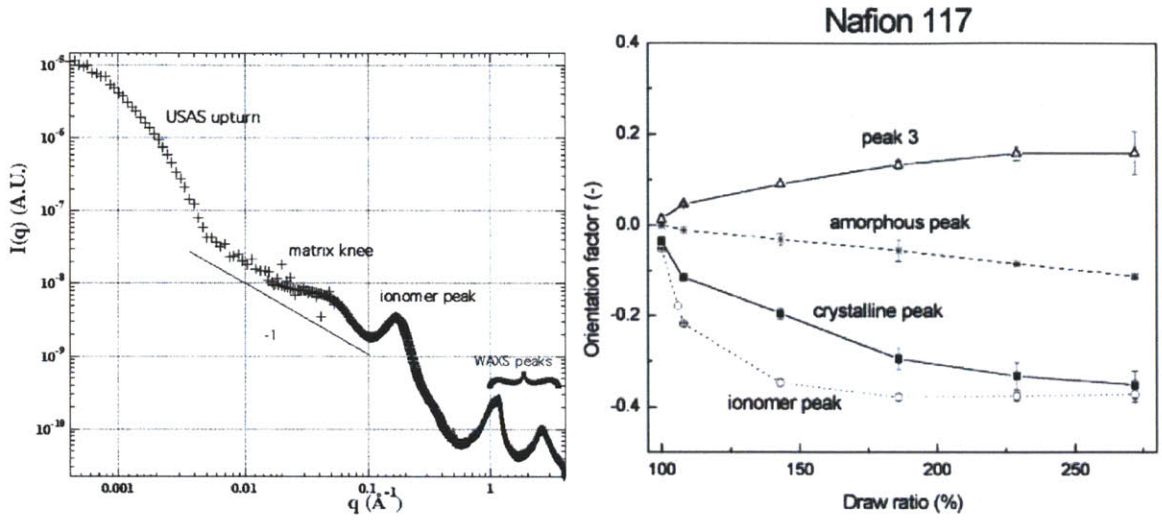

(a) (b)

Figure 30: Combined SAXS and WAXS of water swollen Nafion N117 neutralized with lithium from Heijden et. al. (2004) (a) Intensity vs q-value, (b) Orientation of peak as a function of draw ratio (Heijden et al., 2004b).

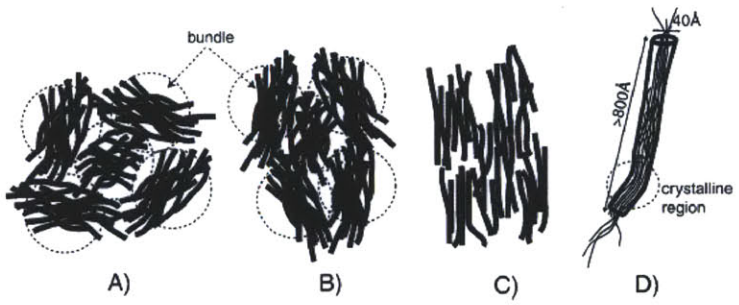

Figure 31: Sketch of the bundle-cluster model of Nafion under deformation from Heijden et al. (2004b) (A) Organization of bundles of aggregates made of more or less aligned and ordered polymeric chains surrounded with ionic groups and water molcules, (B) the bundles rotate to align with the direction of applied strain, (C) at high strains the aggregates are oriented within each bundle (D) a magnification of a single bundle.

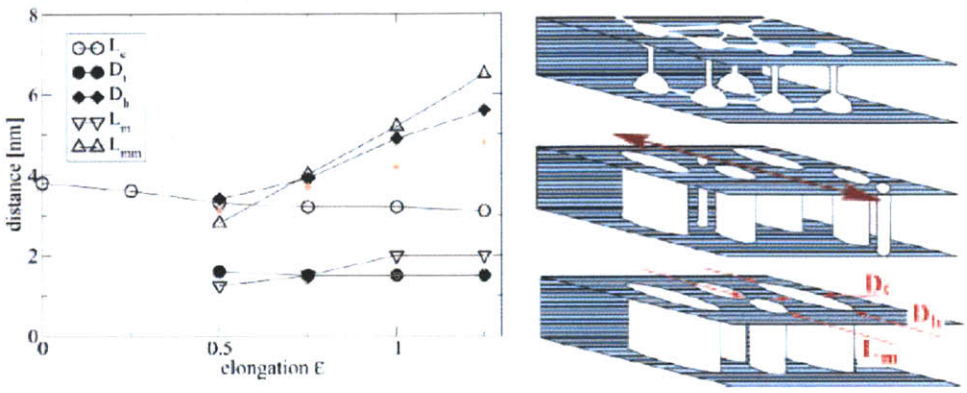

Figure 32: Ionomer peak evolution during uniaxial tension according to chord distribution function analysis by Barbi et al. (2003).

portion, the initially oblong crystallites break up and then align with the applied strain. The structure was also examined after the load was removed from each strain, revealing that most of the microstructural change remains, as expected according to the predominance of macroscopic plastic deformation.

Most recently Schmidt-Rohr and Chen (2008) have performed scattering simulations for several different Nafion microstructural models. They found that the best fit to the available SAXS data came from densely packed locally parallel cylindrical inverted mycelles with a persistence length of tens of nanometers and elongated cylindrical crystallites (Figure 33). This differs from the models discussed previously primarily in that they postulate the water to be contained within the cylinders with the hydration process occurring by a simple swelling of the cylinders without any increase in number of ionic groups per cluster or other structural reorganization. Kong and Schmidt-Rohr (2011) address the water content discrepancies as Nafion transitions from film to dilute polymer solution. They propose that at large water contents the channels could transition into ribbons without major structural transition, but that this water content ($> 20\%$ water volume fraction) is outside the fuel cell operating condition. At elevated (but realistic operational) temperatures one would expect to reach this in-situ, but neither our study nor their study involves non-ambient temperatures. This transition can therefore be neglected in any model discussed herein.

While the above studies taken together start to give a fair picture of the structure of Nafion, the studies do not examine the time or force dependency of the structural changes and they do not fully explain the structural evolution during both hydration and deformation. The SAXS and WAXS study described in this chapter focuses on the orientation of the microstructural features with uniaxial extension and its relation to the stress supported by the membrane. An understanding of this evolution will help elucidate the mechanisms governing the complex mechanical behavior discussed at length in Chapter 2, and could also prove useful in using mechanical strain as a means for manipulating nanochannel alignment to optimize proton transport. This data will be interpreted in the context of the Schmidt-Rohr and Chen (2008) model: the microstructure is assumed to consist of locally aligned hydrophilic cylindrical clusters a few nanometers in diameter and separate crystallite regions also of roughly nanometer scale, the exterior of the clusters and the crystalline regions are hydrophobic.

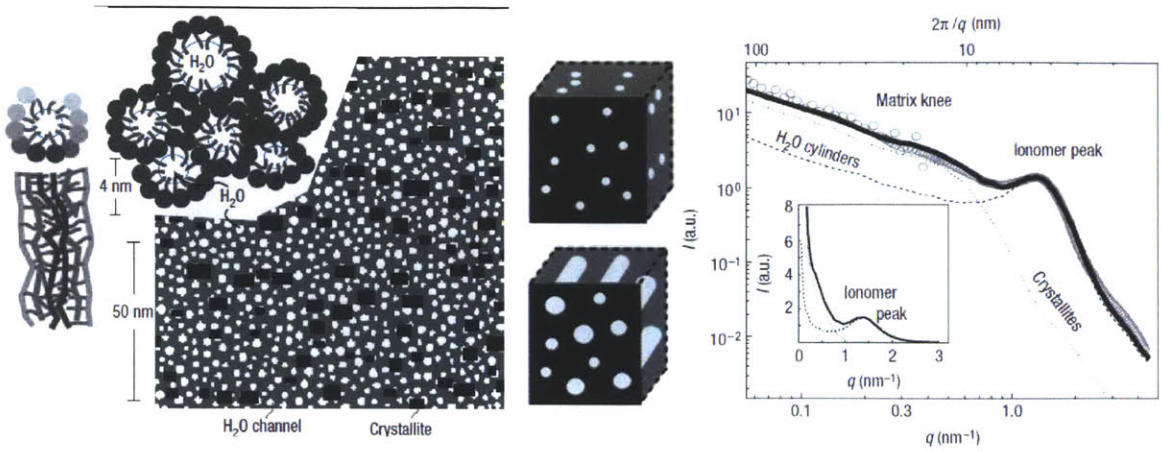

Figure 33: Structural schematic of parallel cylindrical inverted mycelle model from Schmidt-Rohr and Chen (2008). Side view (far left). Top view at two different magnifications (middle left). Revised suggestion of swelling process from ambient conditions to in water conditions (middle right). SAXS data as fit by simulated SAXS of proposed structure (right)(Kong and Schmidt-Rohr, 2011).

3.2 Experiments

3.2.1 Materials

Commercial NRE212 films ($54\mu m$, dispersion cast, Dupont, Ion Power Inc) were used for the experimental characterization of Nafion. The films were stored in a desiccator cabinet upon removal from the initial packaging to minimize variability in data from aging and humidity effects. The film was cut into tensile specimens using a dogbone shaped die with gauge length of $9.54mm$ and gauge width $3.14mm$. The nominal thickness is $54\mu m$. The thickness of each specimen was determined from the average of three measurements taken along the gauge length with a Mitutoyo micrometer.

3.2.2 X-ray scattering

SAXS and WAXS experiments were conducted at Argonne National Laboratory Advanced Photon Source at Sector 5 (Dupont-Northwestern-Dow Collaborative Access Team). The hutch was setup for simultaneous collection of SAXS and WAXS by 2D detectors. The SAXS sensor was configured to collect q-values ranging from $0.07nm^{-1}$ to $1.7nm^{-1}$. The WAXS sensor was configured to collect q-values ranging from $5nm^{-1}$ to $45nm^{-1}$. $q = 4\sin\theta/\lambda$ is the scattering vector where λ is the wavelength of the input beam. Each image was corrected for detector dark current, non-uniformity, and distortion and then normalized to the incident flux. Azimuthal responses were obtained by averaging over the entire 180^o or 360^o 2D detector. Meridional (stretching direction) and equatorial (transverse direction) responses were obtained by averaging over 10 degrees in azimuthal angle. Scattering data was collected while the specimen was subjected to uniaxial loading. All tests were conducted at a nominal strain rate of $0.005s^{-1}$. This value was chosen to allow collection of a sufficient scattering intensity without a significant change in strain. The experimental configuration (Figure 34b) is shown along with a schematic representation (Figure 34a). A Qimaging Retiga 1300 video extensometer was used to track the local strain in the region through which the x-ray beam

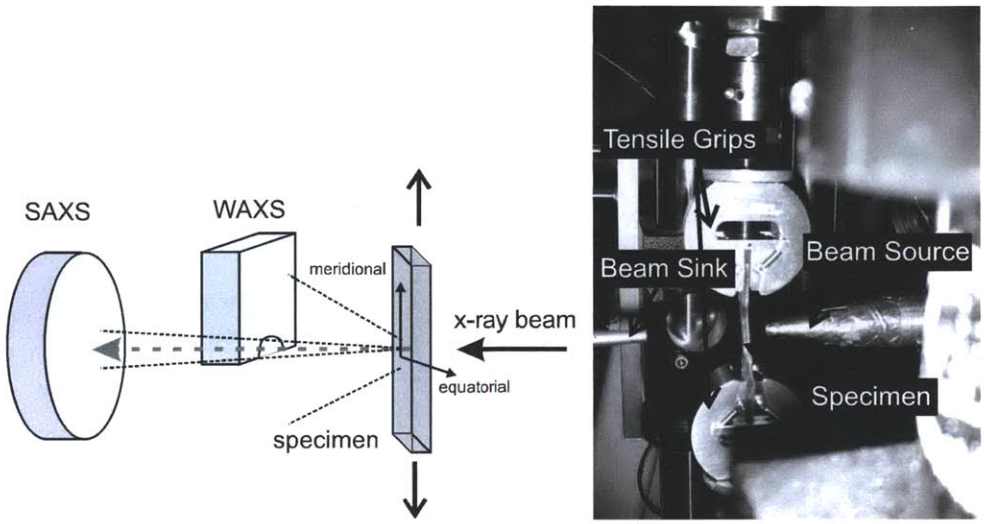

(a) (b)

Figure 34: Experimental setup for simultaneous x-ray scattering and tensile tests.

passed. In-water tests were conducted by soaking the specimen in water prior to mounting. The time required to close the hutch and test at a slow enough rate to collect appropriate scattering information prevented collection of data on deforming wet specimens.

3.3 Results and Analysis

3.3.1 Initial Structure

The two dimensional scattering profiles for both the small angle (SAXS) and wide angle (WAXS) of undeformed Nafion NRE212 are shown in Figure 36. Darker coloring indicates greater scattering intensity. Both profiles are axisymmetric indicating initial isotropy in the membrane plane. This differs from the scattering exhibited by N117 and other extruded forms of Nafion which show anisotropy in the undeformed state (i.e. Figure 29a). This initial isotropy will simplify analysis of structural evolution as the membrane undergoes deformation. The SAXS and WAXS each capture two characteristic peaks, here they will be numbered 1-4 from longest characteristic spacing (smallest q) to shortest characteristic spacing (largest q). These peaks are more clearly evident in line plots of azimuthally integrated intensity versus q-value (Figure 37), where the isotropy is again evident in the overlay of the azimuthal, meridional, and equatorial values at each q. These peak locations can be roughly converted to characteristic distances using the Bragg equation for point scatterers: $\lambda = 2d \sin\theta$, where d is the characteristic distance. Peak 1, commonly referred to as the matrix peak occurs at $q = 0.6nm^{-1}$ corresponding roughly to a spacing of $11nm$; peak 2, commonly referred to as the ionomer cluster peak, occurs at $q = 2.2nm^{-1}$ corresponding roughly to a spacing of $2.9nm$; peak 3 occurs at $q = 12.1nm^{-1}$ corresponding roughly to a spacing of $0.52nm$; and peak 4 occurs at $q = 27.9nm^{-1}$ corresponding roughly to a spacing of $0.23nm$.

Building on the scattering profile analysis of Heijden et al. (2004b) and Schmidt-Rohr and Chen (2008) the structure of Nafion is taken to be composed of randomly oriented cylindrical ionomer clusters consisting of aligned backbone strands with the sulfonated side chains pointing inward and of randomly oriented crystalline regions (Figure 35). According to this interpretation peak 1 results

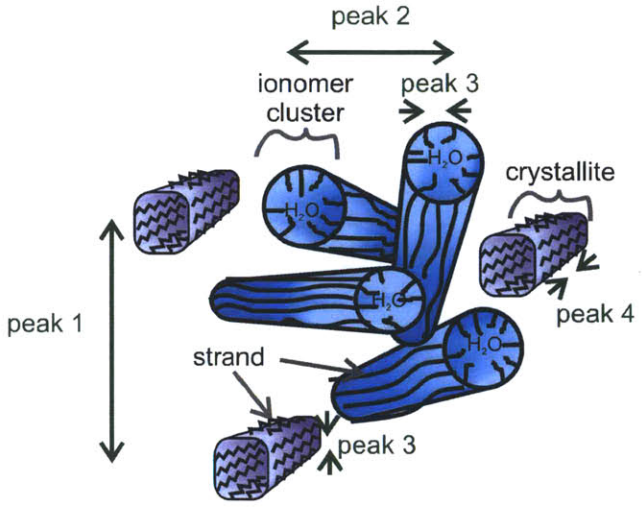

Figure 35: Schematic of Nafion microstructure.

from spacing between crystallites, peak 2 results from spacing between ionomer clusters, peak 3 results from an inter-strand backbone spacing, and peak 4 results from an intra-strand backbone spacing (a strand is a polymer backbone chain locally aligned with other polymer backbone chains; peak 3 backbone/strand spacings arise from both the crystallites and the semi-orderly ionomer clusters, whereas peak 4 backbone/strand spacings arise only from the crystallites).

3.3.2 Deforming structure

Nafion undergoes elastic-plastic deformation under monotonic uniaxial tensile loading as discussed extensively in Chapter 2. Figure 38 shows a typical stress-strain curve with triangles indicating the points at which x-ray scattering profiles will be shown. The features of this curve can be divided into three basic loading regions: there is a linear-elastic region at strains less than about 0.02, the curve then exhibits a gradual rollover as yielding occurs over a strain of roughly 0.06 to 0.10, post-yield strain hardening is then observed with the strain hardening slope increasing with increasing strain.

The scattering profiles evolve anisotropically as Nafion is subjected to uniaxial tension. The SAXS peaks become elliptical with the long axis aligned with the equator and become less intense in the meridional direction, indicating an anisotropic change in their spacing. The WAXS peaks do not undergo a significant change in location, but they do develop anisotropic intensity, with peak 3 becoming most intense along the equator and peak 4 becoming most intense along the meridian (Figure 40), indicating minimal change in feature spacing but a significant change in orientation. The development of anisotropy can also be viewed from the meridional and equatorial line plots shown in Figure 41 at two different strains. As uniaxial tension is increased, both SAXS meridional peaks move to smaller q and both SAXS equatorial peaks move to larger q, implying that both the clusters and crystallites are moving further apart in the stretching direction and closer together in the transverse direction (recall, q relates to inverse spacing). These peaks also change in intensity with applied strain, this is due in part due to changes in the number of scattering objects in the electron beam and in part due to the fact that the q of the peak is changing (related to Porod scattering (Porod, 1948)). There is therefore no straightforward interpretation of the intensity

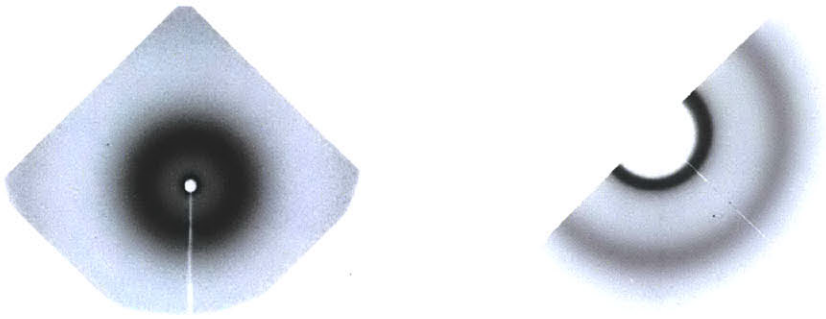

(a) (b)

Figure 36: 2D x-ray scattering pattern of undeformed NRE212: (a)small angle, (b)wide angle.

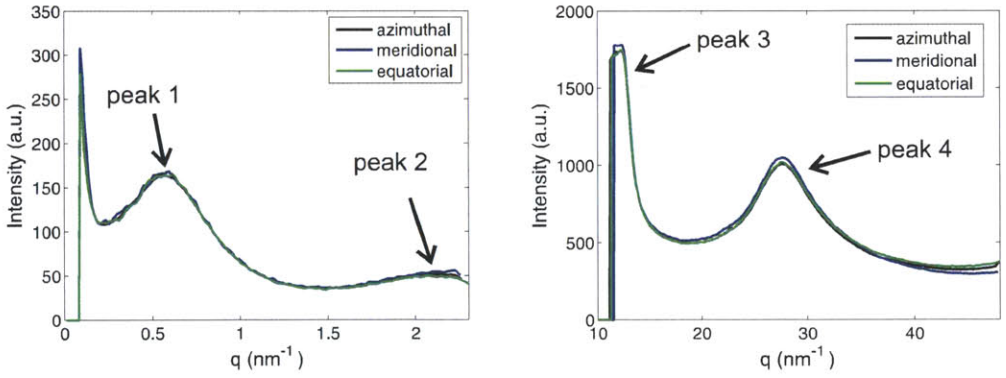

(a) (b)

Figure 37: Azimuthal, meridional, and equatorial x-ray intensity profile of undeformed NRE212: (a)small angle, (b)wide angle.

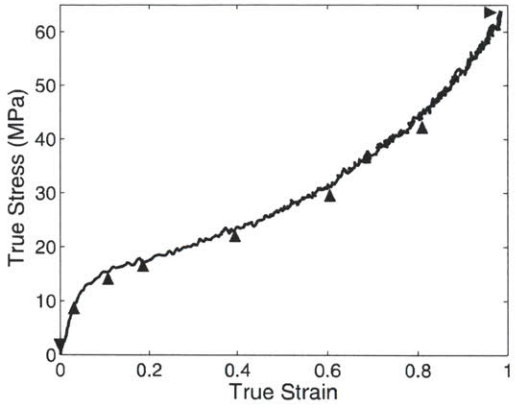

Figure 38: Stress-strain behavior of NRE212 subjected to monotonic uniaxial tension.

changes in these peaks (though they would be picked up in a scattering simulation). WAXS peak 3 shifts to a slightly lower q-value and broadens along the equator, indicating minor deformation of the cluster inter-strand spacing. WAXS peak 3 meridional and peak 4 have negligible shifts. All of the WAXS peak intensities change quite significantly. Peak 3 equatorial and peak 4 meridional increase in intensity with applied strain, whereas peak 3 meridional and peak 4 equatorial decrease in intensity with applied strain. The opposing trends in the two peaks are expected since the features each captures are perpendicular to each other. The WAXS peak intensity evolutions indicate that the clusters and the crystallites are rotating to align with the stretching direction. While both the peaks and stress evolve monotonically with strain there is no obvious correspondence between the peak evolution and the stress beyond this. Clearly a more direct means of monitoring peak evolution is needed.

In order to more directly correlate changes in the x-ray scattering peaks with stress and strain, a Lorentzian fit is performed for each peak at each captured frame. The fit gives the peak intensity, location, and width. Given the trends apparent from the line plots in Figure 41, the analysis here will focus on the location of the SAXS peaks and the intensity of the WAXS peaks. To facilitate intuition, real space is used instead of inverse space for the SAXS data, using $d = 2\pi/q$ which roughly corresponds to (but is known to overestimate (Schmidt-Rohr and Chen, 2008)) the distance (d) between scattering entities. The WAXS peak intensities are normalized by the azimuthal intensity in order to focus on orientation effects and reduce noise.

Figure 42 confirms that each of the peak evolution trends discussed in terms of the 2D images and the intensity vs q line plots is indeed monotonic. Second, we note that peaks 1 and 4 are tracked with the most accuracy. Since peaks 2 and 3 lie at the edge of the SAXS and WAXS detection bands respectively, there is a lot of noise in the fitting procedure. The proceeding analysis will therefore focus primarily on peaks 1 and 4, noting that: (1) over the detectable range SAXS peaks 1 and 2 exhibit similar behavior to each other, and (2) WAXS peaks 3 and 4 exhibit similar behavior to each other, but with the meridional and equatorial trends swapped, thereby implying the same structural information. Peak 1 appears to be linear in both equatorial and meridional spacing, with the meridional (stretching direction) spacing increasing with strain at a greater slope than the equatorial (transverse direction) spacing decreases. Peak 4 appears to be non-linear, with a change in slope occurring around a strain of 0.2. In order to more closely examine these trends they will

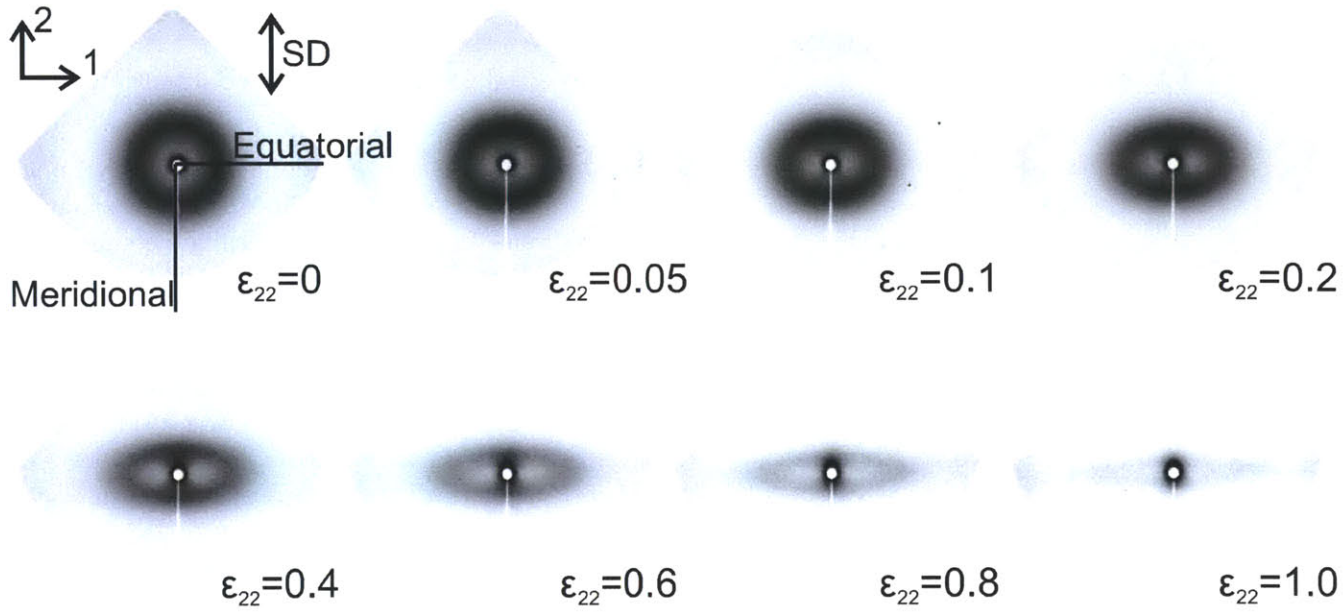

Figure 39: 2D SAXS pattern of NRE212 as a function of monotonic deformation. True strain in the stretching direction (SD) is indicated on each image. Dark regions are intensity peaks. Intensity scale is the same for each image. The equatorial and meridional directions indicated on the first image holds for all images.

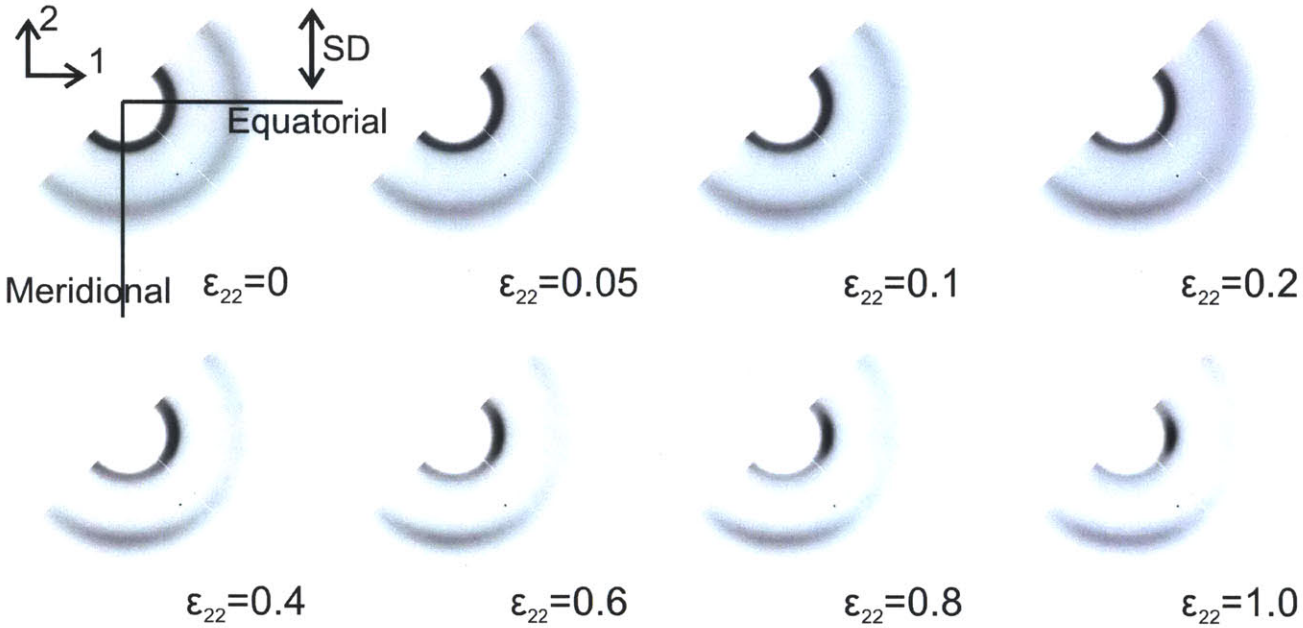

Figure 40: 2D WAXS of NRE212 as a function of monotonic deformation. True strain in the stretching direction (SD) is indicated on each image. Dark regions are intensity peaks. Intensity scale is the same for each image. The equatorial and meridional directions indicated on the first image holds for all images.

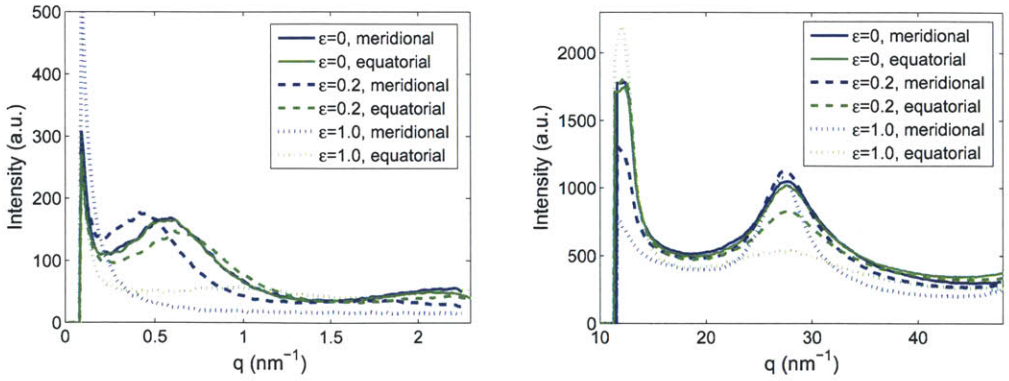

Figure 41: Meridional and equatorial x-ray intensity profile of NRE212 under uniaxial tension: (a)small angle, (b)wide angle.

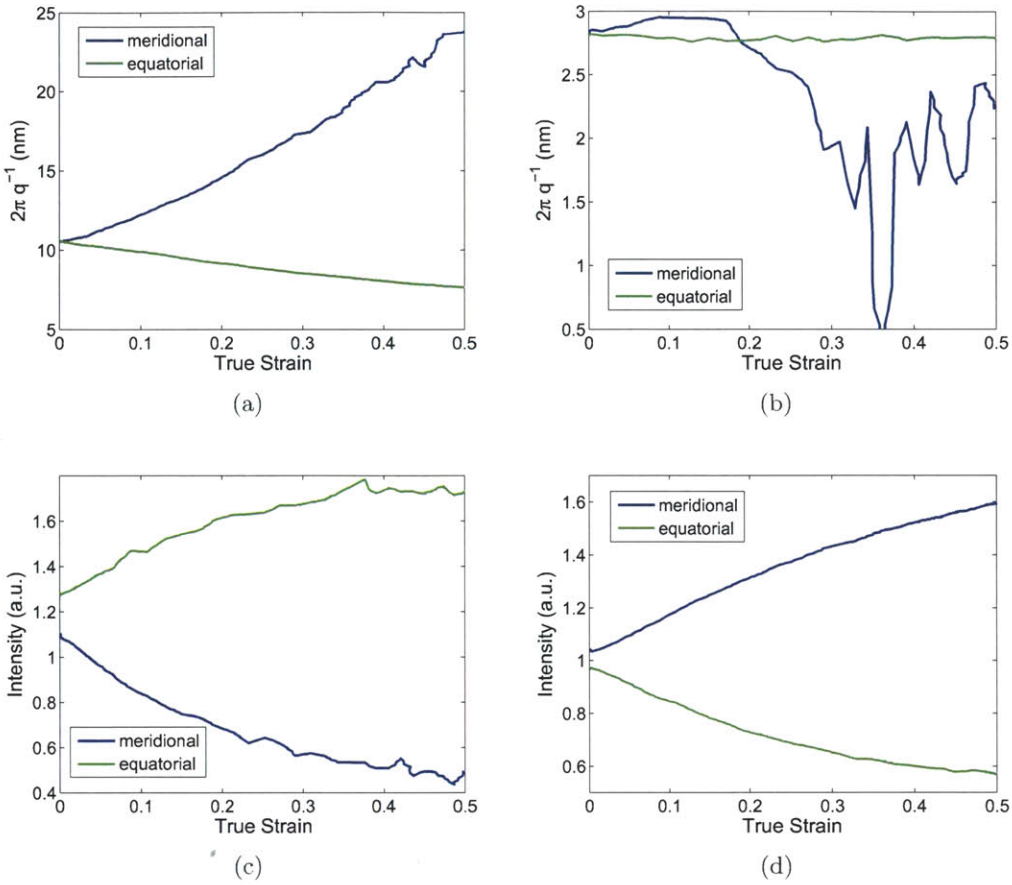

Figure 42: Evolution of the characteristic x-ray scattering peaks of NRE212 when subjected to monotonic uniaxial tension: (a) peak 1 (SAXS) location, (b) peak 2 (SAXS) location, (c) peak 3 (WAXS) intensity, (d) peak 4 (WAXS) intensity.

be compared to the appropriate affine predictions.

Affine displacement of the crystallites and clusters is assessed via the peak 1 and peak 2 spacing evolution respectively. This spacing is converted to a strain like quantity by normalizing by the value in the undeformed state. The crystallites are shown to move closer together in the transverse direction according to the affine deformation prediction, but to move apart with strain in a manner that is greater than predicted by affine deformation (Figure 43a). The ionomer clusters appear to be moving apart affinely or slightly less than affinely at the strains over which they are reasonably well tracked. If the crystallites are assumed to remain rigid while occupying a significant volume fraction (estimated at 10%), the remaining structure would need to locally deform greater than affinely in order to accommodate the applied macroscopic strain, thereby resulting in the aforementioned greater than affine crystallite displacement.

Affine rotation of the aligned backbone regions (both in the crystallites and the clusters) is assessed via the peak 4 intensity evolution. This intensity is normalized by its value in the undeformed state to compare with the relative intensity evolution predicted by affine rotation (Figure 43b). For strains below 0.2 the clusters are seen to rotate roughly affinely to align with the stretch-

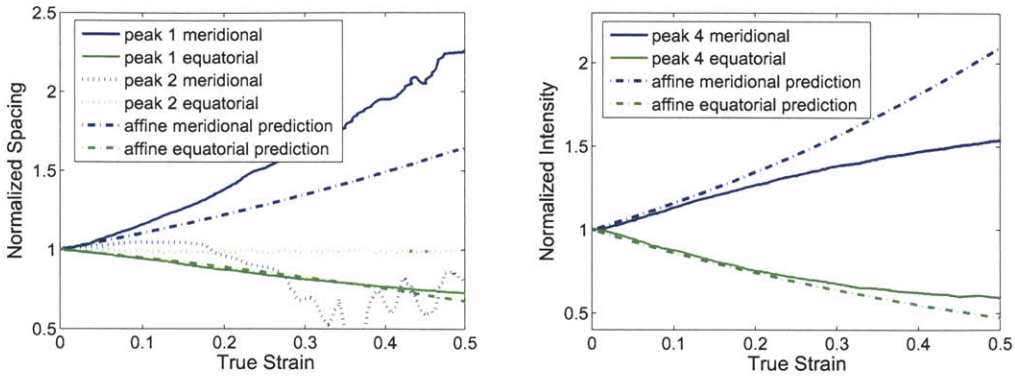

(a) (b)

Figure 43: Evolution of the characteristic x-ray scattering peaks of NRE212 when subjected to monotonic uniaxial tension compared to corresponding affine predictions: (a) peak 1 (SAXS) normalized location, (b) peak 4 (WAXS) normalized intensity.

ing direction whereas at strains greater than 0.2 they rotate less than affinely as indicated by both the meridional and equatorial peaks. This strain is well past the yield strain of 0.05 suggesting (1) that yield does not affect rotation of these rigid segments and (2) a second important microstructural event occurs at this strain which allows the amorphous regions to deform independently of crystallite and cluster rotation.

Strain like values of the peak evolutions are plotted versus Herman's orientation function for affine network deformation and versus stress in order to interrogate other possible microstructural evolution correlations (Figure 44). Herman's orientation function should correlate with the overall network alignment. The crystallite spacing is more linear versus this orientation function than when plotted versus strain. The crystallite rotation on the other hand is less linear. It does not therefore appear that the crystallites are rotating purely with the overall network structure, particularly at larger orientations. There is no particular relationship apparent in the microstructural evolution versus stress plots. The onset of yield is obvious, but only because the microstructure nominally tracks strain as discussed above, and at yield the stress-strain relationship deviates strongly from linearity.

In order to further explore the relations among strain, stress, and microstructural evolution we examine the behavior under non-monotonic loading, specifically: (1) load-unload-reload cycles to moderate strain (Figure 45), (2) cycles to increasing strain values (Figure 46), and (3) stress relaxation at different strains (Figure 47). Taking first the cycles to moderate strain, three of the four microstructural indicators (peak 1 meridional, peak 4 meridional, peak 4 equatorial) unload from a strain of 0.5 at a slightly steeper slope than they originally loaded, peak 1 equatorial unloads at a slightly more gradual slope than originally loaded (Figure 45). Reloading and unloading from the second cycle fall on top of the unload curve from the first cycle for all four. By switching to looking at cycles to smaller strains, the onset of yield is apparent even though it is not apparent under monotonic loading. In the elastic regime all the peaks unload and reload directly along the initial loading path. Right at yield ($\epsilon = 0.08$) the meridional peaks unload and reload at a smaller slope than the initial loading path. From post-yield, ($\epsilon = 0.18$) unload follows the initial curve, but reload occurs at a steeper slope. From well beyond post-yield, ($\epsilon = 0.37$) unload and reload occur at

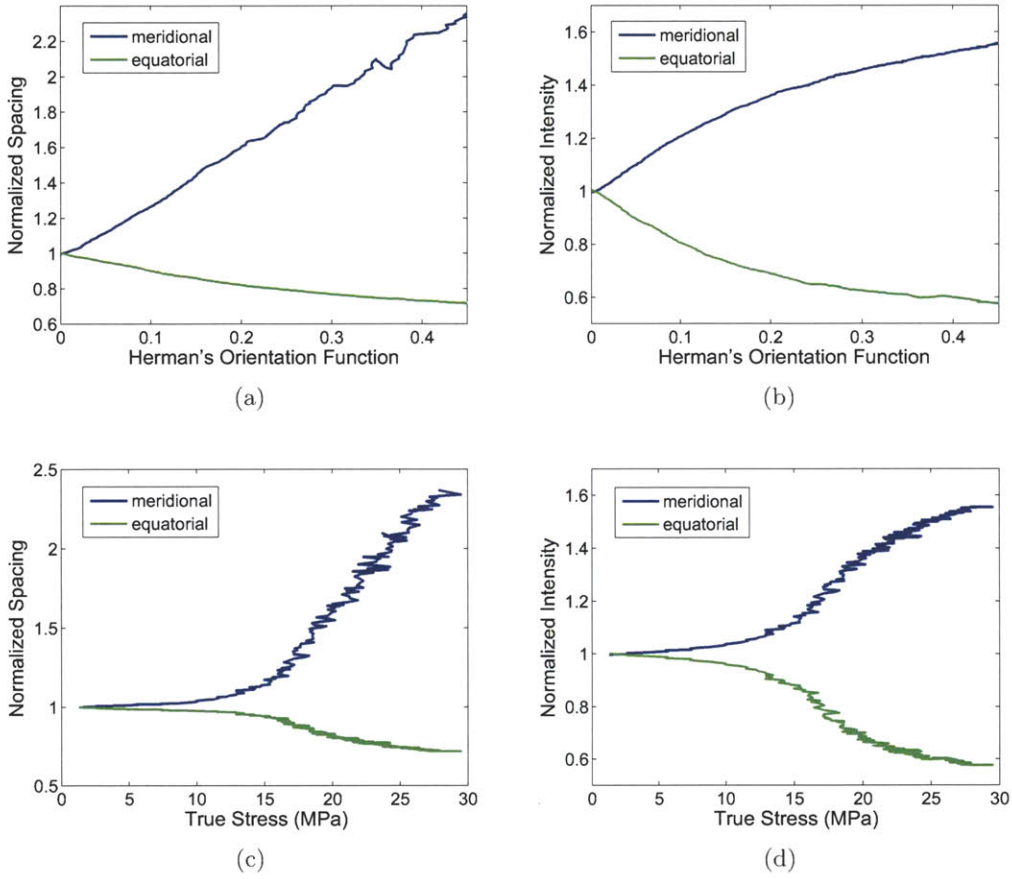

Figure 44: Evolution of the characteristic x-ray scattering peaks of NRE212 when subjected to monotonic uniaxial tension: (a) peak 1 (SAXS) normalized location versus Herman's orientation function , (b) peak 4 (WAXS) normalized intensity versus Herman's orientation function, (c) peak 1 (SAXS) normalized location versus stress, (d) peak 4 (WAXS) normalized intensity versus stress.

a slightly steeper slope than loading. In all these cases the microstructural indicators follow closely with strain, showing that microstructural plasticity correlates closely with macroscopic plasticity. The slight deviations from the 1:1 microstructure to macroscopic strain correlations allude to four regions of interest: elastic, during yield, just past yield, and well past yield (the last associated with deviations from affine rotation).

The stress relaxation experiments show the time dependent evolution of both the stress and the microstructure when strain is held constant (Figure 47). The stress relaxes when strain is held constant, even at supposedly elastic strains, and the magnitude of the relaxation increases as strain increases. When the strain is held constant, the microstructure continues to evolve in the direction the monotonically increasing strain was forcing it. The continued evolution while strain is held constant and stress relaxes is particularly apparent in the orientation versus stress plots (Figure 47d,e). The magnitude of this continued evolution, however, depends on the strain and the particular orientation measure being tracked. For the SAXS peak, which indicates spacing between crystallites, there is a small continued evolution in the "elastic" regime, and a larger evolution at yield and well past yield. This implies that at all non-zero strains the amorphous regions between the microstructural features continue to deform when strain is held constant. For the WAXS peak, which indicates rotation of the microstructural features (clusters and crystallites), there is a small continued evolution in the "elastic" regime, a larger evolution at yield, and almost no evolution well past yield. Combined with the SAXS information, this implies that at small strains the crystallites displace and rotate with the amorphous region as they continue to evolve but that at moderate strains the amorphous regions can shear past the clusters and crystallites without orienting them.

3.3.3 Hydrated structure

Here scattering from hydrated NRE212 is shown primarily for comparison with deformation from mechanical loading. The hydrated structure of Nafion has been extensively studied since the late 1970's. The 2D SAXS and WAXS profiles show that the structure remains isotropic in the membrane plane when hydrated (Figure 48). There is a clear intensity change in the SAXS due to the electron density contrast between water and the surrounding matrix. There is minimal change in the WAXS profile. From the intensity line plots (Figure 49), it is apparent that the cluster-cluster distance increases significantly more than expected from macroscopic swelling (13% versus 3%) while the crystallite-crystallite distance increases less than expected from macroscopic swelling (1.5% versus 3%). Water is believed to be contained within the clusters, such that the centers moving apart is largely a result of the clusters growing in size. Further, it is also believed that at low levels of hydration, such as those present at ambient conditions, initial increases in water content will result in the coalescence of more backbone segments/side chains into a given cluster (Kong and Schmidt-Rohr, 2011). The differential swelling between the clusters and crystallites supports this assertion. The macroscale material does not need to expand as much as the clusters because more of the amorphous material is incorporated into the clusters. This peak shift could also be a result of a change in form factor (i.e. cylinders vs spheres vs ellipsoids), rather than a simple increase in characteristic radius, but that is not simple to assess. All around, this hydration deformation is quite different from the deformation caused by mechanical strain, it is isotropic and affects the ionomer clusters much more significantly than the crystallites.

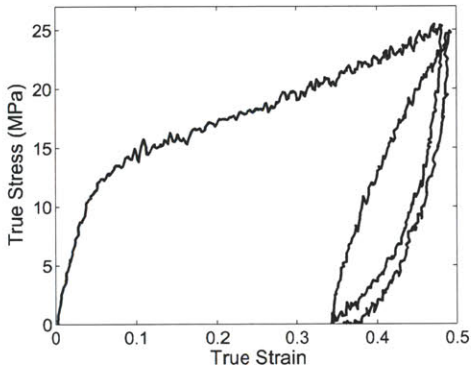

(a)

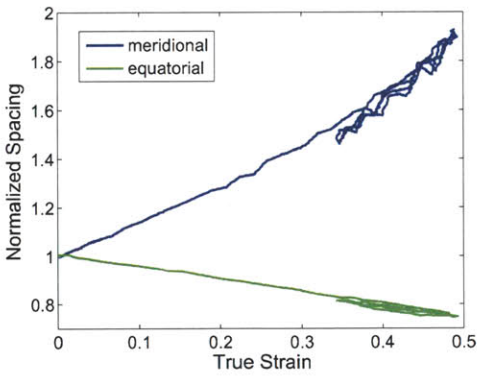

(b)

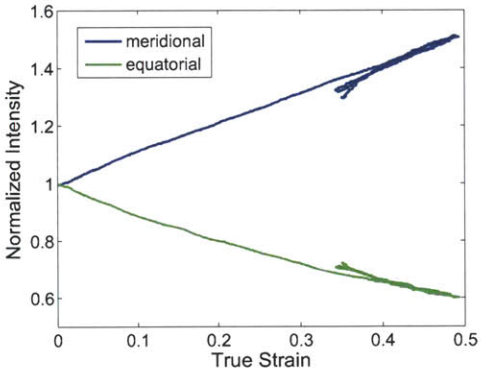

(c)

Figure 45: Evolution of the characteristic x-ray scattering peaks of NRE212 when subjected to two large strain cycles under uniaxial tension: (a) stress-strain response, (b) peak 1 (SAXS) normalized location, (c) peak 4 (WAXS) normalized intensity.

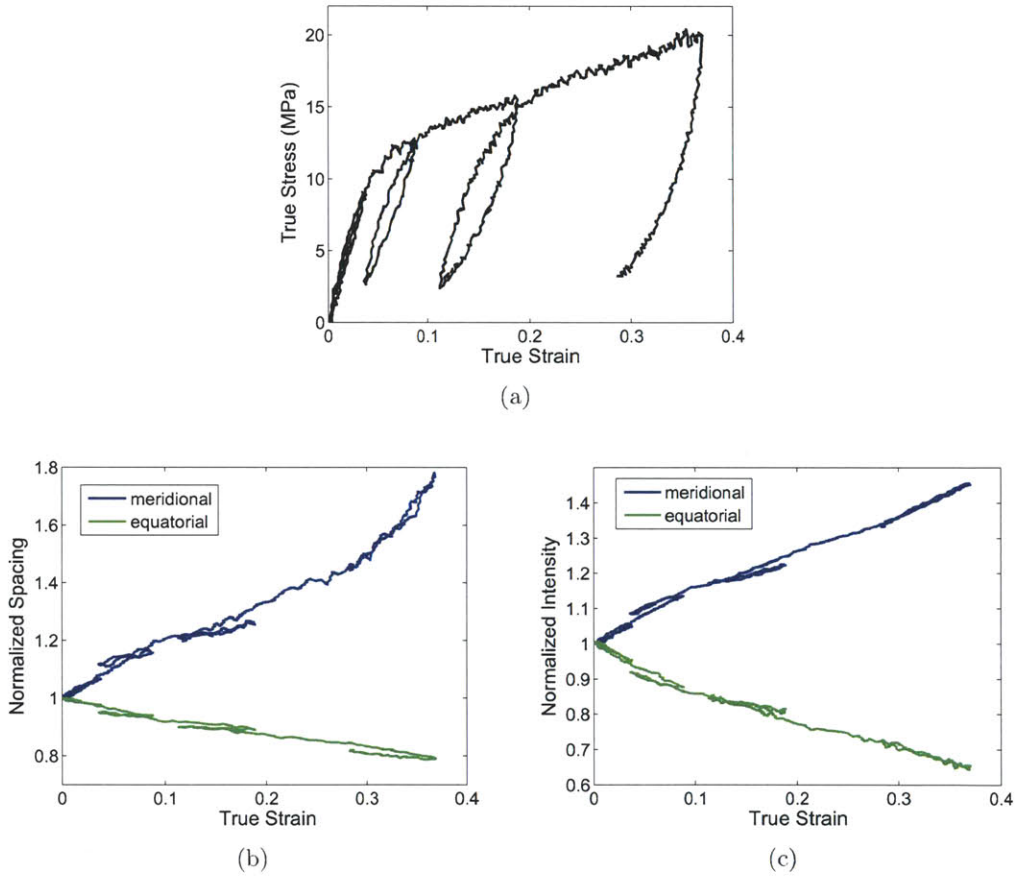

Figure 46: Evolution of the characteristic x-ray scattering peaks of NRE212 when subjected to cycles of increasing strain under uniaxial tension: (a) stress-strain response, (b) peak 1 (SAXS) normalized location, (c) peak 4 (WAXS) normalized intensity.

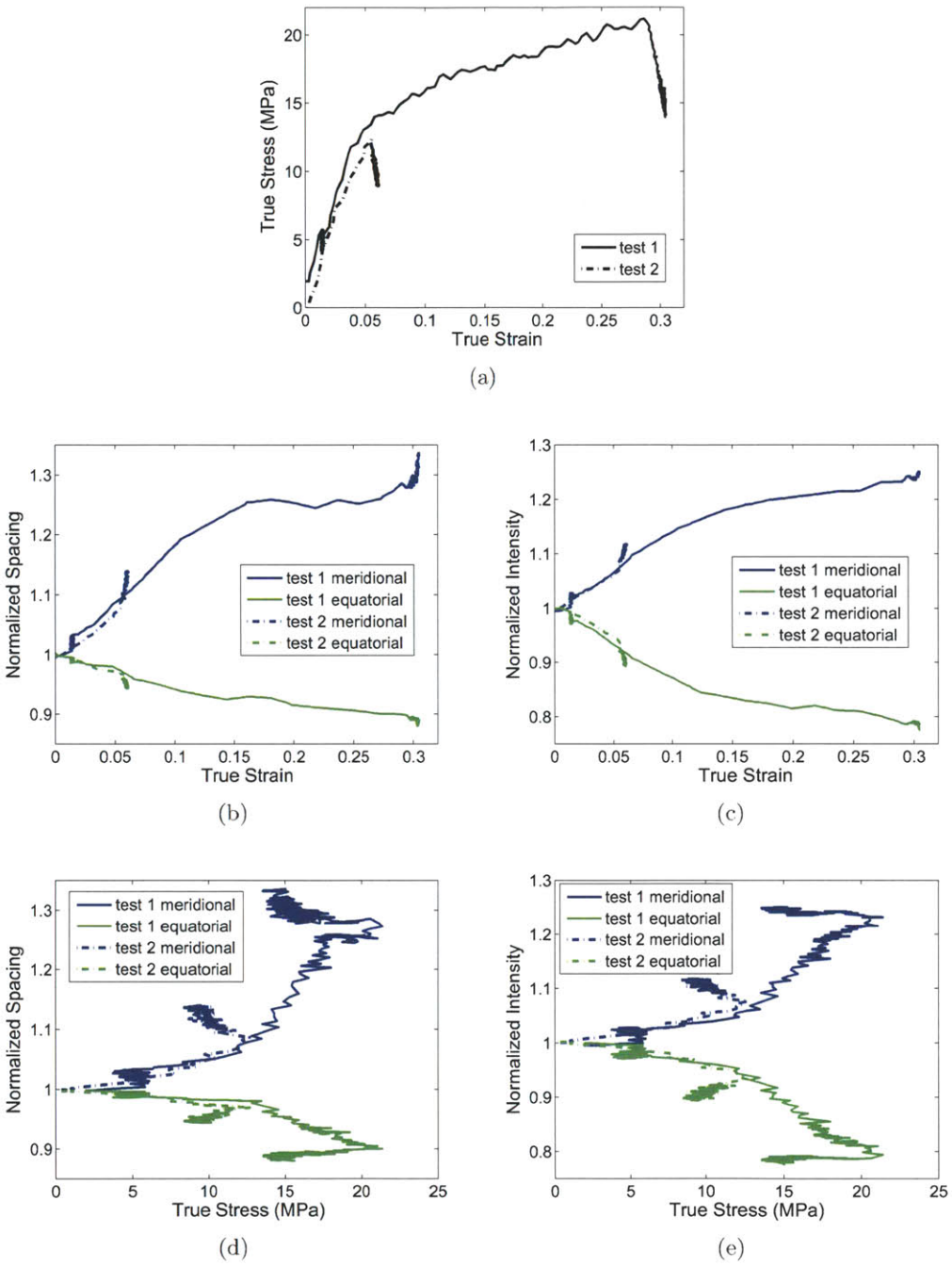

Figure 47: Evolution of the characteristic x-ray scattering peaks of NRE212 when subjected to stress relaxation testing under uniaxial tension: (a) stress-strain response, (b) peak 1 (SAXS) normalized location versus strain, (c) peak 4 (WAXS) normalized intensity versus strain, (d) peak 1 (SAXS) normalized location versus stress, (e) peak 4 (WAXS) normalized intensity versus stress.

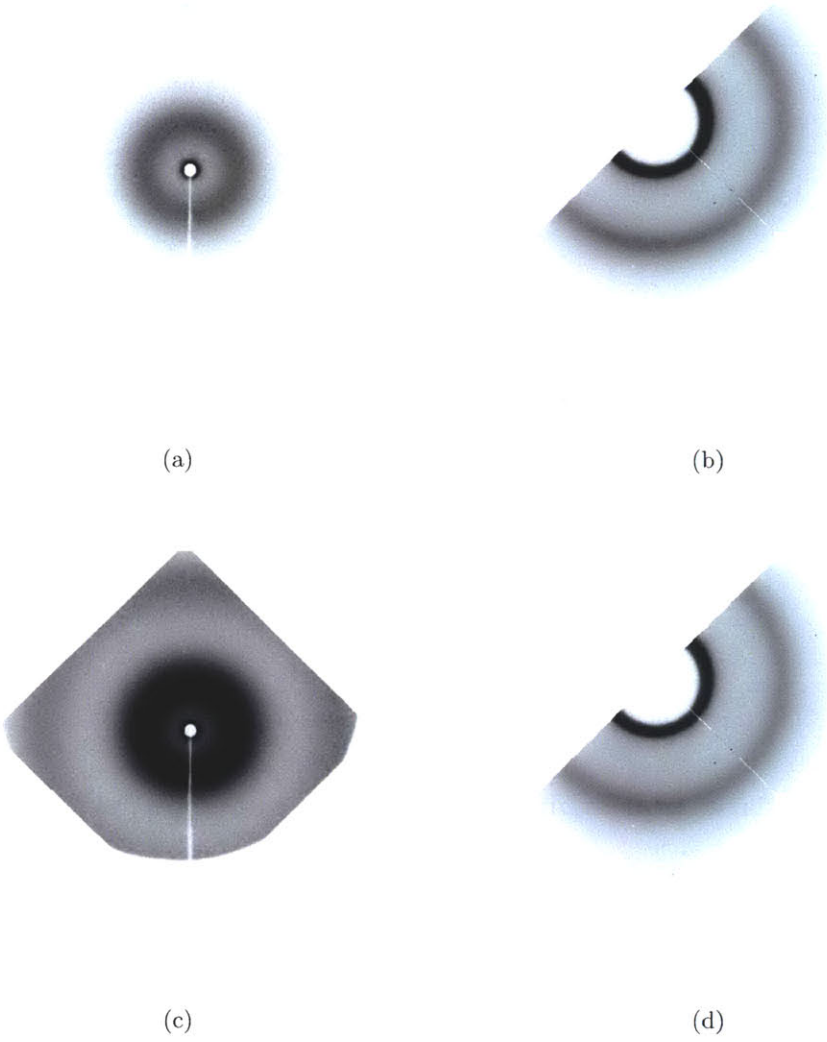

(a) (b)

(c) (d)

Figure 48: 2D x-ray scattering pattern of undeformed NRE212: (a)small angle in air, (b)wide angle in air, (c)small angle in water, (d)wide angle in water.

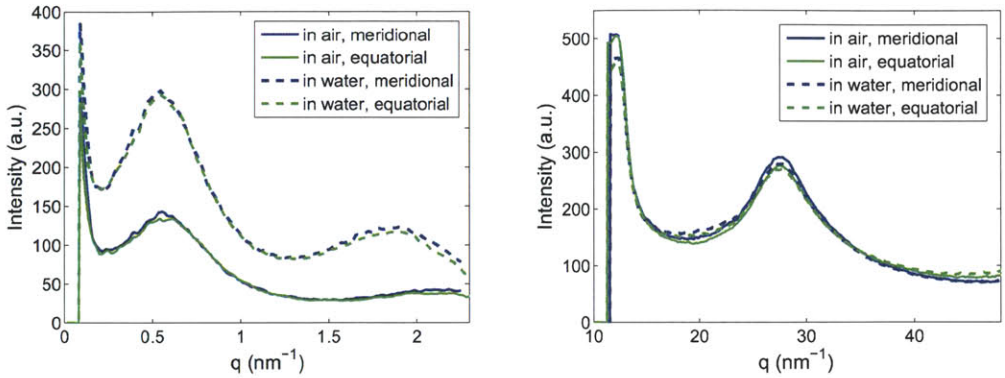

Figure 49: Effect of hydration on meridional and equatorial x-ray intensity profile of NRE212: (a)small angle (b)wide angle.

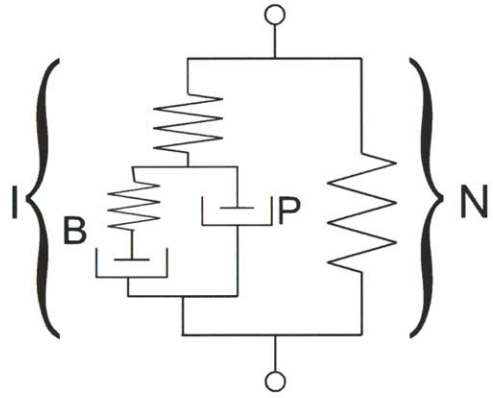

Figure 50: Rheological representation of full Nafion constitutive model.

3.4 Discussion of structural evolution in context of constitutive model

The constitutive model from Chapter 2 is shown rheologically again here in Figure 50. The total material response is the sum of the intermolecular (I) and the network (N) response. There are three main features of the intermolecular response: the linear elastic response, the plastic mechanism (P), and the back stress (B) which develops upon plastic deformation. Figure 17a,c from Chapter 2 is repeated here to show how these separate contributions result in the total stress response under cyclic loading. The "elastic" regime extends to a strain of 0.03 with plasticity beginning to evolve as early as 0.02. Rollover yield lasts until a strain of around 0.1 at which point the back stress starts to become significant. The back stress then saturates out (yields) at a strain of 0.25.

According to the microstructural information from x-ray scattering, the elastic stress samples the elastic compliance of the amorphous regions and the ionomer clusters volume averaged with the rigid crystallites. Plasticity is then governed solely by yield within the amorphous regime, with the gradual evolution (rollover) of the yield stress resulting from the distribution of local constraints (effective free volume) in these amorphous regions. Much of the energy that is dissipated apparently plastically, is in fact stored in the amorphous matrix distorted by the rigidly rotating crystallites.

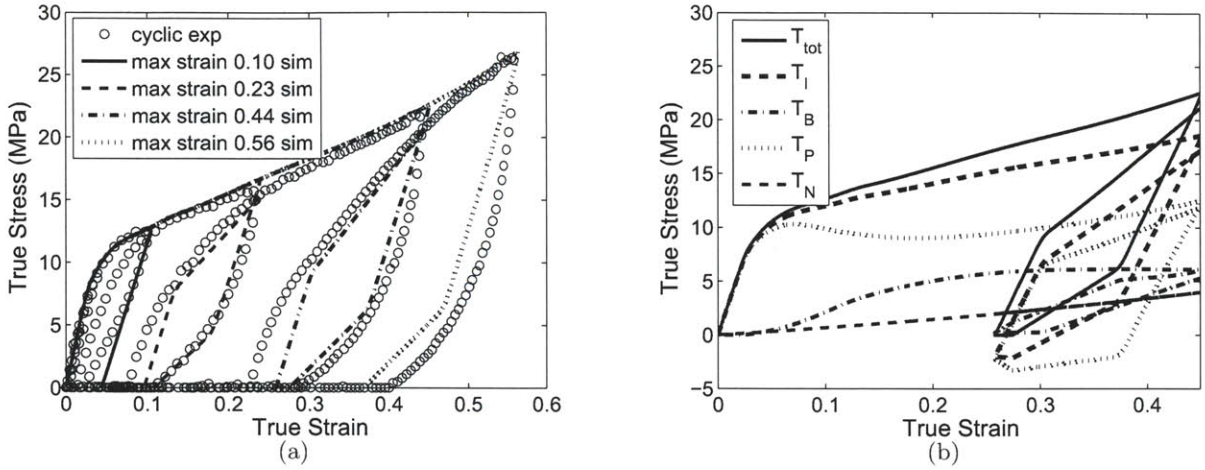

Figure 51: Model II under tensile cyclic loading at ambient conditions (a) comparison to experimental data at different maximum strain values at a strain rate of $0.01s^{-1}$ (b) contribution of the individual mechanisms to the overall response at $0.01s^{-1}$.

Since the amorphous regions are tightly bound to these rigid parts of the matrix, the "plastic work" is stored locally due to the rotation of these parts against a surrounding medium (back stress). At a strain of about 0.2 however, we propose that the stress builds up enough to start plastically shearing the amorphous regions past the rigid crystallites. This correlates to the saturation of the back stress and the deviation of the WAXS peaks from affine rotation.

The strong effect of temperature and hydration on the deformation behavior is evident in the macroscopic stress-strain behavior. Although we have only limited microstructural data at elevated temperature or hydration we can combine our knowledge of the structure under ambient condition with information from the literature to infer the origin of the temperature and hydration effects. First, we know that the water is primarily restricted to the clusters, we therefore expect that the non-cluster amorphous regions and the crystallites will have a stiffness and yield independent of hydration. This is consistent with retention of the elastic-plastic nature in fully hydrated conditions since the amorphous regions control yield. Second, it is well established that glassy amorphous materials have a stiffness and yield that decrease with increasing temperature. Beyond the glass transition temperature ($> 100^oC$) these interactions become rubbery (entropic). Third, we know from literature (Nemat-Nasser, 2008) that material stiffness depends on the ion attached to the cluster (in PEMFC protons are always used, but this can be exchanged in other applications). This means that the clusters contribute significantly to the material compliance. As proposed by several Nafion micromechanics models, the increase in cluster volume with increasing water content leads to a larger volume that does not contribute to tensile stiffness (note that our cylindrical ionomer cluster rotation based microstructural picture does differ significantly from these papers which are solely small strain spherical ionomer cluster based and elastic stiffness focused)(Hsu and Gierke, 1983, 1982; Kusoglu et al., 2008; Nemat-Nasser, 2008). Further, this initial drop in stiffness is more dramatic than upon further hydration due to percolation of the channel structure(Kong and Schmidt-Rohr, 2011). Increases in temperature result in increased cluster water content because

the amorphous region offers less resistance to swelling. The crystallite stiffness is assumed to be independent of both temperature and hydration under fuel cell relevant conditions.

3.5 Concluding remarks

SAXS and WAXS were used to characterize the evolving Nafion microstructure under uniaxial tension. While similar experiments have been carried out before, they did not include force or time dependent information and were on extruded forms of Nafion, making analysis difficult. Three types of uniaxial tensile experiments were conducted: monotonic, cyclic, and stress relaxation. Two peaks each were found in the SAXS and WAXS scattering profiles at $q = 0.6nm^{-1}$, $2.2nm^{-1}$, $12.1nm^{-1}$, and $27.9nm^{-1}$. The WAXS peaks are at the q-values expected from literature, the ionomer peak is at a somewhat higher value than expected ($2.2nm^{-1}$ vs $1.9nm^{-1}$), likely due to the difference in processing between the chemically recast and extruded forms of Nafion. It was found that each of these peaks evolves closely with strain (as opposed to stress) in either location or intensity, but that there is also a time dependent aspect to the evolution which depends on the magnitude of the stress.

The x-ray scattering information was interpreted building on the existing literature. The structure of Nafion is taken to be composed of randomly oriented crystalline regions and randomly oriented cylindrically shaped ionomer clusters consisting of aligned backbone strands with the sulfonated side chains pointing inward with intermediate amorphous regions. The peaks correspond to spacing between crystallites (peak 1), spacing between ionomer clusters (peak 2), inter-strand backbone spacing (peak 3, from both the crystallites and the semi-orderly clusters), and intra-strand backbone spacing (peak 4, from the crystallites). The key findings from this experimental study are:

- Structure is initially transversely isotropic in the membrane plane.
- Microstructure evolution is tied more tightly with macroscopic strain than with stress.
- Microstructure continues to evolve while stress relaxes at constant strain.
- Crystallites displace greater than affinely at all strains.
- Ionomer clusters displace approximately affinely at small strains (behavior at moderate to large strain unknown).
- Crystallite and ionomer clusters rotate to align with applied strain. This rotation is affine until a strain of 0.2 and less than affine at larger strains.

The microstructural evolution was then interpreted within the frame of the continuum model:

- There are three microstructural features that contribute to the overall stress response: crystallites ($\sim 5 - 10\%$ volume fraction), ionomer clusters, intermediate amorphous regions.
- Crystallites are effectively rigid at all relevant temperatures, hydrations, and loading conditions.
- Ionomer clusters are reasonably stiff under ambient conditions but have a compliance strongly positively correlated with water content.

- Amorphous regions have a stiffness and yield dependent on temperature but not hydration.
- Yield is governed by the amorphous regions.
- The back stress results from restrictions of the amorphous region plasticity due to its binding to the crystallites which are then forced to rotate with the matrix.
- The back stress yields when the activation energy is great enough for the amorphous matrix to shear past the crystallites and plastically deforming regions can merge with each other.
- It is unclear what the yield contribution of the clusters is since this peak is barely within the SAXS detection range, the cluster shell may shear with the amorphous yield.

The structural assignment and evolution given here is by and large consistent with the work of Rubatat and coworkers and Schmidt-Rohr and Chen simply by a priori assumption of the Nafion microstructure and its relation to the x-ray scattering peaks. These basic features are the elongated crystallites and cylindrical water containing ionomer clusters that do not change shape significantly. The results are most readily contrasted with Heijden et al. (2004b) and Rubatat and Diat (2007), although both of those papers do focus on the ionomer clusters and in particular SAXS peak 2 (which is not well tracked here) and use an extruded form of Nafion. The concept of crystallites as distinct entities from the ionomer clusters really does not arise until the Schmidt-Rohr and Chen paper in 2008, making the literature on their orientation sparse. Nonetheless some basic comparisons can be made. Over the strain at which the ionomer peak is tracked the clusters are seen to deform affinely as consistent with the bundle cluster model and corresponding SAXS data from Rubatat and Diat (2007). Heijden et al. (2004b) does not follow the matrix peak, but does decompose WAXS peak 3 (by the notation used in this chapter) into amorphous and crystalline contributions. The crystalline portion of WAXS peak 3 and the purely crystalline WAXS peak 4 (peak 3 in their notation) orient with applied strain in perpendicular directions and at a slope that decreases with increasing strain. This monotonic but decreasing slope trend is the same as discussed in this work, but they do not explicitly compare the peak evolution with an affine deformation assumption. The Heijden et al. (2004b) structural evolution interpretation is somewhat self inconsistent due to the lumping of the crystallites within the ionomer bundles, they can only do this by ignoring the matrix peak, as pointed out by Schmidt-Rohr and Chen (2008). They do drop this entirely from their analysis in the 2007 paper. On the other hand, the concept of locally aligned bundles of ionomer clusters that orient/rotate together but can displace relative to each other is both self consistent and in line with the more in depth time and stress dependent study done here. For instance, if there is rate dependence to the amorphous regions between the bundles and between the ionomer clusters then one might expect at constant strain both a continued orientation of these features and a decrease in stress. These models also do not really distinguish between the amorphous regions tightly associated with ionomer clusters and general amorphous regions. This distinction is important, since cluster associated regions will tend to be much more tightly aligned, and SANS data indicated that these do not change shape, there therefore must be an intervening purely amorphous region that is deforming elastically and undergoing yield and is free to change shape.

The interpretation presented here actually suggests that the material might be more physically captured by further breaking down the intermolecular response. Figure 52 presents a rheological schematic of this alternative model. Here the hydration dependent clusters response is separated

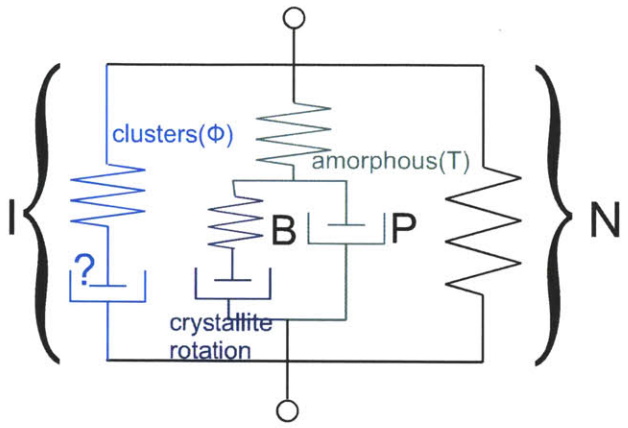

Figure 52: Rheological representation of possible further decomposed Nafion constitutive model.

from the temperature dependent amorphous response and the back stress which results from crystallite rotation. Better coverage of peak 2 evolution and scattering profiles as a function of simultaneous changes in temperature and water content would be needed to justify this approach. It does however have some interesting potential for naturally capturing differences in cluster and macroscopic expansion as a function of temperature.

4 Nafion multiaxial loading

Portions of this chapter have been reprinted from Journal of Power Sources, Vol. 196, M.N. Silberstein and M.C. Boyce, "Hygro-thermal Mechanical Behavior of Nafion During Constrained Swelling", pages 3452-3460, copyright 2011.

Portions of this chapter have been reprinted from Polymer, Vol. 52, M.N. Silberstein, P.L. Pillai, and M.C. Boyce, "Biaxial elastic-viscoplastic behavior of Nafion membranes ", pages 529-539 , copyright 2011.

Cyclic mechanical loading results from water content driven swelling and deswelling of the membrane within the partially constrained environment of the fuel cell. Since the membrane in a fuel cell is highly constrained in the membrane plane and relatively unconstrained in the through-thickness direction, this cyclic loading will result in stress states that are primarily biaxial in nature. This chapter will explore the biaxial, constrained swelling induced, and hydration dependent mechanical response of the material through experiments and through modeling. Biaxial tests are conducted on Nafion at different degrees of biaxiality and then simulated via finite element analysis to validate the multiaxiality of the constitutive model. Bimaterial swelling tests are conducted on the membrane bonded to a gas diffusion layer material, which provides a constrained state of the membrane upon hydration and produces membrane stresses and a clearly visible and measurable deformation, the curvature of the bilayer. The ability of the model to predict constrained swelling loading conditions is assessed with respect to these experiments. The validated model is then applied to a simplified fuel cell duty cycle in order to understand and predict stress and strain evolution and potential failure mechanisms of membranes in operating fuel cells.

4.1 Biaxial Loading

4.1.1 Background

In the previous chapter, the uniaxial tensile behavior of Nafion was characterized under both monotonic and cyclic loading as a function of rate, temperature, and hydration. This data provided the foundation for the development of a constitutive model to describe the hygrothermal elastic-viscoplastic stress-strain behavior of Nafion. The model was shown to capture the stress-strain behavior of Nafion over a wide range of uniaxial loading histories. Here we assess the biaxial behavior of Nafion experimentally under different biaxiality ratios and then use the data to further validate the aforementioned constitutive model. Previous biaxial testing on Nafion has been reported for pressure loaded blister cells(Dillard et al., 2009; Li et al., 2009) which create an equibiaxial tensile stress at the center of the specimen, aimed at determining the stress at which gas leaks occur across the membrane. Biaxial testing by direct biaxial stretching has been conducted on a variety of other polymers such as poly(ethylene terephthalate)(Matthews et al., 1997; Adams et al., 1998; Gerlach et al., 1998; Adams et al., 2000), polypropylene(Sweeney et al., 1997, 2009), polystyrene(Zhang and Ajji, 2003), polyethylene(Zeng et al., 2010), and polyamide(Zeng et al., 2010) for which biaxial draw is an important part of the manufacturing process. Most of these biaxial characterizations were conducted via in-plane extension devices which consist of many grips along each edge of a square specimen that can move independently in the two principal directions. With appropriate slitting or specimen design this can provide a close to homogenous deformation with control over the degree of imposed biaxiality. In characterizing the biaxial behavior of metals, it is typical to use cruciform specimens with a single grip on each edge (i.e. Makinde et al. (1992);

Demmerle and Boehler (1993); Hannon and Tiernan (2008)). The thickness in the central region of the specimen is reduced to ensure that the deformation is localized and slits are introduced in the legs for stress relief. In this paper, the cruciform configuration is used with a single grip on each edge of a uniform thickness specimen. This in-plane biaxial method also allows the desired control of the degree of biaxiality. The thickness reduction and slitting is not practical for the thin Nafion membrane($t = 27\mu m$), consequently the homogeneity of the resulting stress field will be discussed in depth in the results section.

4.1.2 Experimental Methods

Materials

Commercially available dispersion cast NRE211 films (thickness $t = 27\mu m$, Dupont, Ion Power Inc) and NRE212 films (thickness $t = 54\mu m$, Dupont, Ion Power Inc) were used for the experimental characterization of Nafion. NRE211 and NRE212 are identical in chemical composition and processing, differing only in thickness. The films were stored in a desiccator cabinet upon removal from the initial packaging to minimize variability in data from aging and humidity effects.

Biaxial Tension

Biaxial tests were performed on Nafion NRE211 laser cut into the cruciform shape shown in Figure 53a. This particular cruciform geometry is chosen as a compromise between achieving a uniform stress field at the center of the specimen and reaching a reasonably large strain within the range of motion of the experimental setup. Biaxial tests were conducted on the thin film multiaxial tensile machine developed in the Bio-Instrumentation lab at MIT (Figure 53b) modified from the design of A. Herrmann in his master's thesis(Herrmann, 2006). The film was gripped by rubber padded spring loaded clips. Each grip is mounted to an Aerotech ATS125 leadscrew-actuated stage and all actuators are moved such that the membrane center remains in place. For all tests the grips are initially $29mm$ apart. Two of the grips are mounted to FUTEK LSB200 force sensors. The force and stage location are recorded at one second intervals. The deformation is monitored by an Apogee Alta U10 camera. A frame is recorded roughly every 10 seconds as limited by the capabilities of the acquisition system. The stage motion and data acquisition is controlled by a custom LabView code. The image frames are post-processed using the Vic2D strain analysis software to find local displacement values. The force-displacement and processed videos are then converted to the engineering stress components $\bar{\sigma}_{11}$ and $\bar{\sigma}_{22}$ using the initial cross-sectional area of the edge of the central square region ($12mm$ x $27\mu m$) and engineering strain values $\bar{\epsilon}_{11}$ and $\bar{\epsilon}_{22}$ in the biaxial region based on the markers near the edge of the region.

Monotonic experiments consist of grip displacement at a constant rate until reaching a preset displacement value. Cyclic experiments consist of grip displacement at a constant rate until reaching a preset displacement value, followed by grip displacement at the same constant rate in the opposite direction until the grips return to their original location; this process is then repeated. It is typical for the specimens to buckle during the unloading process resulting in a near zero force. During this period the video extensometer continues to track the strain, however, due to the three dimensional nature of the deformation it does not indicate a local material strain.

4.1.3 Experiments: Results and Discussion

Cruciform specimens were subjected to three different biaxial loading conditions where the biaxiality ratio is described as the ratio of the stretching rates in the 1- and 2-directions ($B = \frac{\dot{\lambda}_1}{\dot{\lambda}_2}$). $B = 1.0$

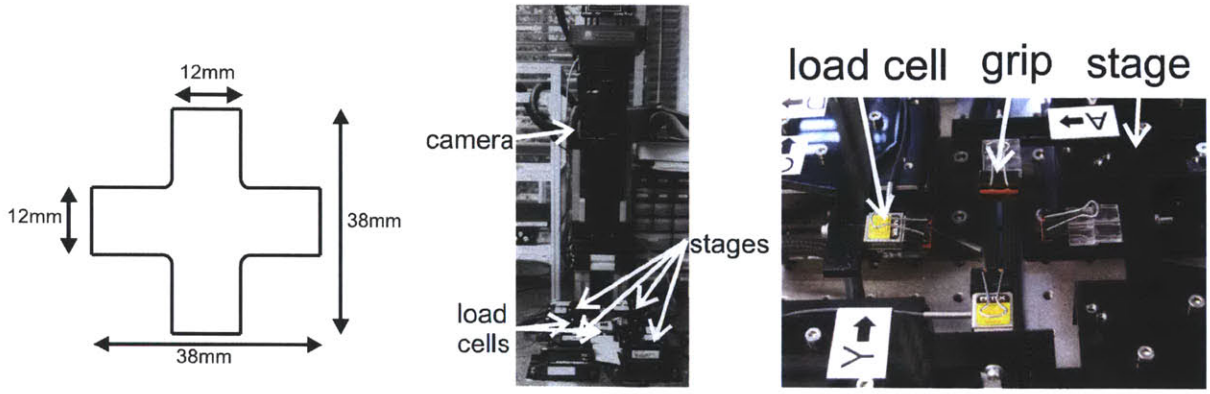

(a) (b) (c)

Figure 53: Experimental setup for biaxial tensile tests (a)specimen shape (b)thin film multi-axial tensile machine (c)close up of stages from thin film multi-axial tensile machine.

corresponds to grips in both directions displaced at the same rate($14\mu m\ s^{-1}$), $B = 0.5$ corresponds to the 1-direction grips displaced at one-half the rate($7\mu m\ s^{-1}$) as the 2-direction grips($14\mu m\ s^{-1}$), and $B = 0.0$ corresponds to the 1-direction grips held fixed while the 2-direction grips are displaced($14\mu m\ s^{-1}$). The biaxial stress-strain response is determined from the strain in the central biaxial region calculated using the video extensometer points in the central square region of the specimen as indicated in Figure 54a. The stress-strain behavior will be reported in terms of engineering stress versus engineering strain.

Images of the deformed specimen for all three cases are shown in Figure 55; only the top right quarter is displayed in order to better correlate with the simulation images which will be shown subsequently. The character of the deformed shapes is most prominent in the legs of the cruciform since that is where the strain is largest. There is a distinct concave curvature between the grip and the central region in the 2-direction leg for all three cases and in the 1-direction leg for $B = 1.0$; this curvature is clearly absent in the 1-direction leg for $B = 0.0$.

Figure 56a shows the monotonic biaxial engineering stress-strain response of all three cases compared to the uniaxial tensile behavior. In all cases the stress-strain behavior exhibits an elastic-plastic response with features similar to the uniaxial behavior. The biaxial effect on the stress-strain response is apparent. For the case of equibiaxial ($B = 1.0$) loading, the initial elastic stiffness is greater than the uniaxial stiffness, as expected (recall, the biaxial modulus is $E/(1-\nu)$ compared to the uniaxial modulus E). The apparent yield stress level required for biaxial yielding is also greater than for uniaxial yielding which is unexpected; the biaxial stress components at yield for equibiaxial tension would be expected to be equal to the uniaxial yield following a Mises or Tresca yield criterion (they would be expected to be lower if there were a pressure dependence). The

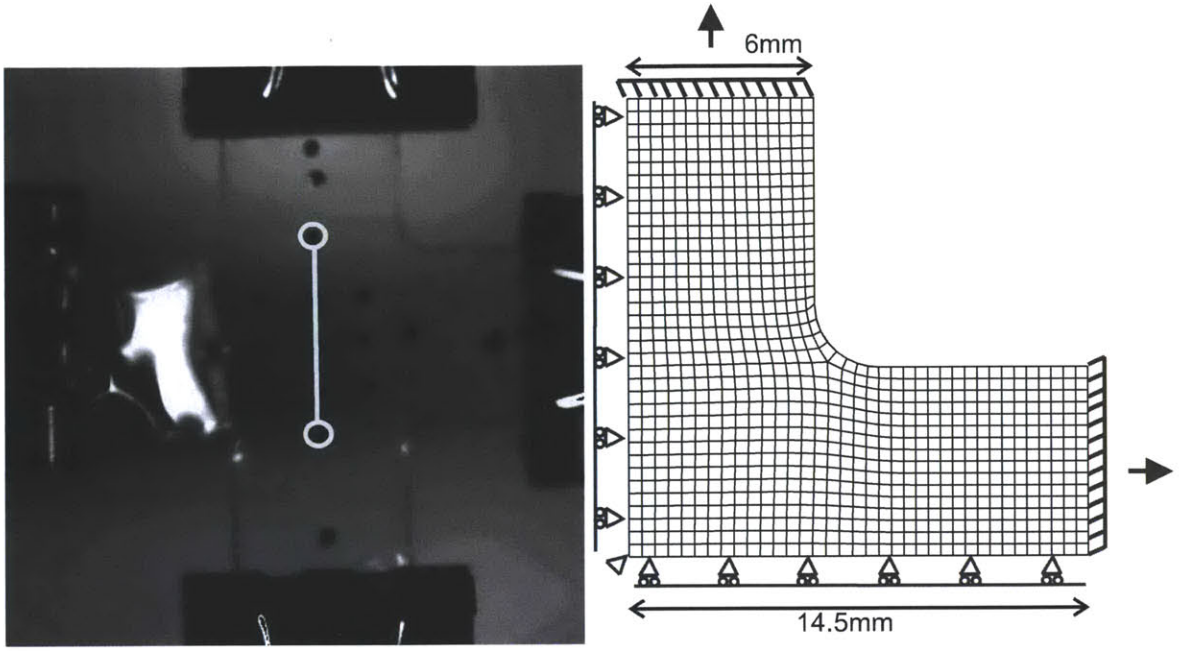

(a) (b)

Figure 54: (a) Specimen with line indicating location of points used for local strain measure of biaxial experiments. (b) Geometry and boundary constraints of biaxial simulation.

unexpected disparity in yield stress between the uniaxial and equibiaxial experiments is a result of: (1) the inhomogeneous stress distribution in the central region of the cruciform which produces a sharper yield transition in the reduced data; and (2) the rollover nature of the yield event which occurs more rapidly with biaxial loading as compared to uniaxial loading. Thus even though yield is technically initiating at the same value for equibiaxial as for uniaxial loading, this very initial yielding cannot be observed directly by this experiment. The specimen geometry effect will be discussed further in Section 4.1.4. There is also a minor strain rate effect since the effective rate driving yield is larger for the equibiaxial case than the uniaxial case, but this is negligible in comparison to the effects of either geometry or rollover yield evolution.

The $B = 0.5$ and the $B = 0.0$ results also reveal the effect of biaxiality on initial stiffness, the yield, and post yield behavior as well as the dramatically different σ_{11} and σ_{22} histories for these non-equibiaxial conditions. In the 2-direction the $B = 0.5$ and the $B = 0.0$ responses follow the trend of the $B = 1.0$ and uniaxial ($B \sim -0.5$) responses with the initial stiffness, yield stress, and post yield hardening decreasing monotonically from $B = 1.0$ to $B = -0.5$. The stress response in the 1-direction decreases as expected going from $B = 1.0$ to $B = 0.5$ to $B = 0.0$ since there is less strain applied in that direction. The cyclic behavior is shown in Figures 56b, c, and d for the $B = 1.0$, $B = 0.5$, and $B = 0.0$ cases, respectively. In each case for both the 1- and 2-directions there is a non-linear unloading and reloading with a reduced yield upon reloading, much as observed earlier in uniaxial tension. The specimens buckle during the process of returning the grips to their initial locations. Further strain recovery is seen to occur in the buckled state, resulting in reloading initiating from a lower strain than that at which zero strain was reached during unloading.

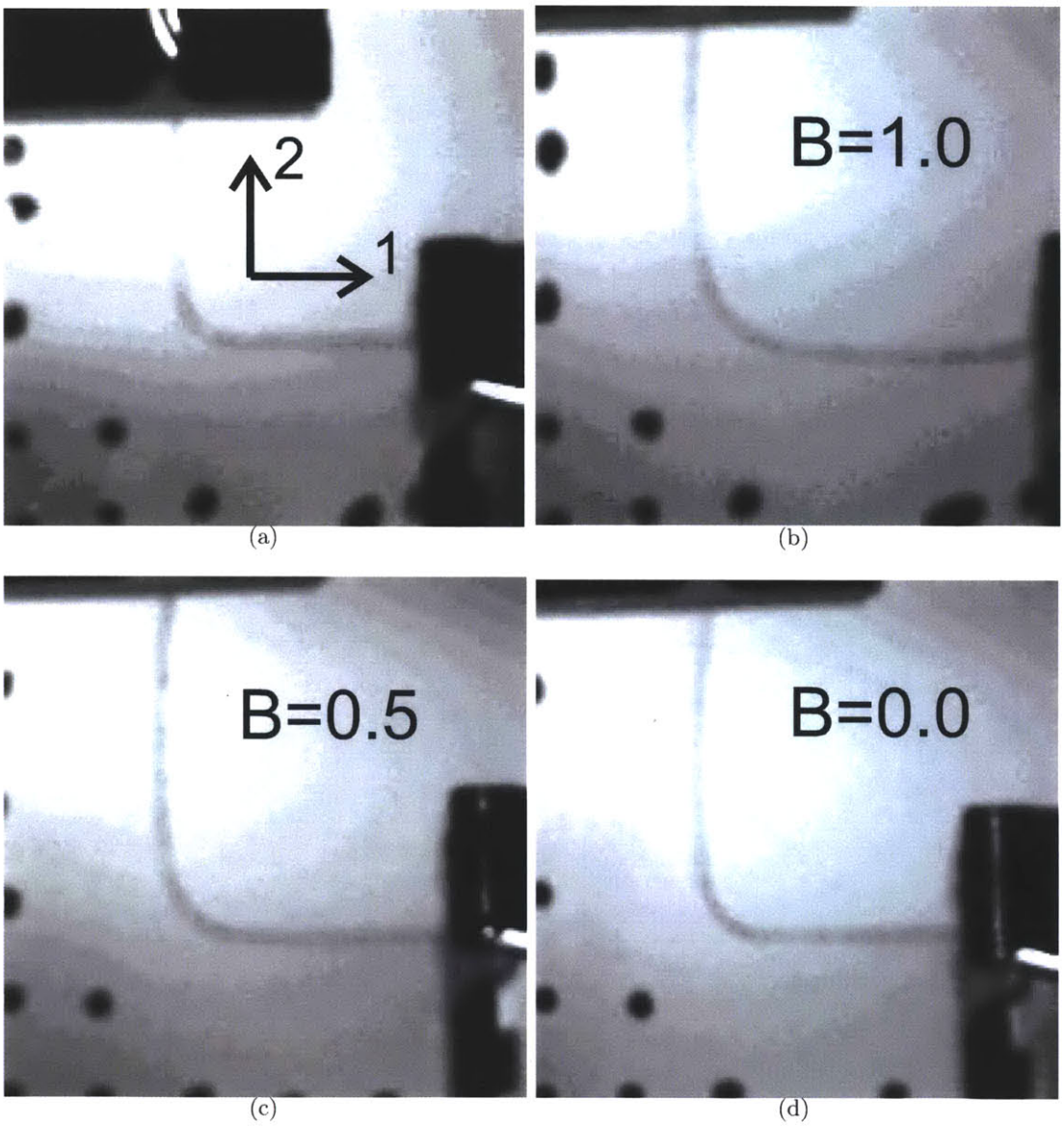

Figure 55: Images of top right quarter of experimental biaxial specimens (a) typical specimen prior to deformation ($\bar{\epsilon}_{22} = 0$) (b) $B = 1.0$ specimen at 2-direction grip displacement $= 2.5mm$ ($\bar{\epsilon}_{22} = 0.05$) (c) $B = 0.5$ specimen at 2-direction grip displacement $= 2.5mm$ ($\bar{\epsilon}_{22} = 0.06$) (d) $B = 0.0$ specimen at 2-direction grip displacement $= 2.5mm$ ($\bar{\epsilon}_{22} = 0.08$).

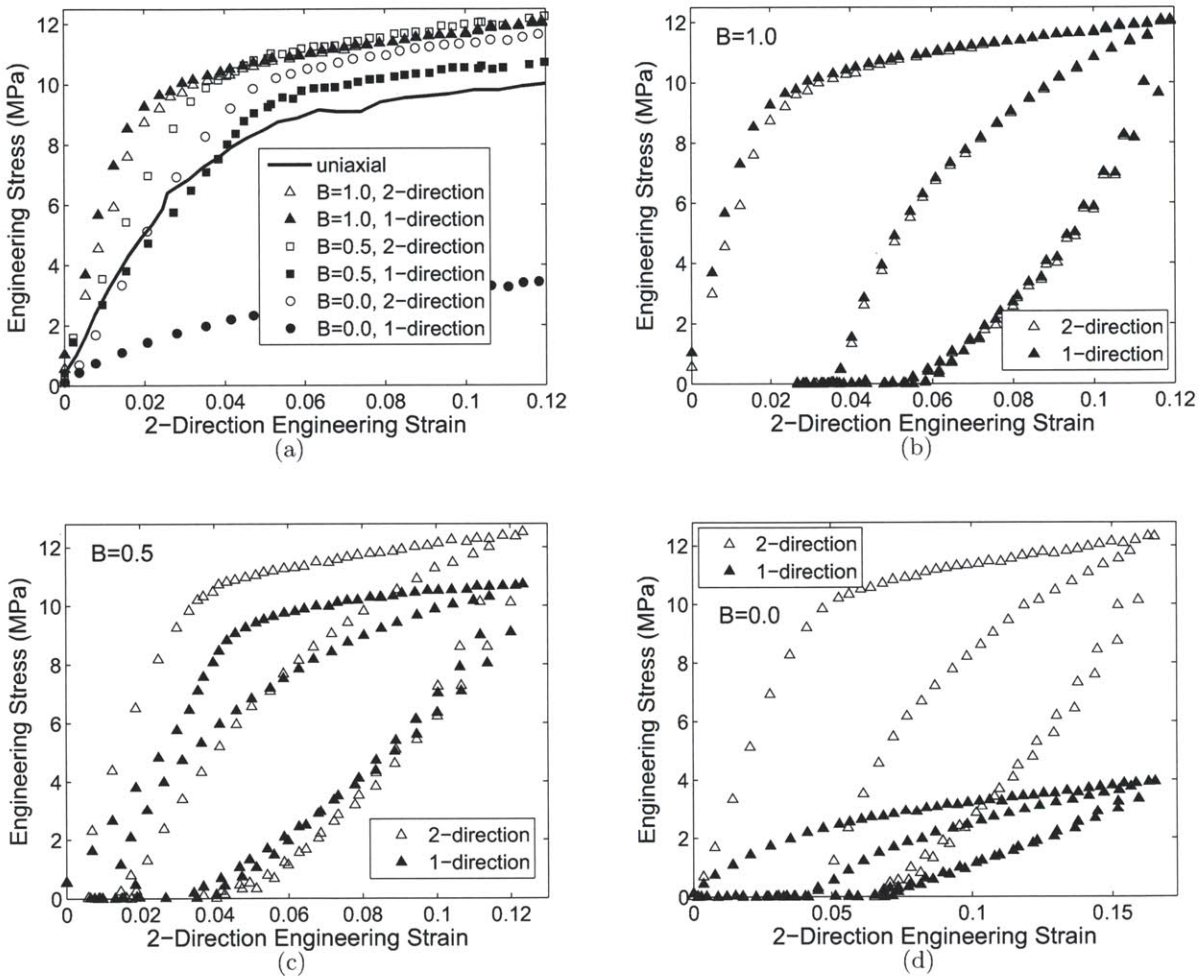

Figure 56: Biaxial experimental data ($\phi = 2$) (a) comparison of different degrees of biaxiality under monotonic loading (uniaxial data at $\phi = 1.5$) (b) cyclic loading with 1- and 2-direction grips displaced at $14\mu ms^{-1}$ ($B = 1.0$) (c) cyclic loading with 2-direction grips displaced at $14\mu ms^{-1}$ and 1-direction grips displaced at $7\mu ms^{-1}$ ($B = 0.5$) (d) cyclic loading with 2-direction grips displaced at $14\mu ms^{-1}$ and 1-direction grips held fixed ($B = 0.0$).

4.1.4 Model

Finite element simulations of each of the biaxial loading tests are conducted. The symmetry of the tests enables a one-fourth model of the specimen with appropriate boundary conditions as shown in Figure 54b; a mesh convergence study was conducted to assess the quality of the mesh. The material behavior is modeled using the constitutive model with the properties determined from the uniaxial tests as given in Chapter 2. Contours of (σ_{11}) and (σ_{22}) in the elastic regime and just past yield are shown for the $B = 1.0$, $B = 0.5$, and $B = 0.0$ cases in Figures 7, 8, and 9, respectively. First, we note that the deformed shape just past yield for each of these figures matches well with the corresponding experimental images taken at the same grip displacement. As in the experiments, there is a distinct concave curvature between the grip and the central region in the 2-direction leg for all three cases and the 1-direction leg for $B = 1.0$ and this curvature is clearly absent in the 1-direction for $B = 0.0$. Second, even though the cruciform specimen shape was chosen to achieve a uniform biaxial stress state at the central region, it is clear from the these simulations that this is not the case. The stress varies by approximately 25% across this central region. It is therefore critical that the finite element results are reduced to biaxial stress-strain results in the same manner as the experimental results for any direct comparison: the reaction forces are measured at the grips and strains are measured from the displacement of points just outside the central square biaxial region. The model results are found to well predict the loading portion of the experimental results in all three cases (Figure 60). The simulations capture the initial stiffness, the yield, and the post-yield behavior as observed for ($\bar{\sigma}_{11}$) and ($\bar{\sigma}_{22}$) histories for all three biaxial conditions, indicating high accuracy of the model in predicting biaxial loading. The unloading and reloading slopes in the model appear to be stiffer than in the experiments. Interestingly, the unload and reload yield shoulders occur as the same stress as in the experiments. This model therefore seems to underestimate the gradual nature of both the forward and reverse plastic deformation processes. The model also underpredicts the strain recovery of the specimen in the buckled state prior to reloading. The magnitude of the uncaptured strain recovery is similar in all cases ($\bar{\epsilon} \sim 0.015$). While the origin of this disparity is not known at this time, it does not appear to be specific to mutli-axial loading. We can see that the framework used to incorporate the uniaxial behavior into a three dimensional model is in fact capable of predicting the multiaxial deformation response of the membrane.

As discussed above, this particular geometry does not provide a perfect homogeneous biaxial stress distribution within the central region. In order to understand the biaxial test itself better and the accuracy of the data for providing the material stress-strain response under different biaxial histories, we compare the stress-strain histories reduced from the test simulation with the model predictions of the corresponding pure homogeneous strain histories (Figure 61). The homogeneous simulations are run with the 2-direction strain rate matched to the initial $\bar{\epsilon}_{22}$ rate of the cruciform. The strain rate variation in $\bar{\epsilon}_{22}$ which never exceeds a factor of three was neglected. Looking first at σ_{22} (Figure 61a), it is evident that the cruciform specimen provides an accurate measure of the elastic regime. However, the yield event occurs in a sharper manner and at a higher stress as compared to the homogenous response indicating that reduction of the cruciform data loses some of the details of the distributed yield event. The cruciform specimen also results in an exaggerated difference in the stress response of $B = 1.0$, $B = 0.5$, and $B = 0.0$ around the yield event. An increase in the magnitude and sharpness of yield is also evident in each of the (σ_{11}) responses (Figure 61b-d). For completeness we also include the simulated uniaxial response at a strain rate matching the 2-direction rate of the homogeneous biaxial simulations. Comparing the homogeneous

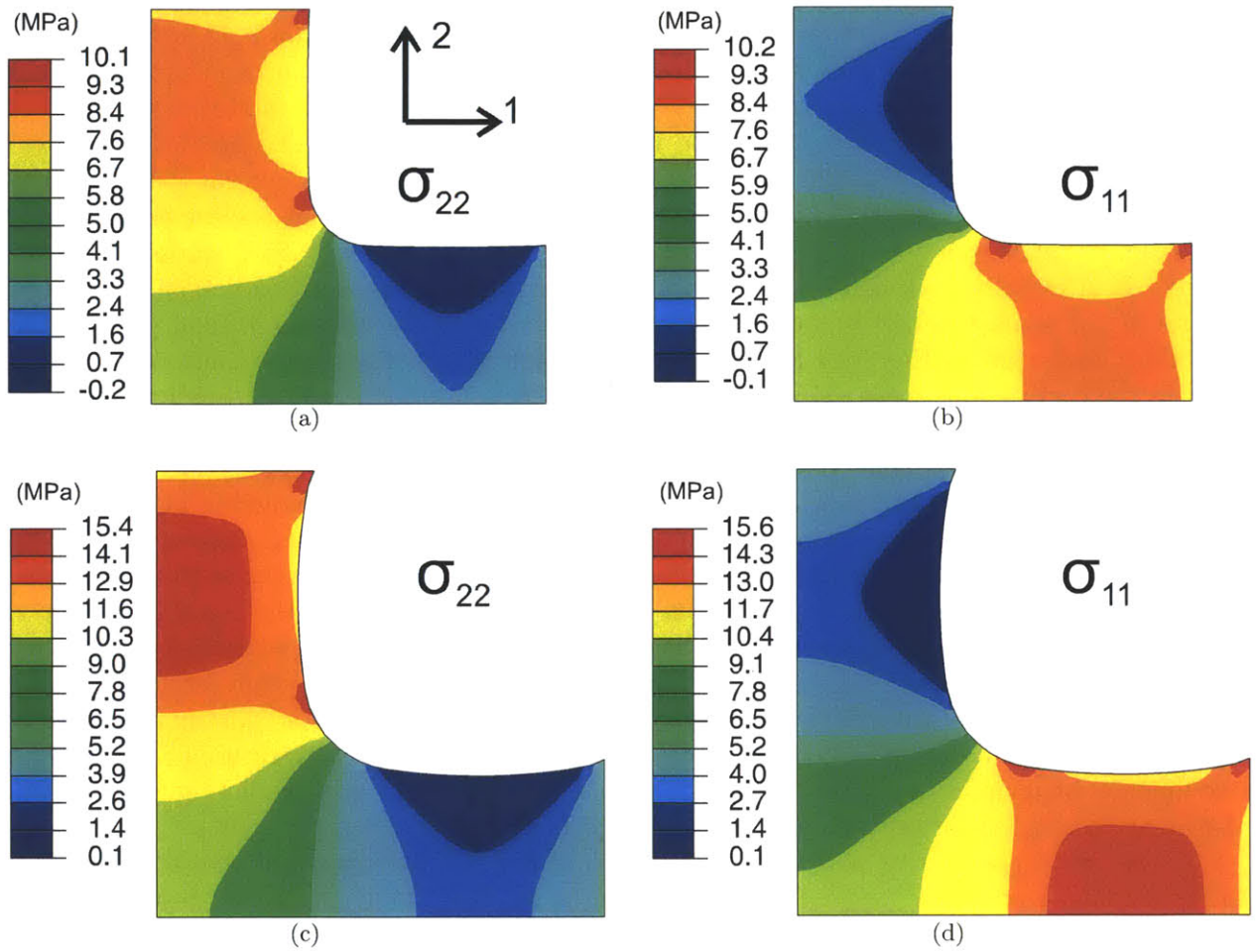

Figure 57: Stress contours from simulated equibiaxial tensile loading ($B = 1.0$) for the 1- and 2-direction grips extended at $14\mu ms^{-1}$: prior to yield (2-direction grip displacement $= 0.42mm$) (a) σ_{22} ($\bar{\sigma}_{22} = 8.0$) (b) σ_{11} ($\bar{\sigma}_{11} = 8.0$) and just after yield (2-direction grip displacement $= 2.5mm$) (c) σ_{22} ($\bar{\sigma}_{22} = 10.7$) (d) σ_{11} ($\bar{\sigma}_{11} = 10.7$).

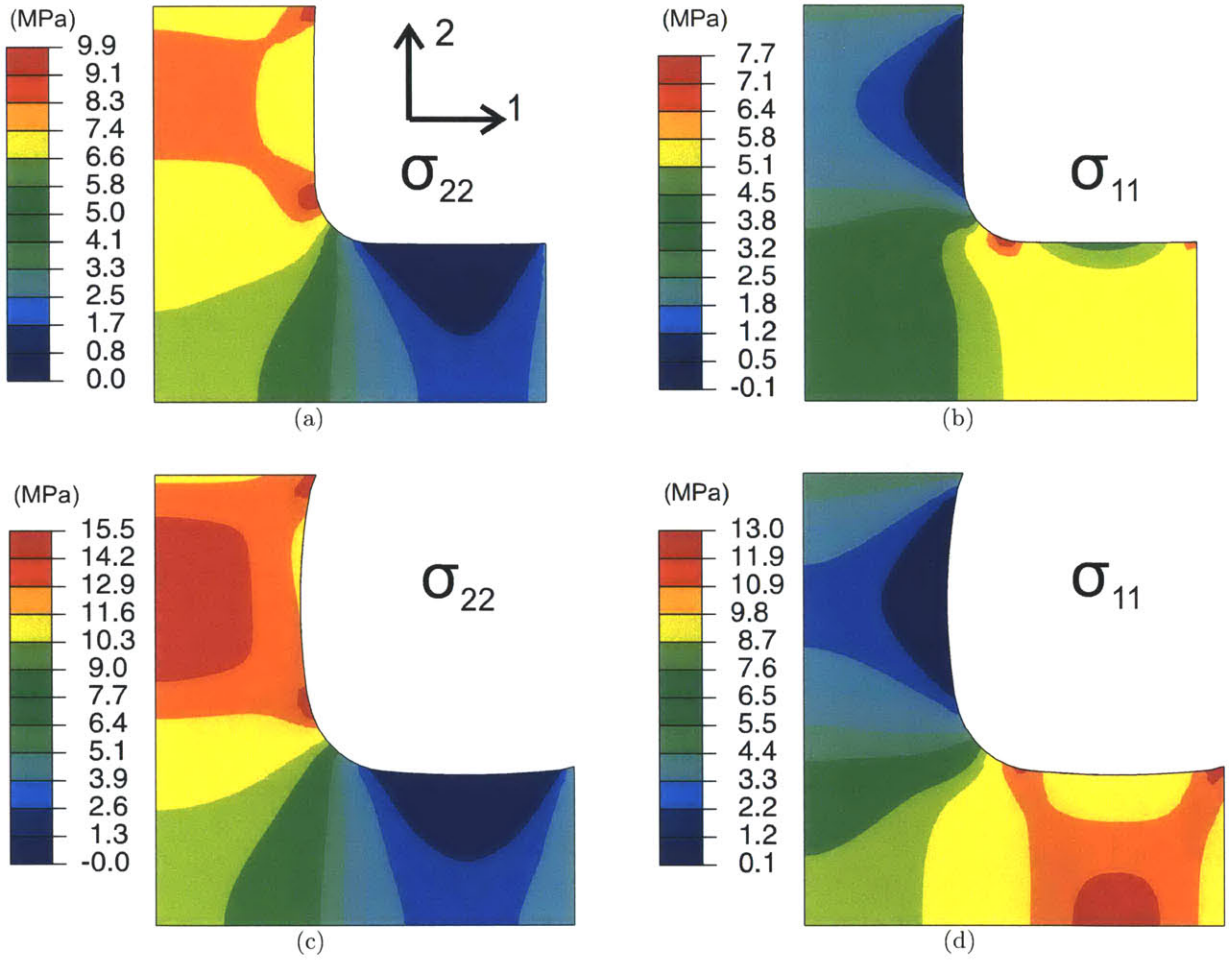

Figure 58: Stress contours from simulated biaxial tensile loading ($B = 0.5$) for the 2-direction grips extended at $14\mu ms^{-1}$ and 1-direction grips extended at $7\mu ms^{-1}$: prior to yield (2-direction grip displacement $= 0.42mm$) (a) σ_{22} ($\bar{\sigma}_{22} = 7.8$) (b) σ_{11} ($\bar{\sigma}_{11} = 5.4$) and just after yield (2-direction grip displacement $= 2.5mm$) (c) σ_{22} ($\bar{\sigma}_{22} = 10.7$) (d) σ_{11} ($\bar{\sigma}_{11} = 9.6$).

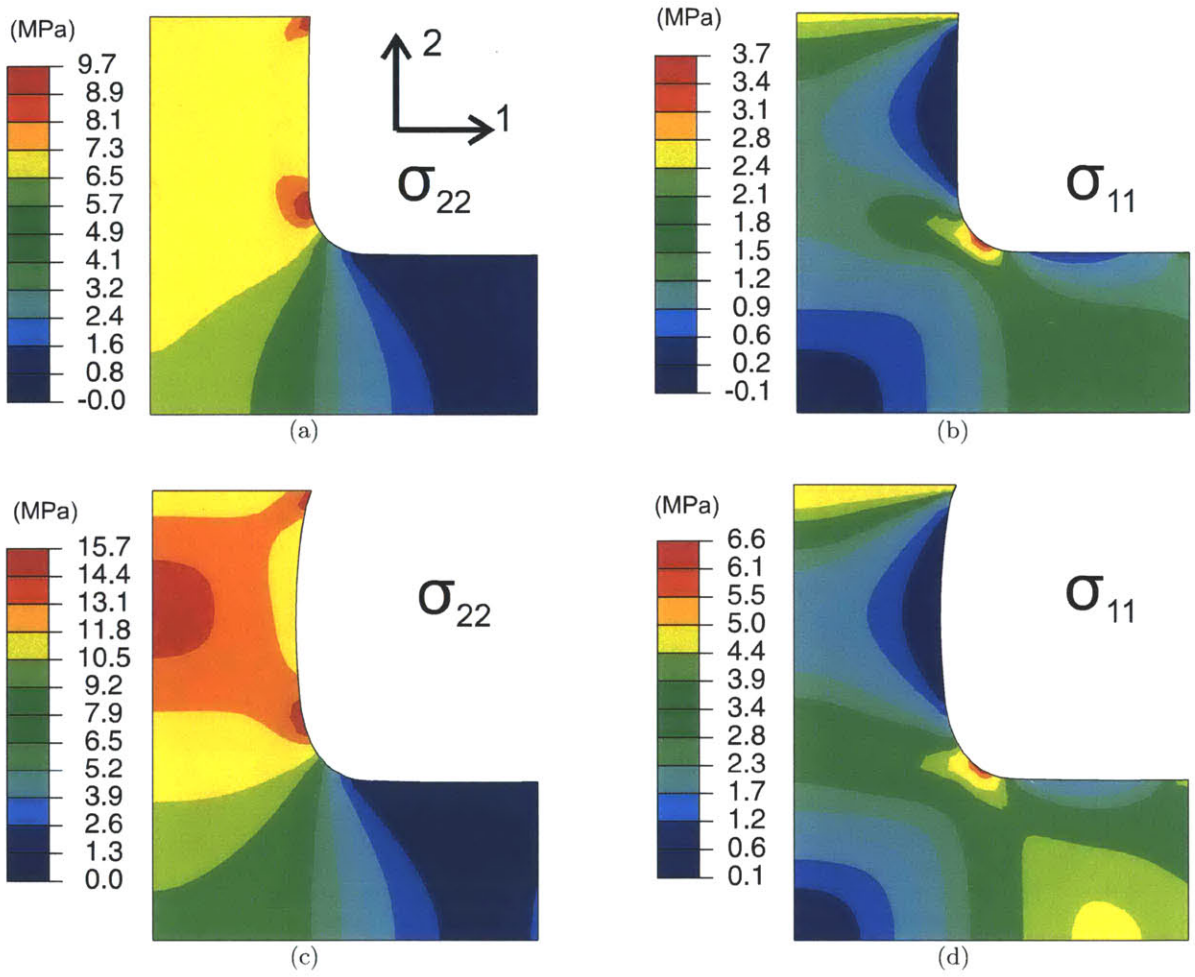

Figure 59: Stress contours from simulated biaxial tensile loading ($B = 0.0$) for the 2-direction grips extended at $14\mu ms^{-1}$ and 1-direction grips held fixed: prior to yield (2-direction grip displacement $= 0.42mm$) (a) σ_{22} ($\bar{\sigma}_{22} = 7.3$) (b) σ_{11} ($\bar{\sigma}_{11} = 1.6$) and just after yield (2-direction grip displacement $= 2.5mm$) (c) σ_{22} ($\bar{\sigma}_{22} = 10.6$) (d) σ_{11} ($\bar{\sigma}_{11} = 3.6$).

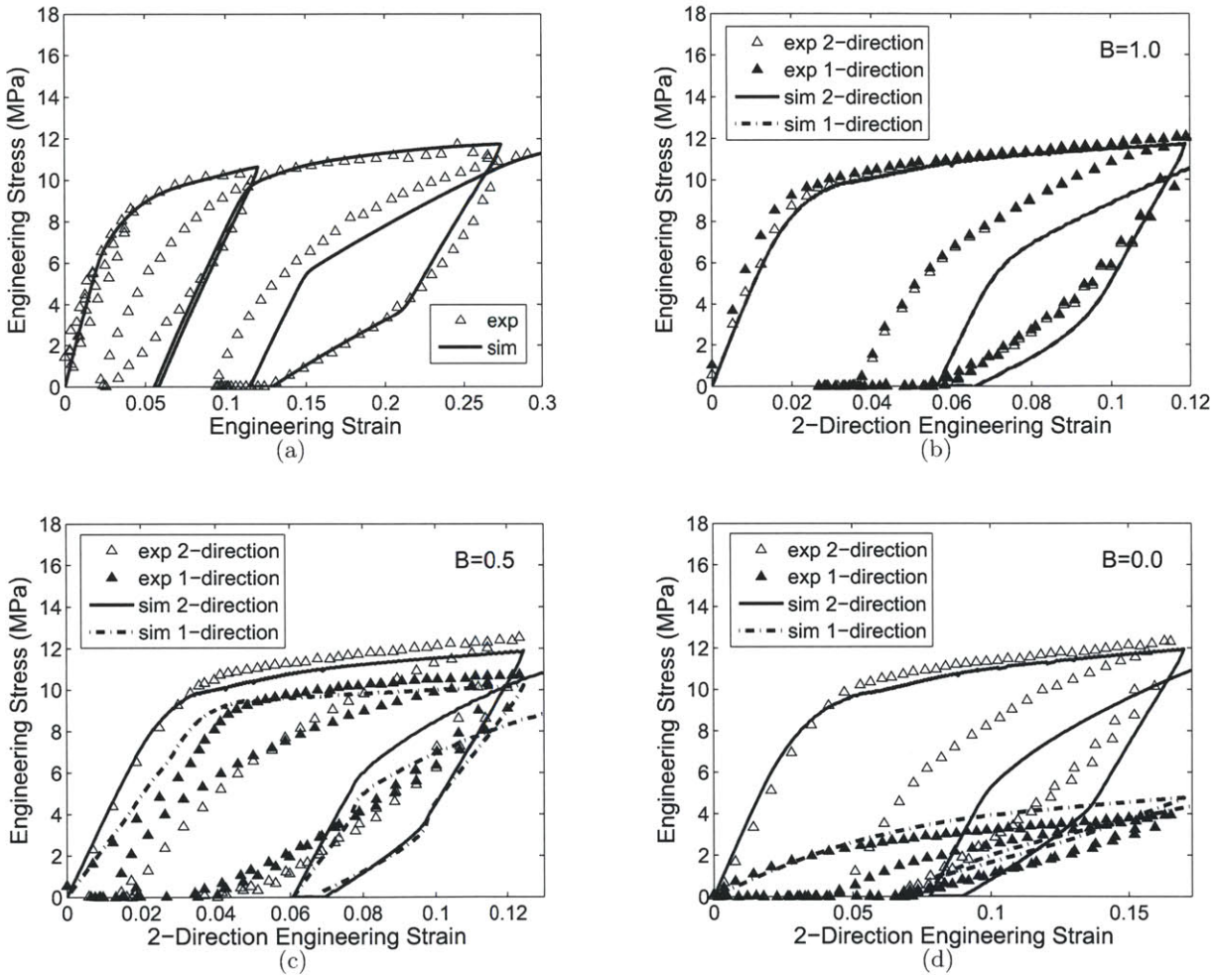

Figure 60: Model compared to experimental data for biaxial tensile loading using video extensometer equivalent strain measure (a) uniaxial behavior for reference ($\phi = 1.5$) (b) 1- and 2-direction grips displaced at $14\mu ms^{-1}$ ($B = 1.0$, $\phi = 2$) (c) 2-direction grips displaced at $14\mu ms^{-1}$ and 1-direction grips displaced at $7\mu ms^{-1}$ ($B = 0.5$, $\phi = 2$) (d) 2-direction grips displaced at $14\mu ms^{-1}$ and 1-direction grips held fixed ($B = 0.0$, $\phi = 2$).

equibiaxial stress-strain response to the uniaxial stress-strain response, it is evident that yield initiates at roughly the same stress for these two loading histories, but the hardening evolves more rapidly for the equibiaxial case, initially as a result of the greater effective strain rate (and hence the greater effective strain at any given axial strain where the yield stress evolves with effective strain) and then as a result of the network stretch. These simulation results indicate that while the experimental data is generally capturing the biaxial material response, it would not be appropriate for direct evaluation of the biaxial yield stress or post yield tangent modulus. Conversely, this method is quite appropriate for model validation since it requires the model to capture not only the homogeneous biaxial response but also the effects of stress and strain distributions.

4.2 Constrained Swelling

4.2.1 Background

The swelling of a bimaterial Nafion/GDL strip was chosen to interrogate the constrained swelling-induced and hydration dependent mechanical stress aspects of Nafion behavior and to assess the ability of the constitutive model to capture this behavior. When water is sprayed on the bilayer, the Nafion membrane will attempt to swell in all directions, but the GDL will constrain expansion in the membrane plane, creating a net compressive force in the membrane and a net tensile force on the GDL which must balance to satisfy force and moment equilibrium. These compatibility and equilibrium conditions will cause the composite bilayer strip to curl, much as the thermostat bimetallic strips with mismatched thermal expansion coefficients bend upon a change in temperature. The bimaterial test has recently been used to estimate the level of stress experienced by the membrane due to constrained swelling(Li et al., 2010). This method required the choice of a substrate with targeted elastic properties to enable an analytical reduction of the data. Here, the constrained swelling of Nafion bonded to a typical GDL substrate is examined.

4.2.2 Experimental Methods

Materials

Commercially available dispersion cast NRE211 films (thickness $t = 27\mu m$, Dupont, Ion Power Inc) and NRE212 films (thickness $t = 54\mu m$, Dupont, Ion Power Inc) were used for the experimental characterization of Nafion. The films were stored in a desiccator cabinet upon removal from the initial packaging to minimize variability in data from aging and humidity effects.

Commercially available LT 1200-N (thickness $t = 180\mu m$, E-Tek, Fuel Cell Store) was used for the GDL material for the bimaterial swelling tests.

Bimaterial Swelling

Bimaterial specimens were prepared by hot pressing Nafion (NRE211 and NRE212) onto a single piece of GDL (thickness $t = 180\mu m$, E-Tek LT 1200-N) at 120^oC for 5 minutes. Specimens were then cut to $1.5mm$ by $15mm$ strips with a razor guided by a straight edge. One end of the specimen was clamped into Zwick screw grips such that $5mm$ of the specimen remained unclamped (Figure 62). The specimen was then sprayed with deionized water from the GDL side. The deformation was imaged over 5 hours via a Qimaging Retiga 1300 camera.

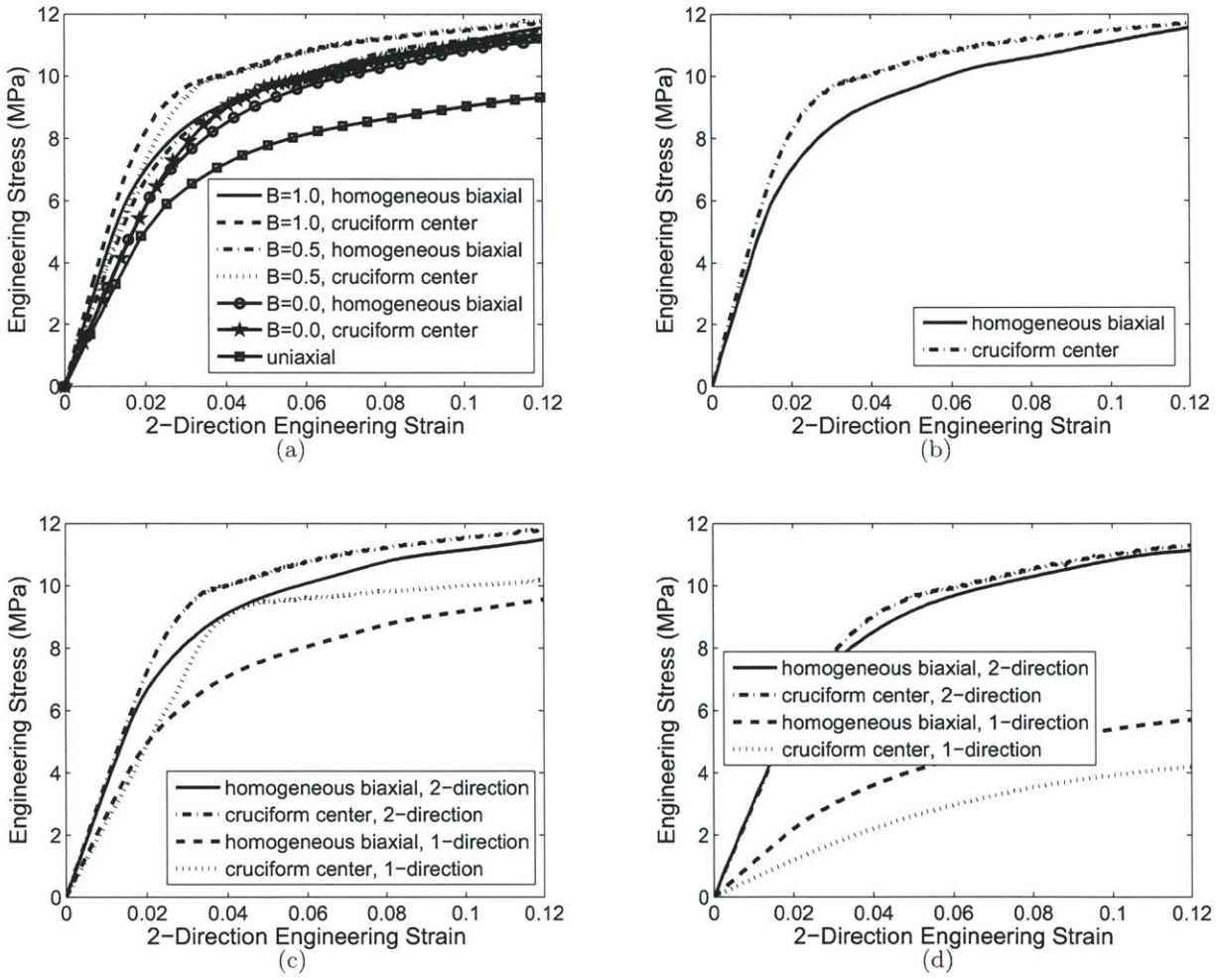

Figure 61: Comparison of simulation result for pure homogeneous biaxial deformation with simulation result for biaxial deformation as conducted experimentally with the cruciform specimen ($\phi = 2$) (a) $\bar{\sigma}_{22}$ for all three degrees of biaxiality (b) 1- and 2-direction grips displaced at $14\mu ms^{-1}$ ($B = 1.0$) (c) 2-direction grips displaced at $14\mu ms^{-1}$ and 1-direction grips displaced at $7\mu ms^{-1}$ ($B = 0.5$) (d) 2-direction grips displaced at $14\mu ms^{-1}$ and 1-direction grips held fixed ($B = 0.0$).

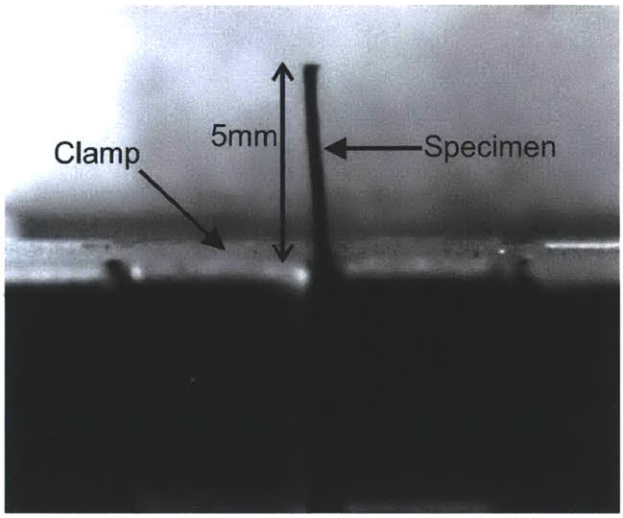

Figure 62: Experimental setup for bimaterial test.

4.2.3 Results and Discussion

Representative images of the NRE212/GDL strip with membrane thickness $54\mu m$ are shown before testing, while hydrated, and after drying in Figure 63. The hydrated state is achieved on the order of seconds, while the drying occurs over 5 hours with most of the drying occurring during the first half hour. This drying rate is influenced by water that collects within the clamp. Upon hydration, the bimaterial strip is observed to curl with the GDL on the concave side and then to gradually straighten during drying, eventually curling in the reverse direction with the membrane on the concave side. This reverse direction curling can be attributed to the plastic deformation that occurs within the membrane during the constrained swelling process. If the swelling deformation were fully elastic the bimaterial strip would have no curvature in the final state. The radii of curvatures in the hydrated and dried state are given in Table 3 along with the corresponding standard deviation.

Table 3 also shows the results for the case of the Nafion NRE211/GDL bilayer where membrane thickness is $27\mu m$; representative images are given in Figure 64. It can be seen that the reduction in membrane thickness results in a decrease in curvature in the hydrated state by a factor of two, scaling roughly with membrane thickness.

The Stoney formula(Freund and Suresh, 2003) provides an expression for the curvature (κ) of a bilayer of a substrate with a stressed thin film:

$$\kappa = \frac{6f}{E_s h_s^2} \tag{88}$$

where f is the film force, E_s is the substrate modulus, and h_s is the substrate thickness. The film force is a result of a strain mismatch with the substrate (in this case, a result of swelling mismatch). The stress may arise from elastic or inelastic behavior of the membrane where the force is the product of the average membrane stress and the membrane thickness. For the case where the membrane is elastic-perfectly plastic with yield stress $\sigma_{y,f}$, $f = \sigma_{y,f} h_f$. Equation 88 then provides a simple relationship to either obtain the curvature given the material behavior or to obtain the

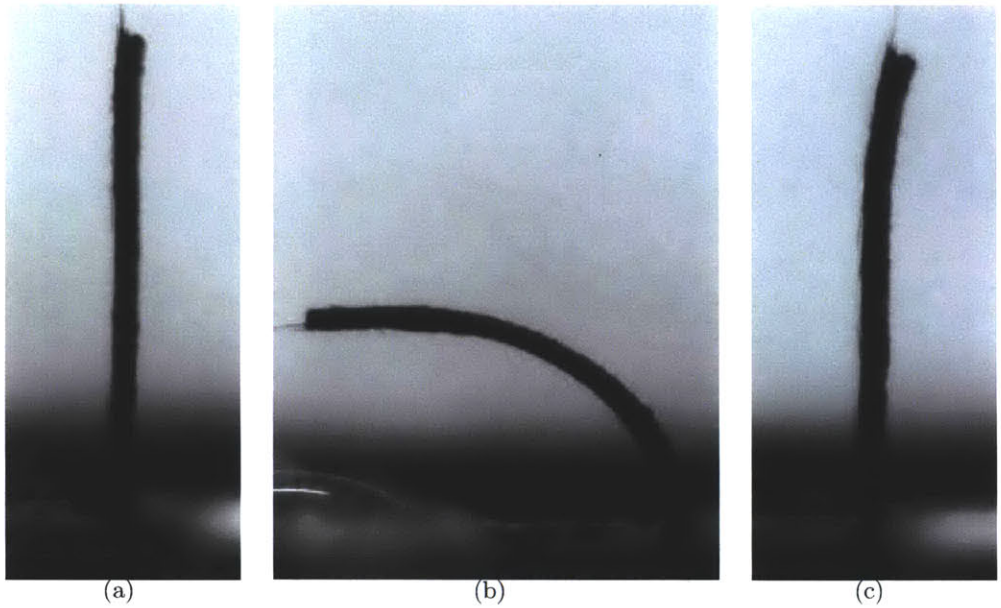

Figure 63: Images of NRE212 bimaterial swelling test ($t_{NRE212} = 54\mu m$, $t_{GDL} = 180\mu m$) (a) initial configuration (b) hydrated (c) dried. Nafion is on the right side of the strip.

membrane force given the curvature. Considering the membrane to have yielded, equation 88 then indicates a factor of two difference in curvature for the two thicknesses considered here which is in good agreement with our measurements. The factor of two arising simply due to the membrane force scaling directly with thickness. Quantitatively, considering the membrane to have yielded at a hydrated yield stress of $5MPa$, equation 88 predicts $\kappa = 139$ for $h_f = 27\mu m$ and $\kappa = 278$ for $h_f = 54\mu m$ which overpredict the observed curvatures.

Taking into account the fact that the film is not thin relative to the substrate, for the case where the film has fully yielded and the membrane is approximated as elastic-perfectly plastic, the curvature is given by:

$$\kappa = \frac{6\sigma_{f,y}}{h_s E_s} m\eta\,(1+\eta) \tag{89}$$

where $m = E_f/E_s$ is the elastic modulus ratio and $\eta = h_f/h_s$ is the thickness ratio. Equation 89 predicts $\kappa = 62$ for $h_f = 27\mu m$ and $\kappa = 140$ for $h_f = 54\mu m$ which is quite similar to the experimental result. This analysis neglects secondary effects of the biaxiality of the loading that results from the finite depth of the specimen ($1.5mm$) which would decrease the curvature and of strain hardening of the membrane which would increase the curvature.

The dried curvature is sensitive to the length of time the strip is hydrated since it is a function of the rate dependent plasticity. It will be discussed in more depth with respect to the finite element simulations.

The constitutive model together with the nonlinear finite element method is used to simulate the bilayer swelling. The GDL is assumed to be linear elastic, characterized by an elastic modulus of $180MPa$ and a Poisson's ratio of 0.25; furthermore, the GDL does not swell. The membrane is

(a) (b) (c)

Figure 64: Images of NRE211 bimaterial swelling test ($t_{NRE211} = 27\mu m$, $t_{GDL} = 180\mu m$) (a) initial configuration (b) hydrated (c) dried. Nafion is on the right side of the strip.

modeled to hydrate over a time period of 10s, held hydrated for 300s, and then dried exponentially over 3600s (with time constant $\tau = 500s$) for NRE212 and 1800s (with time constant $\tau = 250s$) for NRE211. Exponential drying is chosen based on the work of Satterfield and Benziger (2008) which shows that water desorption is controlled by interfacial mass transport. The drying is taken to occur twice as fast for NRE211 since desorption time is directly proportional to thickness.

Side view images from the 3D finite element simulation results are shown before testing, while hydrated, and after drying, for NRE212(Figure 65) and for NRE211(Figure 66). It is evident that the simulation matches the experiment qualitatively with the hydrated curvature for NRE212 approximately twice that for NRE211 and the dried curvature similar for each. In the hydrated state the stress is compressive throughout the membrane and indicates the membrane has yielded (Figure 67a). The nonlinearity in the membrane stress distribution results from plastic deformation. Stress in the GDL is compressive at the outer surface and increases linearly to tensile as it approaches the interface with the membrane. The axis of zero strain is seen to be quite close to the outer surface. In the dried state, the residual stress in the membrane is tensile and mirrors the shape of the hydrated stress but is smaller in magnitude. The stress in the GDL is mostly compressive but is slightly tensile at the outer surface and is significantly lower than in the hydrated state. Table 3 shows that the hydrated and dried curvatures predicted by the model for both NRE212 and NRE211 show excellent quantitative with the experimental data. This indicates that the constitutive model successfully captures and predicts the swelling kinematics and the effect of swelling on the elastic-plastic behavior.

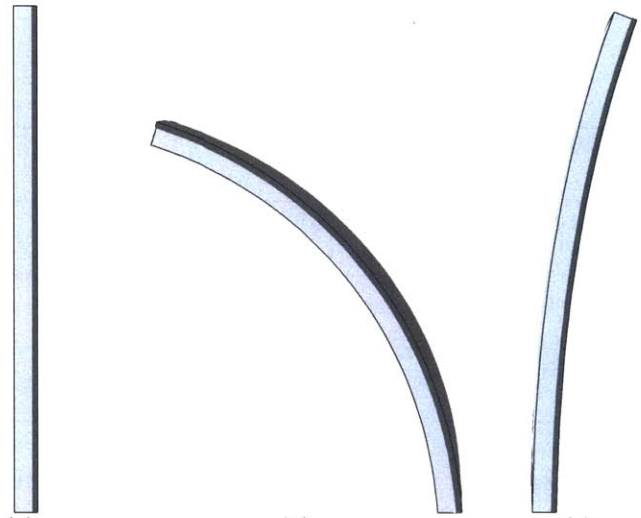

Figure 65: Side view images of the the finite element simulation of bimaterial swelling test with NRE212 (a) initial configuration (b) hydrated (c) dried. Nafion is indicated by dark grey, the GDL is indicated by light grey.

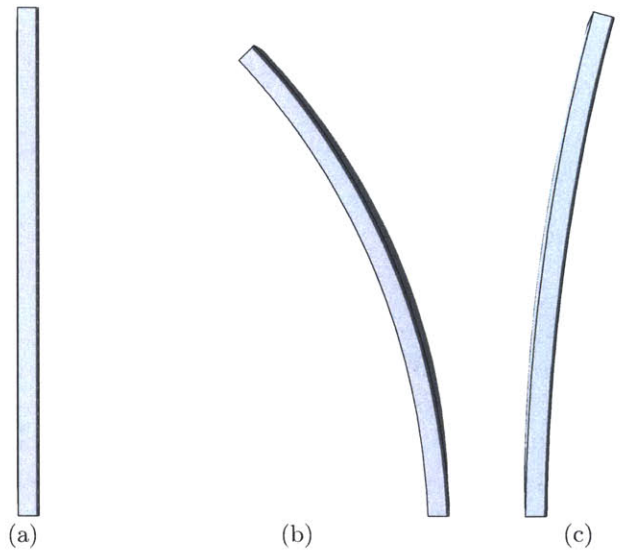

Figure 66: Side view images of the the finite element simulation of bimaterial swelling test with NRE211 (a) initial configuration (b) hydrated (c) dried. Nafion is indicated by dark grey, the GDL is indicated by light grey.

Table 3: Experimental and simulation results of bimaterial swelling test.

		Experiment			**Simulation**	
Material	State	Radius (mm)	Curvature (m^{-1})	Standard Deviation (%)	Curvature (m^{-1})	Error (%)
NRE212	Hydrated ($\phi = 9.5$)	6.8	148	7.4	134	9.5
($t = 54\mu m$)	Dried ($\phi =$ 1.5)	29	35	34	34	2.9
NRE211	Hydrated ($\phi = 9.5$)	14	72	28	73	1.4
($t = 27\mu m$)	Dried ($\phi =$ 1.5)	33	30	19	28	6.7

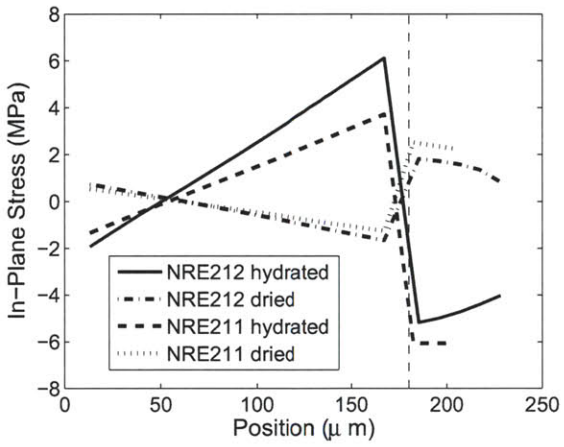

Figure 67: Stress profile across bimaterial strip (thin dashed line indicates GDL/Nafion border).

4.3 In-Situ Fuel Cell

4.3.1 Background

The constitutive model has been shown to be effective in predicting cyclic and rate dependent uniaxial stress-strain behavior, biaxial stress-strain behavior, and bilayer curvature induced by constrained swelling. The model is now applied with confidence to simulate the behavior of Nafion within the constrained loading conditions of a fuel cell. Several groups have simulated in-situ membrane loading using alternative Nafion constitutive models. Karlsson and coworkers used first a linear-elastic and then elastic-plastic models with thermal and hygro-expansion to simulate a membrane within a two dimensional (assuming plane strain in the third direction) fuel cell unit consisting of a land and a channel region of the bipolar plate sandwiching an MEA. They explored fixed displacement and fixed load boundary conditions on the bipolar plates for both aligned and un-aligned channels. Their results showed two key findings when the unit was subjected to hygro-thermal cycling: (i) normal stresses are significantly larger than shear stresses when expressed in

the frame of the membrane; (ii) when plasticity is included in the material model, tensile stresses develop upon dehydration (Tang et al., 2006b; Kusoglu et al., 2006, 2010a). Solasi et al. (2007) simulated the fuel cell as an elastic-plastic membrane subjected to fixed boundary constraints on all four sides and free to expand in the through-plane direction. They found that the stress evolution is a complicated combination of the swelling due to hydration and the change in properties due to temperature and hydration changes. Lai et al. (2009a) performed a similar simulation using a viscoelastic membrane constitutive model. They found that the stress was tensile during drying, that the peak tensile stress increased with each cycle, that its value depended on the rate of hydration/dehydration, and that its value exceeded that of the yield stress suggesting the need for a viscoplastic model. The work presented here employs a geometry similar to that of Karlsson and coworkers in order to study the stress and strain non-uniformity across the channel and land; following the findings of these previous studies attention will be drawn to normal stresses in the dried state and the effect of multiple cycles.

4.3.2 Methods

The geometry used in these simulations is shown in Figure 68a; the $25\mu m$ thick membrane is perfectly bonded to $100\mu m$ thick gas diffusion layers to form the sandwiched membrane electrode assembly (MEA). The MEA is placed within aligned bipolar plates, the land and the vertically open channel are each $0.5mm$. The repeating nature of the unit cell is captured with symmetry boundary conditions where the MEA is not allowed to expand or contract in the horizontal direction. The bipolar plates are subject to a constant force in the vertical direction of $1N$ per unit mm depth corresponding to a nominal stress of $1MPa$ per total area or $2MPa$ per contact area. (The results were found to be qualitatively insensitive to the force applied to the bipolar plates). Plane strain is assumed in the third dimension, creating a biaxial loading condition in the membrane plane. The bipolar plates are taken to be rigid and the gas diffusion layers are modeled as isotropic linear elastic defined by elastic modulus $180MPa$ and Poisson's ratio 0.25. While available data suggests that the typical GDL mechanical behavior is neither isotropic nor linear(Gasteiger and Mathias, 2005; Lai et al., 2008), parametric studies showed these results to be relatively insensitive to a reasonable modulus range and to anisotropy in the GDL given the constant vertical force constraint and the horizontal membrane constraint imposed by the rigid bipolar plates. The membrane is subjected to a uniform history of water content and temperature changes as shown Figure 68b where the water content is varied from 1.5 to 22 and the temperature is varied from 25^oC to 80^oC. Recent simulations by Kusoglu et. al. suggest that a uniform hydration assumption would be reasonable under open circuit voltage conditions where electro-osmotic drag does not factor in(Kusoglu et al., 2010a).

4.3.3 Results and Discussion

When the membrane is hydrated within the fuel cell, the constraints of the GDL and the bipolar plate inhibit the swelling, resulting in significant stress (σ) in the membrane. Representative σ_{11} and σ_{22} contours for the hydrated state are shown in Figure 69a top and bottom, respectively. The membrane experiences compressive stress in both the 1- and 2-directions. σ_{22} is largest beneath the land where the membrane is directly compressed by the clamping force essentially giving a compressive stress of $2MPa$. Typical σ_{11} and σ_{22} contours for the dried state are shown in Figure 69b top and bottom, respectively. σ_{22} is compressive and again largely dependent on the applied

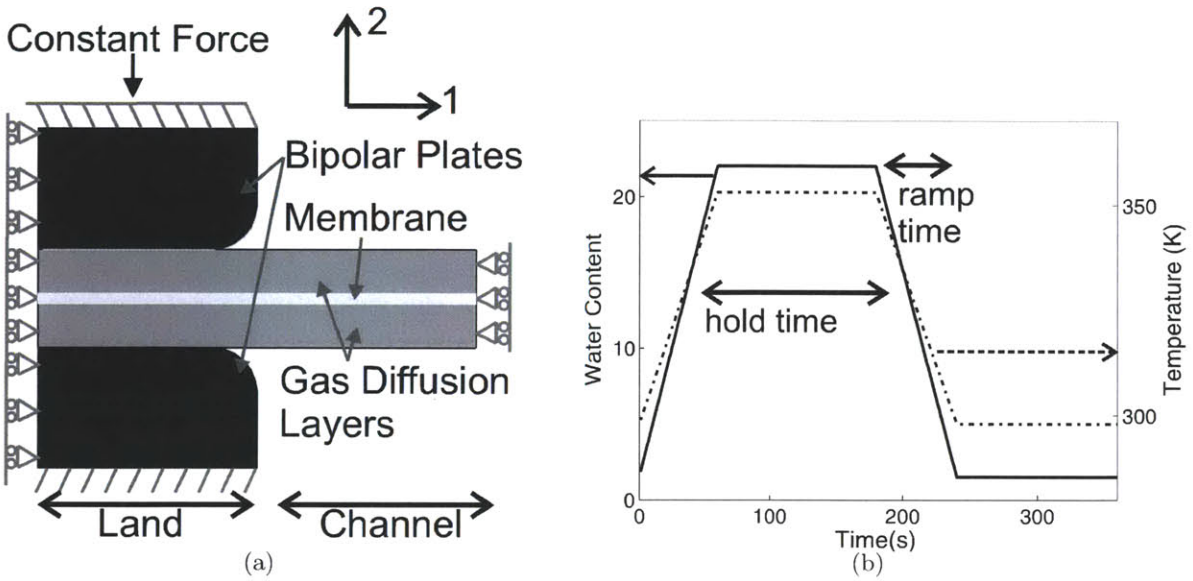

Figure 68: In-situ fuel cell simulation (a) geometry and boundary constraints (b) applied water content and temperature loading.

force constraint. σ_{11} is tensile throughout the membrane and largest just inside the channel. This tensile stress arises due to prior plastic deformation of the membrane during the hydration process. The plastic strain (ϵ^p) in the hydrated and dried states is shown in Figure 70. In both states ϵ^p_{11} is negative throughout the membrane and ϵ^p_{22} is positive throughout the membrane. Both of these components of the plastic strain are greater in the channel as a result of the reduced constraint/pressure and larger Mises stress, this effect is more exaggerated for a larger constant force constraint (not shown). The development of plastic strain and the resulting tensile stress during cycling strongly supports the concept of mechanically driven membrane failure in fuel cells. One of the more subtle aspects of this in-situ modeling is that while the hydration process causes swelling strains, the elastic and plastic properties of the membrane are being reduced as a result of the increase of the water content and temperature. Consequently, similar magnitude stress levels in the hydrated and dried states are likely to cause more plastic deformation in the hydrated state.

For completeness σ_{33} and σ_{12} contours are also included for the hydrated and dried states (Figure 71). σ_{33}, which results from the plane strain boundary condition in the 3-direction, is quite similar to σ_{11}. σ_{33} is compressive throughout the membrane in the hydrated state and tensile throughout in the dried state. In both states the stress is more positive (tensile) in the channel than in the land. This reaffirms: (1) that the 1-direction constraint imposed by the rigidity of the bipolar plates is equivalent to plane strain with stress and strain variation arising from the 2-direction boundary variation; and (2) that the in-situ loading is biaxial. Although failure is not explicitly modeled here it is useful to compare this biaxial stress, which is on the order of $10MPa$ in the dried state, with that shown to cause failure in the literature. Pressure blister tests conducted on NRE211 at 80^oC and $2\%RH$ show that leak occurs at around $100s$ when the biaxial stress is held at $10MPa$ and around $10,000s$ when the biaxial stress is held at $2MPa$(Li et al., 2009). While these environmental conditions do not match those used in the fuel cell simulation, and

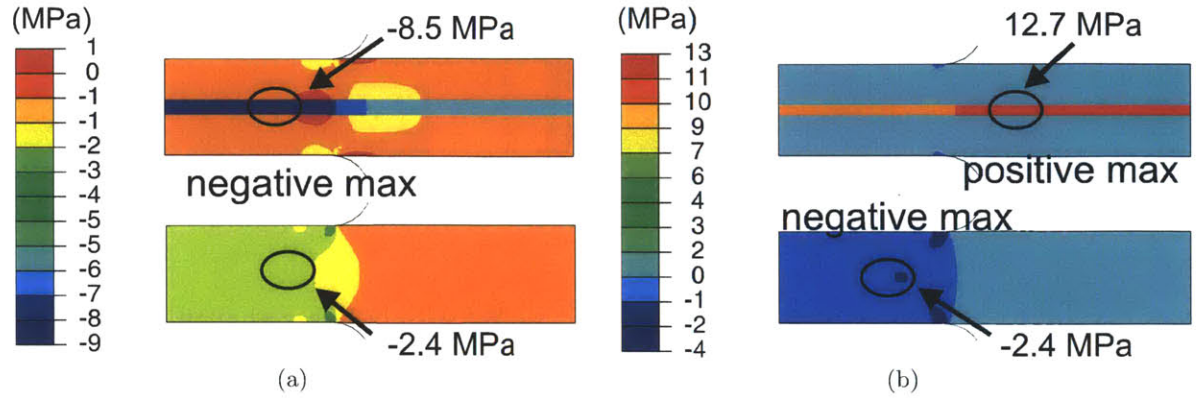

Figure 69: Typical stress contours during hygro-thermal cyclic loading (a) hydrated (b) dried. top:σ_{11}, bottom:σ_{22}

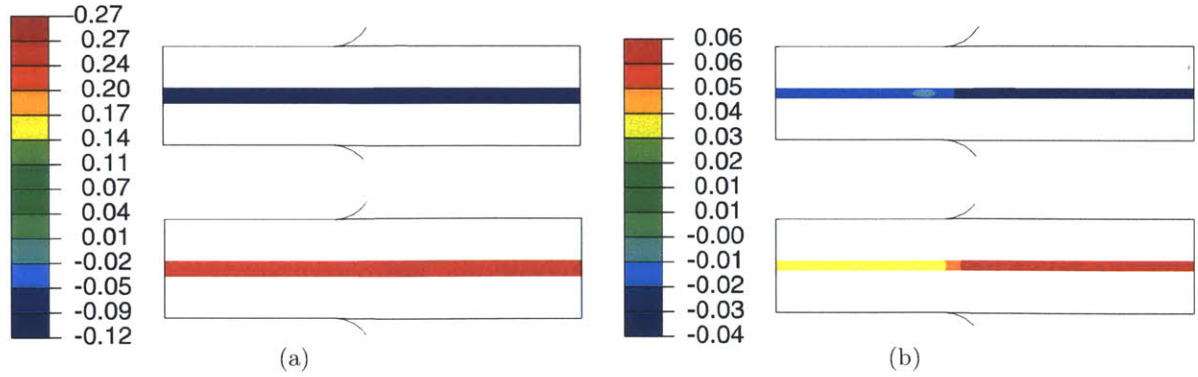

Figure 70: Typical plastic strain contours during hygro-thermal cyclic loading (a) hydrated (b) dried. top:ϵ^p_{11}, bottom:ϵ^p_{22}

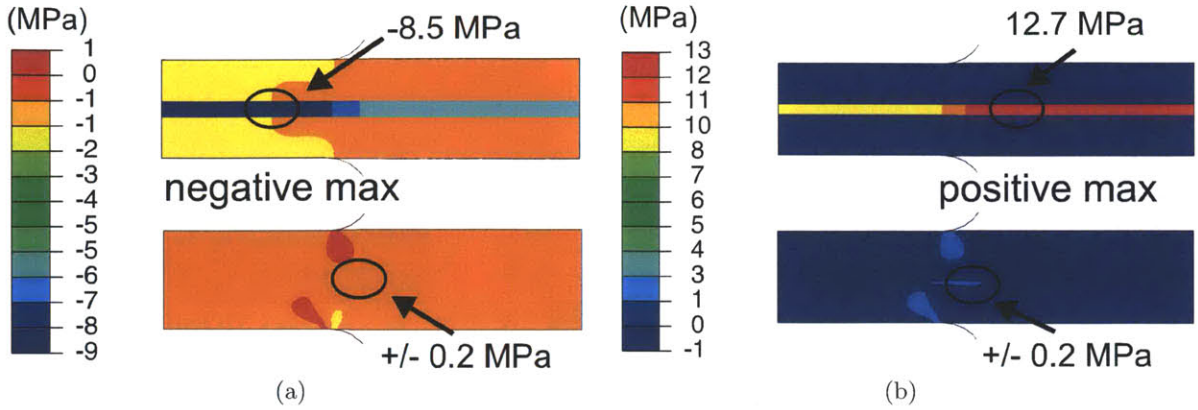

Figure 71: Typical stress contours during hygro-thermal cyclic loading (a) hydrated (b) dried. top:σ_{33}, bottom:σ_{12}

the 2-direction stress may significantly contribute to inhibiting failure, it is clear that the biaxial stresses reached during in-situ hygro-thermal cycling are large in comparison to the fatigue failure criteria. The shear stress σ_{12} is at a maximum right around the land/channel interface however, it is negligible in comparison to the normal stresses in both the hydrated and dried states. σ_{12} never exceeds $0.2MPa$ compared to $2MPa$ typical for σ_{22} and $10MPa$ typical for σ_{11} and σ_{33}.

In the literature, membrane failure is primarily discussed in terms of either pinhole formation or membrane thinning (e.g. Borup et al. (2007a)). These arise from a combination of mechanical and chemical damage and are presumably coupled in their development, but nominally, one could affiliate pinhole formation with some form of cavitation or crazing event resulting from negative hydrostatic pressure (Haung et al., 2006). Focus will now be directed to the negative hydrostatic pressure as an indicator of potential membrane failure. The pressure evolution will be followed through a single hydration/drying cycle and then through multiple cycles as a function of hydrating and drying rates and hold times at each state. The pressure develops similarly to the σ_{11} stress; in the hydrated state the pressure is positive (compressive) and in the dried state the pressure is negative (tensile). Typical contours for these two states are shown in Figure 72a,b top. In the hydrated state the pressure is greatest under the land. In the dried state there is a negative pressure concentration that develops just inside the channel; this is where cavitation or crazing would be expected to occur. Figure 73 shows the pressure history in the membrane in the channel region just outside the land where the maximum negative value occurs and also shows the history of σ_{11} in this same area, revealing the cycling between compressive and tensile states. The pressure in this region cycles from $\sim 4MPa$ in the hydrated state to $\sim -8MPa$ in the dried state. In both the hydrated and dried states the pressure relaxes with time and becomes more uniform as the membrane is held at constant environmental conditions (Figure 72a,b bottom). The time scale of this relaxation is linked both to the intrinsic relaxation of the material as characterized in uniaxial experiments and the stress inhomogeneity that results from the constraint geometry. Most of the relaxation occurs over the first $30s$ with the pressure approaching a steady state. Since the pressure has its greatest negative value immediately after drying/cooling is finished, the pressure at this point in the first and tenth cycles will be used to track the effect of ramp rate and hold time on pressure of the in-situ membrane (Figure 74). Increasing the ramp time (decreasing the ramp rate) decreases the

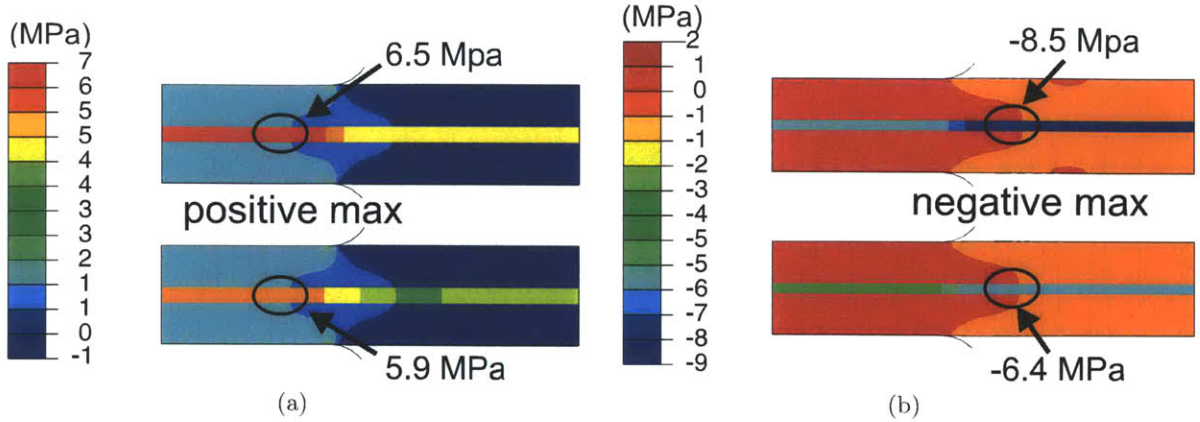

Figure 72: Typical hydrostatic pressure contours during hygro-thermal cyclic loading (a) hydrated (b) dried. top: when environmental state first reached, bottom: after held at environmental state for $60s$.

peak pressure both for the first and tenth cycles as this increases the time the membrane has to relax in response to the applied hygro-thermal load. Increasing the hold time increases the peak pressure for the first cycle but decreases the peak pressure for the tenth cycle. This counterintuitive result can be explained by the fact that relaxation that occurs in the hydrated state will drive the magnitude of the negative pressure to increase while relaxation that occurs in the dried state will drive the magnitude of the negative pressure to decrease, at the first cycle negative peak only the former will have occurred. Across the board the tenth cycle pressure is below that of the initial cycle.

In accelerated mechanical lifetime testing, a particular relative humidity and temperature cycle is applied to the membrane within the fuel cell. It is assumed that these short cycles are equivalent to operating cycles, but it is unclear whether this is an effective method of assessing mechanical durability of a membrane (Li et al., 2009). These in-situ simulations show that in order to properly reproduce the peak pressure, the ramp up and ramp down times in the accelerated test must match the startup and shutdown times in an operational fuel cell. The choice of hold time is less clear since this obviously cannot be matched to that of an actual fuel cell. The most extreme form of loading would be to hold at the hydrated state but not at the dried state; $60s$ would probably be a sufficient hold time.

4.4 Conclusions

First, the behavior of Nafion was experimentally explored under tensile biaxial loading conditions varying the degree of biaxiality. Biaxial testing was conducted via in-plane tensile testing of cruciform shaped specimens. A video extensometer system was used to enable determination of the local biaxial response in the central region. The biaxial response was qualitatively similar to the uniaxial response with the stiffness and strength in a given direction dependent on the degree of biaxiality. The constitutive model developed for Nafion based on uniaxial tensile data was used to simulate these experiments via a finite element implementation. These simulations revealed that the stress distribution is not completely uniform in the central "biaxial" region of the specimen. The

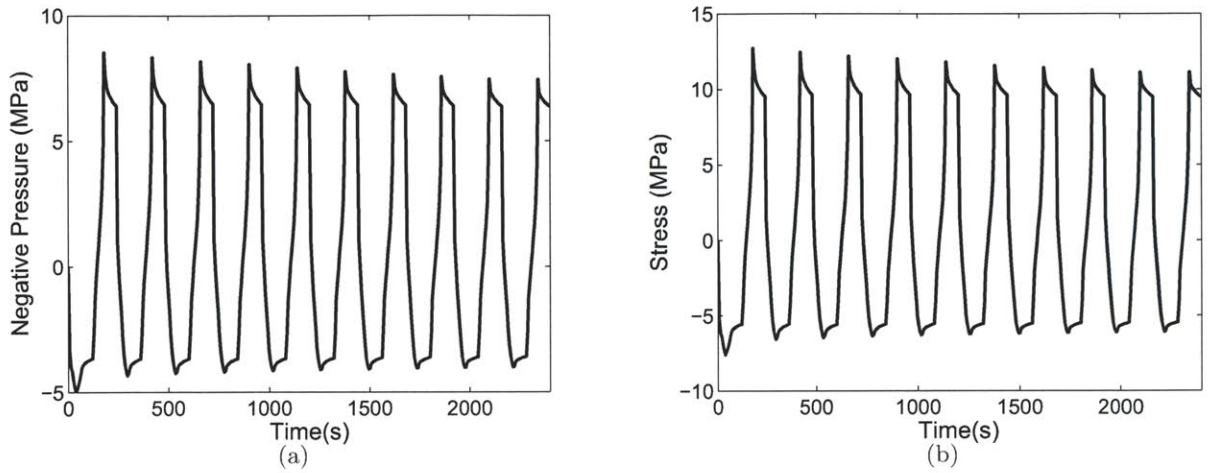

(a) (b)

Figure 73: Evolution of stress values at the concentrated location just inside the channel during hygro-thermal cyclic loading when ramped over $60s$ and held at each state for $60s$ (a) negative hydrostatic pressure (b) σ_{11}.

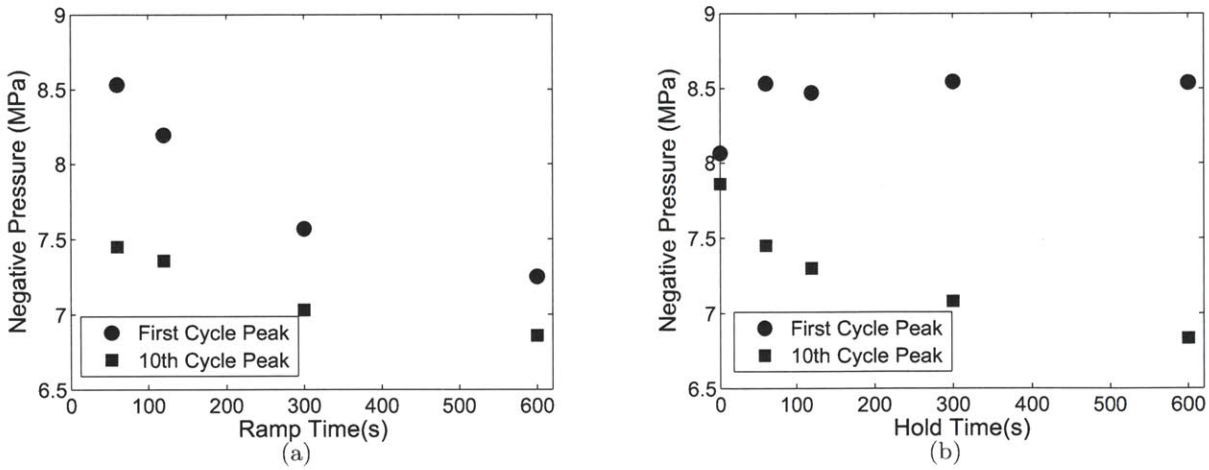

(a) (b)

Figure 74: Peak negative pressure in the membrane during the first and tenth cycle of hygro-thermal cyclic loading (a) as a function of ramp time with $60s$ hold time (b) as a function of hold time with $60s$ ramp time.

cruciform specimens result in a greater and sharper yield event as compared to the pure homogenous biaxial response. Nonetheless, the constitutive model was shown to well predict this complex multiaxial deformation response when the model is implemented in the experimental geometry and reduced by the same methods as the experimental results. These results also indicated that while the initial yield under equibiaxial and uniaxial loading conditions are the same, the evolution in strength with strain (the rollover nature of yield) gives the appearance of a greater yield stress during biaxial loading compared to uniaxial loading - an effect captured by the model. It should be noted that no material parameters were modified to fit the biaxial data, the success therefore demonstrates the truly predictive capability of the model. The biaxial testing method and predictive constitutive modeling have broad relevance to polymeric membranes, especially considering the need for robustness to biaxial loading for polymer membranes in a wide range of separation and transport processes.

Bimaterial strip swelling was used then to probe the partially constrained swelling behavior of Nafion. When the strip was hydrated the membrane swelled causing the strip to curl with the membrane on the convex side until the force from the membrane was balanced by a moment in the GDL. The bending stiffness of the GDL induced compressive plastic deformation in the membrane which then induced a slight curvature upon drying with the membrane on the concave side. The ratio between the hydrated radii for the two thicknesses of Nafion were found to agree with that predicted by a simple modification of the Stoney formula which relies on the assumption that the entire membrane has yielded. The hydrated and dried radii were found to agree with the finite element simulation predictions for two thicknesses of Nafion to within experimental error.

Finally, the model was used to simulate a simplified fuel cell cycle. The particular hygro-thermal cycles chosen were not meant to precisely duplicate those of an operating fuel cell, but rather to demonstrate the power of a three dimensional continuum model and assess potential mechanical damage mechanisms. Simulations of this nature are useful in guiding startup and shutdown procedures for fuel cells, for designing/validating potential procedures for accelerated lifetime testing, and for designing alternative fuel cell geometries. The findings of previous researchers were confirmed that a tensile stress arises in the plane of the membrane upon drying. Further, a negative hydrostatic pressure develops in the channel suggesting a driving force for cavitation or crazing. A study of the effect of ramp rate and hold time revealed a significant time dependence of the pressure, which is not surprising given the significant rate dependence observed for Nafion under uniaxial mechanical loading. The model could be further strengthened with the inclusion of a set of failure criteria.

Future prospects for this modeling effort lay along two primary paths: transport and failure. *Transport:* In its current iteration the model takes water content at a given location as an input. In order for the membrane model to be integrated into a fuel cell model in a realistic manner, the water content should instead be solved based on water transport and boundary conditions. The determination of water content from boundary conditions would then also enable the incorporation of the effects of stress on water content. Further, when an electrical field is active, water transport is heavily influenced by proton transport. The model would therefore have to be capable of modeling both proton and water transport and the interaction between the two. If it is assumed that these transports are uncoupled with mechanical deformation in anyway, then they could be modeled through fairly standard electrochemical equations (e.g. Nernst-Plank), although flexible implementation within Abaqus is non-trivial. Of course the combined mechanical and transport model becomes much more interesting when coupling is included. For instance one would expect

current to increase (resistance to ion transport to decrease) with decreasing thickness of the membrane. One might also expect there to be a correlation between through thickness resistance to transport and molecular alignment within the membrane as it evolves through time within the fuel cell. Validating such coupled relations, however, would require sophisticated experimental setups and is outside the realm of this thesis.

Failure: One of the main goals of developing this model is to understand why Nafion membranes fail mechanically in fuel cells. This failure has been discussed generally in terms of the stress state and the negative hydrostatic pressure. It would be more useful to have failure at a material point as a direct model output. Further, these in-situ failures are known to occur after many cycles of loading. Therefore, a fatigue failure criteria is needed. Many researchers have begun to evaluate membrane failure including such methods as strain to break(Tang et al., 2006a), knife slit(Patankar et al., 2010), trouser tear, double edged notched tension(Li et al., 2008), creep rupture(Solasi et al., 2010), and pressure-loaded blister test(Dillard et al., 2009; Li et al., 2009). The creep and pressure-loaded blister methods in particular were aimed at characterizing the fatigue failure. With further advancements in the understanding of fatigue failure in polymers, information from one or several of these could be incorporated into the continuum model.

5 Composite polymer electrolyte membrane design overview

5.1 Background

This research focuses on mechanical aspects of the design of new polymer electrolyte membranes for direct methanol fuel cells (DMFC) which are a special case of PEMFC. DMFC operate under the same principal as PEMFC, however the fuel is liquid methanol rather than hydrogen. The high energy density of methanol makes DMFC particularly promising for portable applications where they could replace Li-ion batteries. Some systems are commercially available, but they are not cost competitive. Desirable traits in PEM for DMFC include: high proton conductivity, low methanol diffusion, chemical durability, mechanical durability, operation at temperatures over 100^oC, low catalyst diffusion, and low cost (Neburchilov et al., 2007). In contrast to PEMFC, fuel crossover is a major design concern even when the membrane is fully intact. While Nafion is considered the benchmark membrane for DMFC, it does not significantly outperform alternative membranes. Excessive methanol crossover in Nafion drives the use of thicker membranes and diluted fuel feed which in turn decreases system efficiency and power (Neburchilova et al., 2007). Nafion is also quite expensive, accounting for around 20% of the total fuel cell cost.

A wide range of alternative membranes have been developed for DMFC ranging from slight modifications of Nafion to completely different chemistries. See e.g. Jannasch (2003); Hickner et al. (2004); Neburchilov et al. (2007) for a comprehensive review of recent materials development for DMFC membranes. In short, the common approaches can be sorted into Nafion derivatives and distinct chemistries. Within the Nafion derivatives, membranes can have the same backbone chemistry but different side chains/side chain length, or there can be inorganic additives designed to decrease methanol crossover. The distinct chemistries commonly consist of an organic/inorganic hybrid and/or acid-base pairing (e.g. polyvinylidene fluoride, sulfonated poly(ether ether ketone), and polybenzimidazole). Each of these are deficient in at least one of: conductivity, crossover, cost, manufacturability, and durability and as such no clear winner has emerged in the DMFC market.

Given the multi-functionality of a DMFC PEM, it is natural to look to a composite solution. Again, a PEM must have low resistance to proton transport, high resistance to fuel transport, and be mechanically robust enough to remain solid and fracture free through the lifetime of the fuel cell. For the proton transport and fuel crossover resistance we use a chemistry and synthesis technique developed in the Hammond lab at MIT. This membrane is itself a composite of sulfonated Poly(2,6-dimethyl 1,4-phenylene oxide) (sPPO) and poly(diallyl dimethyl ammonium chloride) (PDAC) assembled via layer-by-layer (LBL) deposition (Lutkenhaus and Hammond, 2007; Argun et al., 2008). The LBL technique offers the advantage of precise compositional and thickness control and the flexibility to deposit directly onto other fuel cell components. Details of the development of this membrane and its electrochemical performance are available in Ashcraft (2009). Unfortunately these films tear easily under dry conditions and are almost fluid like under hydrated conditions as will be shown subsequently. This PDAC/sPPO membrane must therefore be combined with a mechanical support component. The skeletal support of the membrane mat should provide the composite with solid like mechanical properties and resistance to tearing, have limited macroscopic swelling under hydrated conditions, and still allow for an abundance of continuous pathways for rapid proton conduction. To achieve these performance requirements we turn to electrospinning, a technique which allows the creation of high porosity mats composed from a wide range of materials. In particular, amorphous polyamide is used for the prototype membrane due to the relative ease of control of mat porosity, fiber size, and fiber shape. In order to best optimize this design a model

needs to be developed to characterize the mechanical and transport behavior of the composite.

My contribution to the PEM design effort consists of developing a micromechanical model of the composite mechanical behavior. To this end an experimental mechanical characterization is conducted of the uncoated polyamide electrospun fiber mat (EFM), the stand alone PDAC/sPPO layer-by-layer film (LBL), and the composite. A model is then developed for the EFM and the LBL separately, with primary emphasis placed on the broadly applicable model for EFM directly based on the microstructure. Simple methods for combining the two material behaviors are then explored in order to develop a composite model. Here, the processing, characteristics, and behavior of the composite mat and each of its components will be briefly discussed. Each material and the corresponding model will be further discussed in Chapters 6 and 7.

5.2 Experimental Characterization

5.3 Materials

All LBL films were processed in the Hammond lab at MIT by graduate student J. Nathan Ashcraft as part of his doctoral research. PPO (Mw = 23,000) was obtained from Sigma-Aldrich, Inc. PDAC (Mw = 240,000) was obtained from Polysciences, Inc. PPO was sulfonated to yield highly sulfonated sPPO. A home-built automated spraying setup was used to assemble the films on either untreated Teflon substrates or polystyrene coated silicon wafers. An automated program run by a logic relay controlled the apparatus, spraying the PDAC and sPPO solutions for 3 seconds, with 10 seconds of rinse water spray in between the polymer sprays. The films were then gently peeled off after assembly to create stand alone films for mechanical characterization.

All EFM materials were processed in the Rutledge lab at MIT by graduate students Chia-Ling Pai, Matthew M. Mannarino, or J. Nathan Ashcraft as part of their doctoral research. The fiber mats are electrospun from amorphous polyamide. A 30 wt% solution of polyamide PA6(3)T was dissolved in dimethylformamide(DMF). The parallel-plate electrospinning setup described by Hohman et al. (2001) was used. The flow rate, plate-to-plate distance, and voltage were set to 0.005 mL/min, 42 cm, and 34 kV, respectively. Randomly oriented non-woven meshes were collected on a grounded sheet of aluminum foil. Several single fibers produced under the same conditions were collected on paper templates.

All LBL spray coated EFM mats were processed in the Hammond lab at MIT by graduate students J. Nathan Ashcraft or David Liu as part of their doctoral research. EFM samples about 4 x 4 in size were directly placed onto a 3 in diameter plastic funnel fitted with a steel mesh for support. Sprayed films were fabricated using the same polymer and rinse solutions described above. A mild vacuum was applied to the back of the EFM using a venturi pump supplied with nitrogen. The process was repeated numerous times to generate thick coatings. The mat was then flipped and the coating process was repeated from the other side.

Further details on all of the processing methods can be found in Ashcraft (2009).

5.4 Experimental Methods

5.4.1 Morphological Characterization

For morphological characterization by scanning electron microscopy (SEM) (JEOL-6060SEM, JEOL Ltd., Japan), fiber samples were sputter-coated with a $3 - 4nm$ layer of gold using a Desk II cold

sputter/etch unit (Denton Vacuum LLC). SEM was used to observe the surface structure of fibers at $5kV$ acceleration voltage and $15mm$ working distance.

5.4.2 Mechanical Characterization

Uniaxial tensile tests were conducted on each of the materials (LBL, EFM, and LBL coated EFM). The EFM and coated EFM were cut into rectangular specimens $10mm$ wide and $30mm$ long and the LBL film was cut into specimens $7mm$ wide and $25mm$ long with a razor guided by a straight edge for uniaxial testing. The thickness of each specimen was determined from the average of 3 measurements with a Mitutoyo force-controllable micrometer. All tensile tests were conducted at a constant engineering strain rate of $0.01s^{-1}$ on a Bose Electroforce 3200 (ELF) with an initial grip-to-grip distance of $20mm$ for the EFM and coated EFM and $15mm$ for the LBL films. Both axial and transverse strain were monitored with either a Qimaging Retiga 1300 or a Point Grey Grasshopper video extensometer and analyzed with the Vic2d software package from Correlated Solutions. The force-displacement data as taken from the ELF and the video extensometer, respectively, were reduced to true stress-true strain results. A membrane stress was used, neglecting changes in the thickness but accounting for changes in width. True stress is thus defined as the ratio of force to current (deformed) cross-sectional area (neglecting thickness changes) and true strain is defined as the natural logarithm of the ratio of current length to original length (length being the axial distance between video-imaged marks).

5.5 Experimental Results

Figure 75 shows the morphology of the bare and layer-by-layer (LBL) spray coated electrospun fiber mats (EFM). The mats are non-woven and the fibers have a random distribution. The coating process does not change the distribution of the fibers, it does however pack them more densely in the through thickness direction. The spray coating process forms a mat that is not fully dense: all of the fibers are conformally coated with the LBL polymer, and many of the fibers are bound together by the LBL, but many voids remain. This LBL spray coating process is still under development, these voids are unacceptable in terms of electrochemical performance.

Each material exhibits a distinct behavior under uniaxial tension at ambient conditions. The elastic modulus and yield stress of each are listed in Table 4. The LBL mat is elastic-plastic and subject to tearing at low strains when dry. It has a Poisson's ratio of 0.08 in the elastic regime, followed by a transition to a transverse strain ratio of -0.5 at yield. The EFM is also elastic-plastic when dry, but is about $1/20^{th}$ the stiffness of the LBL and highly extensible. The transverse strain behavior is quite different from that of the LBL, there is a small initial regime at which the Poisson's ratio is close to zero followed by a drastic change in slope to a transverse contraction to axial strain ratio greater than 1. The composite shows an intermediate behavior in terms of stiffness and yield stress, but takes on the failure strain and transverse contraction of the LBL. Video extensometer images of the three materials in the undeformed state and under uniaxial tension at either a strain of 0.2 or just prior to fracture are shown in Figure 77. It is clear that when dry the LBL dominates the composite transverse contraction behavior.

In the hydrated state the relative behavior of the three materials changes significantly. The stand-alone LBL is nearly fluid like, dropping by a factor of 100 in yield stress, and becoming extensible to large strains without tearing. The EFM remains elastic-plastic and highly extensible with less than a factor of 2 drop in stiffness and minimal change in transverse strain behavior.

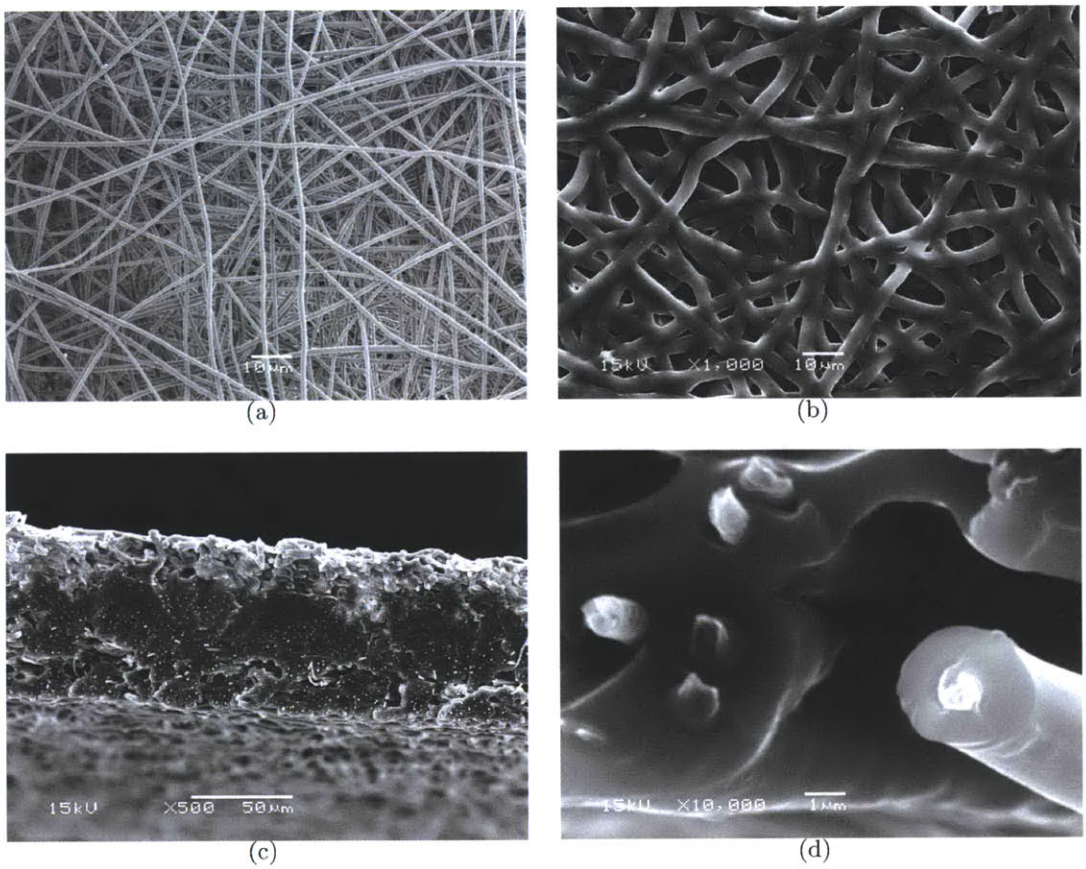

(a) (b) (c) (d)

Figure 75: Scanning electron microscopy images (a) top view of bare EFM (b) top view of LBL spray coated EFM (c) cross-sectional view of LBL spray coated EFM (d) zoomed in cross-sectional view of LBL spray coated EFM.

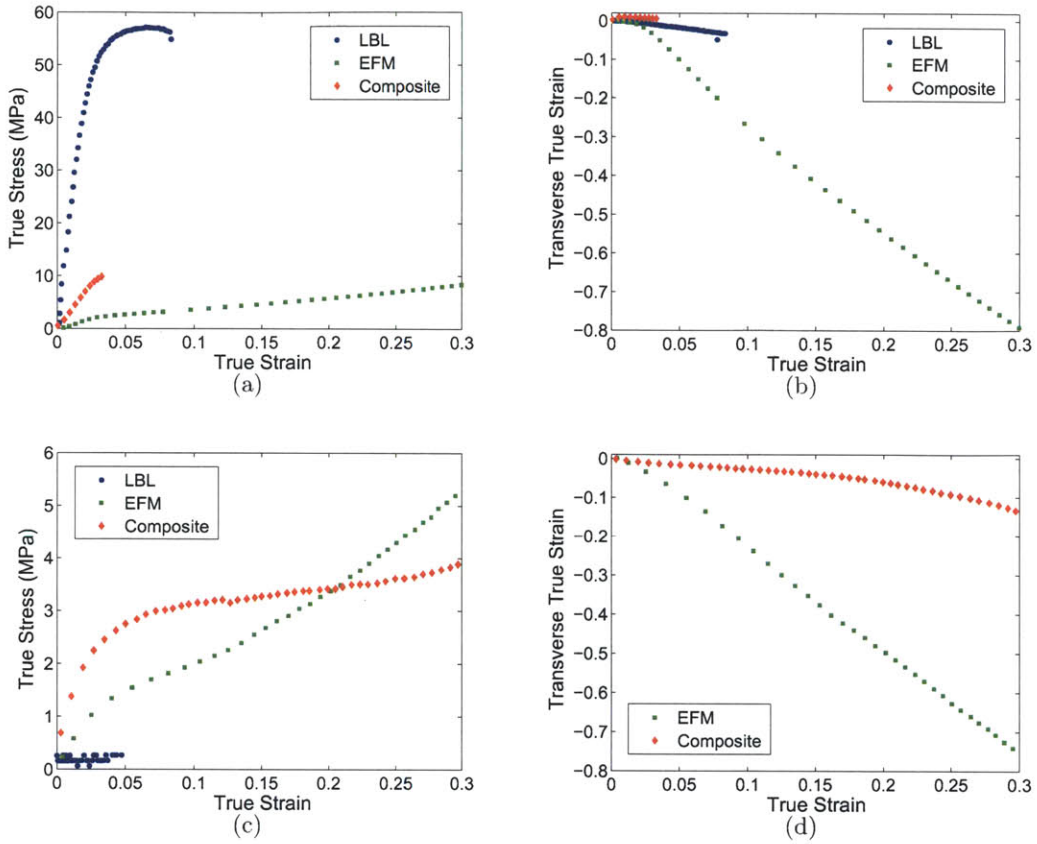

Figure 76: Experimental results of the composite and its constituents subjected to uniaxial tension: (a) dry stress-strain, (b) dry transverse strain versus axial strain, (c) wet stress-strain, (d) wet transverse strain versus axial strain.

The coated mat in the hydrated state remains elastic-plastic, drops in stiffness and yield by a factor of 5, becomes highly extensible, and is stiffer than either the LBL or the EFM in this state. The coated mat transverse strain is similar in the hydrated state to that in the dried state. In other words, the LBL is able to lend axial stiffness and resistance to transverse contraction to the EFM in the hydrated state even though it has minimal stiffness on its own under uniaxial tension. The transverse contraction resistance of the LBL is also evident in the video extensometer images (Figure 77) which show the wet composite to have a shape intermediate to the dry composite and the EFM (dry and hydrated).

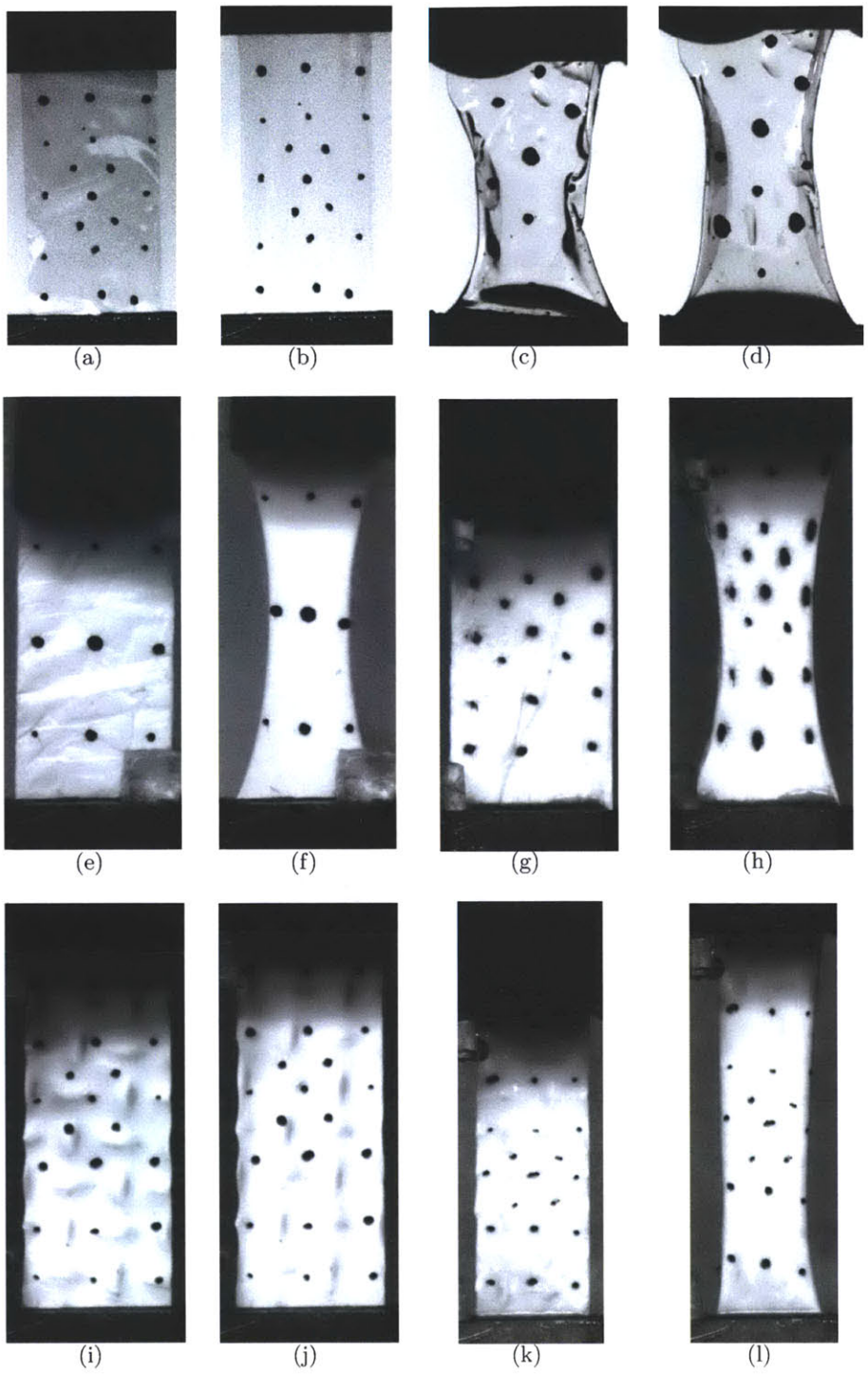

Figure 77: Video extensometer images of the composite and its component materials: (a)LBL film, dry, prior to deformation (b)LBL film, dry, just prior to fracture after uniaxial tension to a strain of 0.08 (c)LBL film, wet, prior to deformation (d) LBL film, wet, after uniaxial tension to a strain of 0.2, (e)EFM, dry, prior to deformation (f)EFM, dry, after uniaxial tension to a strain of 0.2, (g)EFM, wet, prior to deformation (h)EFM, wet, after uniaxial tension to a strain of 0.2, (i)composite, dry, prior to deformation (j)composite, dry, just prior to fracture after uniaxial tension to a strain of 0.02 (k)composite, wet, prior to deformation (l) composite, wet, after uniaxial tension to a strain of 0.2.

Table 4: Composite and component material properties.

Material Property	**Layer-by-Layer**	**Electrospun Fiber Mat**	**Composite**
E_{dry}	$1700MPa$	$81MPa$	$410MPa$
$\sigma_{y,dry}$	$36MPa$	$2.6MPa$	NA
E_{wet}	NA	$40MPa$	$64MPa$
$\sigma_{y,wet}$	$< 0.3MPa$	$1.4MPa$	$2.6MPa$

6 Polyamide electrospun fiber mat

6.1 Background

Electrostatic fiber formation or "electrospinning" is a robust method for creating non-woven mats of fibers from a wide variety of polymers. These fibers are continuous with diameters ranging from tens of microns down to tens of nanometers, resulting in low weight mats with high surface area and porosity (Pai et al., 2011). Hence, micro- and nano-fibrous mats provide an ideal mechanical scaffold for numerous applications either alone or as part of a composite membrane where a matrix can be used to impart other functionality. To design mats, an understanding of the relationship between the macroscopic mechanical behavior of the mat and the underlying single fiber behavior and mat network structure is required. A micromechanical model of the mat based on the mat microstructure and deformation mechanisms will provide insights and enable quantitative exploration of the composite design space. The aim of this work is to develop a predictive model for the mechanical behavior of randomly oriented non-woven fiber mats.

Micromechanically-based constitutive models of non-woven fibrous networks primarily focus on elastic behavior. Cox (1952) proposed a first model for the elastic modulus of paper based on the fiber network, assuming that all fibers extend from one end of the mat to the other and that the fibers stretch but do not bend. However, the relatively low bending stiffness of fibers and their random orientation make bending an important feature in many fibrous networks, particularly when there is no supporting medium (Petterson, 1959; Wu and Dzenis, 2005). Since a fiber network deforms cooperatively, a combination of stretching and bending of different fibers collectively accommodate the imposed deformation. Biopolymer network models (MacKintosh et al., 1995; Wilhelm and Frey, 2003; Palmer and Boyce, 2008), based on the concepts of rubber elasticity but addressing semiflexible molecules, have begun to address the contributions of fiber bending and stretching for nonlinear elastic behavior. This tradeoff between local axial stretching and bending deformation of the fibers will be important in the electrospun non-woven mats considered here. The mats are observed to exhibit elastic-plastic behavior. Micromechanical modeling efforts concerning the inelastic deformation of paper, while limited, do begin to provide insights into inelastic effects. Studies that used a microstructurally based approach found that it was necessary to assign a lower yield stress to the fibers under compression (Ramasubramanian and Perkins, 1988; Bronkhorst, 2003). The authors attributed this to a likely bending or buckling of the fibers, and in the case of Ramasubramanian and Perkins (1988), found that the reduced yield axial compression simplification was insufficient to capture the full material behavior with a single set of material parameters. Bronkhorst (2003) explicitly modeled discrete randomly generated networks composed of elastic-plastic fibers but found that neglecting the mutual constraint effect of the adjacent layers by using a single layer two-dimensional model caused a significant disparity with experimental results. In addition to micromechanical models, phenomenological continuum models have been developed which propose non-associative flow rules and non-quadratic yield surfaces (Figure 78) (Xia et al., 2002; Mäkelä and Östlund, 2003; Harrysson and Ristinmaa, 2008; Isaksson, 2010). Jearanaisilawong (2008) developed a microstructurally based continuum mechanical model for needlepunched nonwovens, describing the mechanical response of the network in terms of elastic fiber deformation and elastic and inelastic texture evolution (resisted by inter-fiber friction) related to the distribution of fiber realignment. Recently, non-wovens have been examined for energy absorption properties. There is a need for micromechanically based models which can capture the elastic-plastic deformation which precedes failure (Ridruejo et al., 2010, 2011).

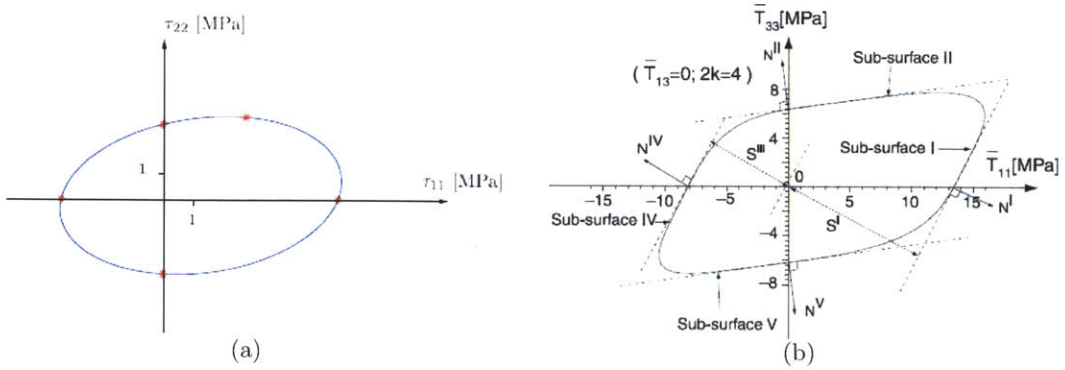

Figure 78: (a) Yield surface of corrugated cardboard from Harrysson and Ristinmaa (2008), and (b) yield surface of paperboard from Xia et al. (2002).

Here, experiments will first be conducted on an exemplar mat system. Amorphous polyamide is used as a model system due to its relative ease of processibility and the ability to form non-porous circular cross-section fibers of controllable diameter (Pai et al., 2011). The mat morphology is characterized with scanning electron microscopy (SEM) and porosimetry measurements. The mechanical properties of the mat and constituent single fibers are then measured under uniaxial tension. Video extensometry is key to characterizing the mat behavior, providing information about the axial and transverse strain during tension.

In the model proposed herein, the non-woven mat is idealized as a layered network using a representative volume element (RVE) approach. The random isotropic nature of the network structure is captured with a triangulated network; the layered nature is captured by layering RVEs of differing orientation. The fiber stress-strain behavior is modeled as elastic-plastic; an initial curvature of the fiber enables capturing the important effects of bending (unbending) and stretching. This approach enables a relatively straight forward microstructurally-based continuum-level model that maintains a strong connection to the mat microstructure and one which naturally captures plastic strain evolution. The predictive capability of the model will be assessed in comparison to tensile loading experiments under different constraints. This microstructurally-based and computationally inexpensive approach should allow for a broad application of the fiber network model.

6.2 Experimental Methods

6.2.1 Morphological Characterization

For morphological characterization by scanning electron microscopy (SEM) (VP438, Leo TM), fiber samples were mounted on an SEM compatible uniaxial tensile stage with open loop displacement control. The mat is cut into rectangular specimens $1mm$ wide and $10mm$ long with a razor guided by a straight edge for the uniaxial testing. The gage length is set to $5mm$. The SEM was operated in variable pressure mode using the back scatter detector. No metallic coating was used so as to avoid modifying the microstructural evolution mechanisms. A $20kV$ acceleration was used at a working distance of $20mm$.

Porosity was determined by finding the ratio of the measured mass of the specimen with the mass of a fully dense specimen of the same size by measuring the thickness (with constant force),

width, and length of the specimen. It has been found that this method gives similar results to a mercury porosimeter method developed by Rutledge et al. (2009).

6.2.2 Mechanical Characterization

Uniaxial tensile tests were conducted on both electrospun single fibers and the mat as a whole. Tensile testing of the single fibers was conducted at a constant engineering strain rate of $0.001s^{-1}$ on an MTS Nano Bionix universal tensile testing system. An initial gauge length of $15mm$ was used (Pai et al., 2009).

The mat was cut into rectangular specimens $10mm$ wide and $30mm$ long with a razor guided by a straight edge for uniaxial testing. The thickness of each specimen was determined from the average of 3 measurements with a Mitutoyo force-controllable micrometer. All tensile tests were conducted at a constant engineering strain rate of $0.01s^{-1}$ on a Bose Electroforce 3200 (ELF) with an initial grip-to-grip distance of $20mm$. Both axial and transverse strain were monitored with a Point Grey Grasshopper video extensometer and analyzed with the Vic2d software package from Correlated Solutions. The force-displacement data as taken from the ELF and the video extensometer, respectively, were reduced to true stress-true strain results. A membrane stress was used, neglecting changes in the thickness but accounting for changes in width. True stress is thus defined as the ratio of force to current (deformed) cross-sectional area (neglecting thickness changes) and true strain is defined as the natural logarithm of the ratio of current length to original length (length being the axial distance between video-imaged marks).

6.3 Experimental Results

6.3.1 Single Fiber

The results of the single fiber uniaxial tensile tests are shown in Figure 79. Each fiber was found to be elastic-plastic with significant post-yield strain hardening. Little variation was found in the elastic modulus among the fibers studied here, however the yield stress, post yield hardening slope, and break strain were found to vary significantly from fiber to fiber. The minimum, maximum, and average properties are given in Table 5. It was found that the strain rate dependence was far less than the fiber to fiber variation for a given strain rate (not shown).

Table 5: PA6(3)T electrospun single fiber mechanical properties.

Property	Average	Minimum	Maximum	Standard Deviation (%)
Elastic modulus (MPa)	4100	3000	5800	18
Yield stress (MPa)	86	63	140	28
Post-yield slope (MPa)	760	330	1600	45
Break strain	0.32	0.15	0.69	49

6.3.2 Mat characterization

SEM micrographs of the mat during uniaxial tensile testing show the mat morphology and its evolution with applied strain (Figure 80). The undeformed SEM image shows a randomly oriented network structure which indicates initial isotropy in the mat-plane. The average fiber diameter was found to be $1.2\mu m$ with average radius of curvature $210\mu m$, and the porosity was determined to

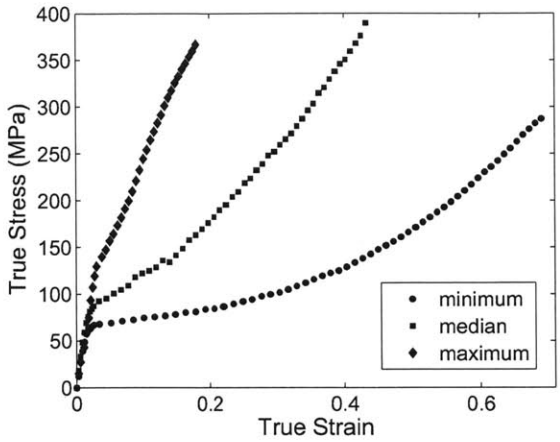

Figure 79: True stress-true strain characterization of single fibers of electrospun PA6(3)T.

be 0.89. The average distance between bonded junctions is estimated to be around $20\mu m$, however it is difficult to determine whether a point where fibers cross is a bonded junction. Three features of the microstructural deformation are readily apparent in the SEM images of the mat undergoing uniaxial tension: (1) the majority of the fibers align with the direction of applied strain, (2) fibers oriented transverse to the applied strain tend to bend, and (3) there is a significant densification of the mat.

The uniaxial tensile stress-strain behavior of the mat as a whole was found to be elastic-plastic with significant post-yield hardening (Figure 81a). There is some variation in the elastic modulus, yield stress, and post-yield strain hardening, though less than for the single fiber data. The elastic modulus and yield stress of the mat are respectively around 2% and 3% of those of the individual fibers (Table 6). Accurate reduction of the raw force-displacement behavior into true stress-true strain behavior requires both the axial and transverse strain data from the video extensometer. Furthermore, the specimen deformation is influenced by the grips and the effects with grip constrain and specimen aspect ratio are shown later in the paper. For the case of a specimen with length:width aspect ratio of 2, representative video extensometer images are shown in Figure 82 in the initial and deformed states, showing the influence of the grip constraint. While there appears to be a slight shear deformation, this in fact arises from the markers laying on a line at a slight angle from the horizontal line combined with the relatively large ratio of the magnitudes of transverse strain to axial strain acting to amplify this angle. The level of shear is small and will be neglected (shear strain is approximately 10% of the axial strain for all three strains shown here). The vertical and horizontal central axes of the specimen are used to determine the axial and transverse strain, respectively. Although the axial strain measurement extends into the region strongly influenced by the grip, it was found that the local axial strain measure is only weakly influenced by the grip region. The transverse contraction behavior shows the mat to exhibit a near zero elastic Poisson's ratio that may be either slightly positive or slightly negative, followed by a large transverse contraction beginning at an axial strain of 0.02 (ratio of negative transverse contraction to axial strain $> 1:1$) (Figure 81b). The transverse contraction suggests a consolidation of the fibrous structure.

The response of the mat to uniaxial cyclic (load-unload-reload) loading gives further insight into the deformation mechanisms (Figure 83). The stress-strain curve during unloading and reloading

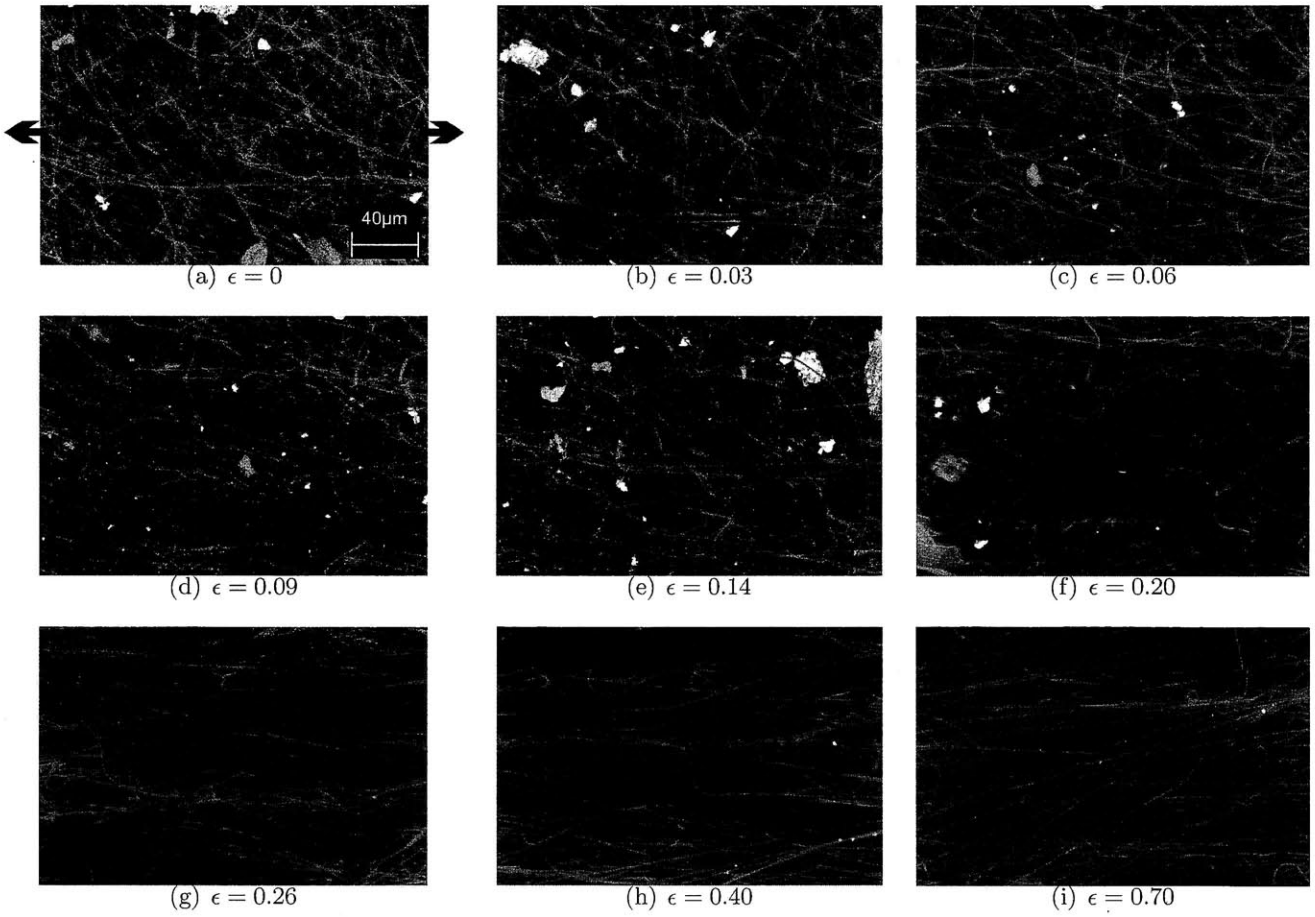

(a) $\epsilon = 0$ (b) $\epsilon = 0.03$ (c) $\epsilon = 0.06$

(d) $\epsilon = 0.09$ (e) $\epsilon = 0.14$ (f) $\epsilon = 0.20$

(g) $\epsilon = 0.26$ (h) $\epsilon = 0.40$ (i) $\epsilon = 0.70$

Figure 80: SEM images of electrospun PA6(3)T mat subjected to uniaxial tension in-situ. Approximate true strain is indicated below each image. Scale bar and strain direction indicated on (a) holds for all the images.

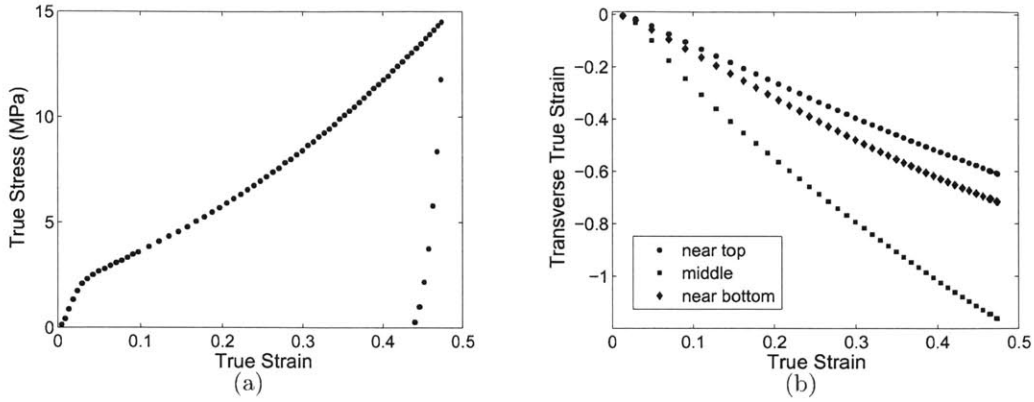

Figure 81: Uniaxial tensile characterization of electrospun PA6(3)T mat: (a)stress versus strain, (b)axial strain versus transverse strain from different locations on the specimen.

Table 6: PA6(3)T electrospun fibermat mechanical properties.

Property	**Average**	**Minimum**	**Maximum**	**Standard Deviation (%)**
Elastic modulus (MPa)	81	42	122	27
Yield stress (MPa)	2.6	1.3	3.9	30
Post-yield slope (MPa)	28	6.6	49	50

shows a near linear behavior until approaching zero stress, at which point there is a small rollover and reloading hysteresis. There is a sharp yield when the reloading curve meets the monotonic curve such that the cyclic stress-strain curve then follows the monotonic curve. One subtle but interesting feature is the continual increase in the unloading and reloading slopes with increasing strain (Figure 84). This increase in modulus with strain likely arises due to both the densification of the mat and the alignment of the fibers. The cyclic transverse strain is similar to the monotonic transverse strain with slight deviations due to plastic deformation.

6.4 Constitutive Model

A constitutive model for the elastic-plastic membrane stress-strain behavior of a randomly oriented two dimensional non-woven network is constructed based on the mechanical behavior of the constituent fibers, the fiber geometry, and the network connectivity. A representative volume element (RVE) of the network connectivity is constructed assuming a triangulated network structure. The layered and isotropic nature of the network geometry is approximated as layers of triangulated networks. The constituent fiber behavior is modeled as elastic-plastic based on single fiber experimental data, capturing both axial and bending deformation during end-to-end axial loading. The constitutive model development is then based on balancing the work needed to deform the network with the internal energy storage and dissipation mechanisms of the structure during deformation.

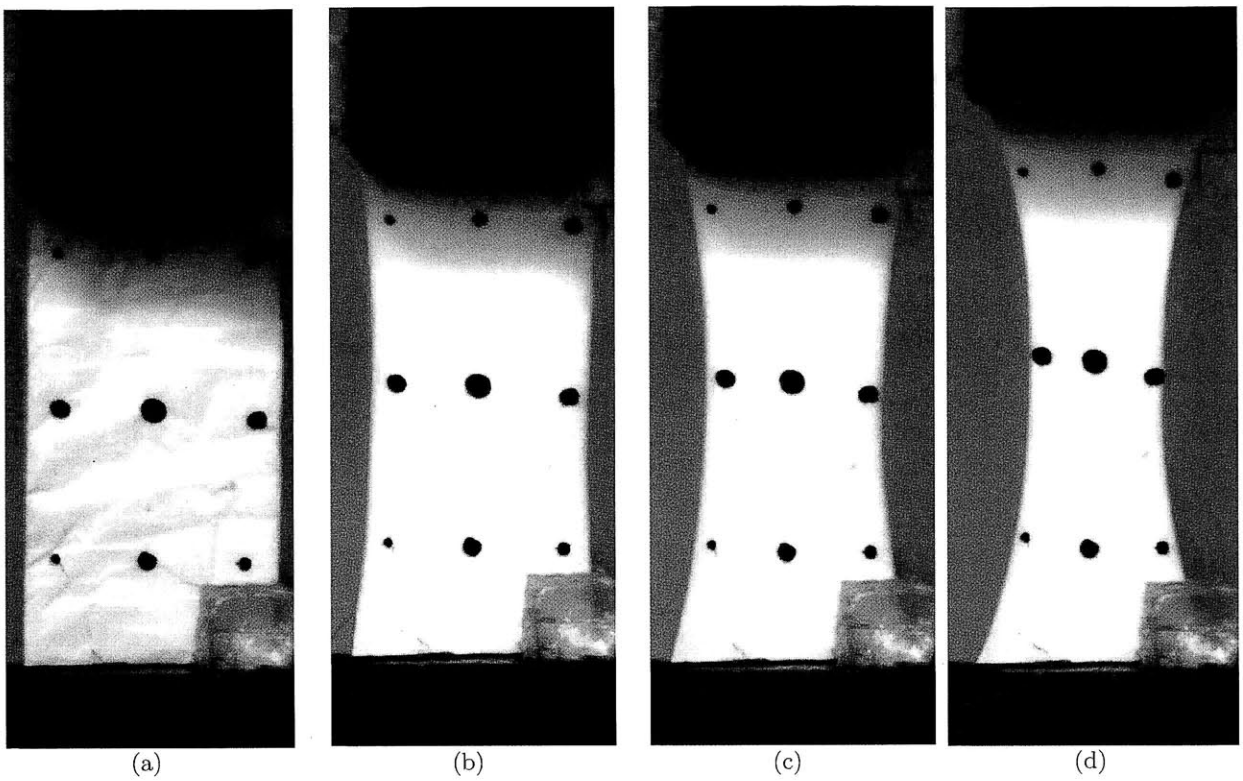

Figure 82: Video extensometer images of electrospun PA6(3)T mat: (a)prior to deformation; after uniaxial tension to a strain of (b) 0.05 (c) 0.1 (d) 0.2.

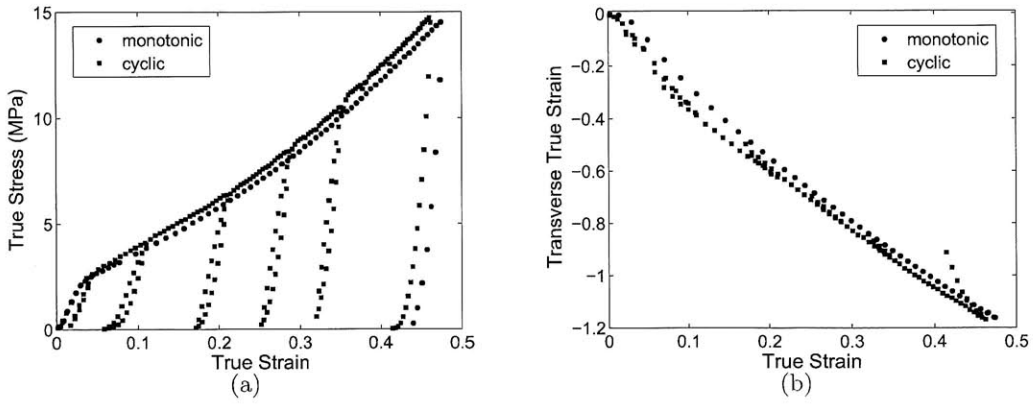

Figure 83: Cyclic uniaxial tensile characterization of electrospun PA6(3)T mat: (a)stress versus strain, (b)axial strain versus transverse strain.

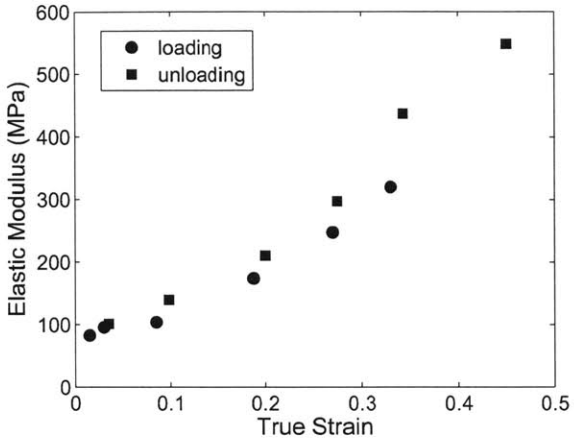

Figure 84: Evolution of elastic modulus for unloading and reloading during cyclic uniaxial testing of PA6(3)T mat.

6.4.1 Thermodynamic Framework

The constitutive model for the elastic-plastic material is derived beginning with a thermodynamic or strain energy based framework. Here we follow a notation close to that presented in Holzapfel (2000) and consider an isothermal condition.

The Helmholtz free energy per unit reference volume ψ is expressed as a function of the deformation gradient $\mathbf{F}$ and internal state variables ξ_i:

$$\psi = \hat{\psi}\left(\mathbf{F}, \xi_1, \xi_2, ...\right) \tag{90}$$

where $\mathbf{F} = \frac{\partial \mathbf{x}}{\partial \mathbf{X}}$, $\mathbf{X}$ is the original position, $\mathbf{x}$ is the deformed position, and the ξ_i represent aspects of the microstructural state such as plastic stretch and the curvature of fibers. The second law gives:

$$\left(\mathbf{T}_o : \dot{\mathbf{F}} - \frac{\partial \psi}{\partial \mathbf{F}} : \dot{\mathbf{F}}\right) - \sum_i \frac{\partial \psi}{\partial \xi_i} : \dot{\xi}_i \geq 0 \tag{91}$$

which gives the first Piola-Kirchoff stress $\mathbf{T}_o$ to be:

$$\mathbf{T}_o = \frac{\partial \psi}{\partial \mathbf{F}} \tag{92}$$

The Cauchy (true) stress is then given by:

$$\mathbf{T} = \frac{1}{J} \frac{\partial \psi}{\partial \mathbf{F}} \mathbf{F}^{\mathsf{T}} \tag{93}$$

where $J = \det \mathbf{F}$ is the surface area ratio ($A_{deformed} : A_{original}$) for the two dimensional membrane (where we do not account for thickness change).

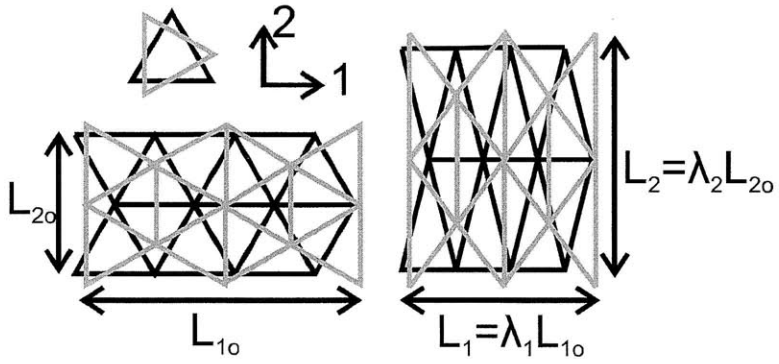

Figure 85: Conceptual schematic of a double layer triangulated network model: undeformed isolated triangles (top left), undeformed double layer network (bottom left), deformed double layer network (right).

6.4.2 Representative Volume Element

A triangulated network model is proposed to represent the network of fibers that constitute the non-woven mat. The mat structure is approximated to consist of bonded layers of planar triangulated networks. Each member of a representative triangle is taken to exhibit the behavior of a single fiber.

Kinematics:

An equilateral triangle geometry is chosen for the representative volume element (RVE) both for simplicity and initial elastic isotropy. Due to the triangulated structure, the mapping of the macroscopic deformation of the mat to the microscopic deformation (i.e. to the deformation of the individual fibers within the RVE) is dictated simply by kinematics. This results in a direct relation between the end-to-end extension of each of the constituent fibers in the triangle and the applied macroscale deformation gradient.

An equilateral triangle with members of initial end-to-end length l_o (where l_o is the distance between fiber-fiber junctions) composes the RVE. For a single layer triangle RVE with one member aligned with the horizontal (1-direction) axis, the axial stretch on each member (${}^i\lambda$; $i = A, B, C$) is kinematically determined in terms of the membrane deformation gradient F_{ij} (Arslan and Boyce, 2006).

$$ {}^A\lambda = \frac{1}{2}\left[\left(F_{11} - F_{12}\sqrt{3}\right)^2 + \left(F_{21} - F_{22}\sqrt{3}\right)^2\right]^{\frac{1}{2}} \tag{94} $$

$$ {}^B\lambda = \frac{1}{2}\left[\left(F_{11} + F_{12}\sqrt{3}\right)^2 + \left(F_{21} + F_{22}\sqrt{3}\right)^2\right]^{\frac{1}{2}} \tag{95} $$

$$ {}^C\lambda = \left(F_{11}^2 + F_{21}^2\right)^{\frac{1}{2}} \tag{96} $$

where the left superscripts A, B, and C refer to the three members of the triangle and C is the member aligned with the 1-axis (for initial orientation defined as 0^o, Figure 86).

The multilayer nature of the mat is captured by adding a second triangulated layer at a different orientation. The second layer of triangles captures the multilayer mutual constraint effect in the

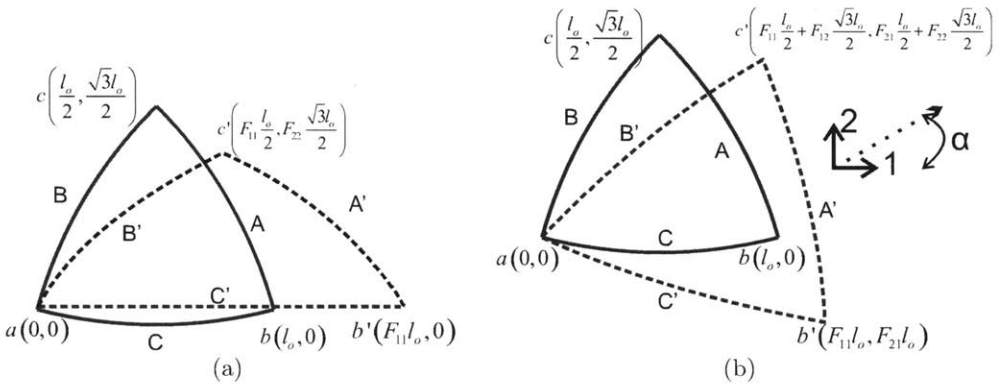

Figure 86: Schematic of repeat unit of single triangle model: (a)subjected to 1-direction extension and 2-direction contraction, (b)under arbitrary deformation.

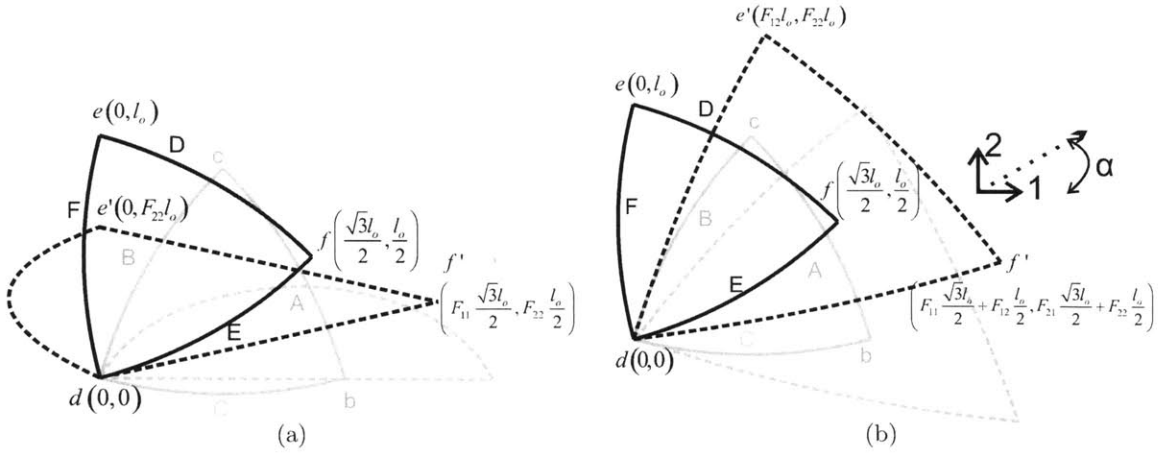

Figure 87: Schematic of repeat unit of double triangle model: (a)subjected to 1-direction extension and 2-direction contraction, (b) under arbitrary deformation.

electrospun mat. The two triangles stretch according to the same deformation gradient. The specific kinematics are shown for the superposition of two triangles with the second triangle rotated 30° counterclockwise from the first (Figure 87). The stretch of each member of the second triangle in terms of F_{ij} is given by:

$$^{D}\lambda = \frac{1}{2}\left[\left(F_{11}\sqrt{3} - F_{12}\right)^2 + \left(F_{21}\sqrt{3} - F_{22}\right)^2\right]^{\frac{1}{2}} \tag{97}$$

$$^{E}\lambda = \frac{1}{2}\left[\left(F_{11}\sqrt{3} + F_{12}\right)^2 + \left(F_{21}\sqrt{3} + F_{22}\right)^2\right]^{\frac{1}{2}} \tag{98}$$

$$^{F}\lambda = \left(F_{12}^2 + F_{22}^2\right)^{\frac{1}{2}} \tag{99}$$

where the left superscripts D, E, and F refer to the three members of the second triangle.

The behavior for the cases of a single layer of triangles and a double layer of triangles in tension at different orientations will be examined. As will be discussed in Section 6.6, for the double layer cases, the layers do impose mutual constraints to satisfy equilibrium which, in turn, affect the deformation gradient for a given membrane stress state.

Mat strain energy:

The strain energy density of the mat (ψ) is the sum of the strain energies of the triangle members ($^{i}\Psi$) scaled by the member number density.

$$\psi = \frac{\nu}{6}\sum_{i=A\ldots F} {}^{i}\Psi \tag{100}$$

where ν is the number density of members (number of fiber segments per unit volume). Expressions for the member elastic strain energy will be provided later as a function of member stretch $^{i}\lambda$ and internal state variables.

The membrane Cauchy stress can now be specified as:

$$\mathbf{T} = \frac{\nu}{6J}\sum_{i=A\ldots F} \frac{\partial\left({}^{i}\Psi\right)}{\partial\left({}^{i}\lambda\right)}\frac{\partial\left({}^{i}\lambda\right)}{\partial\mathbf{F}}\mathbf{F}^{\mathsf{T}} \tag{101}$$

Recognizing that the force (^{i}f) on a member is:

$${}^{i}f = \frac{1}{l_o}\frac{\partial\left({}^{i}\Psi\right)}{\partial\left({}^{i}\lambda\right)} \tag{102}$$

the stress can then be written as:

$$\mathbf{T} = \frac{\nu l_o}{6J}\sum_{i=A\ldots F} {}^{i}f\frac{\partial\left({}^{i}\lambda\right)}{\partial\mathbf{F}}\mathbf{F}^{\mathsf{T}} \tag{103}$$

Therefore, to obtain the mat stress-strain behavior, the fiber force ^{i}f is needed as a function of fiber stretch $^{i}\lambda$.

6.5 Single Fiber Constitutive Model

An expression for the elastic-plastic force-stretch behavior of a single fiber is required in order to determine the behavior of the mat. The fibers are modeled in two ways: (1) fibers are taken to be initially straight and to remain straight with deformation, and (2) fibers are taken to possess a small initial curvature such that they undergo a combination of bending and stretching when subjected to end axial loads.

6.5.1 Straight Fibers

Kinematics: For simplicity, the fibers are first assumed to be initially straight and deform by axial extension or contraction. Each member is assumed to have an initial end-to-end distance l_o which corresponds to the distance between fiber-fiber junctions. The total fiber stretch is defined as ${}^i\lambda = {}^il/l_o$, where ${}^il$ is the current end-to-end distance of fiber i. The axial stretch of the fiber is accommodated by elastic and plastic deformation as captured through the Kroner-Lee decomposition:

$$ {}^i\lambda = {}^i\lambda^e\left({}^i\lambda^p\right) \tag{104} $$

where ${}^i\lambda^e$ is the elastic stretch and ${}^i\lambda^p$ is the plastic stretch on fiber i.

The corresponding rate kinematics are described by the velocity gradient ${}^iD = {}^i\dot{\lambda}\left({}^i\lambda\right)^{-1}$ which can be decomposed into elastic and plastic contributions:

$$ {}^iD = {}^iD^e + {}^iD^p \tag{105} $$

where ${}^iD^e = {}^i\dot{\lambda}^e\left({}^i\lambda^e\right)^{-1}$ is the elastic velocity gradient and ${}^iD^p = {}^i\dot{\lambda}^p\left({}^i\lambda^p\right)^{-1}$ is the plastic velocity gradient. ${}^iD^p$ will be constitutively prescribed later.

Constitutive: A simple one dimensional elastic-plastic model is used for the fiber behavior. The member elastic strain energy ${}^i\Psi$ due to axial stretching is given a Hookean-like definition:

$$ {}^i\Psi = \frac{1}{2}E\pi r_o^2 l_o\left({}^i\lambda^e - 1\right)^2 \tag{106} $$

where the fiber is assumed to be incompressible ($r_o l_o = {}^ir^il$), r_o is the initial fiber radius, and ${}^ir$ is the current fiber radius. The resulting fiber force is given by:

$$ {}^if = \frac{\partial\left({}^i\Psi\right)}{\partial\left({}^il\right)} = \frac{E\pi r_o^2}{{}^i\lambda^p}\left({}^i\lambda^e - 1\right) \tag{107} $$

The elastic stretch ${}^i\lambda^e$ is found by ${}^i\lambda^e = {}^i\lambda/{}^i\lambda^p$. To obtain ${}^i\lambda^p$, the rate of plastic stretching ${}^iD^p$ is needed. ${}^iD^p$ is constitutively prescribed to follow a rate dependent process driven by the axial stress:

$$ {}^iD^p = \dot{\epsilon}^o \sinh\left[\frac{{}^i\sigma}{{}^is}\right] \tag{108} $$

where ${}^i\sigma = {}^if/\left(\pi\left({}^ir\right)^2\right)$ is the axial Cauchy stress, ${}^ir = r_o/\sqrt{{}^i\lambda}$ is the current fiber radius, $\dot{\epsilon}^o$ is a pre-exponential coefficient, and ${}^is$ is the resistance to yield. To capture the observed post-yield strain hardening, the resistance ${}^is$ is assumed to increase with plastic stretch such that

$$^{i}s = s_o\left(^{i}\lambda^{p}\right)^{n} \tag{109}$$

where s_o is the initial value and n is the strain hardening exponent. $^{i}\lambda^{p}$ is then obtained by integrating $^{i}\dot{\lambda}^{p} = {}^{i}D^{p}\left(^{i}\lambda^{p}\right)$.

6.5.2 Curved Fibers

The fibers in a mat typically possess an initial curvature. The change in the end-to-end length of a fiber is hence accommodated by a combination of fiber bending (or unbending) and fiber stretching (where stretching corresponds to changes in the contour length of the fiber). For the case under consideration here, the initial curvature is slight and has negligible impact on the fiber end-to-end tensile behavior (i.e. the elastic-plastic model for the straight fiber model still applies for fiber extension) and negligible effect on the initial slope during end-to-end compression. However, as the fiber end-to-end distance is further decreased during compression, the force response becomes increasingly compliant as the section bending moment within the fiber increases and the change in end-to-end fiber length in compression becomes dominated by fiber bending. Fiber bending will be large enough that elastic-plastic bending must be taken into account during compression. The elastic-plastic extension-compression behavior of a curved fiber is shown in Figure 88 as captured using a finite element model. The fiber is given a slight initial curvature ($\rho_o/l_o = 10.6$, where ρ_o is the initial radius of curvature) and is assigned elastic-plastic behavior with moderate strain hardening as seen in the single fiber data. Figure 88 contrasts the initially curved elastic-plastic fiber with an initially curved elastic fiber and a straight elastic-plastic fiber. As indicated earlier, the behavior in tension is essentially the same for the initially curved fiber as for the straight fiber. In compression however, the initially curved behavior deviates significantly from the straight fiber as it is compressed. First examining the elastic curved fiber, it is evident that the force-stretch response rolls over at an order of magnitude lower stress than the straight fiber yield stress (Figure 88b). The effective fiber response hardens slightly due to the competing influences of the increasing bending energy and structural softening due to the increasing moment arm. When plasticity is incorporated into the fiber constitutive behavior the rollover upon compression is unaffected since it is an elastic phenomenon. Plasticity acts to reduce the effective fiber-stretch hardening slope. While this change in slope is subtle, it is important to include as plastic deformation due to the fiber behavior upon unloading. This difference in load-unload compressive behavior will be critical to model cyclic mat behavior. A simplified mathematical representation of this fiber behavior is presented below for use in the mat network model.

For the behavior under compression when completely elastic, the force versus end-to-end behavior is essentially an Euler-elastica formulation (albeit in compression) which can be approximated by a piecewise polynomial for the purposes of simplicity and to provide an analytical expression for use in the overall mat constitutive model:

$$^{i}f = \begin{cases} A_2\left(^{i}\lambda^{b}\right)^{2} + B_2\,{}^{i}\lambda^{b} + C_2, & \text{when } {}^{i}\lambda^{*} \leq {}^{i}\lambda^{b}; \\ A_3\,{}^{i}\lambda^{b} + B_3, & \text{when } {}^{i}\lambda^{b} < {}^{i}\lambda^{*}. \end{cases} \tag{110}$$

where $^{i}\lambda^{b}$ is the bending stretch (corresponding to a change in end-to-end length without a change in contour length) of fiber i; A_2 and A_3 are material properties defining the elastic fiber bending force response; and B_2, B_3, C_2, and $^{i}\lambda^{*}$ uniquely satisfy continuity requirements in the force-stretch

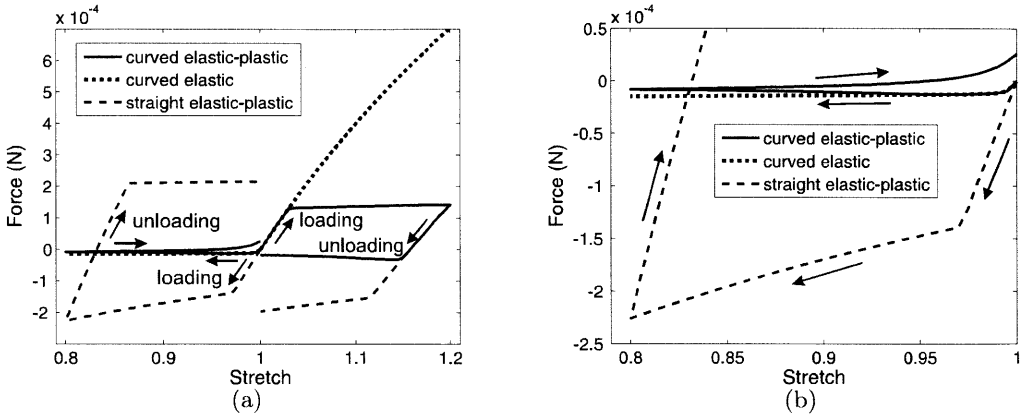

Figure 88: Fiber force-stretch behavior as determined via an explicit finite element simulation of the fiber using realistic elastic-plastic properties, curvature, and geometry: (a)load-unload behavior in both tension and compression, (b)zoomed in on load-unload behavior under compressive axial force.

behavior. The bending stretch is constrained to be compressive (${}^i\lambda^b \leq 1$) in accordance with the aforementioned small initial curvature assumption.

The fiber is also capable of undergoing plastic deformation under compression. In this case the bending stretch is decomposed into elastic and plastic contributions:

$$ {}^i\lambda^b = {}^i\lambda^{b,e}\left({}^i\lambda^{b,p}\right) \tag{111} $$

where ${}^i\lambda^{b,e}$ and ${}^i\lambda^{b,p}$ are the elastic and plastic bending stretch on the fiber respectively.

The corresponding bending rate kinematics, which are required to describe the plastic evolution, are described by the velocity gradient ${}^iD^b = {}^i\dot{\lambda}^b\left({}^i\lambda^b\right)^{-1}$ which can be decomposed into elastic and plastic contributions:

$$ {}^iD^b = {}^iD^{b,e} + {}^iD^{b,p} \tag{112} $$

where ${}^iD^{b,e} = {}^i\dot{\lambda}^{b,e}\left({}^i\lambda^{b,e}\right)^{-1}$ is the elastic velocity gradient and ${}^iD^{b,p} = {}^i\dot{\lambda}^{b,p}\left({}^i\lambda^{b,p}\right)^{-1}$ is the plastic velocity gradient.

${}^iD^{b,p}$ is constitutively prescribed similarly to the axial stretching plasticity to follow a rate dependent process driven by the axial compressive stress:

$$ {}^iD^{b,p} = \dot{\epsilon}^o \sinh\left[\frac{-{}^i\sigma}{{}^is^b}\right] \tag{113} $$

where ${}^i\sigma = {}^if/\left(\pi r_o^2\right)$ is the axial Cauchy (tensile) stress, the fiber radius r_o is approximated to remain constant, $\dot{\epsilon}^o$ is a pre-exponential factor proportional to the attempt frequency, and ${}^is^b$ is the resistance to yield in bending. The pre-exponential factor is the same as that used for the axial plasticity, but the resistance to yield will be different since this plasticity occurs due to a combination of the axial load and the fiber curvature. To capture the post-yield strain hardening, the resistance ${}^is^b$ is assumed to increase with plastic stretch such that

$$ {}^{i}s^{b} = s_o^b \left({}^{i}\lambda^{b,p} \right)^{n_b} \tag{114} $$

where s_o^b is the initial value and n_b is the strain hardening exponent. ${}^{i}\lambda^{b,p}$ is then obtained by integrating ${}^{i}\dot{\lambda}^{b,p} = {}^{i}D^{b,p}\left({}^{i}\lambda^{b,p}\right)$.

Summary of curved fiber equations:

The end-to-end fiber stretch, ${}^{i}\lambda$, is decomposed into bending, ${}^{i}\lambda^{b}$, and axial stretching, ${}^{i}\lambda^{a}$ (change in contour length) contributions:

$$ {}^{i}\lambda = {}^{i}\lambda^{b}\left({}^{i}\lambda^{a}\right) \tag{115} $$

Each of these is further decomposed into elastic and plastic contributions.

$$ {}^{i}\lambda^{b} = {}^{i}\lambda^{b,e}\left({}^{i}\lambda^{b,p}\right) \tag{116} $$

$$ {}^{i}\lambda^{a} = {}^{i}\lambda^{a,e}\left({}^{i}\lambda^{a,p}\right) \tag{117} $$

where ${}^{i}\lambda^{b,e}$ is the elastic bending stretch, ${}^{i}\lambda^{b,p}$ is the plastic bending stretch, ${}^{i}\lambda^{a,e}$ is the elastic axial stretch and ${}^{i}\lambda^{a,p}$ is the plastic axial stretch.

As part of the analytical simplification of the fiber behavior the following constraints are imposed:

$$ {}^{i}\lambda^{b,e} \leq 1 \tag{118} $$

$$ {}^{i}\lambda^{a,e} \geq 1 \tag{119} $$

$$ {}^{i}\lambda^{b,e} \bigvee {}^{i}\lambda^{a,e} = 1 \tag{120} $$

This simplifies the formulation for operational purposes without losing the dominant behaviors.

The rate kinematics are described by the velocity gradient ${}^{i}D = {}^{i}\dot{\lambda}\left({}^{i}\lambda\right)^{-1}$ which can be decomposed into elastic and plastic bending and axial contributions:

$$ {}^{i}D = {}^{i}D^{b,e} + {}^{i}D^{b,p} + {}^{i}D^{a,e} + {}^{i}D^{a,p} \tag{121} $$

${}^{i}D^{b,p}$ and ${}^{i}D^{a,p}$ are required to update the bending and axial plastic stretches, respectively, and are constitutively prescribed by:

$$ {}^{i}D^{b,p} = \dot{\epsilon}^{o} \sinh\left[\frac{-{}^{i}\sigma}{{}^{i}s^{b}}\right] \tag{122} $$

$$ {}^{i}D^{a,p} = \dot{\epsilon}^{o} \sinh\left[\frac{{}^{i}\sigma}{{}^{i}s}\right] \tag{123} $$

$$ {}^{i}s^{b} = s_o^b \left({}^{i}\lambda^{b,p} \right)^{n_b} \tag{124} $$

$$ {}^{i}s = s_o \left({}^{i}\lambda^{a,p} \right)^{n} \tag{125} $$

Table 7: Model parameters used to fit the range of single fiber data.

Data Set	$\dot{\epsilon}_o$ (s^{-1})	s_o (MPa)	n
median	$9.91 \times 10^{18} s^{-1}$	6.0	4.3
minimum	$9.91 \times 10^{18} s^{-1}$	4.3	1.5
maximum	$9.91 \times 10^{18} s^{-1}$	8.9	12

where ${}^i\sigma = {}^if / \left(\pi \left({}^ir\right)^2\right)$ is the axial Cauchy stress; ${}^ir = r_o/\sqrt{{}^i\lambda^a}$ is the current fiber radius; $\dot{\epsilon}^o$ is a pre-exponential factor proportional to the attempt frequency; ${}^is^b$ and ${}^is$ are the resistance to yield in bending and axial deformation; s_o^b and s_o, n^b and n are the initial values and strain hardening exponents associated with ${}^is^b$ and ${}^is$ respectively. ${}^i\lambda^{b,p}$ is obtained by integrating ${}^i\dot{\lambda}^{b,p} = D^{b,p}\left({}^i\lambda^{b,p}\right)$. ${}^i\lambda^{a,p}$ is obtained by integrating ${}^i\dot{\lambda}^{a,p} = {}^iD^{a,p}\left({}^i\lambda^{a,p}\right)$.

The fiber force is then obtained by:

$$ {}^if = \begin{cases} \frac{E\pi r_o^2}{{}^i\lambda^{a,p}}\left({}^i\lambda^{a,e} - 1\right), & \text{when } {}^i\lambda^{a,e} \geq 1; \\ A_2\left({}^i\lambda^{b,e}\right)^2 + B_2{}^i\lambda^{b,e} + C_2, & \text{when } {}^i\lambda^* \leq {}^i\lambda^{b,e} < 1; \\ A_3{}^i\lambda^{b,e} + B_3, & \text{when } {}^i\lambda^{b,e} < {}^i\lambda^*. \end{cases} \tag{126} $$

6.5.3 Fiber material parameter determination

The parameters required to define the fiber tensile behavior are the elastic modulus (E) and the material properties governing plasticity ($\dot{\epsilon}_o$,s_o,n) where $\dot{\epsilon}_o$ and s set the rate dependent yield stress, n assigns the post-yield strain hardening. The elastic modulus is set to the average single fiber elastic modulus. The fiber plasticity properties are fit to the minimum, maximum, and median single fiber data (Figure 89, Table 7). It will be shown that fiber behavior near the maximum is required for a good prediction of the mat model assuming straight fibers whereas fiber behavior near the median is required for the mat model assuming initially curved fibers.

There are four parameters required to define the fiber behavior under compression: A_2 and A_3 which determine the elastic behavior, and s_o^b and n_b which determine the plastic behavior. These four parameters are fit according to the transverse strain behavior under cyclic tensile loading as will be shown in Section 6.6.3. A_2 and s_o^b determine the behavior at strains less than ~ 0.05; A_3 and n_b determine the behavior at strains greater than ~ 0.05. An increase in A_2 or a decrease in A_3 results in a decrease in the fiber force-stretch response and consequently an increase in mat transverse strain. An increase in s_o^b or n_b results in a decrease in fiber plasticity thereby increasing the fiber force-stretch response and decreasing mat transverse strain. B_2, B_3, C_2, and ${}^i\lambda^{tr,e}$ uniquely satisfy continuity requirements in the force-stretch behavior; both the slopes and the force values of the three part force-stretch polynomial must match at the transition between the different regions. The fiber behavior that is used in the model that includes initially curved fibers is shown in Figure 89. The fully elastic bent fiber and straight fiber behaviors are also shown for comparison. Note that while there area a number of property parameters required for the fiber elastic-plastic bending model, the behavior is simply one of elastic-plastic bending and the parameters facilitate an analytical description.

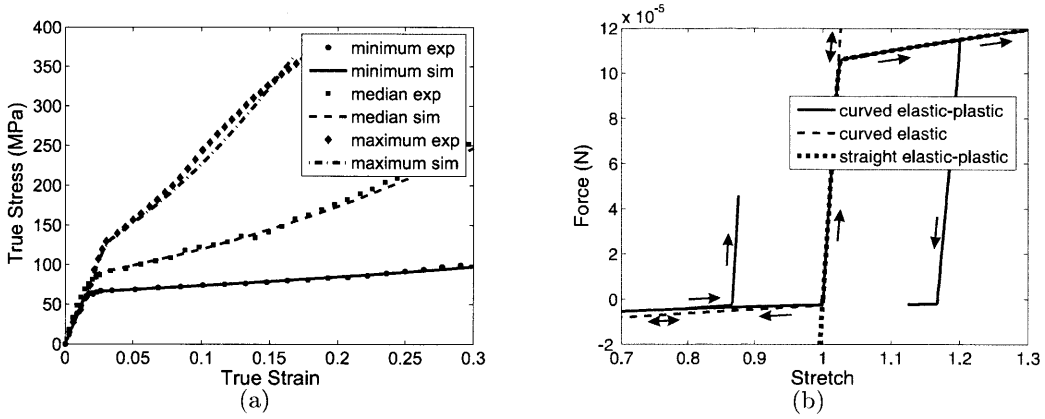

Figure 89: Model of fiber force-stretch behavior: (a)tensile fiber model behavior compared to experimental data, (b)comparison of straight, curved, and elastic curved fibers.

6.5.4 Hydration dependence

Hydration is taken to scale the fiber force-stretch response. Specifically it will reduce the elastic modulus and yield stress of the fiber, this will then naturally result in changes in the force-stretch response under bending as given by the continuity requirements described in the previous section.

$$E = E_{dry} - (E_{dry} - E_{wet})\,\phi \tag{127}$$

$$s_o = s_{o,dry} - (s_{o,dry} - s_{o,wet})\,\phi \tag{128}$$

where ϕ is a scalar representing the water content. It is taken that $\phi = 0$ under ambient conditions ($30\%RH$) and $\phi = 1$ when the mat is in water. E_{dry} and $s_{o,dry}$ correspond to the elastic modulus and yield, respectively, measured in the single fiber tensile testing. E_{wet} and $s_{o,wet}$ are then determined by fitting the hydrated mat model to the elastic modulus and yield respectively, of the in water experiment.

6.6 Results and discussion

The contribution of various features of the model on the predicted stress-strain behavior of the mat will be presented in stages, including the effects of RVE orientation and layering, and the effects of fiber stretching and bending. Specifically, model results will be shown for the following cases: 1) a single layer triangle RVE with straight members; 2) a double layer triangle RVE with straight members; and 3) a double layer triangle RVE with initially curved members. Results are mostly shown for "homogeneous" mats where the triangulated structure is uniform. However, it will be shown that a distribution of triangle orientation within a layer has a modest effect on the results. Also the geometry of the tensile specimen influences the behavior, therefore the constraint associated with different specimen aspect ratios will be examined to validate the predictive capability of the model. Results will be presented for tensile strains up to 0.2; at this strain distributed fiber failure begins to have a noticeable effect on the mat behavior. The model is then applied to predict the dependence of stress-strain and transverse strain on fiber geometry and mat network structure.

6.6.1 Single layer triangle RVE with straight members

A single layer equilateral triangle RVE exhibits initial isotropic elasticity and captures aspects of the cooperative deformation of the fibers to accommodate the applied macroscopic deformation. The material parameters required for this model are the fiber geometry (r_o,l_o), the single fiber elastic (E) and yield/post-yield ($\dot{\epsilon}_o$,s,n) properties, and the number density of fibers (ν). The fiber geometry is taken as average values directly from the SEM images. The fiber constitutive properties are set to just below the maximum fiber behavior as this is needed to achieve the appropriate mat strain hardening (Figure 90d). Ideally, the fiber number density should be related to the mat porosity via the volume occupied by the fibers in the RVE:

$$\nu_{theory} = \frac{1-\varphi}{\pi r_o^2 l_o} \tag{129}$$

where φ is the porosity. For this version of the model a $\nu = 0.54\nu_{theory}$ ($2.22 \times 10^{15} m^{-2}$ versus $4.86 \times 10^{15} m^{-2}$) was found to fit the modulus of the mat to the experimental data. The fact that the ν needed to capture the mat modulus is of the order of the ν approximated by the porosity measurement suggests that the most significant features of the mat structure are captured. The parameters used to fit the single layer triangle RVE model are given in Table 8.

The uniaxial stress-strain response of the mat captured by the single layer triangle RVE is shown in Figure 90a for tension at different angles relative to the triangle orientation. This simplified model of a single layer RVE of straight elastic-plastic fibers is able to capture the elastic-plastic nature of the mat network. The elastic response, is seen to be independent of the angle at which uniaxial tension is applied due to the symmetry of the equilateral triangle RVE. The yield and post-yield behavior depends on the orientation of the applied tension since the mat yield point is governed by the first yielding of fibers in the triangulated network and the occurrence of fiber yield depends on the fiber orientation with respect to the applied tension(Figure 90a,c). The evolution of strain and force of each member is shown for 0^o and 30^o loading directions in Figure 90c. In the case of macroscopic tension applied at 0^o, member C is aligned with the tensile axis and is directly axially strained whereas members A and B primarily rotate to accommodate the imposed tension and hence experience negligible strain. The impact of the rotation of A and B is evident in the macroscopic transverse strain behavior (Figure 90b) for the 0^o loading which shows a transverse contraction. Macroscopic tensile loading at 30^o extends members B and C (Figure 90c) and contracts member A. The need to compress member A to give transverse strain results in less transverse strain for the 30^o loading as compared to the 0^o loading (Figure 90b). Although the model captures the occurrence of transverse strain in the mat during uniaxial tension, the amount of transverse strain is significantly under predicted in comparison to the experimental data.

The single layer triangle RVE of straight fibers nominally captures the salient features of the elastic-plastic axial stress-strain behavior. However, it is apparent from the comparison of the single layer triangle RVE model with experiments that there are three major discrepancies between the model and experiments: the model predicts a slight anisotropic yield and post-yield behavior; the model predicts a constant slope for the transverse contraction ratio; and the model under predicts the post-yield transverse strain.

In order to capture the observed isotropy of the yield and post-yield behavior, the initial heterogeneous distributed nature of the triangle orientations should be taken into account. This is done here using a finite element discretization of the membrane where the material behavior of each element is provided by the constitutive model of the triangulated network. The elements are

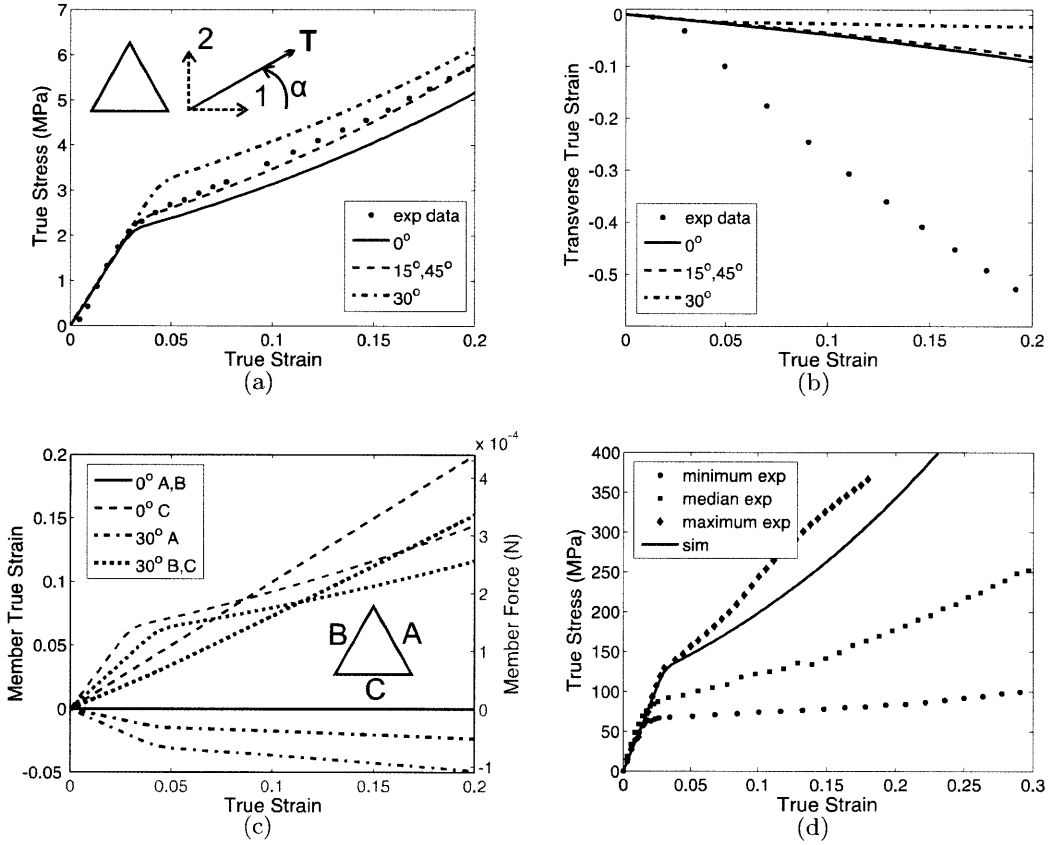

Figure 90: Deformation of the straight member single layer triangle RVE model subjected to uniaxial tension: (a)stress-strain behavior as a function of angle α from the 1-direction, (b)transverse strain versus axial strain as a function of angle α from the 1-direction, (c)strain(black) and force(grey) of each member of the triangle versus strain as a function of angle α from the 1-direction, (d)single fiber tensile fit used in model compared to the single fiber experimental data.

Table 8: Material parameters used to match the straight leg single and double layer triangle RVE model to experimental data.

Model Component	**Material Parameter**	**Value**
Fiber properties	E	$4100MPa$
	$\dot{\epsilon}_o$	$9.9 \times 10^{18} s^{-1}$
	s_o	$8.9MPa$
	n	8.0
Mat geometry	r_o	$6 \times 10^{-7} m$
	l_o	$2 \times 10^{-5} m$
	ν	$2.2 \times 10^{15} m^{-2}$

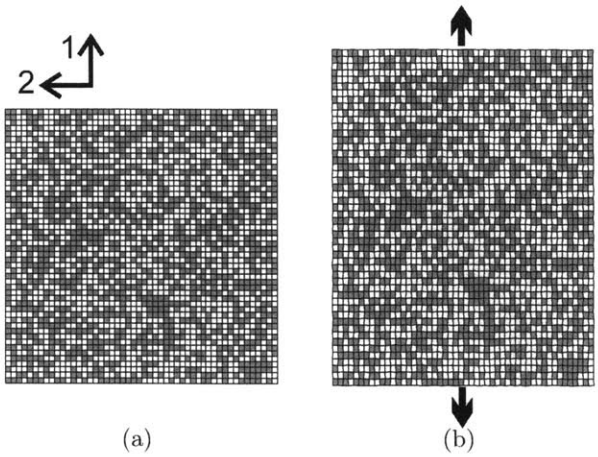

Figure 91: Mesh and geometry used for multi-orientation finite element simulations with periodic boundary conditions of single layer triangle RVE with straight members. (a)Initial, (b)20% strain when initial RVE orientations randomly assigned to 0^o and 30^o (an intermediate behavior). Grey and white indicate different initial RVE orientations.

randomly assigned one of two initial triangle orientations (Figure 91a). The very modest amount of transverse strain predicted by the model is evident in the membrane deformed to 20% axial strain (Figure 91b). Figure 92 shows the corresponding stress-strain and transverse strain response. The simulations with two initial orientations exhibit a yield stress, post-yield hardening, and transverse strain behavior which lies between the behavior for the 0^o and the 30^o orientation behavior. The variation among the responses of these multi-orientation simulations is reduced from that of the single orientation simulations. The presence of two orientations promotes cooperative deformation among adjacent elements so that they are better able to rotate to accommodate the applied deformation. The inclusion of additional initial orientations only improves the isotropy slightly (not shown). Accounting for a distribution of orientations is fairly effective in capturing isotropy, but still fails to capture the level of transverse strain seen in the experiments, indicating that additional features and mechanisms must be taken into account.

6.6.2 Double layer triangle RVE with straight members

The layered nature of the network structure of the mat is modeled by forming an RVE with two layers of triangles at different initial orientations. This layering captures the mutual constraint effect of the different layers of fibers in the electrospun mat. The double layer RVE behavior (Figure 93) is shown with the same material parameters as used for the single layer RVE model. The double layer system has a similar stress-strain and transverse strain response to uniaxial tension as the single layer RVE however there is negligible dependence of the stress-strain behavior on angle of loading α (Figure 93a). There is also a negligible dependence of the transverse strain behavior on α (Figure 93b). The contraction is still much less than that observed in the experiments with the members under compression barely deforming (Figure 93c). Figure 93d shows how the stress is distributed among the two triangles for $\alpha = 0^o$. The stress contribution in the direction of applied strain is nearly equal for the two triangles even though independently they would have quite different responses (compare 0^o and 30^o in Figure 90a). The transverse stress on the two triangles balance

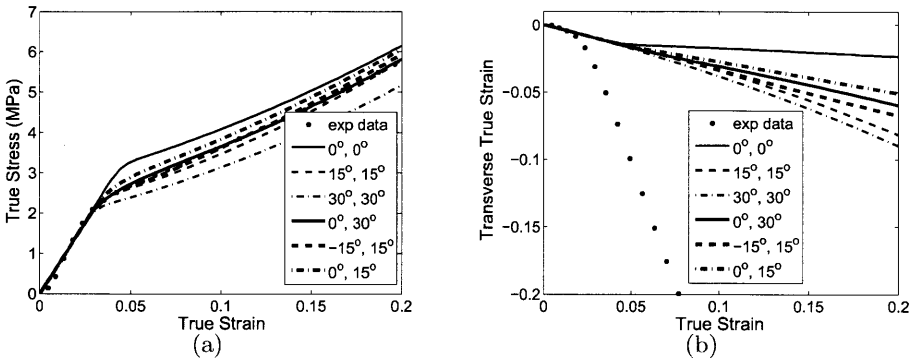

Figure 92: Deformation of the finite element model of a multi-orientation single layer triangle mat subjected to periodic boundary conditions and uniaxial tension in the 1-direction. The model consists of elements randomly assigned the behavior of a straight fiber single layer triangle RVE constitutive model oriented at one of two angles indicated (orientation defined as the angle between member C and the 1-axis). (a)Stress-strain behavior as a function of initial triangle orientation from the 1-direction, (b)transverse strain versus axial strain as a function of initial triangle orientation from the 1-direction.

each other and are significantly smaller than the axial stress, though not negligible. This layered effect is an important constraint which fundamentally distinguishes the double layer triangle model from the single layer triangle model and which distinguishes these electrospun mats from a single layer random network.

In order to further visualize the cooperative deformation of the double layer RVE as compared to the single layer RVE, each geometry is discretely modeled as truss elements using a finite element model. The members are modeled as elastic-plastic with moderate strain hardening as seen in the experimental single fiber data. The triangles are subjected to a deformation gradient as described in Section 6.4.2. The member deformation as a function of applied uniaxial tension is shown for each of the triangles when deforming as isolated single layers and when deforming subject to their mutual constraint in the double layer configuration (Figure 94). The superposition of the two layers of triangles results in a somewhat decreased rotation and increased stretching of two of the members in triangle 1 and a somewhat increased compression of one of the members of triangle 2. It is also clear that the restriction on the fibers to remain straight (only extending or contracting in length) greatly inhibits the magnitude of transverse strain.

6.6.3 Double layer triangle RVE with initially curved members

The RVE as presented thus far has only allowed for axial extension or contraction of the fiber length and has not allowed for fiber bending. As is evident in Figures 93c,d, some members experience compressive forces. Since these members have an aspect ratio around ten to one it is energetically favorable for the members to bend rather than axially compress. Furthermore, most fibers also possess some level of initial curvature which facilitates bending.

The deformation of the triangle RVEs including initially curved members is visualized for the case of uniaxial tension in Figure 95. A tesselated version of this RVE visualization is shown in Figure 96 where it is compared side-by-side with the straight member version. The two single layer

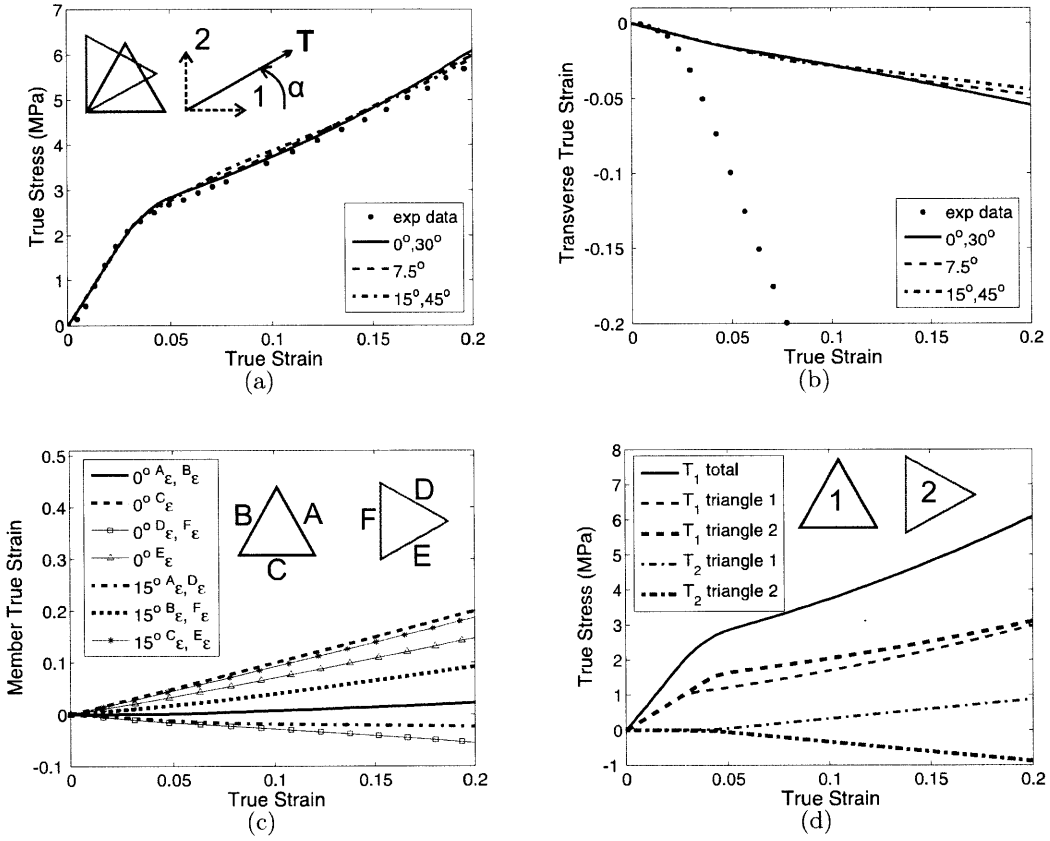

Figure 93: Deformation of the straight fiber double layer triangle RVE subjected to uniaxial tension: (a)stress-strain behavior as a function of angle α from the 1-direction, (b)transverse strain versus axial strain as a function of angle α from the 1-direction, (c)deformation of each member of the triangle versus axial strain as a function of angle α from the 1-direction, (d)individual triangle contributions to tension applied at $\alpha = 0^o$ from the 1-direction.

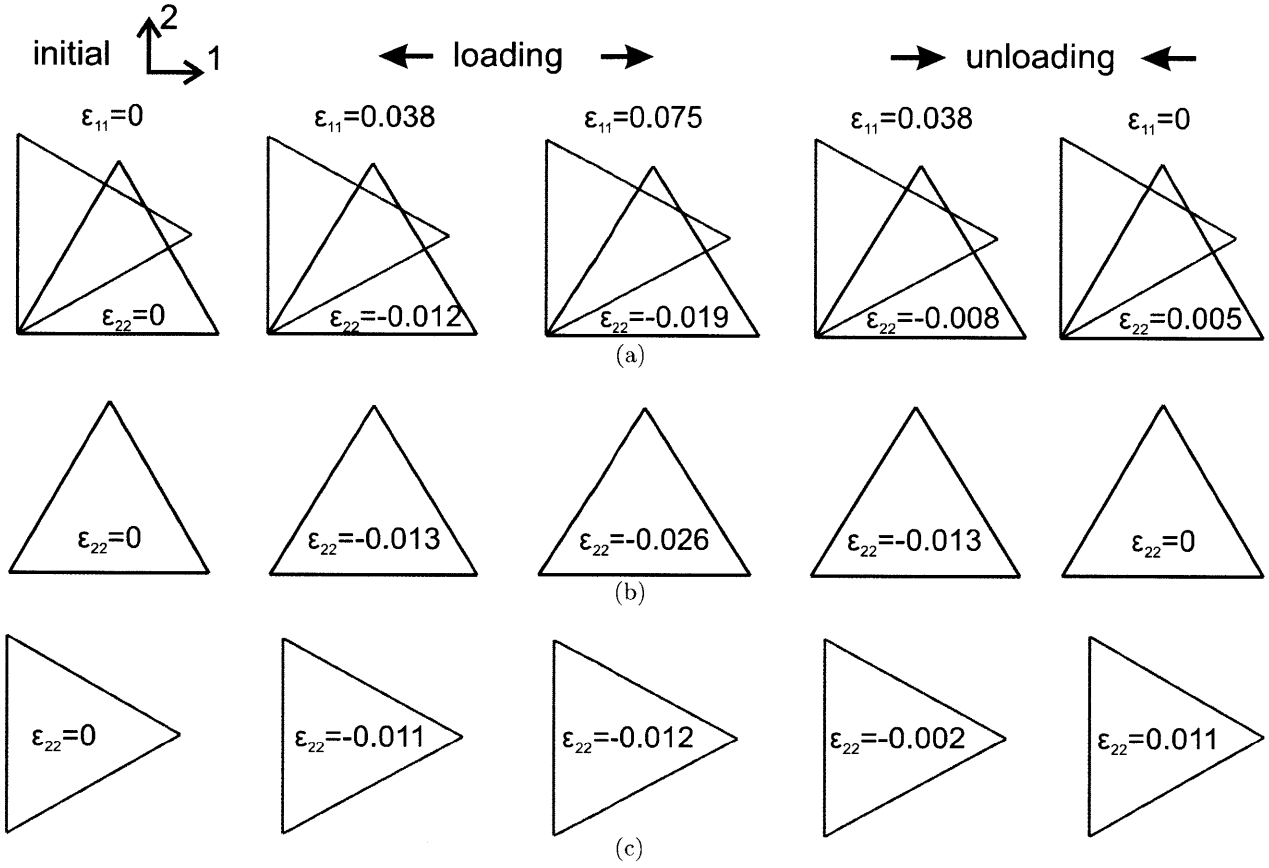

Figure 94: Visualization of straight member RVE component deformation. Each member is directly modeled as a truss element via finite element implementation. The RVE is subjected to uniaxial tension in the 1-direction. (a)Triangle pair in double layer configuration, (b)triangle 1 alone in single layer configuration, (c)triangle 2 alone in single layer configuration.

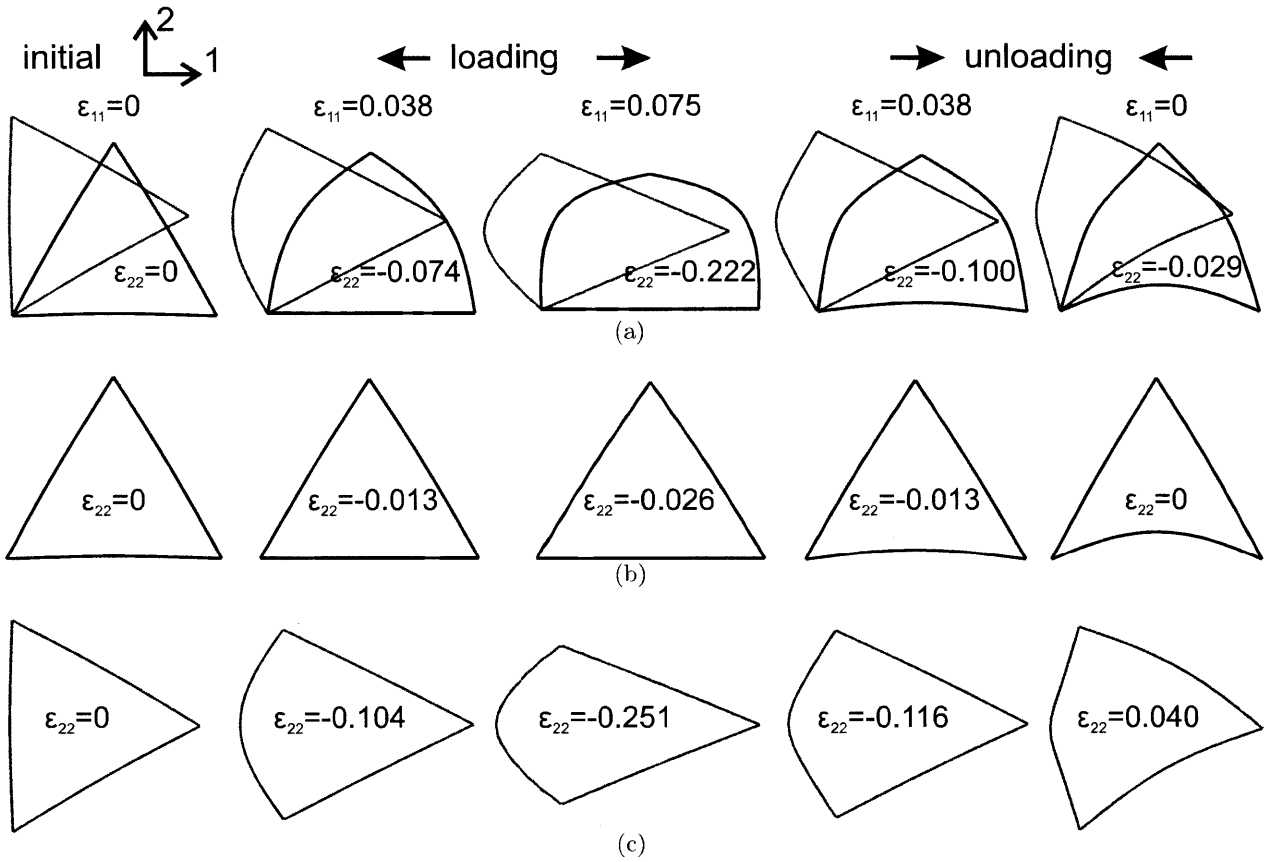

Figure 95: Visualization of curved member RVE component deformation. Each member is directly modeled as a beam element via finite element implementation. The RVE is subjected to uniaxial tension in the 1-direction. (a)Triangle pair in double layer configuration, (b)triangle 1 alone in single layer configuration, (c)triangle 2 alone in single layer configuration.

RVEs and the double layer RVE are discretely modeled as beam elements, with each member given a slight curvature as measured in the SEM images of the electrospun mat. The member stress-strain behavior is modeled as the experimentally observed elastic-plastic behavior with moderate strain hardening. Two important mechanisms are immediately apparent in this figure. The first is the importance of allowing bending of the fibers, enabling significant transverse contraction during uniaxial tension. The second is the mutual constraint effect in the double layer RVE; the mutual constraint leads to different member forces when compared to the isolated layer response which leads to subtle but noticeable effects on stretching and bending of the various members.

The axial stress-strain and the transverse strain behavior of the double layer RVE-curved fiber (composed of initially curved members) constitutive model is shown in Figure 97a-c. This data was captured using a tensile fiber behavior much closer to the median fiber behavior (as compared to near "maximum" behavior with strong post-yield hardening used when considering straight fibers). Here fiber alignment and consolidation are able to occur, and capture the mat strain hardening. The reduced strain energy contribution of fibers in compression reduces their contribution to mat modulus. The member number density ν required to match the RVE stiffness to the mat elastic

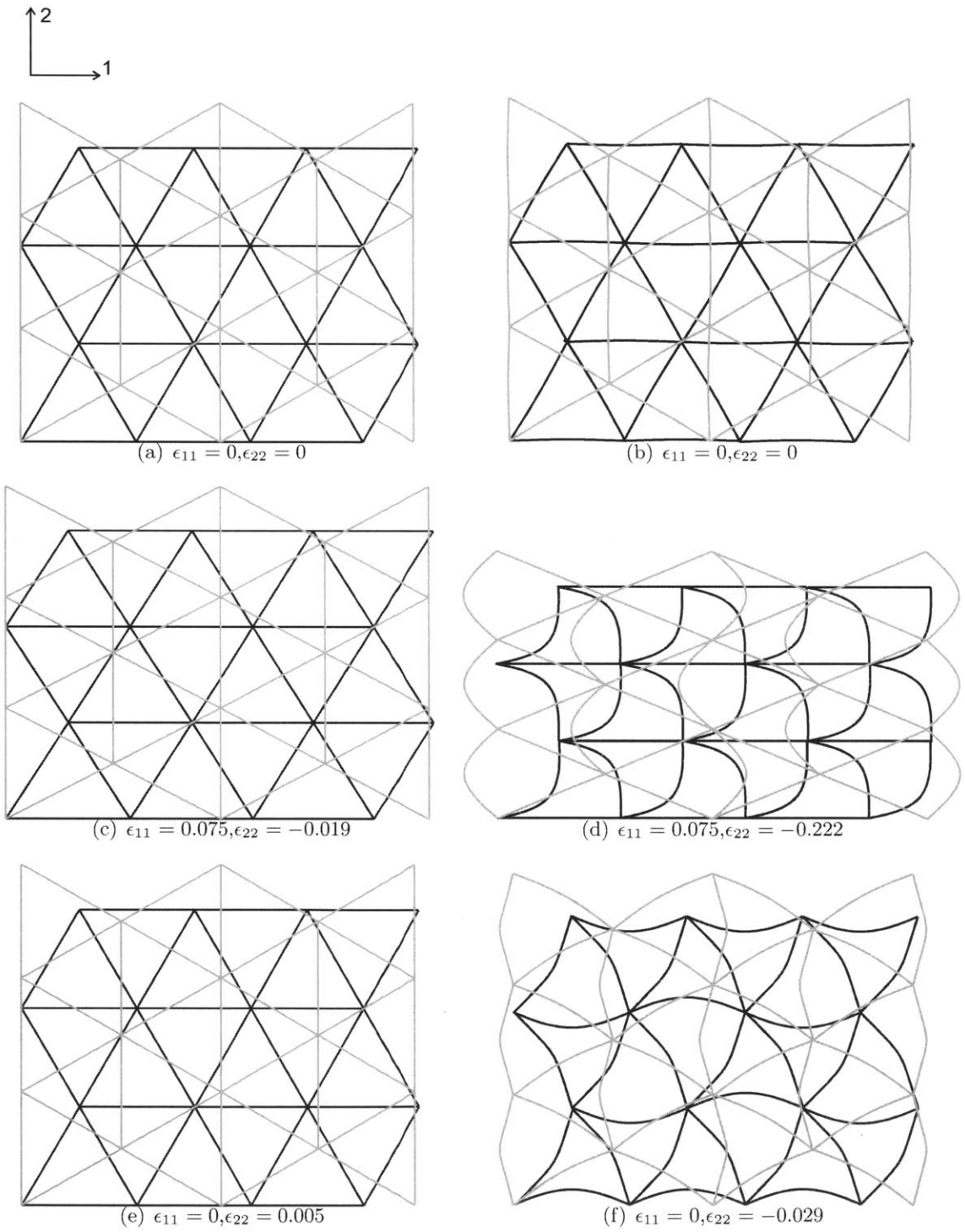

Figure 96: Visualization of the straight and curved member RVE component deformation. Each member is directly modeled via finite element implementation. The RVE is subjected to uniaxial tension in the 1-direction. (a,b) Initial configuration, (c,d) uniaxially loaded to $\epsilon_{11} = 0.075$ (e,f) $\epsilon_{11} = 0$ after prior loading to $\epsilon_{11} = 0.075$. (a,c,e) Members are required to remain straight; (b,d,f) members are allowed to bend.

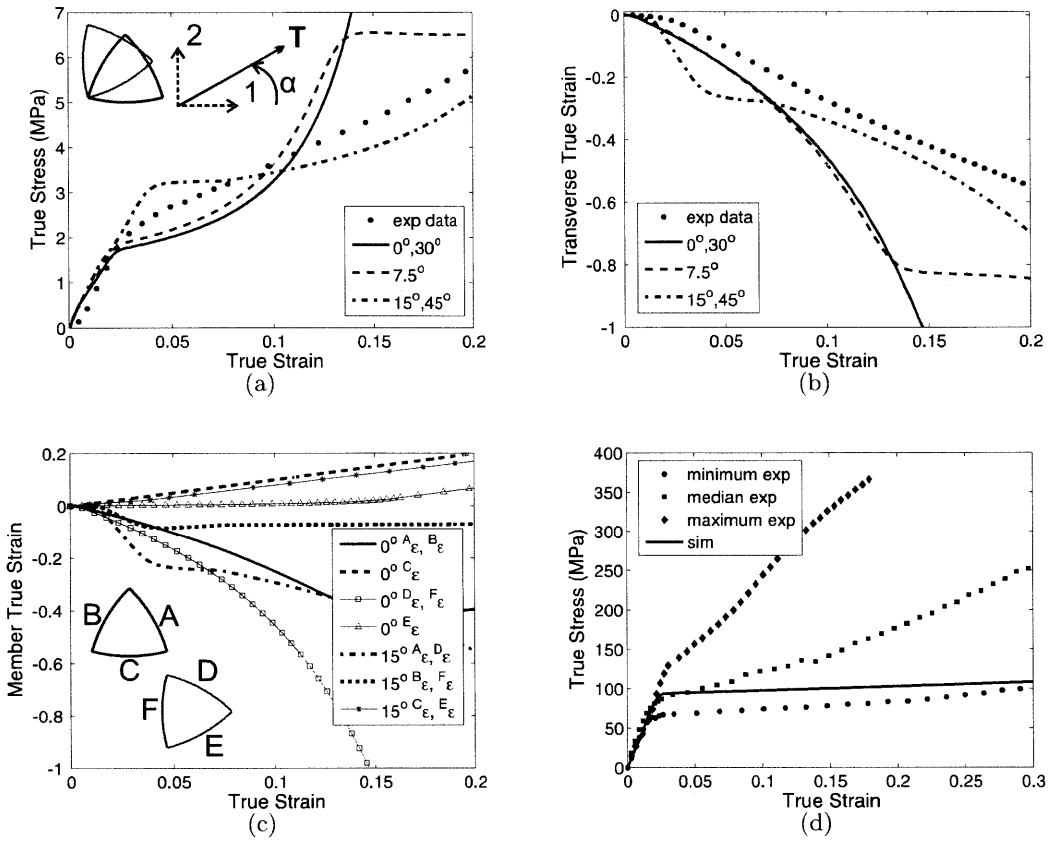

Figure 97: Double layer triangle RVE-curved fiber model subjected to monotonic uniaxial tensile loading: (a)stress-strain behavior as a function of angle α from the 1-direction, (b)transverse strain versus axial strain as a function of angle α from the 1-direction, (c)deformation of each member of the triangles versus strain as a function of angle α from the 1-direction, (d)single fiber tensile fit used in model compared to the single fiber experimental data.

modulus has consequently increased to within 20% of the theoretical estimate of ν based on porosity ($3.9 \times 10^{15} m^{-2}$ versus $4.86 \times 10^{15} m^{-2}$, Table 9). The occurrence of fiber bending also strongly influences the mat yield stress, for the same reasons underlying this influence on modulus. The occurrence of fiber bending allows fibers which are under compression to undergo much larger end-to-end compressive strains which, in turn, captures the transverse strain behavior of the mat.

The inclusion of initially curved fibers in the RVE introduces a strong dependence on the angle α at which loading is applied as is evident in Figure 97a-c. This arises due to the sensitivity of the RVE to any single fiber member bending, which is in turn sensitive to the initial orientation of that member relative to the direction of applied load. Hence, in order to capture the observed isotropy, the initial heterogeneous nature of the triangle orientations should again be taken into account. This is done using a finite element discretization with each material point assigned a double layer constitutive model, and with four initial orientations randomly distributed across the mesh (recall orientation is defined as the angle between member C and the 1-axis). The finite element discretization is shown undeformed and at 20% strain (Figure 98). There is a stark

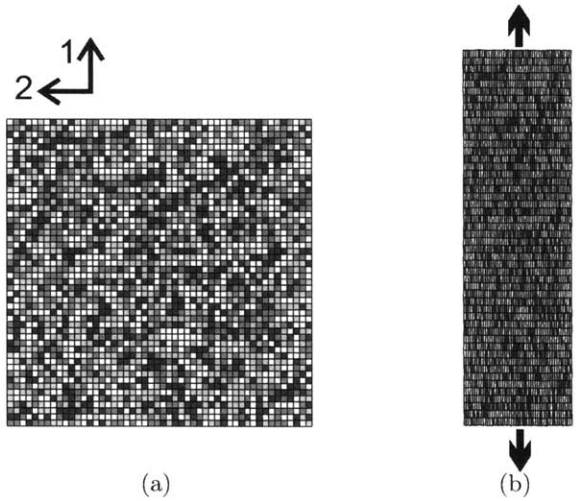

Figure 98: Mesh and geometry used for multi-orientation finite element simulations with periodic boundary conditions of double layer triangle RVE-curved fiber model: (a)initial, (b)20% strain when initial RVE orientations (orientation defined as the angle between member C and the 1-axis) randomly assigned to 0^o, 7.5^o, 15^o, and 22.5^o. Shades of grey indicate different initial RVE orientations.

contrast in the transverse strain behavior between this deformed configuration and the earlier deformed configuration (Figure 92b) that did not allow for fiber bending. The stress-strain and transverse strain response are shown in Figure 99 for different initial orientation combinations. With a distribution of two orientations the response depends on the choice of orientations, however with a distribution of four orientations the response is insensitive to the choice of those orientations. Alternatively, the superposition of additional layers at appropriately offset angles can be used to impose isotropy within a single element(not shown), but that approach is not chosen as it would disregard the heterogeneity characteristic of the mat.

In order to accurately capture the experiment, the full specimen is simulated, including the specimen aspect ratio with a zero lateral contraction condition at the grips, and the grip displacement rate. Only the top right quarter of the specimen is simulated, taking advantage of symmetry conditions, as shown in Figure 100 where each element is assigned one of four initial orientations. The monotonic response for the full specimen geometry is shown in Figure 101 where the double layer RVE-curved fiber model is compared to the double layer RVE-straight fiber model. The axial stress-strain and transverse strain responses are well captured with the double layer RVE when fiber bending is included.

The cyclic (load-unload-reload) response of the double layer RVE-curved fiber model is shown in Figure 102. The model captures the unload and reload with a small hysteresis and the sharp yield upon reload as the curve meets the monotonic curve. The unloading and reloading slopes from the model do increase with strain as seen in the experimental data because of the increased member alignment and consolidation. The cyclic transverse strain behavior is also well captured by the RVE-curved fiber model; in contrast the RVE-straight fiber model exhibits minimal transverse strain.

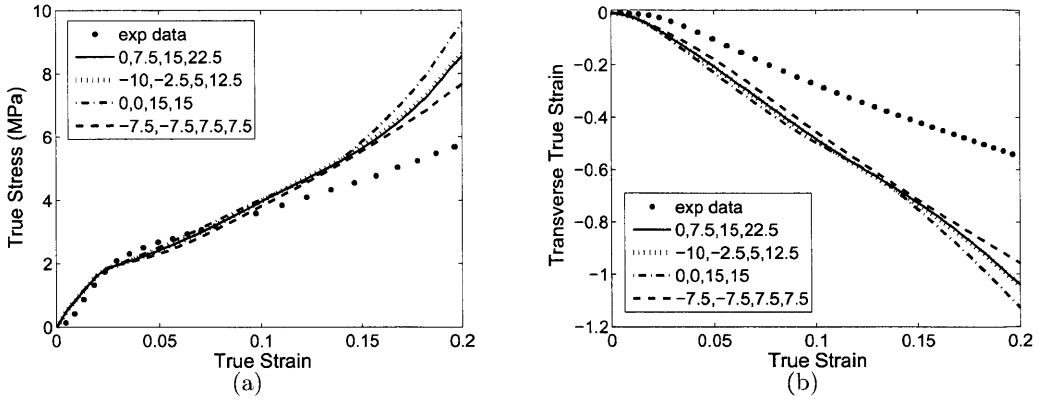

Figure 99: Response of the finite element model of the double layer triangle mat subjected to periodic boundary conditions and uniaxial tension in the 1-direction. The model consists of elements randomly assigned the behavior of a double layer triangle RVE-curved fiber model oriented at one of four angles indicated (orientation defined as the angle between member C and the 1-axis): (a)stress-strain behavior as a function of initial triangle orientation from the 1-direction, (b)transverse strain versus axial strain as a function of initial triangle orientation from the 1-direction.

6.6.4 Effect of number of layers

This chapter has included a discussion of the importance of the mutual constraint effect of a double layer versus a single layer triangle RVE. It is clear however from Figure 97 that on the single element (single orientation) level that the double layer triangle RVE-curved fiber response is not isotropic. A natural question is whether the addition of more layers (1) improves isotropy and (2) significantly changes the response. The pure uniaxial tensile of the model is simulated using a finite element discretization analogous to that of Figure 98a, for different combinations of layers and initial element orientations. Figure 103 contrasts the uniaxial tensile response for 1 to 8 layers, where the number of layers within each RVE and the number of distributed orientations among different elements multiplies to 8 in each case (where in all cases orientation is defined as before as the angle between member C on the first layer triangle and the 1-axis; N layers are evenly distributed within a single element such that there are $60^o/N$ between subsequent members). From these plots it is evident that while there is a strong difference between the single layer and double layer RVE, there is only a minimal effect from the further superposition of layers. Adding more layers does improve the smoothness of the response and the isotropy of a single element orientation. 8 layers with 1 element orientation and 4 layers with 2 element orientations are both roughly equivalent to 2 layers with 4 element orientations.

6.6.5 Fiber orientation

The direct microstructural basis of the model enables tracking of fiber alignment/orientation with macroscopic deformation. This adds insight to the physical deformation process and could be useful for model validation in conjunction with a more in depth analysis of SEM tensile experiments. Figure 104a shows how the member angles evolve with axial strain. It can be seen that all the members orient towards the axis of applied strain (towards 0^o) except for member F which is

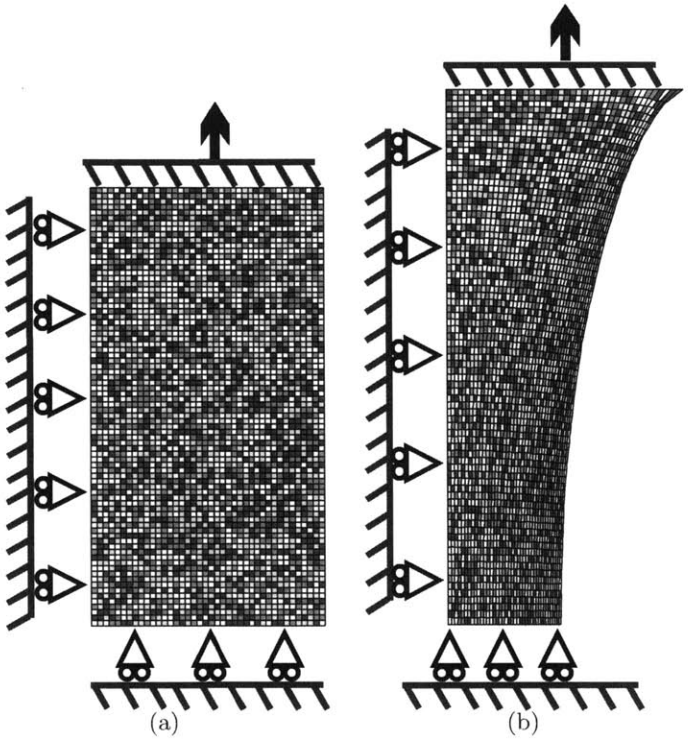

Figure 100: Mesh and geometry used for multi-orientation finite element simulations with actual specimen geometry and boundary conditions of double layer triangle RVE-curved fiber model compared to the double layer straight fiber model and the single layer curved fiber model: (a)initial, (b)20% strain when initial RVE orientations randomly assigned to 0^o, 7.5^o, 15^o, and 22.5^o(orientation defined as the angle between member C and the 1-axis). Shades of grey indicate different initial RVE orientations.

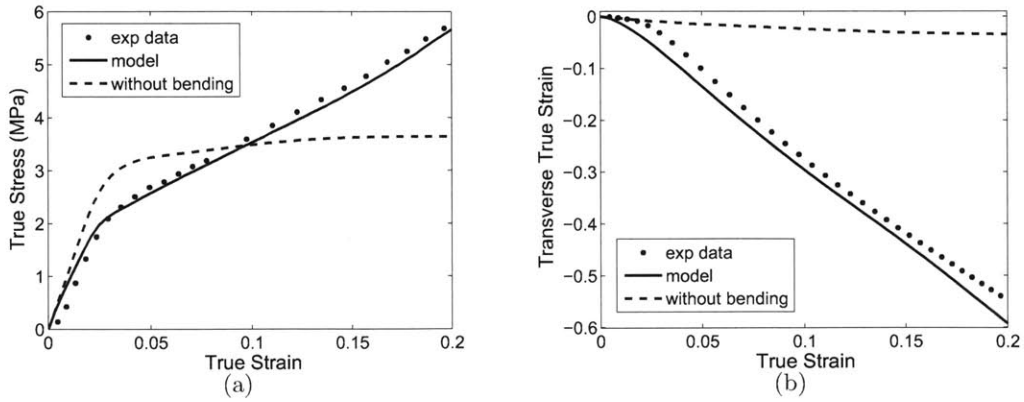

Figure 101: Full specimen response to monotonic uniaxial tensile loading for the double layer RVE-curved fiber model: (a)stress versus strain, (b)transverse versus axial strain.

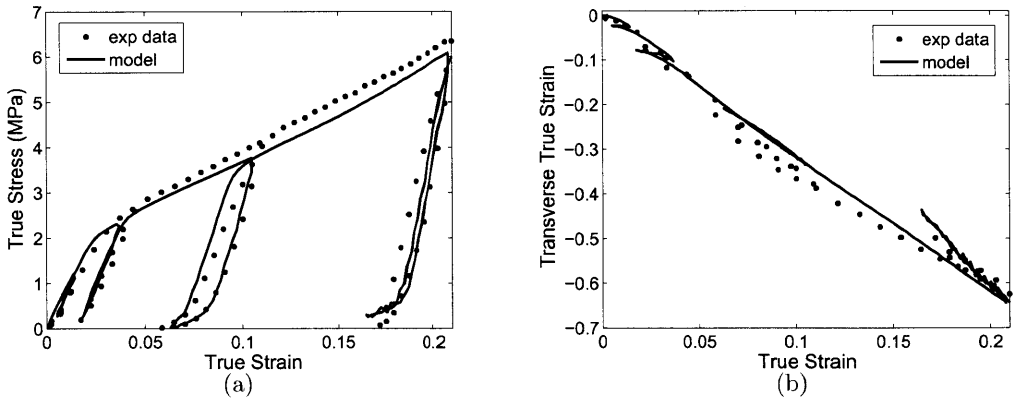

Figure 102: Full specimen response to load-unload-reload uniaxial tensile cycling for the double layer RVE-curved fiber model: (a)stress versus strain, (b)transverse versus axial strain.

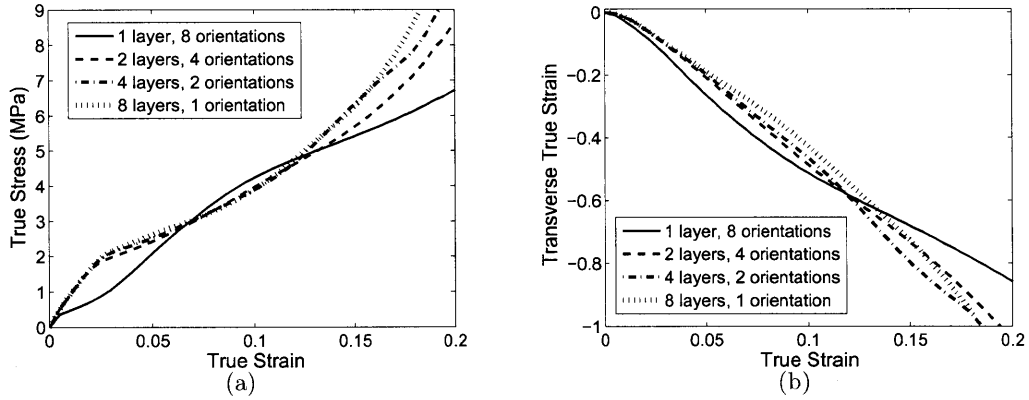

Figure 103: Effect of triangle layering on RVE-curved fiber model response to uniaxial tension: (a)stress versus strain, (b)transverse versus axial strain.

initially oriented perpendicular (90^o) to the axis of applied strain and remains at that orientation throughout (recall, it bends rather than orients, as reminiscent of the SEM images). When the fibers are constrained to remain straight, all the members except F orient towards to axis of applied strain, however they do so to a much lesser extent. Since member F is not able to bend, the rotation of the remaining members is much more restricted.

The important effect of fiber bending on network fiber alignment is also evident via an aggregate fiber orientation measure. A common method for tracking orientation is to use Herman's orientation function, defined as:

$$h = \frac{1}{2}\left[3 < \cos^2 \alpha > -1\right] \tag{130}$$

where h is the orientation function which ranges from -0.5 when perpendicularly oriented to 1 when fully oriented, and α is the angle between the objects of interest (in this case the fibers) and the axis of alignment (in this case the 1-direction). For the equilateral triangle geometry the Herman's

Table 9: Material parameters used to match the double layer triangle RVE-curved fiber model to experimental data.

Model Component	Material Parameter	Value
Fiber axial properties	E	$4100MPa$
	$\dot{\epsilon}_o$	$9.91 \times 10^{18} s^{-1}$
	s_o	$6.33MPa$
	n	0.6
Fiber bend properties	A_2	$2.0N$
	A_3	$1.8 \times 10^{-5} N$
	s_o^b	$0.14MPa$
	n_b	-4
Mat geometry	r_o	$6 \times 10^{-7} m$
	l_o	$2 \times 10^{-5} m$
	ν	$3.9 \times 10^{15} m^{-2}$
Fiber Hydration properties	E_{wet}	$2900MPa$
	$s_{o,wet}$	$5.9MPa$

factor is initially equal to 0.25 because the fibers are all located within a given plane, and not randomly oriented in the three dimensional sense described by the Herman's factor. We therefore define an alternative orientation function $h2D$ to describe orientation within a plane.

$$h2D = 2 < \cos^2 \alpha > -1 \tag{131}$$

which ranges from -1 when perpendicularly oriented to 1 when fully oriented. For this two dimensional orientation function the equilateral triangle geometry is initially equal to 0. When strain is applied in the 1-direction the factor increases towards 1, whereas when strain is applied in the 2-direction the factor decreases towards -1 (Figure 104b). Due to the constraints inherent in the double layer triangle geometry, the fibers can never actually reach these extremes of fully aligned or completely unaligned. Here again, for the RVE in which the fibers are constrained to remain straight, the member alignment (and anti-alignment) is significantly inhibited.

6.6.6 Hydration

A model of how the mat behavior changes in water is important, since the properties of the composite will operate in water. Figure 105 shows that scaling of the fiber elastic response and yield stress with water content can capture the hydrated mat behavior in terms of both stress-strain and transverse strain. This scaling with hydration is realistic for polyamide (e.g. Lagarón et al. (2001); Bell et al. (2008)). The success of the hydration scaling also further supports this overall RVE model concept of a material behavior dominated by the stretch, alignment, and consolidation of fibers.

6.6.7 Model validation

To further assess the predictive capability of the constitutive model, uniaxial tensile loading experiments are conducted at two additional specimen aspect (length:width) ratios, resulting in a total of

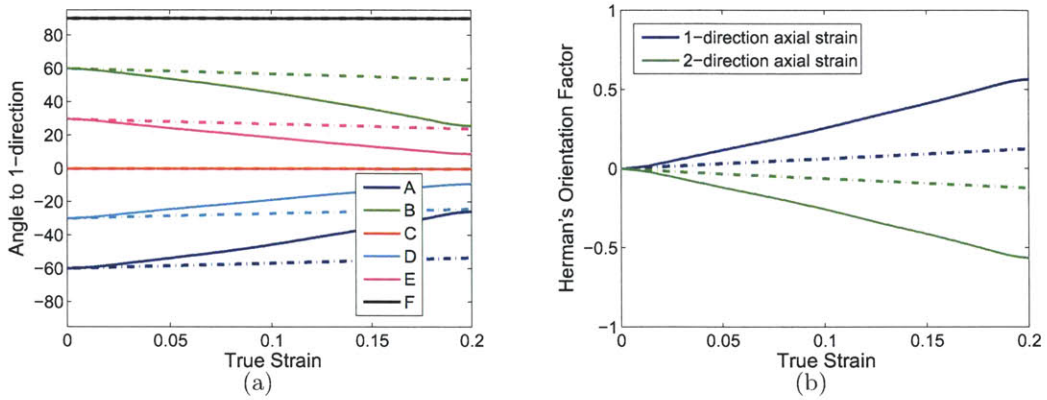

(a) (b)

Figure 104: Evolution of fiber orientation according to single element 8-layer RVE model. Solid lines are RVE-curved fiber model; dotted lines are RVE-straight fiber model. (a) Angles of the members relative to the 1-direction in two of the layers as a function of axial strain in the 1-direction; the two layers displayed are those explicitly described in the model formulation. (b) 2D Herman's orientation function relative to the 1-direction of all the members in the 8-layers as a function of axial strain.

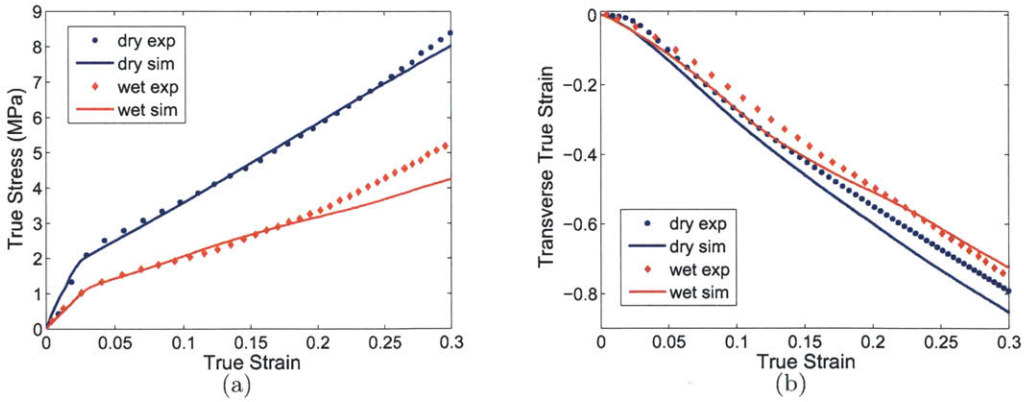

(a) (b)

Figure 105: Effect of hydration on full specimen response to monotonic uniaxial tensile loading for the double layer RVE-curved fiber model: (a)stress versus strain, (b)transverse versus axial strain.

three aspect ratios for comparison: $L : W$ = 1,2,3. Since there is a strong tendency for transverse straining and fiber consolidation upon uniaxial loading, it is expected that there will be a significant dependence of the mat response on specimen aspect ratio due to the boundary conditions imposed by the grips. The experimental results of deformed specimen shape, stress-strain response, and transverse strain response are compared with the model predictions for all three specimen geometries. The membrane stress-strain response is reduced, in both the experiments and the model, using the axial and transverse strain from the markers on the central axes of the specimen for each geometry. Note that the axial strain as measured over the lengthspan between markers is nearly the same as the local axial strain at the center of the specimen and hence the stress-strain behavior reported approximates that at the specimen center. Nonetheless, each simulation is reduced using the same strain tracking locations as in the corresponding experiment in order to maximize the fidelity of the comparisons.

Specimens of each aspect ratio are shown in the initial configuration and at an axial strain of 0.2 (Figures 106-108a,b). The influence of the grip constraint on the three aspect ratio specimens is apparent by comparing the three deformed images. The case of $L : W = 1$ provides a nearly plane strain condition while the $L : W = 3$ specimen is nearly uniaxial tension at the center. Representative stress-strain and transverse strain responses for each aspect ratio are shown in Figure 109. The elastic modulus of the three specimens is similar to within experimental error where we note that this is related to their being relatively little transverse strain during the elastic stage of uniaxial tension. Yield is moderately affected by the specimen geometry, with the yield stress decreasing with increasing aspect ratio since more of the fibers are free to bend, thereby contributing less to the load (mat strain energy) at yield. The post-yield slope increases significantly with increasing specimen $L : W$ as a consequence both of the greater alignment of the fibers and the greater consolidation in the larger aspect ratio geometry due to the greater magnitude of transverse strain (Figure 109b).

A silhouette of the simulated deformed specimen is overlayed on the deformed experimental image (Figures 106-108a,b) for each $L : W$. In each of the three cases the simulated shape is quite similar to the experimental shape. These specimen deformation comparisons indicate that the model captures the gradual transition from the grip constraint on each end to the region of maximum contraction at the center. The grip effect on each specimen geometry is evident in the contours of axial and transverse normal strain (Figures 106-108c,d). For a given aspect ratio, the influence of the grips on restricting the transverse strain over a broader area with reduced $L : W$ is clear. The model stress-strain and transverse strain responses are compared to the experimental responses in Figure 109. The model predicts the effect of specimen aspect ratio on the yield stress, post-yield hardening, and transverse strain to within experimental error, naturally capturing the difference in fiber bending between the geometries. The difference among the three aspect ratio specimens is also evident in the evolution of the average specimen porosity and the fiber alignment in the specimen center (Figure 110). The largest aspect ratio specimen consolidates the most for a given strain, corresponding to the smallest porosity and the greatest average fiber orientation with the axial strain direction. This consolidation and alignment variation with specimen geometry arises naturally from the triangulated geometry and compressive deformation accommodation by fiber bending, leading to the multiaxial predictive capabilities of the model.

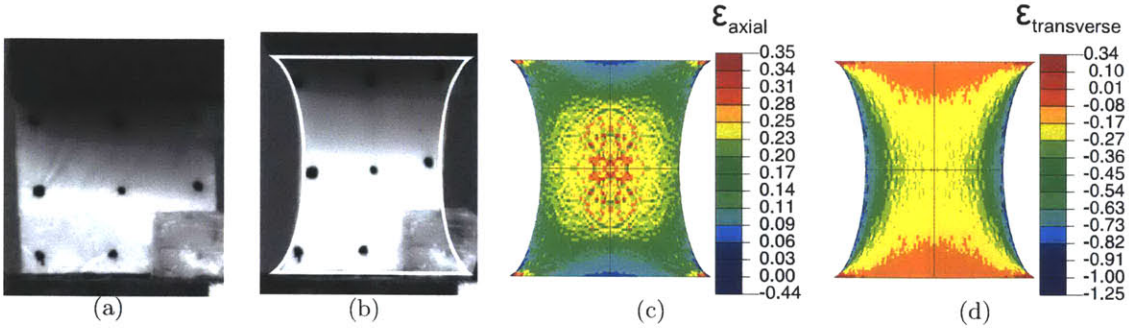

Figure 106: Images of electrospun PA6(3)T mat with a length to width aspect ratio of 1:1 (a)video extensometer prior to deformation, (b)video extensometer after uniaxial tension to a strain of 0.2 with silhouette of corresponding double layer RVE-curved fiber model simulation in white, (c)axial true strain contour from simulation at a strain of 0.2, (d)transverse true strain contour from simulation at a strain of 0.2.

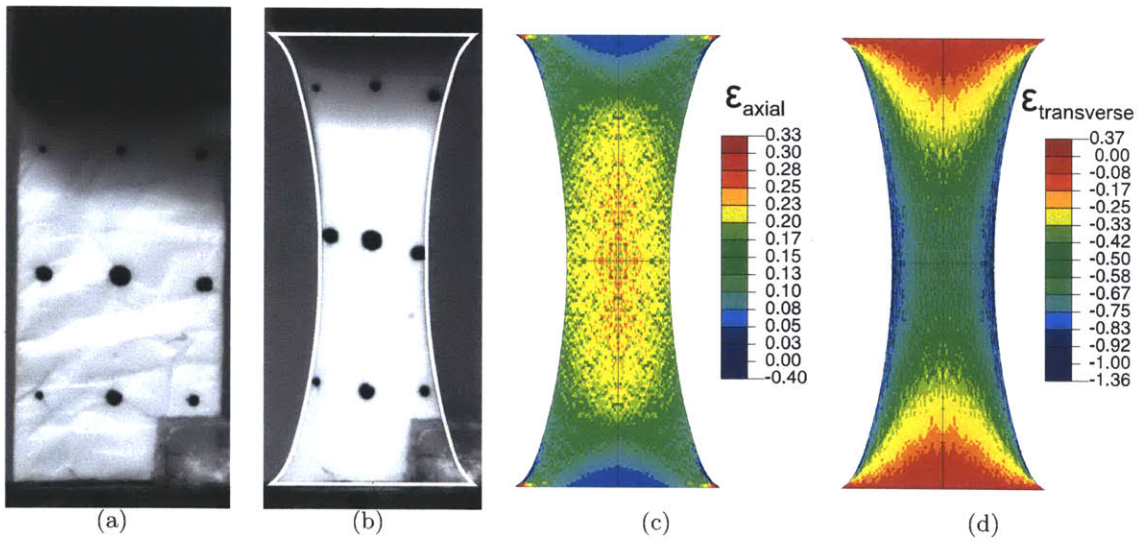

Figure 107: Images of electrospun PA6(3)T mat with a length to width aspect ratio of 2:1 (a)video extensometer prior to deformation, (b)video extensometer after uniaxial tension to a strain of 0.2 with silhouette of corresponding double layer RVE-curved fiber model simulation in white, (c)axial true strain contour from simulation at a strain of 0.2, (d)transverse true strain contour from simulation at a strain of 0.2.

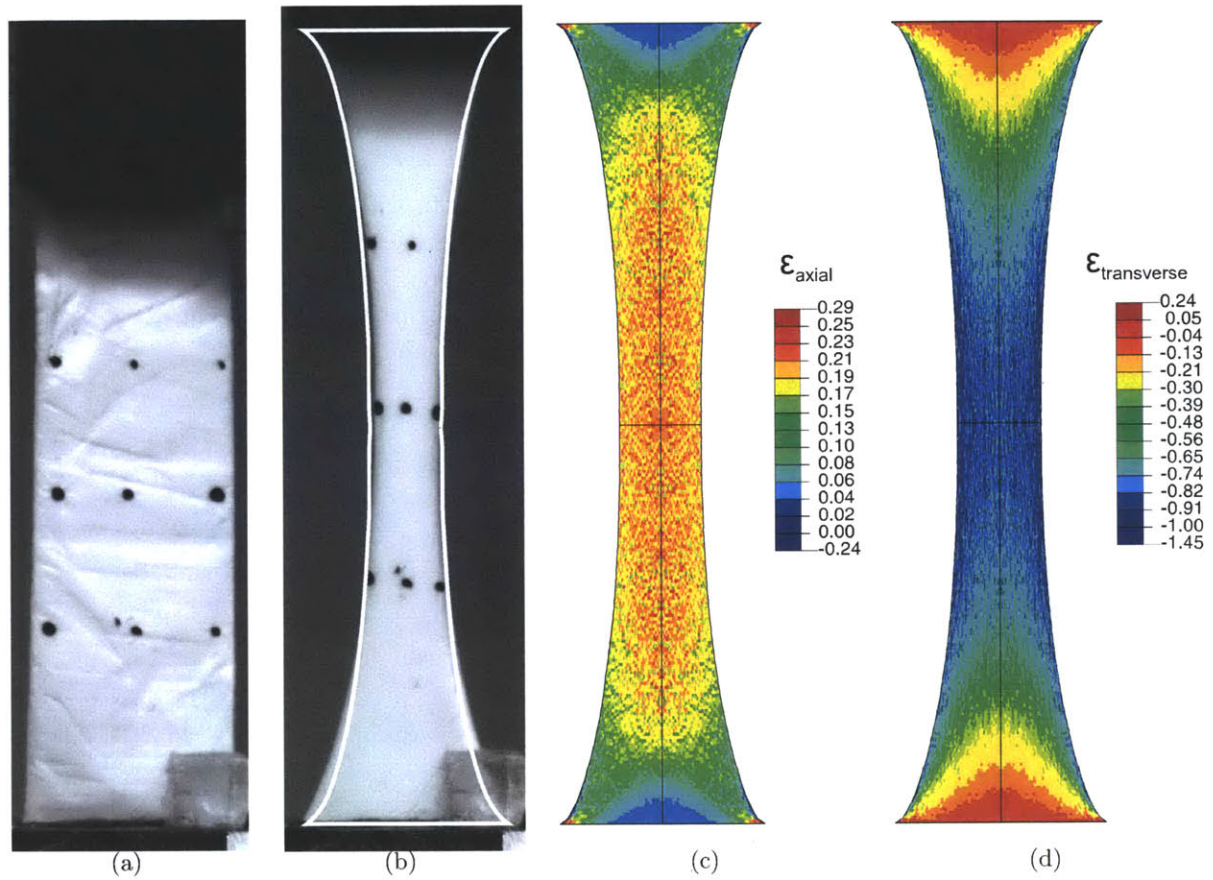

Figure 108: Images of electrospun PA6(3)T mat with a length to width aspect ratio of 3:1 (a)video extensometer prior to deformation, (b)video extensometer after uniaxial tension to a strain of 0.2 with silhouette of corresponding double layer RVE-curved fiber model simulation in white, (c)axial true strain contour from simulation at a strain of 0.2, (d)transverse true strain contour from simulation at a strain of 0.2.

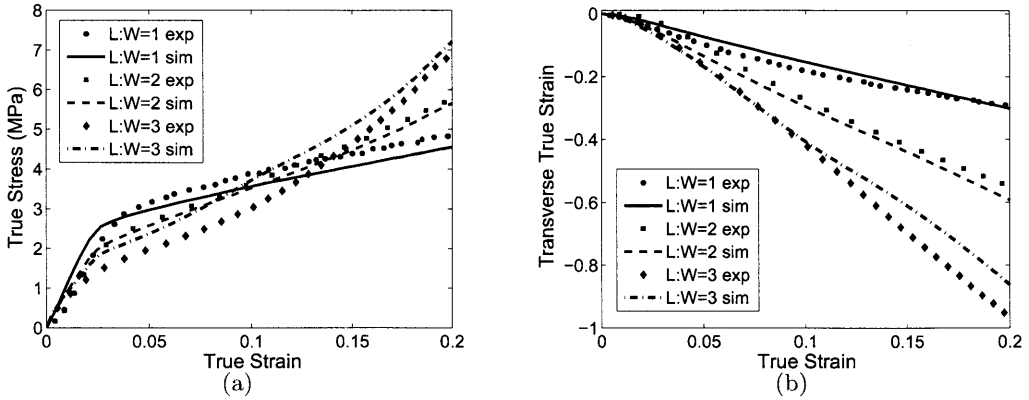

Figure 109: Experimental behavior of electrospun PA6(3)T and double layer triangle RVE-curved fiber model predictions of the full specimen response at three different specimen length (L) to width (W) ratios to uniaxial tensile loading: (a)stress versus strain, (b)transverse versus axial strain.

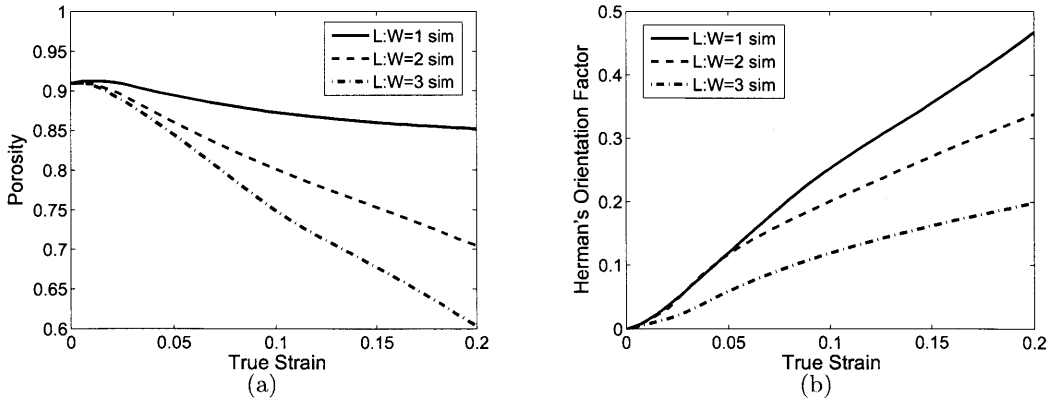

Figure 110: Evolution of microstructural features with axial strain during uniaxial tension as a function of specimen length (L) to width (W) ratio for double layer triangle RVE-curved fiber model: (a) Mat porosity of the whole specimen, (b) 2D Herman's orientation factor of fiber alignment with the axial strain direction at the center of the specimen.

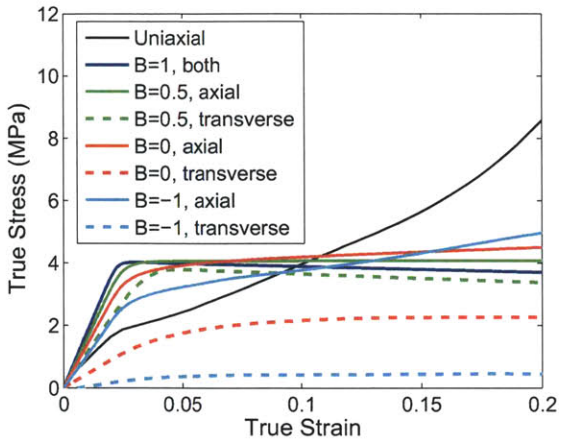

Figure 111: Biaxial tensile response of electrospun PA6(3)T according to the RVE-curved fiber model. $B = \frac{\dot{\lambda}_{transverse}}{\dot{\lambda}_{axial}}$ is the degree of biaxiality.

6.6.8 Biaxial loading

While varying the L:W ratio in uniaxial testing starts to probe multiaxiality, biaxial loading can be directly simulated. Different degrees of biaxiality are simulated using periodic boundary conditions with the RVE-curved fiber model, where the biaxiality ratio B is defined as the ratio of stretching rates in the axial and transverse directions ($B = \frac{\dot{\lambda}_{transverse}}{\dot{\lambda}_{axial}}$). Biaxiality has a strong effect on the elastic modulus, yield stress, and post-yield hardening (Figure 111). In the axial direction, increasing the biaxial ratio increases the elastic modulus and yield stress and decreases the post yield hardening. The increase in elastic modulus and yield stress occurs because a lower percentage of the fibers are bent, or from an alternative viewpoint, a greater percentage of the fibers are loaded in tension and thereby contributing to the axial stress. The decrease in post-yield hardening is also directly related to this lack of fiber bending. The stress does not increase as much under biaxial loading because the fibers do not align and consolidate in a particular direction. As can be seen from the stress in the transverse direction, even at $B = -1$, the transverse direction is still in tension, meaning that fiber bending is more restricted than under pure uniaxial tension.

The yield surface that arises from the RVE-curved fiber model is quite different than that typically used in dense polymer modeling (such as the one used in the Nafion model). This yield surface is shown along with the Mises and Tresca yield surfaces in Figure 112. It is somewhat similar to the phenomenological yield surfaces used for paperboard (Xia et al., 2002; Mäkelä and Östlund, 2003; Harrysson and Ristinmaa, 2008; Isaksson, 2010) exhibiting distinct changed in curvature as well as relatively flat regions, suggesting clear changes in deformation mechanism for yield under different stress states (compare to Figure 78). There is a sharp change in slope of the yield surface at a transverse stress (relative to the yield stress) of approximately 0.3. This change in slope corresponds to the transition from loading modes under which some of the members are under local compression and bending (much less stiff than the elastic tensile stiffness) to loading modes under which all the members are in tension and contributing to the elastic stiffness and the stress at yield. This sharp transition also occurs in the material when the fibers are prohibited from bending, however it occurs at principal stresses of 1 and -1 because when bending is prohibited the

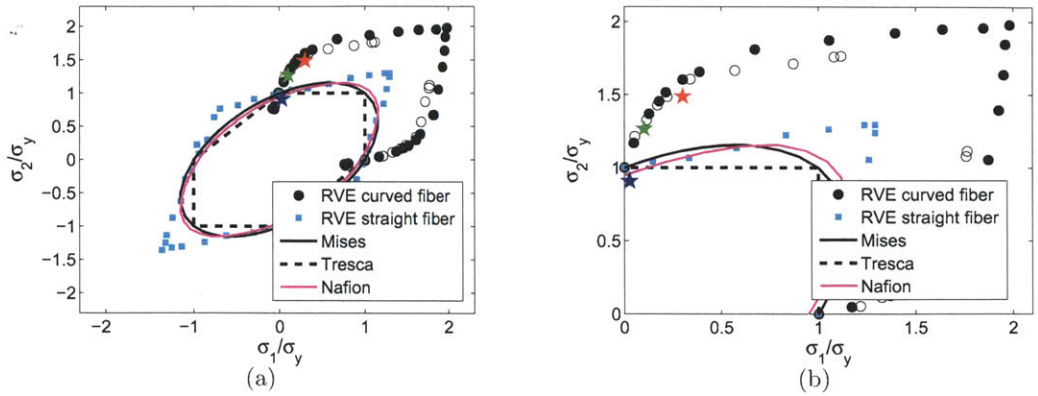

Figure 112: Yield surface of the RVE-curved fiber model using the 8-layer formulation compared to the Mises and Tresca yield criteria and the Nafion yield surface at ambient conditions and a strain rate of $0.01s^{-1}$. Each material is normalized to its own uniaxial yield stress. (a) Full yield surface and (b) upper right quadrant of yield surface. Closed circles determined by simultaneous loading in the principal directions, open circles determined by sequential loading in the principal directions (note the 8-layer formulation is used to allow single element implementation, the yield stress is negligibly different from the 2-layer formulation). The blue, green, and red stars represent the yield points from the $L : W = 3, 2, 1$ aspect ratio experiments respectively according to the transverse stress estimated from the aspect ratio simulations. The yield stresses for the curved and straight fiber models are $2.0MPa$ and $3.1MPa$ respectively.

fiber stiffness is the same in tension and compression until the fiber stress reaches axial yield stress in either direction. In general the sharp corners occur because distinct fibers are being yielded under tension (or compression) rather than a dense material yielding under shear stress. The three "uniaxial" tests with varied aspect ratios are also included on the yield surface. It is apparent that the $L : W = 3, 2$ aspect ratio specimens are nominally uniaxial, but that the $L : W = 1$ aspect ratio specimen is at the transition to biaxiality. Either smaller aspect ratio specimens or biaxial experiments would be needed to validate the rest of the yield surface.

6.6.9 Design potential

Since the constitutive model is directly based on mat microstructure, it is straightforward to use the model to predict the effect of specific aspects of the mat geometry on the macroscopic mat deformation response. Such a capability will be useful for tailoring non-wovens to desired properties and can also be used to better understand the origin of the mat stiffness, yield, post-yield hardening, and transverse behavior. Here, the deformation response for a few simple cases are presented: (1) doubling fiber radius while holding junction-junction spacing and porosity constant, (2) doubling junction-junction spacing while holding fiber radius and porosity constant, (3) decreasing porosity (by doubling member number density) while holding fiber radius and junction-junction spacing constant (Table 10). Each of these cases are simulated using a true uniaxial tension condition (with periodic boundary conditions) according to the discretization described in Section 6.6.3.

Predicted stress-strain and transverse strain responses to uniaxial tension are shown in Figure 113. Modification of the fiber radius has a strong qualitative and quantitative effect on the response

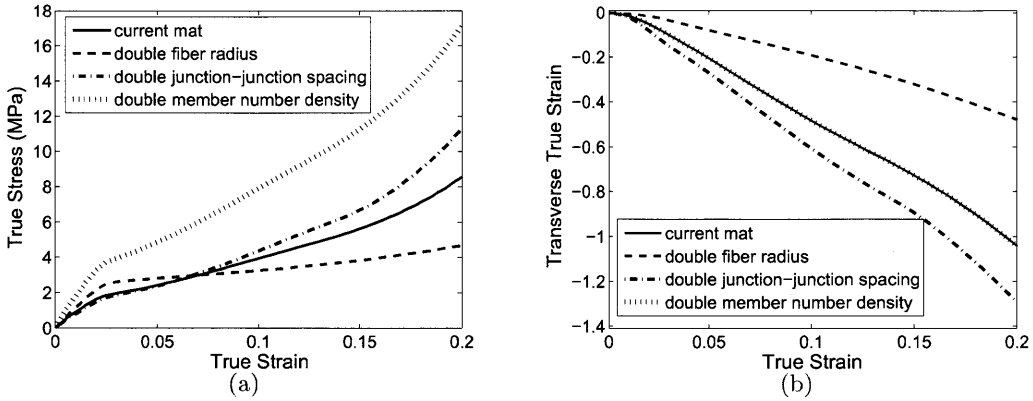

Figure 113: Predictions of random non-woven response to uniaxial tension: (a)stress versus strain, (b)transverse versus axial strain.

since fiber bending stiffness increases with r_o^4. The fiber axial stiffness, yield stress, and post-yield hardening do also increase (with r_o^2), but this increase is exactly canceled on the mat scale by maintaining porosity. The mat with thicker fibers has a stiffer elastic response and greater yield stress due to the increased strain energy contribution from fibers under compression, and a decreased post-yield hardening and transverse strain contraction due to decreased fiber alignment and consolidation as inhibited by the reduced fiber bending. Had the fiber radius been doubled while maintaining member number density rather than porosity, the stress-strain response would be four times as large but the transverse strain response would be unchanged. Doubling the junction-junction spacing only weakly effects the response. This doubling halves the force at which the fiber force-stretch response rolls over under compression, but this resistance is already quite low compared to the tensile response so this further decrease is only weakly reflected as a slight decrease in elastic modulus and yield stress and a slight increase in post-yield hardening and transverse strain contraction relative to the reference geometry. Decreasing the mat porosity by doubling the member number density, doubles the elastic modulus, yield stress, and post-yield hardening and has no effect on the transverse strain response. This is expected since the member number density is essentially a scaling factor and does not influence the cooperative mat deformation. This model framework can also be readily extended to incorporate initial network anisotropy by using non-equilateral triangles that have fiber orientation distributions corresponding to the mat fiber orientation distribution (not shown).

Table 10: Geometry values used in model predictions of the effect of geometry variations on macroscopic random non-woven mat response.

Modified Geometry	r_o	l_o	ν	φ
reference	$6 \times 10^{-7} m$	$2 \times 10^{-5} m$	$3.9 \times 10^{15} m^{-2}$	0.91
double radius	$1.2 \times 10^{-6} m$	$2 \times 10^{-5} m$	$9.8 \times 10^{14} m^{-2}$	0.91
double junction-junction spacing	$6 \times 10^{-7} m$	$4 \times 10^{-5} m$	$1.9 \times 10^{15} m^{-2}$	0.91
double member number density	$6 \times 10^{-7} m$	$2 \times 10^{-5} m$	$7.8 \times 10^{15} m^{-2}$	0.82

6.7 Concluding Remarks

Randomly oriented non-woven electrospun mats have been experimentally characterized under different tensile loading conditions. Experimental mechanical characterization of fibers electrospun from amorphous polyamide revealed that the fibers are elastic-plastic with a wide spread in yield stress and post-yield hardening. Experimental mechanical characterization of random mats electrospun from the same polymer solution revealed that these mats are elastic-plastic with significant post-yield hardening. At small strains the initial Poisson's ratio is near zero implying an initial structural rigidity opposing fiber alignment. This resistance is then overcome and the transverse strain decreases more than the vertical strain increases. Under cyclic loading the mats are seen to unload and reload in a nearly linear manner and exhibit an elastic modulus that increases significantly with strain. The post-yield hardening and the apparent increase in elastic modulus with cycling to larger strains arise from consolidation and alignment of the fibers. The consolidation and alignment are also underlying the observed transverse strain behavior. The specimen aspect ratio was found to significantly influence the reduced stress-strain and transverse strain response with a 1:1 ratio giving a nearly plane strain constraint, constraining contraction.

A micromechanically-based constitutive model for the elastic-plastic behavior of non-woven mats is constructed. The mat structure is idealized as a triangulated network of elastic-plastic fibers. The layered network is captured by a representative volume element consisting of a double layer structure where each layer is a triangulated network and the layers are offset 30^o from each other. The layers impose mutual kinematic constraints emulating the layered structure of real mats, providing greater isotropy to the yield and post-yield behavior. The behavior of the constituent fibers was taken to be elastic-plastic accounting for stretching and bending of the fibers when subjected to end tensile and compressive loads; the bending of the fibers when a fiber is locally under compression was found to be the key mechanism enabling the mat to consolidate during tensile loading. The resulting double layer triangulated network of fibers which exhibit elastic-plastic stretch and bending was found to capture all features of the uniaxial behavior of the mats including:

- elastic-plastic axial stress-strain behavior including elastic stiffness, yield, and post-yield hardening
- transverse strain
- fiber orientation evolution
- cyclic load-unload-reload behavior
- evolution in elastic stiffness with plastic strain
- dependence of the elastic-plastic behavior on hydration

The model is further validated via comparison to experiments of axial loading subject to different axial constraints, from nearly uniaxial to nearly plane strain. The model is found to match the deformed specimen shape, stress-strain, and transverse strain responses for this range of grip induced constraint. Predictions of the material response with modifications to mat geometry made with the model, show a strong dependence of the elastic-plastic response on fiber radius and porosity and a weak dependence of the elastic-plastic response on junction-junction spacing. Since the physics

in this model is not specific to polyamide beyond the choice of fiber constitutive properties, it is expected that this model will be transferable to other electrospun materials and to other layered random networks more generally.

7 Composite polymer electrolyte membrane

7.1 PDAC/sPPO layer-by-layer film

7.1.1 Experimental behavior

The LBL film acts an elastic-plastic solid when dry and nearly as a viscous fluid when wet as discussed in Chapter 5. Here the monotonic LBL data is shown along with the cyclic response (Figure 114) and video extensometer images (Figure 115). Due to the limited LBL material available for mechanical characterization there is no transverse strain data in the hydrated state. A model for this material will need to capture the initial elasticity, the plastic yield event, and the highly compliant behavior when hydrated.

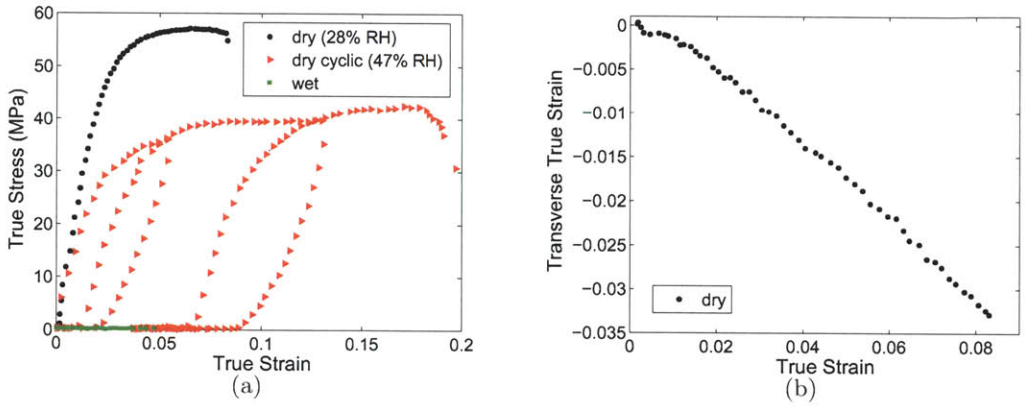

Figure 114: Experimental results of layer-by-layer film subjected to uniaxial tension: (a)stress-strain, (b)transverse strain versus axial strain.

7.1.2 Constitutive model

The LBL film exhibits an elastic-plastic behavior when dry and a highly viscous fluid-like behavior when hydrated. This behavior is constitutively captured via a single mechanism consisting of a linear elastic element in series with a viscoplastic element. The model, which is fully three-dimensional but will be used only to capture the membrane response, is depicted rheologically in Figure 116.

Kinematics:

The total deformation gradient $\mathbf{F} \equiv \frac{\partial \mathbf{x}}{\partial \mathbf{X}}$, mapping a material point from the reference position $\mathbf{X}$ to its current location $\mathbf{x}$, acts in full on the single main component of the model. Following polar decomposition, the deformation gradient can be expressed as the product of a stretch and a rotation:

$$\mathbf{F} = \mathbf{VR} \tag{132}$$

where $\mathbf{V}$ is the left stretch tensor and $\mathbf{R}$ is the rotation.

The deformation gradient for the film can be decomposed into its elastic and plastic contributions (Figure 117).

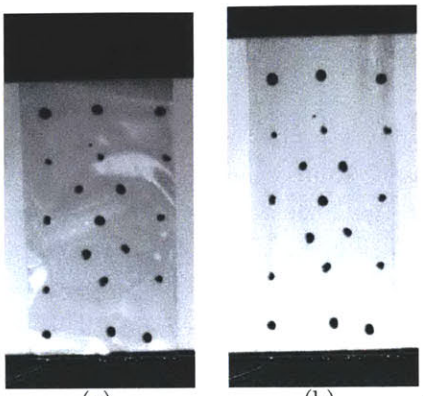

Figure 115: Video extensometer images of the layer-by-layer film: (a)dry, prior to deformation (b) dry, just prior to fracture after uniaxial tension to a strain of 0.08 (c) wet, prior to deformation (d) wet, after uniaxial tension to a strain of 0.2.

Figure 116: Rheological schematic of layer-by-layer constitutive model

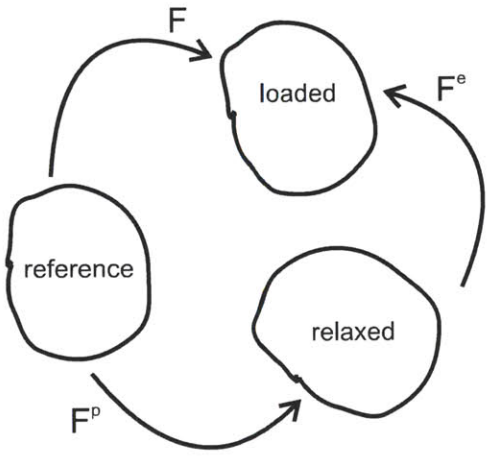

Figure 117: Schematic representation of elastic-viscoplastic framework.

$$\mathbf{F} = \mathbf{F}^e \mathbf{F}^p \tag{133}$$

where $\mathbf{F}^e$ and $\mathbf{F}^p$ are the elastic and plastic deformation gradients. Plastic deformation is assumed to be incompressible such that $J^p = \det \mathbf{F}^p = 1$. The elastic and plastic deformation gradients can each be decomposed into stretch and rotation components.

$$\mathbf{F}^e = \mathbf{V}^e \mathbf{R}^e \tag{134}$$

$$\mathbf{F}^p = \mathbf{V}^p \mathbf{R}^p \tag{135}$$

where $\mathbf{V}^e$ is the elastic left stretch tensor, $\mathbf{R}^e$ is the elastic rotation, $\mathbf{V}^p$ is the plastic left stretch tensor, and $\mathbf{R}^p$ is the plastic rotation.

The rate kinematics are described by the velocity gradient $\mathbf{L} \equiv \dot{\mathbf{F}}\mathbf{F}^{-1}$ which can be decomposed into its elastic ($\mathbf{L}^e$) and plastic ($\mathbf{L}^p$) components.

$$\mathbf{L} = \mathbf{L}^e + \tilde{\mathbf{L}}^p = \mathbf{L}^e + \mathbf{F}^e \mathbf{L}^p \left(\mathbf{F}^e\right)^{-1} \tag{136}$$

$$\mathbf{L}^e = \dot{\mathbf{F}}^e (\mathbf{F}^e)^{-1} \tag{137}$$

$$\mathbf{L}^p = \dot{\mathbf{F}}^p (\mathbf{F}^p)^{-1} \tag{138}$$

where $\mathbf{L}^p$ is defined in the relaxed configuration and $\tilde{\mathbf{L}}^p$ is the plastic velocity gradient in the loaded configuration. The plastic velocity gradient in the loaded configuration can be taken as the sum of the rate of stretching and the rate of spin.

$$\tilde{\mathbf{L}}^p = \tilde{\mathbf{D}}^p + \tilde{\mathbf{W}}^p \tag{139}$$

where $\tilde{\mathbf{D}}^p$ (symmetric tensor) is the rate of plastic stretching and $\tilde{\mathbf{W}}^p$ is the rate of plastic spin. Without loss of generality we choose $\tilde{\mathbf{W}}^p = 0$. The plastic deformation gradient is then updated by:

$$\dot{\mathbf{F}}^p = \mathbf{L}^p \mathbf{F}^p = (\mathbf{F}^e)^{-1} \tilde{\mathbf{D}}^p \mathbf{F} \tag{140}$$

where $\tilde{\mathbf{D}}^p$ must be constitutively prescribed.

Material Description:

The material stress state is related to the deformation by the constitutive law for a linear elastic spring:

$$\mathbf{T} = \frac{1}{J} \mathcal{L}^e \left[\ln \mathbf{V}^e\right] \tag{141}$$

where $\mathbf{T}$ is the Cauchy (true) stress, $J = \det \mathbf{F}^e$ is the volume change, $\mathcal{L}^e$ is the fourth-order modulus tensor, and $\ln \mathbf{V}^e$ is the Hencky strain. It is assumed that the material is initially isotropic and can therefore be defined by any two elastic constants. Here we choose the shear modulus μ_L and the bulk modulus κ_L.

$$\mathcal{L}^e = 2\mu_L \mathcal{I} + \left(\kappa_L - \frac{2}{3}\mu_L\right) \mathbf{I} \otimes \mathbf{I} \tag{142}$$

where $\mathcal{I}$ and $\mathbf{I}$ are the fourth-order and second-order identity tensors, respectively. The shear modulus is taken to be a function of water content ϕ; the bulk modulus is assumed to be independent of water content ($\phi = 0$ under ambient conditions ($30\%RH$) and $\phi = 1$ when the film is in water).

$$\mu_L = \hat{\mu}_L(\phi) = \mu_{L,dry} - (\mu_{L,dry} - \mu_{L,wet})\,\phi \tag{143}$$

The plastic behavior is now prescribed. The plastic stretching tensor in the loaded configuration is given as the product of the scalar rate of plastic deformation and a direction tensor:

$$\tilde{\mathbf{D}}^p = \dot{\gamma}^P \mathbf{N}^p \tag{144}$$

where the direction $\mathbf{N}^p$ is taken to be coaxial with the deviatoric portion of the film stress tensor $\mathbf{T}'$.

$$\mathbf{N}^p = \frac{\mathbf{T}'}{|\mathbf{T}'|} \tag{145}$$

The scalar rate of plastic deformation is constitutively prescribed to follow a rate dependent process driven by the shear stress:

$$\dot{\gamma}^P = \dot{\gamma}_L^o \sinh\left[\frac{\tau}{s_L}\right] \tag{146}$$

where $\dot{\gamma}_L^o$ is a pre-exponential coefficient, $\tau = \sqrt{\frac{1}{2}\mathbf{T}'\mathbf{T}'}$ is the effective shear stress, and s_L is the resistance to yield. The resistance to yield is taken to be a function of water content; the pre-exponential factor is assumed to be independent of water content ($\phi = 0$ under ambient conditions ($30\%RH$) and $\phi = 1$ when the film is in water).

$$s_L = \hat{s}_L(\phi) = s_{L,dry} - (s_{L,dry} - s_{L,wet})\,\phi \tag{147}$$

7.1.3 Material Parameters

This model requires the determination of two parameters defining elasticity (μ_L and κ_L), two parameters defining plasticity (s_L and $\dot{\gamma}_L^o$), and the dependence of μ_L and s_L on water content. The material parameters used in this model are listed in Table 11.

The elastic modulus and Poisson's ratio at ambient conditions are obtained from uniaxial stress-strain and transverse strain data. The shear and bulk moduli are then obtained from their relations to the elastic modulus and Poisson's ratio.

$$\mu_L = \frac{E_L}{2(1+\nu_L)} \tag{148}$$

$$\kappa_L = \frac{E_L}{3(1-2\nu_L)} \tag{149}$$

The parameters defining plasticity at ambient conditions are chosen to result in the appropriate yield stress as determined from uniaxial tensile testing, and do give minimal rate dependence. This is not a unique fit. The rate dependence here is used to simplify model implementation and does not represent a true material property. The actual rate dependent properties were not obtained due to the small quantity of material available for mechanical testing.

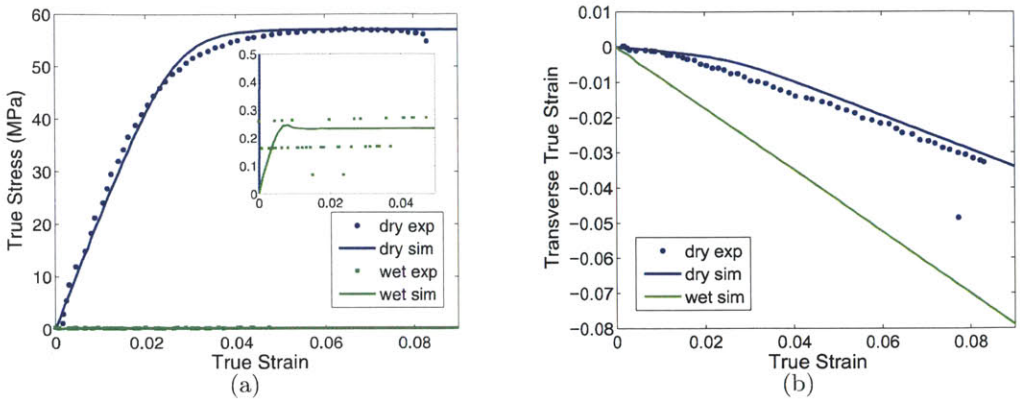

Figure 118: Deformation of the layer-by-layer model subjected to monotonic uniaxial tension compared to experiments: (a)stress-strain, (b)transverse strain versus axial strain.

Hydration in the model is modeled over a continuous spectrum of water content from atmospheric conditions (30% relative humidity) to in water, however it is only validated at these two extremes and will only be used to predict behavior at these two extremes. As such the shear modulus and resistance to yield in the "in water" state are required.

Table 11: Model parameters used in the layer-by-layer model.

Parameter	**Value**
$\mu_{L,dry}$	$1000MPa$
$\mu_{L,wet}$	$150MPa$
κ_L	$920MPa$
$\dot{\gamma}^o$	$2.8 \times 10^{-15} s^{-1}$
$s_{L,dry}$	$1.1MPa$
$s_{L,wet}$	$0.17MPa$

7.1.4 Results and discussion

The LBL dry data is well fit by the model both in terms of stress-strain and transverse strain (Figure 118). The model is able to capture the initial elastic region, the yield event, and the flat post yield region prior to fracture. It also captures the transition in the transverse to axial strain ratio at yield. The model set to the "in water" state approximates an upper bound to the experimental data.

This model does not capture any of the cyclic or rate dependent aspects of the LBL behavior (Figure 119). A much more sophisticated model could be developed along the lines of the Nafion model from Chapter 2, however there is not enough material to get the appropriate data needed to fit such a model, and this is tangential to the goals of this portion of the work.

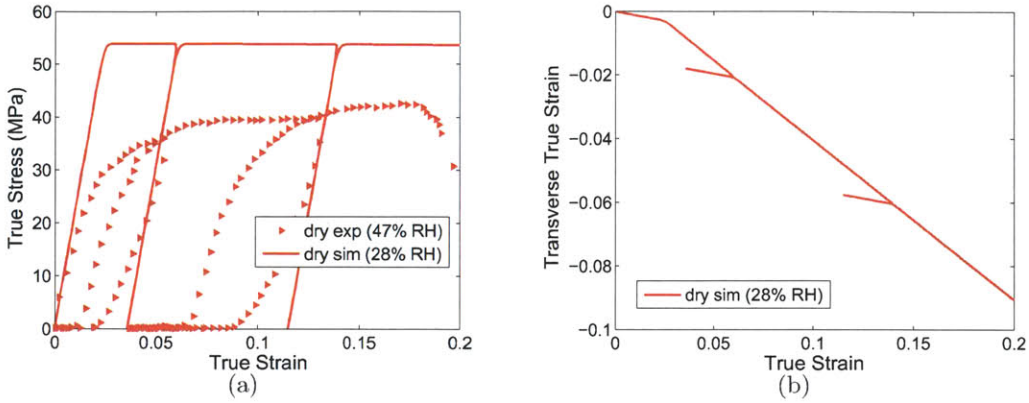

Figure 119: Deformation of the layer-by-layer model subjected to cyclic uniaxial tension compared to experiments: (a)stress-strain, (b)transverse strain versus axial strain.

7.2 Composite model

With a model established for the EFM and LBL behavior separately, a composite model can now be constructed.

7.2.1 Formulation

As a first approximation the composite model is taken simply as a weighted average of the electrospun fiber mat and the layer-by-layer film behaviors. This approximation is taken as reasonable since the two materials are essentially each continuous and interpenetrating. Following this, the deformation gradient $\mathbf{F} \equiv \frac{\partial \mathbf{x}}{\partial \mathbf{X}}$, mapping a material point from the reference position $\mathbf{X}$ to its current location $\mathbf{x}$, is taken to act in full upon both the EFM and the LBL film:

$$\mathbf{F} = \mathbf{F}_{EFM} = \mathbf{F}_{LBL} \tag{150}$$

where $\mathbf{F}_{EFM}$ is the deformation gradient on the EFM and $\mathbf{F}_{LBL}$ is the deformation gradient on the LBL film.

The Cauchy (true) stress ($\mathbf{T}$) is then the weighted sum of the stress on each of the materials.

$$\mathbf{T} = N_{EFM}\mathbf{T}_{EFM} + N_{LBL}\mathbf{T}_{LBL} \tag{151}$$

where N_{EFM} is the EFM weighting factor, $\mathbf{T}_{EFM}$ is the stress on the EFM, N_{LBL} is the LBL weighting factor, and $\mathbf{T}_{LBL}$ is the stress on the LBL coating. The weighting factors N_{EFM} and N_{LBL} are in fact the weight per unit composite volume of the EFM and the LBL coating in the composite relative to their stand-alone densities respectively. $\mathbf{T}_M$ is given by the EFM model as described in Chapter 6. $\mathbf{T}_{LBL}$ is given by the LBL model as described in section 7.1.

7.2.2 Material parameters

Two additional parameters (N_{EFM},N_{LBL}) are needed to create the composite model from the separate EFM and LBL models. Since the EFM is compressed by the LBL spray process its weighting factor is greater than 1 and given by the ratio of the composite thickness to the bare

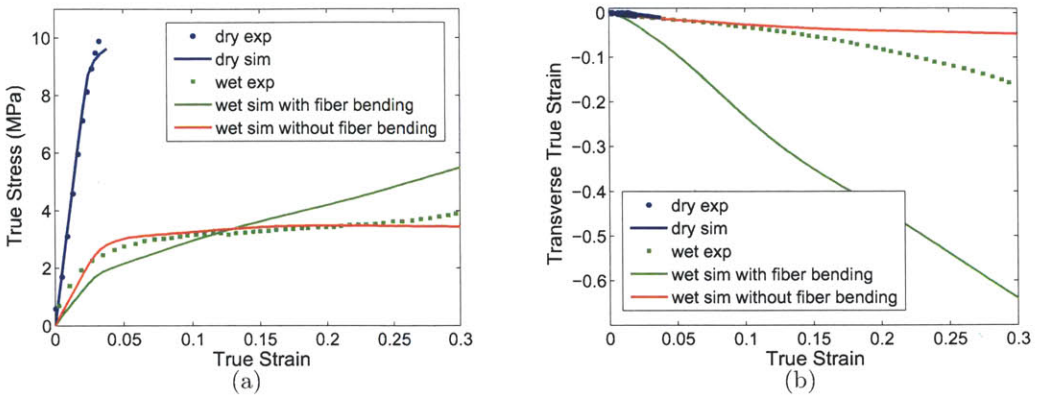

Figure 120: Deformation of the composite model subjected to uniaxial tension compared to experiments: (a)stress-strain, (b)transverse strain versus axial strain.

EFM thickness ($N_{EFM} = 1.4$). The LBL weighting factor is set to give the appropriate composite mat stiffness under dry conditions ($N_{LBL} = 0.09$) which corresponds to an effective LBL density.

7.2.3 Results and discussion

The composite model results are compared to the experiment both in terms of stress-strain and transverse strain in Figure 120. The experimental data is well fit in the dry state where the LBL and EFM behaviors contribute about equally to the total stress response. The LBL significantly inhibits transverse contraction relative to the bare EFM. Since the two materials are constrained to follow the same deformation gradient, the EFM model has quite a different response than it does on its own, in particular it is stiffer in the elastic regime and would have less post yield hardening if the composite did not fracture first.

This simple weighted model does not fit the experimental data well in the wet state. In the model of the wet state the LBL component is very compliant and the composite behavior is dominated by the EFM. This predicts a composite behavior which has lower elastic stiffness and yield stress, greater post yield hardening, and more transverse contraction than that shown in the experimental behavior. To resolve this discrepancy it is proposed that the LBL inhibits EFM fiber bending. Even though the LBL has a low resistance to shear yield in the hydrated state, it still has a large bulk modulus and therefore could significantly influence local deformation mechanisms if loaded volumetrically. It is shown in Figure 120 that the composite model fits the experimental data well if the fibers in the EFM are not allowed to bend (straight fiber model from section 6.5.1). There is some deviation at moderate strain in terms of both strain hardening and transverse strain, suggesting that under enough compression the fibers are able to bend. A more thorough strain energy balance of the LBL filling deformation and the fiber axial and bending deformation could provide a means to get at this effect. Alternatively, there may be a flow of the LBL filling out of the way of the fibers as they try to bend, tests at different rates or stress relaxation tests would be helpful in determining whether this is indeed the governing physics.

An interesting means of comparing the dry and hydrated behavior with and without fiber bending allowed is the look at the yield surfaces of each. This is shown in Figure 121 where each yield surface is normalized by its own uniaxial tensile yield stress. Much as in the uncoated EFM,

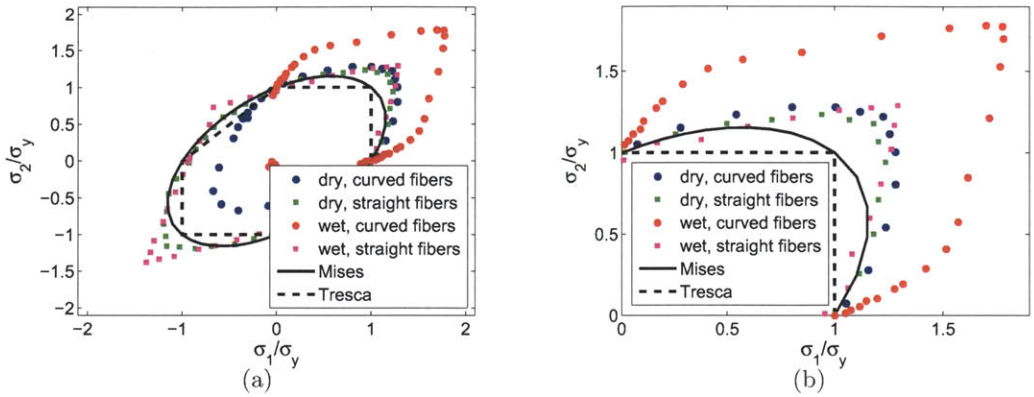

Figure 121: Yield surface of the LBL/EFM composite (using the 8-layer EFM formulation) compared to the Mises and Tresca yield criteria (note the 8-layer formulation is used to allow single element implementation, the yield stress is negligibly different from the 2-layer formulation). Each state is normalized to its own uniaxial yield stress. (a) Full yield surface and (b) upper right quadrant of yield surface. The yield stresses for the four models are as follows: dry straight fiber: $9.1MPa$, dry curved fiber: $8.8MPa$, wet straight fiber: $2.7MPa$, wet curved fiber: $2.0MPa$.

when fiber bending is prohibited, the yield surface is centered about zero stress, but has sharper corners than the Mises or Tresca criteria. The dry straight fiber composite, which has a larger contribution from the LBL material, is more rounded (similar to a Mises material) than the wet composite. The yield surface shifts to the upper right hand quadrant when the fibers are allowed to bend. This shift is more extreme for the wet composite because the EFM dominates the behavior. These yield surfaces show the strong influence of the assumption that the LBL coating restricts fiber bending on not just uniaxial loading, but also on the multiaxial deformation behavior of the composite.

7.3 Concluding remarks

A coarse characterization of the stand alone LBL film mechanical behavior was conducted via uniaxial tensile testing in air and in water. A bare bones constitutive model was then developed to capture the key LBL features including:

- elastic-plastic axial stress-strain behavior including elastic stiffness and yield with minimal post-yield hardening when dry
- transverse strain that changes at yield when dry
- viscous fluid like behavior when hydrated

The composite was also characterized under monotonic tensile loading in air and in water. A composite model was created by combining the EFM and LBL models. It was found that a composite model consisting of a weighted summation of the two component behaviors could capture the dry behavior, but not the hydrated behavior. In the hydrated state, the LBL, which is

itself quite compliant under uniaxial loading, was found to inhibit fiber bending, thereby lending initial elastic stiffness and reducing post-yield hardening in a non-additive manner.

Significant development is still required for this composite. The first is an improvement of the LBL spray process to create a more densely filled EFM that is electrochemically viable. Second, the expected mechanical loading needs to be more clearly defined. Unlike the Nafion system, this composite has relatively small hygrothermal expansion $(1-2\%)$, the main loading will then be during assembly of the cell, which occurs in the dry state. An explicit understanding of the expected assembly process is needed in order to set targets for composite damage resistance. Third, the PEM will be exposed to a water/methanol solution on the anode side in situ, the effect of methanol on the LBL, EFM, and composite therefore needs to be investigated. If the methanol effect were found to be significantly different than water than this could drive towards different material choices or lead to restrictions in the methanol concentrations that can be used in the cell.

There are also a number of development possibilities from a modeling perspective. First of all, more extensive testing is required to assess the details of the LBL/EFM interaction. In the dry state it would be good to be directly measuring the content of LBL coating, perhaps by weighing the EFM before and after coating, in order to validate this against the volume fractions used in the model. There could be some unexpected effects due to the lack of density of the LBL. In the hydrated state, rate dependent uniaxial testing would be useful in determining the nature of the LBL restriction of the EFM deformation. Experimental characterization of different but related material combinations could also be helpful in validating/broadening the model.

Beyond these validation efforts, it would be useful for the model to be expanded past just describing mechanical properties. The EFM composite system lends itself naturally to multiphysics modeling. In the PEM examined here, the electrochemical functionality is through the pores which are occupied by the proton conductive LBL filling. One might expect in the hydrated state that as uniaxial mechanical loading is applied that the through thickness conductivity will decrease since the porosity decreases. Alternatively one might expect that membrane plane biaxial loading would increase the through thickness conductivity. A model that also evaluated the proton transport would be useful for simultaneous optimization of the material design for electrochemical and mechanical performance as well as in mechanically manipulating an existing composite to improve electrochemical performance.

8 Conclusions and future outlook

This thesis has spanned two primary focus areas: (1) characterization and modeling of Nafion in order to understand the behavior of the industrially established proton exchange membrane and (2) mechanical characterization and modeling toward the development of an alternative polymer electrolyte membrane. These two research thrusts were united both by a common technological application and the broader field of microstructurally and micromechanically informed constitutive modeling. The intersection of clean energy and micromechanics is a field that has started to emerge over the last decade. Increasingly, materials systems which have been designed primarily for electrochemical performance, are approaching commercial viability and encountering mechanics limited performance. While the research presented here has focused on fuel cell membranes, the approaches could be useful in guiding design of other energy materials, particularly those that are polymer based.

8.1 Nafion characterization and micromechanical modeling

Chapters 2 through 4 focused on Nafion, the benchmark polymer electrolyte membrane (PEM) for low temperature fuel cells. This polymer has been widely studied due to its use not only in fuel cells, but also for chlorine production and electromechanical actuation (ionic polymer metal composites). Despite decades of experimental characterization and a concerted mechanical modeling effort in the last 10 years, no model had previously been developed that could capture the elastic-plastic cyclic behavior, let alone simultaneously describe the rate dependence, stress relaxation, and creep behavior. The model developed herein captures these features under uniaxial and biaxial loading, as well as the effects of temperature and hydration. The environmental dependence of the mechanical behavior is particularly vital since the membrane frequently operates within the atypically broad glass transition regime, and the presence of water further contributes to the material plasticization. The novel aspects of this model include the back stress which results in inelastic recovery during unloading and the particulars of the hygrothermal property dependence. While these are not inherently unique solutions to the uniaxial experimental data, the success of the Nafion model in predicting a wide range of behavior speaks to the validity of this particular choice of constitutive laws and model parameters.

In Chapter 2 the mechanical behavior of the Nafion (NRE212), which typically serves as the polymer electrolyte membrane in low temperature fuel cells, has been experimentally characterized as a function of rate, temperature, and hydration for both monotonic and cyclic loading. These experiments provide details on the subtleties of the time, temperature, and hydration dependence as well as new details on the cyclic behavior which are critical to understanding membrane deformation and failure in fuel cell operation. The behavior of NRE212 was found to be transversely isotropic and quantitatively, but not qualitatively, dependent on the chemical pre-treatment. Dynamic mechanical analysis showed that, under dry ($30\%RH$) conditions, the material begins to transition from the glassy to the rubbery state at 75^oC, with a glass transition of 105^oC. DMA further revealed that the fully hydrated state is significantly more compliant than the dry state, with the material beginning to transition from the glassy to the rubbery state at 40^oC. Large strain monotonic tensile tests revealed an initial elastic response followed by a rollover type yield and moderate post-yield strain hardening. The rate-dependent stress-strain behavior was seen to be highly dependent on temperature and hydration: the dry state transitions from an elastic-plastic behavior at 25^oC to an increasingly rubbery behavior with decreasing elastic modulus and yield stress as temperature

is increased through the glass transition to 100^oC. At all temperatures, increasing hydration acts to decrease the elastic stiffness and yield stress. Unloading from different strains revealed the elastic-plastic nature of the behavior even for the elevated temperature and hydrated states. Cyclic loading-unloading-reloading excursions to different strains showed significant nonlinear recovery at all strains past yield with a highly nonlinear reloading behavior which has an apparent reduced yield stress and then rejoins the initial loading path.

A constitutive model was developed in two stages to capture the mechanical behavior of Nafion NRE212; the first to capture all the key elements of monotonic loading and the second to capture all the key elements of more general loading histories. Model I, consisting of a linear elastic-plastic intermolecular component and a nonlinear network component, was shown to be capable of capturing the rate, temperature, and hydration dependence of monotonic loading but not the unloading or reloading behavior. The intermolecular resistance captures the local intermolecular barriers to initial elastic deformation and also captures the thermally-activated nature of yield; these intermolecular barriers are modeled to decrease with increasing temperature and hydration, in particular mimicking the reduction in these barriers as the material approaches and enters the glass transition regime, successfully capturing the strong temperature and hydration dependence of the stress-strain behavior. Model II, a version of Model I enhanced with the addition of a back stress to the viscoplastic element in the intermolecular component, was shown to additionally be capable of capturing the rate, temperature, and hydration dependence of the cyclic response. The back stress has similar properties to the intermolecular elastic-plastic element, with an initial elastic portion, a rate dependent saturation, and barriers which decrease in the same way with temperature and hydration. The back stress develops during inelastic deformation and then helps to drive reverse deformation during unloading. The back stress enables the model to capture the highly nonlinear nature of unloading and reloading including the reduction in reloading yield stress which occurs with increasing strain. Impressively, this model captures the temperature and hydration dependence of the cyclic behavior without any additional material parameters. Model II is capable of capturing the behavior of Nafion over the wide range of strains, environmental conditions, and loading conditions relevant to modeling the membrane within the fuel cell. The additional features of Model II will enable analysis of the pertinent complex hygrothermal-mechanical loading conditions. The constitutive model has been formulated for use within nonlinear finite element analysis enabling more general application.

In Chapter 3 the small and wide angle x-ray scattering (SAXS and WAXS) were used to characterize the evolving Nafion microstructure under uniaxial tension. While similar experiments have been carried out before, they did not include force or time dependent information and were on extruded forms of Nafion, making analysis difficult. Three types of uniaxial tensile experiments were conducted: monotonic, cyclic, and stress relaxation. Two peaks each were found in the SAXS and WAXS scattering profiles at $q = 0.6nm^{-1}$, $2.2nm^{-1}$, $12.1nm^{-1}$, and $27.9nm^{-1}$. The WAXS peaks are at the q-values expected from literature, the ionomer peak is at a somewhat higher value than expected ($2.2nm^{-1}$ vs $1.9nm^{-1}$), likely due to the difference in processing between the chemically recast and extruded forms of Nafion. It was found that each of these peaks evolves closely with strain (as opposed to stress) in either location or intensity, but that there is also a time dependent aspect to the evolution which depends on the magnitude of the stress.

The x-ray scattering information was interpreted building on the existing literature. The structure of Nafion was taken to be composed of randomly oriented crystalline regions and randomly oriented cylindrically shaped ionomer clusters consisting of aligned backbone strands with the sul-

fonated side chains pointing inward with intermediate amorphous regions. The peaks correspond to spacing between crystallites (peak 1), spacing between ionomer clusters (peak 2), inter-strand backbone spacing (peak 3, from both the crystallites and the semi-orderly clusters), and intra-strand backbone spacing (peak 4, from the crystallites). The key findings from this experimental study were:

- Structure is initially transversely isotropic in the membrane plane.
- Microstructure evolution is tied more tightly with macroscopic strain than with stress.
- Microstructure continues to evolve while stress relaxes at constant strain.
- Crystallites displace greater than affinely at all strains.
- Ionomer clusters displace approximately affinely at small strains (behavior at moderate to large strain unknown).
- Crystallite and ionomer clusters rotate to align with applied strain. The rotation is affine until a strain of 0.2 and less than affine at larger strains.

The microstructural evolution was then interpreted within the frame of the continuum model:

- There are three microstructural features that contribute to the overall stress response: crystallites, ionomer clusters, intermediate amorphous regions.
- Crystallites are effectively rigid at all relevant temperatures, hydrations, and loading conditions.
- Ionomer clusters are reasonably stiff under ambient conditions but have a compliance strongly positively correlated with water content.
- Amorphous regions have a stiffness and yield dependent on temperature but not hydration.
- Yield is governed by the amorphous regions.
- The back stress results from restrictions of the amorphous region plasticity due to its binding to the crystallites which are then forced to rotate with the matrix.
- The back stress yields when the activation energy is great enough for the amorphous matrix to shear past the crystallites and plastically deforming regions can merge with each other.
- It is unclear what the yield contribution of the clusters is since this peak is barely within the SAXS detection range.

In chapter 4, the biaxial and constrained swelling behavior of Nafion was investigated via experiments and modeling. Biaxial testing was conducted via in-plane tensile testing of cruciform shaped specimens. A video extensometer system was used to enable determination of the local biaxial response in the central region. The biaxial response was qualitatively similar to the uniaxial response with the stiffness and strength in a given direction dependent on the degree of biaxiality. The constitutive model developed for Nafion based on uniaxial tensile data was used to simulate these experiments via a finite element implementation. These simulations revealed that the stress

distribution was not completely uniform in the central "biaxial" region of the specimen. The cruciform specimens result in a greater and sharper yield event as compared to the pure homogenous biaxial response. Nonetheless, the constitutive model was shown to well predict this complex multiaxial deformation response when the model is implemented in the experimental geometry and reduced by the same methods as the experimental results. These results also indicated that while the initial yield under equibiaxial and uniaxial loading conditions are the same, the evolution in strength with strain (the rollover nature of yield) gives the appearance of a greater yield stress during biaxial loading compared to uniaxial loading - an effect captured by the model. It should be noted that no material parameters were modified to fit the biaxial data, the success therefore demonstrates the truly predictive capability of the model. The biaxial testing method and predictive constitutive modeling have broad relevance to polymeric membranes, especially considering the need for robustness to biaxial loading for polymer membranes in a wide range of separation and transport processes.

Bimaterial strip swelling was used then to probe the partially constrained swelling behavior of Nafion. When the strip was hydrated the membrane swelled, causing the strip to curl with the membrane on the convex side until the force from the membrane was balanced by a moment in the GDL. The bending stiffness of the GDL induced compressive plastic deformation in the membrane which then induced a slight curvature upon drying with the membrane on the concave side. The hydrated and dried radii were found to agree with the finite element simulation predictions for two thicknesses of Nafion to within experimental error.

Finally, the Nafion constitutive model was used to simulate a simplified fuel cell cycle. Simulations of this nature are useful in guiding startup and shutdown procedures for fuel cells, for designing/validating potential procedures for accelerated lifetime testing, and for designing alternative fuel cell geometries. The particular hygro-thermal cycles chosen were not meant to precisely duplicate those of an operating fuel cell, but rather to demonstrate the power of a three dimensional continuum model and assess potential mechanical damage mechanisms. The findings of previous researchers were confirmed that a tensile stress arises in the plane of the membrane upon drying. Further, a negative hydrostatic pressure develops in the channel suggesting a driving force for cavitation or crazing. A study of the effect of ramp rate and hold time revealed a significant time dependence of the pressure, which is not surprising given the significant rate dependence observed for Nafion under uniaxial mechanical loading.

8.2 Composite polymer electrolyte membrane design

Chapters 5 through 7 concern the mechanical aspects of the design of an alternative polymer electrolyte membrane for direct methanol fuel cells. The alternative membrane was constructed from the highly proton conductive and methanol resistant layer-by-layer (LBL) assembled PDAC/sPPO vacuum deposited onto a mechanically robust electrospun polyamide fiber mat (EFM). Each of the material components was separately characterized and modeled. Particular emphasis was placed on developing a microstructurally-based constitutive model to describe the elastic-plastic behavior of non-woven mats. The non-woven mat model ties the fiber constitutive behavior and mat geometry directly to a macroscopic constitutive response. The model is designed to be quite general, applying to any layered non-woven in which fiber behavior dominates over the bond effects such as rotational stiffness or bond slippage. Efforts towards developing a composite model showed that a simple weighted average approach is not sufficient to describe the composite mechanical behavior and helped elucidate the interactions between the EFM and the LBL.

In chapter 5 the direct methanol fuel cell membrane, which is being developed in conjunction with the Hammond lab in chemical engineering at MIT, was introduced. In the design, a material that performs well electrochemically but poorly mechanically, is combined with a material that serves no electrochemical function, but performs well mechanically. Specifically, poly(diallyl dimethyl ammonium chloride) and sulfonated Poly(2,6-dimethyl 1,4-phenylene oxide) are deposited via the layer-by-layer method onto a highly porous electrospun polyamide mat. Each of the materials (stand alone layer-by-layer film, electrospun mat, and composite) is characterized under monotonic loading at ambient conditions and when wet. The LBL mat is elastic-plastic and subject to tearing at low strains when dry. It has a Poisson's ratio of 0.08 in the elastic regime, followed by a transition to a transverse strain ratio of -0.5 at yield. The EFM is also elastic-plastic when dry, but is about $1/20^{th}$ the stiffness of the LBL and highly extensible. The transverse strain behavior is quite different from that of the LBL, there is a small initial regime at which the Poisson's ratio is close to zero followed by a drastic change in slope to a transverse contraction to axial strain ratio greater than 1. The composite shows an intermediate behavior in terms of stiffness and yield stress, but takes on the failure strain and transverse contraction of the LBL. It is clear that when dry the LBL dominates the composite transverse contraction behavior. In the hydrated state the relative behavior of the three materials changes significantly. The stand-alone LBL is nearly fluid like, dropping by a factor of 100 in yield stress, and becoming extensible to large strains without tearing. The EFM remains elastic-plastic and highly extensible with less than a factor of 2 drop in stiffness and minimal change in transverse strain behavior. The coated mat in the hydrated state remains elastic-plastic, drops in stiffness and yield by a factor of 5, becomes highly extensible, and is stiffer than either the LBL or the EFM in this state. The LBL is able to lend axial stiffness and resistance to transverse contraction to the EFM in the hydrated state even though it has minimal stiffness on its own under uniaxial tension.

In chapter 6, the randomly oriented non-woven electrospun mats were first experimentally characterized and then modeled. Experimental mechanical characterization of fibers electrospun from amorphous polyamide revealed that the fibers are elastic-plastic with a wide spread in yield stress and post-yield hardening. Experimental mechanical characterization of random mats electrospun from the same polymer solution revealed that these mats are elastic-plastic with significant post-yield hardening. At small strains the initial Poisson's ratio is near zero implying an initial structural rigidity opposing fiber alignment. This resistance is then overcome and the transverse strain decreases more than the vertical strain increases. Under cyclic loading the mats are seen to unload and reload in a nearly linear manner and exhibit an elastic modulus that increases significantly with strain. The post-yield hardening and the apparent increase in elastic modulus with cycling to larger strains arise from consolidation and alignment of the fibers. The consolidation and alignment are also underlying the observed transverse strain behavior. The specimen aspect ratio was found to significantly influence the reduced stress-strain and transverse strain response with a 1:1 ratio giving a nearly plane strain constraint, constraining contraction.

A microstructurally-based constitutive model for the elastic-plastic behavior of non-woven mats was constructed. In the model, the mat structure is idealized as a triangulated network of elastic-plastic fibers. The layered network is captured by a representative volume element consisting of a double layer structure where each layer is a triangulated network and the layers are offset 30^o from each other. The layers impose mutual kinematic constraints emulating the layered structure of real mats, providing greater isotropy to the yield and post-yield behavior. The behavior of the constituent fibers was taken to be elastic-plastic accounting for stretching and bending of the fibers

when subjected to end tensile and compressive loads; the bending of the fibers when a fiber is locally under compression was found to be the key mechanism enabling the mat to consolidate during tensile loading. The resulting double layer triangulated network of fibers which exhibit elastic-plastic stretch and bending was found to capture all features of the uniaxial behavior of the mats including:

- elastic-plastic axial stress-strain behavior including elastic stiffness, yield, and post-yield hardening
- transverse strain
- cyclic load-unload-reload behavior
- evolution in elastic stiffness with plastic strain
- dependence of the elastic-plastic behavior on hydration

The model was further validated via comparison to experiments of axial loading subject to different axial constraints, from nearly uniaxial to nearly plane strain. The model was found to match the deformed specimen shape, stress-strain, and transverse strain responses for this range of grip induced constraint. Biaxial loading predictions and the corresponding yield surface further highlight the critical influence of fiber bending under local compression. Predictions of the material response with modifications to mat geometry made with the model, show a strong dependence of the elastic-plastic response on fiber radius and porosity and a weak dependence of the elastic-plastic response on junction-junction spacing. Since the physics in the EFM model is not specific to polyamide beyond the choice of fiber constitutive properties, it is expected that this model will be transferable to other electrospun materials and to other layered random networks more generally.

In chapter 7 a coarse characterization of the stand alone LBL film mechanical behavior was conducted via uniaxial tensile testing in air and in water. A bare bones constitutive model was then developed to capture the key LBL features including:

- elastic-plastic axial stress-strain behavior including elastic stiffness and yield with minimal post-yield hardening when dry
- transverse strain that changes at yield when dry
- viscous fluid like behavior when hydrated

A composite model was created by combining the EFM and LBL models. It was found that a composite model consisting of a weighted summation of the two component behaviors could capture the dry behavior, but not the hydrated behavior. In the hydrated state, the LBL, which is itself quite compliant under uniaxial loading, was found to inhibit fiber bending, thereby lending initial elastic stiffness and reducing post-yield hardening in a non-additive manner.

8.3 Future directions

The future paths for both the Nafion and the composite PEM modeling lay along two interrelated directions, captured in short by "microstructurally and micromechanically motivated modeling" and "multiphysics".

Microstructurally and micromechanically informed modeling:

A microstructurally and micromechanically informed model should allow prediction of a broad range of mechanical behavior of a material (whatever is relevant to the application) with as few experiments as possible. While the current Nafion model is broadly tied to microstructural and molecular mechanisms, significant progress can still be made. Nafion has several components of relevant structure: crystallites, structured amorphous regions (ionomer clusters), and unstructured amorphous regions. The interaction and evolution of the structural features is complex and difficult to track through existing experimental approaches. Even more fundamentally, modeling the deformation response of any one of these quantitatively from a molecular level is challenging. Because polymers are active at many time and length scales, molecular dynamics approaches to modeling mechanical properties have proved intransigent (e.g. Riggleman et al. (2010); Capaldi et al. (2002); Lyulin et al. (2005); Meijer and Govaert (2005)). Nonetheless, this could be an interesting material for the application of a multiscale modeling approach. Since there are identifiable nano-to-micro scale features, Nafion could be a useful test case for building simulations towards quantitatively accurate material parameters. For instance, molecular dynamics could be used to investigate the interface between the amorphous regions and the crystallites. Existing micromechanical models for Nafion which seek to numerically relate the material properties to the underlying structure have been limited to scaling of the elastic modulus with ion type and solvent content (e.g Kusoglu et al. (2008); Nemat-Nasser (2008)).

The composite and non-woven mat models already rely heavily upon the microstructure. The underlying constitutive behavior of the material which composes the fibers in the electrospun fiber mat (EFM) can be taken as a known input since within a given mat the fiber material and geometry are features which can be controlled from a design perspective. The main model improvement that is required is a direct means of determining the effective force-stretch response of the fibers under compression when contained within the mat. In the current model, the force-stretch relation under compression was determined by fitting the mat transverse behavior to the experimental behavior. Perhaps finite element simulations of small regions of the mat with fiber-fiber contact active could help elucidate this relation. Primarily though, the non-woven model would benefit from further validation. Among EFM, it needs to be verified for other fiber radii, cross-link densities, porosities, and materials. The EFM model should then also be assessed for other non-wovens. The composite model is relatively undeveloped, although it does benefit from relying on quite tangible physical concepts. More extensive testing is required to assess the details of the LBL/EFM interaction. It would then be useful to generalize the composite model to other combinations of materials.

Multiphysics modeling:

"Multiphysics" refers to a situation in which multiple physical phenomena are relevant/active at the same time and often coupled. Multiphysics concerns are quite typical of energy materials. Electrochemical systems in particular will have an ongoing solvent and ion transport during mechanical loading. Model functionality would be vastly expanded via explicit incorporation of electrochemical aspects. The importance of multiphysics modeling has already been touched upon to some extent within the Nafion model discussion. The water and ion transport is needed to realistically simulate mechanical loading of the membrane within a fuel cell. Beyond the benefit to direct mechanical modeling, a coupled mechanical-electrochemical membrane model could be incorporated into the overall fuel cell models that are being developed (e.g. Yoon and Huang (2010)). Such a model is most typically used in bipolar plate channel design to manipulate fuel flow/distribution, but can also be used to investigate susceptibility to instabilities (say if a temporary local hot spot develops,

will it cascade and lead to rapid local membrane failure).

The EFM composite system lends itself naturally to multiphysics modeling. The electrochemical functionality can either be along the fibers or through the pores (spaces between the fibers), both rapidly identifiable physical features. In the PEM examined here, the functionality is through the pores which are occupied by the proton conductive LBL filling. One might expect in the hydrated state that as uniaxial mechanical loading is applied that the through thickness conductivity will decrease since the porosity decreases. Alternatively one might expect that membrane plane biaxial loading would increase the through thickness conductivity. Of course there may well be some complex relation owing to an evolving orientation of proton conducting channels within the LBL. The point is that with a micromechanically based model the evolution of critical features (pore size in the aforementioned example) can be tracked. The information from the model can then be used in conjunction with electrochemical experiments (4-point electrochemical impedance spectroscopy in this case) to posit constitutive relations between mechanical features and electrochemical performance. A multiphysics composite model would be useful for simultaneous optimization of the material design for electrochemical and mechanical performance as well as in mechanically manipulating an existing composite to improve electrochemical performance.

References

Adams, A., Buckley, C., Jones, D., 1998. Biaxial hot drawing of poly(ethylene terephthalate): measurements and modelling of strain-stiffening. Polymer 39, 5761–5763.

Adams, A., Buckley, C., Jones, D., 2000. Biaxial hot drawing of poly(ethylene terephthalate): measurements and modelling of strain-stiffening. Polymer 41, 771–786.

Ames, N., Srivastava, V., Chester, S., Anand, L., 2009. A thermo-mechanically coupled theory for large deformations of amorphous polymers: Part II: Applications. International Journal of Plasticity 25, 1495–1539.

Anand, L., Ames, N., Srivastava, V., Chester, S., 2009. A thermo-mechanically coupled theory for large deformations of amorphous polymers: Part I: Formulation. International Journal of Plasticity 25, 1474–1494.

Argun, A., Ashcraft, J., Hammond, P., 2008. Highly conductive methanol resistant polyelectrolyte multilayers. Advanced Materials 20, 1539–1543.

Arruda, E., Boyce, M., 1993. Evolution of plastic anisotropy in amorphous polymers during finite straining. International Journal of Plasticity 9, 697–720.

Arruda, E., Boyce, M., Jayachandran, R.. 1995. Effects of strain rate, temperature, and thermo-mechanical coupling on the finite strain deformation of glassy polymers. Mechanics of Materials 19, 193–212.

Arslan, M., Boyce, M., 2006. Constitutive modeling of the finite deformation behavior of membranes possessing a triangulated network microstructure. Transactions of the ASME 73, 536–543.

Ashcraft, J., August 2009. Tuning the transport properties of layer-by-layer thin films for fuel cell applications. Phd thesis, Massachusetts Institute of Technology, Cambridge, MA.

Barbi, V., Funari, S., Gehrke, R., Scharnagl, N., Stribeck, N., 2003. Nanostructure of Nafion membrane material as a function of mechanical load studied by SAXS. Polymer 44, 4853–4861.

Bell, G., Bieliński, D., Beake, B., 2008. Influence of water on the nanoindentation creep response of nylon 6. Journal of Applied Polymer Science 107, 577582.

Bergstrom, J., Boyce, M., 1998. Constitutive modeling of the large strain time-dependent behavior of elastomers. Journal of Mechanics and Physics of Solids 46, 931–954.

Bergstrom, J., Hilbert, L., 2005. A constitutive model for predicting the large deformation thermo-mechanical behavior of fluoropolymers. Mechanics of Materials 37, 899–913.

Borup, R., Meyers, J., Pivovar, B., Kim, Y., Mukundan, R., Garland, N., Myers, D., Wilson, M., Garzon, F., Wood, D., Zelenay, P., More, K., Stroh, K., Zawodzinski, T., Boncella, J., McGrath, J., Inaba, M., Miyatake, K., Hori, M., Ota, K., Ogumi, Z., Miyata, S., Nishikata, A., Siroma, Z., Uchimoto, Y., Yasuda, K., Kimijima, K., Iwashita, N., 2007a. Scientific aspects of polymer electrolyte fuel cell durability and degradation. Chemical Reviews 107, 3904–3951.

Borup, R., Meyers, J., Pivovar, B., Kim, Y. S., Mukundan, R., Garland, N., Myers, D., Wilson, M., Garzon, F., Wood, D., Zelenay, P., More, K., Stroh, K., Zawodzinski, T., Boncella, J., McGrath, J. E., Inaba, M., Miyatake, K., Hori, M., Ota, K., Ogumi, Z., Miyata, S., Nishikata, A., Siroma, Z., Uchimoto, Y., Yasuda, K., Kimijima, K., Iwashita, N., 2007b. Scientific aspects of polymer electrolyte fuel cell durability and degredation. Chemical Reviews 107, 3904–3951.

Boyce, M., Arruda, E., 2001. Swelling and mechanical stretch of elastomeric materials. Mathematics and Mechanics of Solids 6, 641–659.

Boyce, M., Parks, D., Argon, A., 1988. Large inelastic deformation of glassy-polymers. 1. Rate dependent constitutive model. Mechanics of Materials 7, 15–33.

Boyce, M., Socrate, S., Llana, P., 2000. Constitutive model for the finite deformation stress-strain behavior of poly(ethylene terephthalate) above the glass transition. Polymer 41, 2183–2201.

Bronkhorst, C., 2003. Modelling paper as a two-dimensional elastic-plastic stochastic network. International Journal of Solids and Structures 40, 5441–5454.

Bruce, P., Vincent, C., 1993. Polymer electrolytes. Journal of the Chemical Society-Faraday Transactions 89, 3187–3203.

Buckley, C., Jones, D., 1995. Glass-rubber constitutive model for amorphous polymers near the glass transition. Polymer 36, 3301–3312.

Capaldi, F., Boyce, M., Rutledge, G., 2002. Enhanced mobility accompanies the active deformation of a glassy amorphous polymer. Physical Review Letters 89, 175505–1–4.

Cox, H., 1952. The elasticity and strength of paper and other fibrous materials. British Journal of Applied Physics 3, 72–79.

Demmerle, S., Boehler, J., 1993. Optimal-design of biaxail tensile cruciform specimens. Journal of Mechanics and Physics of Solids 41, 143–181.

Dillard, D., Li, Y., Grohs, J., Case, S., Ellis, M., Lai, Y., Budinski, M., Gittleman, C., 2009. On the use of pressure-loaded blister tests to characterize the strength and durability of proton exchange membranes. Journal of Fuel Cell Science and Technology 6, 031014–1–8.

Dupaix, R., Boyce, M., 2007. Constitutive modeling of the finite strain behavior of amorphous polymers in and above the glass transition. Mechanics of Materials 39, 39–52.

Elliott, J., Hanna, S., Elliott, A., Cooley, G., 2000. Interpretation of the small-angle x-ray scattering from swollen and oriented perfluorinated ionomer membranes. Macromolecules 33, 4161–4171.

Escoubes, M., Pineri, M., Robens, E., 1984. Application of coupled thermal-analysis techniques to thermodynamic studies ofwater interactions with a compressible ionic polymer matrix. Thermochimica Acta 82, 149–160.

Flory, P., Rehner, J., 1943. Mechanics of cross-linked polymer networks 2, swelling. Journal of Chemical Physics 11, 521–526.

Freund, L., Suresh, S., 2003. Thin Film Materials: Stress, Defect Formation and Surface Evolution. Cambridge University Press.

Gasteiger, H., Mathias, M., 2005. Fundamental research and development challenges in polymer electrolyte fuel cell technology. Proton Conducting Membrane Fuel Cells III, Proceedings 2002, 1–24.

Gebel, G., Aldebert, P., Pineri, M., 1993. Swelling study of perfluorosulphonated ionomer membranes. Polymer 34, 333–339.

Gerlach, C., Buckley, C., Jones, D., 1998. Development of an integrated approach to modelling of polymer film orientation processes. Chemical Engineering Research and Design 76, 38–44.

Hannon, A., Tiernan, P., 2008. A review of planar biaxial tensile test systems for sheet metal. Journal of Materials Processing Technolgy 198, 1–13.

Harrysson, A., Ristinmaa, M., 2008. Large strain elasto-plastic model of paper and corrugated board. International Journal of Solids and Structures 45, 3334–3352.

Hasan, O., Boyce, M., 1993. Energy storage during inelastic deformation of glassy polymers. Polymer 34, 5085–5092.

Hasan, O., Boyce, M., 1995. A constitutive model for the nonlinear viscoelastic viscoplastic behavior of glassy polymers. Polymer and Engineering Science 35, 331–344.

Haung, X., Solasi, R., Zou, Y., Feshler, M., Reifsnider, K., Condit, D., Burlatsky, S., Madden, T., 2006. Mechanical endurance of polymer electrolyte membrane and PEM fuel cell durability. Journal of Polymer Science Part B: Polymer Physics 44, 2346–2357.

Hector, L., Lai, Y., Tong, W., Lukitsch, M., 2007. Strain accumulation in polymer electrolyte membrane and membrane electrode assembly materials during a single hydration/dehydration cycle. Journal of Fuel Cell Science and Technology 4, 19–28.

Heijden, P., Bouzenad, F., Diat, O., 2004a. Birefringence study of drawn Nafion films. Journal of Polymer Science: Part B: Polymer Physics 42, 2857–2870.

Heijden, P., Rubatat, L., Diat, O., 2004b. Orientation of drawn Nafion at molecular and mesoscopic scales. Macromolecules 37, 5327–5336.

Herrmann, A., February 2006. Instrumentation for multiaxial mechanical testing of inhomogeneous elastic membranes. MS thesis, Massachusetts Institute of Technology, Cambridge, MA.

Hickner, M., Ghassemi, H., Kim, Y., Einsla, B., McGreth, J., 2004. Alternative polymer systems for proton exchange membranes (PEMs). Chemical Reviews 104, 4587–4612.

Hohman, M., Shin, M., Rutledge, G., Brenner, M., 2001. Electrospinning and electrically forced jets. II. Applications. Physics of Fluids 13, 2221–2236.

Holzapfel, G., 2000. Nonlinear Solid Mechanics: A Continuum Approach for Engineering. John Wiley and Sons.

Hsu, W., Gierke, T., 1982. Elastic theory for ionic clustering in perfluorinated ionomers. Macromolecules 15, 101–105.

Hsu, W., Gierke, T., 1983. Ion-transport and clustering in Nafion perfluorinated membranes. Journal of Membrane Science 13, 307–326.

Hubner, G., Roduner, E., 1999. EPR investigation of HO radical initiated degradation reactions of sulfonated aromatics as model compounds for fuel cell proton conducting membranes. Journal of Materials Chemistry 9, 409–418.

Inaba, M., Kinumoto, T., Kiriake, M., Umebayashi, R., Tasaka, A., Ogumi, Z., 2006. Gas crossover and membrane degradation in polymer electrolyte fuel cells. Electrochimica Acta 51, 5746–5753.

Isaksson, P., 2010. An implicit stress gradient plasticity model for describing mechanical behavior of planar fiber networks on a macroscopic scale. Engineering Fracture Mechanics 77, 1240–1252.

James, P., Elliott, J., McMaster, T., Newton, J., Elliott, A., Hanna, S., Miles, M., 2000. Hydration of Nafion studied by AFM and X-ray scattering. Journal of Materials Science 25, 5111–5119.

Jannasch, P., 2003. Recent developments in high-temperature proton conducting polymer electrolyte membranes. Current Opinion in Colloid and Interface Science 8, 96102.

Jearanaisilawong, P., May 2008. A continuum model for needlepunched nonwoven fabrics. Phd thesis, Massachusetts Institute of Technology, Cambridge, MA.

Kar, K., 2007. http://www.iitk.ac.in/infocell/iitk/newhtml/storyoftheweek42.htm.

Kong, X., Schmidt-Rohr, K., 2011. Water polymer interfacial area in Nafion: Comparison with structural models. Polymer xxx, 1–4.

Kundu, S., Simon, L., Fowler, M., Grot, S., 2005. Mechanical properties of nafion electrolyte membranes under hydrated conditions. Polymer 46, 11707–11715.

Kusoglu, A., Karlsson, A., Santare, M., Cleghorn, S., Jonhson, W., 2006. Mechanical response of fuel cell membranes subjected to a hygro-thermal cycle. Journal of Power Sources 161, 987–996.

Kusoglu, A., Santare, M., Karlsson, A., Cleghorn, S., Johnson, W., 2010a. Numerical investigation of mechanical durability in polymer electrolyte membrane fuel cells. Journal of The Electrochemical Society 157, B705–B713.

Kusoglu, A., Santare, M., Karlsson, A., Cleghorn, S., Jonhson, W., 2008. Micromechanics model based on the nanostructure of PFSA membranes. Journal of Polymer Science: Part B: Polymer Physics 46, 2404–2417.

Kusoglu, A., Tang, Y., Lugo, M., Karlsson, A., Santare, M., Cleghorn, S., Johnson, W., 2010b. Constitutive response and mechanical properties of pfsa membranes. Journal of Power Sources 195, 483–492.

Kusoglu, A., Tang, Y., Santare, M., Karlsson, A., Cleghorn, S., Johnson, W., 2009. Stress-strain behavior of perfluorosulfonic acid membranes at various temperatures and humidities: Experiments and phenomenological modeling. Journal of Fuel Cell Science and Technology 6.

Lagarón, J., Giménez, E., Gavara, R., Saura, J., 2001. Study of the influence of water sorption in pure components and binary blends of high barrier ethylene-vinyl alcohol copolymer and amorphous polyamide and nylon-containing ionomer. Polymer 42, 9531–9540.

Lai, Y., Mittelsteadt, C., Gittleman, C., Dillard, D., 2009a. Viscoelastic stress analysis of constrained proton exchange membranes under humidity cycling. Journal of Fuel Cell Science and Technology 6, 021002–1–13.

Lai, Y., Mittlesteadt, C., Gittleman, C., Dillard, D., 2009b. Viscoelastic stress analysis of constrained proton exchange membranes under humidity cycling. Journal of Fuel Cell Science and Technology 6, 021002–1–13.

Lai, Y., Rapaport, P., Ji, C., Kumar, V., 2008. Channel intrusion of gas diffusion media and the effect on fuel cell performance. Journal of Power Sources 184, 120–128.

Li, B., Wang, L., Kang, B., Wang, P., Qiu, Y., 2006. Review of recent progress in solid-state dye-sensitized solar cells. Solar Energy Materials and Solar Cells 90, 549–573.

Li, Y., Dillard, D., Case, S., Ellis, M., Lai, Y., Gittleman, C., Miller, D., 2009. Fatigue and creep to leak tests of proton exchange membranes using pressure-loaded blisters. Journal of Power Sources 194, 873–879.

Li, Y., Dillard, D., Lai, Y., Case, S., Ellis, M., Budinski, M., Gittleman, C., 2010. Measuring hygrothermal stresses in constrained proton exchange membranes using a bimaterial curvature method. Experimental Mechanics submitted.

Li, Y., Quincy, J., Case, S., Ellis, M., Dillard, D., Lai, Y., Budinski, M., Gittleman, C., 2008. Characterizing the fracture resistance of proton exchange membranes. Journal of Power Sources 185, 374–380.

Liu, D., Hickner, M., Case, S., Lesko, J., 2006a. Relaxation of proton conductivity and stress in proton exchange membranes under strain. Journal of Engineering Materials and Technology 128, 503–508.

Liu, D., S.Kyriakides, Case, S., Lesko, J., Li, Y., McGrath, J., 2006b. Tensile behavior of Nafion and sulfonated poly(arylene ether sulfone) copolymer membranes and its morphological correlations. Journal of Polymer Science Part B: Polymer Physics 44, 1453–1465.

Lutkenhaus, J., Hammond, P., 2007. Electrochemically enabled polyelectrolyte multilayer devices: from fuel cells to sensors. Soft Matter 3, 804–816.

Lyulin, A., Vorselaars, B., Mazo, M., Balabaev, N., Michels, M., 2005. Strain softening and hardening of amorphous polymers: Atomistic simulation of bulk mechanics and local dynamics. Europhysics Letters 71, 618–624.

MacKintosh, F., Kas, J., Jamney, P., 1995. Elasticity of semiflexible biopolymer networks. Physical Review Letters 75, 4425–4428.

Majsztrik, P., Bocarsly, A., Benziger, J., 2008. Viscoelastic response of nafion. effects of temperature and hydration on tensile creep. Macromolecules 41, 9849–9862.

Mäkelä, P., Östlund, S., 2003. Orthotropic elastic-plastic material model for paper materials. International Journal of Solids and Structures 40, 5599–5620.

Makinde, A., Thibodeau, L., Neale, K., 1992. Design of a biaxial extensometer for measuring strains in cruciform specimens. Experimental Mechanics 32, 138–144.

Matthews, R., Duckett, R., Ward, I., Jones, D., 1997. The biaxial drawing behaviour of poly(ethylene terephthalate). Polymer 38, 4795–4802.

Matthey, J., 2007. Fuel cells. http://www.fuelcelltoday.com/reference/image-bank/Schematics/In-depth-PEM-schematic.

Mauritz, K., Moore, R., 2004. State of understanding of Nafion. Chemical Reviews 104, 4535–4585.

Meijer, H., Govaert, L., 2005. Mechanical performance of polymer systems: The relation between structure and properties. Progress in Polymer Science 30, 915–938.

Meyer, W., 1998. Polymer electrolytes for lithium-ion batteries. Advanced Materials 10, 439–448.

Morris, D., Sun, X., 1993. Water-sorption and transport properties of Nafion 117-H. Journal of Applied Polymer Science 50, 1445–1452.

Mulliken, A., Boyce, M., 2006. Mechanics of the rate-dependent elastic-plastic deformation of glassy polymers from low to high strain rates. International Journal of Solids and Structures 43, 1331–1356.

Neburchilov, V., Martin, J., Wang, H., Zhang, J., 2007. A review of polymer electrolyte membranes for direct methanol fuel cells. Journal of Power Sources 169, 221–238.

Neburchilova, V., Martina, J., Wang, H., Zhanga, J., 2007. A review of polymer electrolyte membranes for direct methanol fuel cells. Journal of Power Sources 169, 221–238.

Nemat-Nasser, S., 2008. Electrochemomechanics of ionic polymer metal composites. Springer.

Oosawa, F., 1971. Polyelectrolytes. Marcel Dekker.

Pai, C., Boyce, M., Rutledge, G., 2009. Morphology of porous and wrinkled fibers of polystyrene electrospun dimethylformamide. Macromolecules 42, 2102–2114.

Pai, C., Boyce, M., Rutledge, G., 2011. Mechanical properties of individual electrospun pa 6(3)t fibers and their variation with fiber diameter. submitted.

Palmer, J., Boyce, M., 2008. Constitutive modeling of the stress-strain behavior of F-actin filament networks. Acta Biomaterialia 4, 597–612.

Patankar, K., Dillard, D., Case, S., Ellis, M., Li, Y., Lai, Y., Budinski, M., Gittleman, C., 2010. Characterizing fracture energy of proton exchange membranes using a knife slit test. Journal of Polymer Science: Part B: Polymer Physics 48, 333–343.

Petterson, D., 1959. Mechanics of nonwoven fabrics. Industrial and Engineering Chemistry 51, 902–903.

Porod, G., 1948. Acta Phys. Austr. 3, 255–292.

Ramasubramanian, M., Perkins, R., 1988. Computer simulation of the uniaxial elastic-plastic behavior of paper. Journal of Engineering Materials and Technology 110, 117–123.

Ridruejo, A., Gonzlez, C., Llorca, J., 2010. Damage micromechanisms and notch sensitivity of glass-fiber non-woven felts: An experimental and numerical study. Journal of the Mechanics and Physics of Solids 58, 1628–1645.

Ridruejo, A., Gonzlez, C., Llorca, J., 2011. Micromechanisms of deformation and fracture of polypropylene nonwoven fabrics. International Journal of Solids and Structures 48.

Riggleman, R., Lee, H., Edigerb, M., de Pabloc, J., 2010. Heterogeneous dynamics during deformation of a polymer glass. Soft Matter 6, 287–291.

Rubatat, L., Diat, O., 2007. Stretching effect on Nafion fibrillar nanostructure. Macromolecules 40, 9455–9462.

Rubatat, L., Gebel, G., Diat, O., 2004. Fibrillar structure of Nafion: Matching fourier and real space studies of corresponding films and solutions. Macromolecules 37, 7772–7783.

Rubatat, L., Rollet, A., Gebel, G., Diat, O., 2002. Evidence of elongated polymeric aggregates in Nafion. Macromolecules 35, 4050–4055.

Rutledge, G., Lowery, J., Pai, C., 2009. Characterization by mercury porosimetry of nonwoven fiber media with deformation. Journal of Engineered Fibers and Fabrics 4, 1–13.

Salamantina, O., Rudnev, S., Voenniy, V., Oleynik, E., 1992. Heat and stored energy of plastic-deformation of solid polymers and hetergenous blends. Journal of Thermal Analysis 38, 1271–1281.

Satterfield, M., Benziger, J., 2008. Non-Fickian water vapor sorption dynamics by Nafion membranes. Journal of Physical Chemistry B 112, 3693–3704.

Satterfield, M., Benziger, J., 2009. Viscoelastic properties of nafion at elevated temperature and humidity. Journal of Polymer Science: Part B: Polymer Physics 47, 11–24.

Satterfield, M., Majsztrik, P., Ota, H.. Benziger, J., Bocarsly, A., 2006. Mechanical properties of nafion and titania/Nafion composite membranes for polymer electrolyte membrane fuel cells. Journal of Polymer Science Part B: Polymer Physics 44, 2327–2345.

Schmidt-Rohr, K., Chen, Q., 2008. Parallel cylindrical water nanochannels in Nafion fuel-cell membranes. Nature Materials 7, 75–83.

Silberstein, M., February 2008. Mechanics of proton exchange membranes: Time, temperature, and hydration dependence of the stress-strain behavior of persulfonated polytetrafluoroethylene. Ms thesis, Massachusetts Institute of Technology, Cambridge, MA.

Silverman, T., Meyers, J., Beaman, J., 2010. Modeling water transport and swelling in polymer electrolyte membranes. Journal of the Electrochemical Society 157, B1376–B1381.

Solasi, R., Huang, X., Reifsnider, K., 2010. Creep and stress-rupture of Nafion membranes under controlled environment. Mechanics of Materials 42, 678–685.

Solasi, R., Zou, Y., Huang, X., 2008. A time and hydration dependent viscoplastic model for polyelectrolyte membranes in fuel cells. Mechanics of Time-Dependent Materials 12, 15–30.

Solasi, R., Zou, Y., Huang, X., Reifsnider, K., Condit, D., 2007. On mechanical behavior and in-plane modeling of constrained PEM fuel cell membranes subjected to hydration and temperature cycles. Journal of Power Sources 167, 366–377.

Sweeney, J., Collins, T., Coates, P., Ward, I., 1997. Application of an elastic model to the large deformation, high temperature stretching of polypropylene. Polymer 38, 5991–5999.

Sweeney, J., Spares, R., Woodhead, M., 2009. A constitutive model for large multiaxial deformations of solid polypropylene at high temperature. Polymer Engineering and Science 49, 1902–1908.

Tang, Y., Karlsson, A., Santare, M., Gilbert, M., Cleghorn, S., Johnson, W., 2006a. An experimental investigation of humidity and temperature effects on the mechanical properties of perfluorosulfonic acid membranes. Materials Science and Engineering A 45, 297–304.

Tang, Y., Santare, M., Karlsson, A., Cleghorn, S., Johnson, W., 2006b. Stresses in proton exchange membranes due to hygro-thermal loading. Journal of Fuel Cell Science and Technology 119, 119–124.

DuPont, 2004. Product information, DuPont Nafion PFSA membranes.

Vielstich, W., Lamm, A., Gasteiger, H., 2003. Handbook of fuel cells : fundamentals, technology, and applications. Wiley & Sons.

Wang, Y., 2009. Recent research progress on polymer electrolytes for dye-sensitized solar cells. Solar Energy Materials and Solar Cells 93, 1167–1175.

Weber, A., Newman, J., 2004. A theoretical study of membrane constraint in polymer-electrolyte fuel cells. American Institute of Chemical Engineers Journal 50, 3215–3226.

Wilhelm, J., Frey, E., 2003. Elasticity of stiff polymer networks. Physical Review Letters 91, 108103–1–4.

Wu, X.-F., Dzenis, Y. A., 2005. Elasticity of planar fiber networks. Journal of Applied Physics 98, 093501–1–9.

Xia, Q., Boyce, M., Parks, D., 2002. A constitutive model for the anisotropic elastic-plastic deformation of paper and paperboard. International Journal of Solids and Structures 39, 4053–4071.

Yeo, S., Eisenberg, A., 1977. Physical properties and supermolecular structure of perfluorinated ion-containing (Nafion) polymers. Journal of Applied Polymer Science 21, 875–898.

Yoon, W., Huang, X., 2010. A multiphysics model of PEM fuel cell incorporating the cell compression effects. Journal of the Electrochemical Society 157, B680–B690.

Zeng, F., Grognec, P. L., Lacrampe, M., Krawczak, P., 2010. A constitutive model for semi-crystalline polymers at high temperature and finite plastic strain: Application to PA6 and PE biaxial stretching. Mechanics of Materials 42, 686–697.

Zhang, X., Ajji, A., 2003. Biaxial orientation behavior of polystyrene: Orientation and properties. Journal of Applied Polymer Science 89, 487–496.